



**TURUN  
YLIOPISTO**  
UNIVERSITY  
OF TURKU

# BIOMECHANICAL TUMOUR MATRIX

---

Jasmin Kaivola





**TURUN  
YLIOPISTO**  
UNIVERSITY  
OF TURKU

# **BIOMECHANICAL TUMOUR MATRIX**

---

Jasmin Kaivola

## University of Turku

---

Faculty of Medicine  
Institute of Biomedicine  
Medical Biochemistry and Genetics  
Turku Doctoral Programme of Molecular Medicine  
Turku Bioscience Centre

## Supervised by

---

Professor Johanna Ivaska  
Turku Bioscience Centre  
University of Turku and  
Åbo Akademi  
Turku, Finland

## Reviewed by

---

Associate Professor Anniina Färkkilä  
FIMM and HiLife  
University of Helsinki  
Helsinki, Finland

Associate Professor Valerio Izzi  
Faculty of Biochemistry and  
Molecular Medicine  
University of Oulu  
Oulu, Finland

## Opponent

---

Professor Rachel Lennon  
Wellcome Centre for Cell-Matrix Research  
School of Biological Science  
Faculty of Biology, Medicine and Health  
University of Manchester  
Manchester, United Kingdom

The originality of this publication has been checked in accordance with the University of Turku quality assurance system using the Turnitin OriginalityCheck service.

ISBN 978-951-29-9937-8 (PRINT)  
ISBN 978-951-29-9938-5 (PDF)  
ISSN 0355-9483 (Print)  
ISSN 2343-3213 (Online)  
Painosalama, Turku, Finland 2024

*To my mother Angelina*

UNIVERSITY OF TURKU  
Faculty of Medicine  
Institute of Biomedicine  
Medical Biochemistry and Genetics  
Turku Bioscience Centre  
JASMIN KAIVOLA: Biomechanical Tumour Matrix  
Doctoral Dissertation, 225 pp.  
Turku Doctoral Programme of Molecular Medicine  
November 2024

## ABSTRACT

The interplay between mechanical forces and the tumour microenvironment is critical in cancer progression, influencing tumour growth, metastasis and therapy resistance. Integrins, which mediate cell adhesion to the extracellular matrix (ECM), transmit mechanical signals that regulate key cellular processes including proliferation and migration. These mechanical forces modulate integrin activity, altering the cytoskeleton and signalling networks, thereby promoting cancer invasiveness and metastasis. The tumour matrix's physical properties, such as stiffness, further drive cancer progression. Cancer-associated fibroblasts remodel the ECM, increasing matrix stiffness and enhancing mechanotransduction pathways. Moreover, cancer-associated adipocytes contribute to metabolic reprogramming and inflammation, creating a feedback loop that accelerates tumour growth. Understanding these molecular mechanisms is crucial for developing therapies that disrupt these pathways to inhibit cancer progression and metastasis.

In this thesis, I have explored how reintroducing mechanical forces lost in cancer, owing to increased tissue rigidity, can downregulate oncogenic signalling activity. Specifically, stretching and vibrating vocal fold cancer cells lead to nucleocytoplasmic localisation of the oncogenic transcription factors YAP/TAZ and  $\beta$ -catenin. Additionally, I have investigated the role of healthy adipocytes in the breast tumour microenvironment, demonstrating that secretion of the adipocrine factor IGFBP2 can act as a protective barrier against breast cancer progression. Lastly, I examined the role of the integrin inactivator SHANK3 in KRAS-driven cancers, showing that disrupting the SHANK3-KRAS interaction can induce cell death in KRAS-mutant cancer cells through hyperactivation of the MAPK-ERK pathway. Collectively, these findings offer novel strategies to inhibit and target cancer progression across different cancer types.

**KEYWORDS:** biomechanics, mechanosensing, extracellular matrix, cell-cell adhesion, cell-ECM adhesion, cancer

TURUN YLIOPISTO

Lääketieteellinen tiedekunta

Biolääketieteen laitos

Lääketieteellinen biokemia ja genetiikka

Turun biotiedekeskus

JASMIN KAIVOLA: Biomekaaninen kasvainmatriksi

Väitöskirja, 225 s.

Molekyyli­lääketieteen tohtoriohjelma

Marraskuu 2024

## TIIVISTELMÄ

Mekaanisten voimien ja kasvaimen mikroympäristön välinen vuorovaikutus on kriittinen syövän etenemisessä, vaikuttaen kasvaimen kasvuun, etäpesäkkeiden muodostumiseen ja hoitoresistenssiin. Integriinit, jotka välittävät solun adheesiota soluväliaineeseen, välittävät mekaanisia signaaleja, jotka säätelevät solun keskeisiä prosesseja, kuten proliferaatiota ja migraatiota. Nämä mekaaniset voimat säätelevät integriinien aktiivisuutta, muuttaen solutukirankaa ja signalointireittejä, ja täten edistäen syövän invasiivisuutta sekä etäpesäkkeiden muodostumista. Kasvainmatriksin fysikaaliset ominaisuudet, kuten jäykkyys, edistävät edelleen syövän etenemistä. Syöpään liittyvät fibroblastit muokkaavat soluväliainetta lisäämällä matriksin jäykkyyttä ja tehostaen mekaanisia signalointireittejä. Syöpään liittyvät adiposyytit vuorostaan edistävät aineenvaihdunnan uudelleenohjelmointia ja tulehdusta luoden palautesilmukan, joka nopeuttaa kasvaimen kasvua. Näiden molekyyli­mekanismien ymmärtäminen on ratkaisevan tärkeää kehitettäessä hoitoja, jotka estävät näitä reittejä ja siten syövän etenemistä sekä etäpesäkkeiden muodostumista.

Tässä väitöskirjassa olen tutkinut, kuinka syövässä menetettyjen mekaanisten voimien palauttaminen voi heikentää onkogeenista signaalitoimintaa. Äänihuuli­syövän solujen venyttäminen ja värähdyttäminen johtavat onkogeenisten transkriptiotekijöiden YAP/TAZ:n ja  $\beta$ -kateniinin vähentyneeseen nukleosyttoplasmiseen lokalisaatioon. Lisäksi olen tutkinut terveiden rasvasolujen roolia rintakasvaimen mikroympäristössä osoittaen, että adipokriinisen tekijän IGF2P2 erittyminen voi toimia suojaavana tekijänä rintasyövän etenemistä vastaan. Lopuksi tutkin integriini­inaktivaattorin SHANK3:n roolia KRAS-syövässä osoittaen, että SHANK3-KRAS-vuorovaikutuksen häiritseminen voi aiheuttaa solukuolemaa KRAS-mutatoituneissa syöpäsoluissa MAPK-ERK-reitin hyperaktivoinnin kautta. Yhdessä nämä havainnot tarjoavat uusia strategioita syövän etenemisen estämiseksi eri syöpätyypeissä.

AVAINSANAT: biomekaniikka, mekaaninen aistiminen, soluväliaine, solu-solu adheesiot, solu-soluväliaine adheesiot, syöpä

# Table of Contents

<b>Abbreviations .....</b>	<b>9</b>
<b>List of Original Publications .....</b>	<b>11</b>
<b>1 Introduction .....</b>	<b>12</b>
<b>2 Review of the Literature .....</b>	<b>14</b>
2.1 Biomechanics in the tumour matrix .....	14
2.2 Integrin-adhesion complexes (IAC's) in the tumour matrix.....	15
2.2.1 IAC structure .....	16
2.2.2 IAC formation and regulation.....	19
2.2.3 IAC function .....	22
2.3 Tumour – Tumour matrix interaction.....	25
2.3.1 Extracellular matrix (ECM) .....	27
2.3.2 Cancer-associated fibroblasts (CAFs).....	30
2.3.3 Cancer-associated adipocytes (CAAs).....	31
2.4 Cellular mechanosensing .....	33
2.4.1 Mechanical forces in homeostasis and cancer .....	35
2.4.2 Cell-cell and ECM mediated mechanotransduction .....	36
2.4.3 Oncogenic functions of mechanosensitive transcriptional mediators .....	39
<b>3 Aims .....</b>	<b>44</b>
<b>4 Materials and Methods .....</b>	<b>45</b>
4.1 Cell culture (I, II, III).....	45
4.2 Plasmid DNA and siRNA transfections (II) .....	46
4.3 Antibodies and antibody detection (I, II, III).....	46
4.4 Gene and protein expression (I, II) .....	48
4.4.1 Quantitative real-time PCR (II) .....	48
4.4.2 RNA sequencing .....	48
4.4.3 Western blot assay (I, II) .....	48
4.5 Methods to study cell growth (I, II).....	49
4.5.1 Proliferation assay (I, II) .....	49
4.5.2 Viability assay (I, II) .....	49
4.5.3 Flow cytometry (II).....	49
4.5.4 3D spheroid formation assay (I, II).....	50
4.6 Methods to study cell migration and invasion (I).....	50
4.6.1 Migration assay (I).....	50
4.6.2 Wound healing assay (I).....	50



4.6.3	Invasion assay (I) .....	51
4.7	In vivo methods (I, II, III) .....	51
4.7.1	Chick embryo chorioallantoic membrane assay (II) .....	51
4.7.2	Subcutaneous tumour xenograft (II, III) .....	51
4.7.3	Patient samples (I) .....	52
4.8	Methods to study cell mechanics (I) .....	52
4.8.1	Cell stretching (I) .....	52
4.8.2	Cell vibration (I) .....	53
4.8.3	Cell growth on elastic surfaces (I).....	53
4.9	Imaging techniques (I, II).....	53
4.9.1	Immunolabeling (I, II).....	53
4.9.2	Imaging fixed samples (I) .....	54
4.9.3	Live imaging (I, II).....	54
4.10	Genomic databases (I) .....	54
4.10.1	The Cancer Genome Atlas (TCGA) (I).....	54
4.10.2	Cancer Dependency Map (DepMap) (I).....	54
4.11	Statistical analysis (I, II).....	55
<b>5</b>	<b>Results .....</b>	<b>56</b>
5.1	Tumour reversion by mechanical stimuli in vocal fold cancer (I).....	56
5.1.1	ECM remodelling and increased rigidity supports migration and invasion in VFC.....	56
5.1.2	Laminin-binding integrins modulate VFC monolayer dynamics and cell clustering.....	57
5.1.3	Uncovering a previously unobserved motility state in VFC cells.....	59
5.1.4	Mimicking mechanical stimuli in the vocal folds induces cytoskeletal changes, junctional alterations and cell extrusion .....	60
5.1.5	Mimicking mechanical stimuli in the vocal folds decreases nuclear and total YAP levels .....	60
5.1.6	Therapeutic potential of YAP-TEAD inhibition .....	62
5.2	Signalling overdose to target KRAS-mutant cancers (II).....	62
5.2.1	SHANK3's interaction with active KRAS and modulation of MAPK/ERK signalling.....	63
5.2.2	SHANK3 in KRAS-mutant cancer cell viability .....	64
5.2.3	SHANK3 depletion leads to tumour suppression <i>in vivo</i> .....	64
5.2.4	SHANK3-induced cell death via RAS-MAPK pathway hyperactivation .....	64
5.2.5	Therapeutic potential of targeting the SHANK3-KRAS interaction .....	65
5.3	Mammary adipocytes restrict breast cancer invasion (III) .....	66
5.3.1	IGFBP2 secretion inhibits cancer cell invasion .....	67
5.3.2	IGFBP2 mechanism of action.....	67
5.3.3	IGFBP2 expression limits invasion <i>in vivo</i> .....	68
5.3.4	IGFBP2 secretion by mammary adipocytes and its therapeutic implications .....	68
<b>6</b>	<b>Discussion .....</b>	<b>70</b>

6.1	Mechanical intervention as a therapeutic approach (I) .....	70
6.2	Exploiting targeted signalling overdose (II).....	74
6.3	Secretion of barrier-reinforcing factors in cancer (III).....	76
<b>7</b>	<b>Conclusions .....</b>	<b>78</b>
	<b>Acknowledgements.....</b>	<b>80</b>
	<b>References .....</b>	<b>82</b>
	<b>Original Publications.....</b>	<b>111</b>

# Abbreviations

AFM	Atomic force microscopy
AKT	Protein kinase B
AMOTL2	Angiomotin-like protein 2
ARR	Ankyrin repeat region
BM	Basement membrane
CAA	Cancer-associated adipocyte
CAF	Cancer-associated fibroblast
CAM	Chorioallantoic membrane
CCL2	C–C motif chemokine ligand 2
CCL5	C–C motif chemokine ligand 5
COL I	Collagen I
CRC	Colorectal cancer
DCIS	Ductal carcinoma in situ
ECM	Extracellular matrix
EGF	Epidermal growth factor
EGFR	Epidermal growth factor receptor
EMT	Epithelial-mesenchymal transition
ERK	Extracellular signal-regulated kinase
FA	Focal adhesion
FAK	Focal adhesion kinase
FAO	Fatty acid oxidation
FAP	Fibroblast activation protein
FBS	Fetal bovine serum
FFA	Free-fatty acid
FN	Fibronectin
GFP	Green fluorescent protein
GPCR	G-protein coupled receptor
IAC	Integrin-adhesion complex
IDC	Invasive ductal carcinoma
IGF-II	Insulin-like growth factor 2
IGFBP2	Insulin-like growth factor-binding protein 2

IL-6	Interleukin 6
ILK	Integrin-linked kinase
KO	Knockout
KRAS	Kirsten rat sarcoma viral oncogene homolog
LM	Laminin
MAPK	Mitogen-activated protein kinase
MMP	Matrix-metalloproteinase
MRTF	Myocardin-related transcription factor
NSCLC	Non-small cell lung cancer
PBS	Phosphate-buffered saline
PDAC	Pancreatic ductal adenocarcinoma
PDGF	Platelet-derived growth factor
PDMS	Polydimethylsiloxane
PFA	Paraformaldehyde
PT	Phase transition
RA	Ras-association
RBD	Ras-binding domain
RNAi	Ribonucleic acid interference
ROCK	Rho-associated protein kinase
SHANK3	SH3 and multiple ankyrin repeat domains 3
siRNA	Small interfering ribonucleic acid
SMA	Smooth muscle actin
SPN	Shank/ProSAP N-terminal domain
SRF	Serum response factor
TAZ	Transcriptional coactivator with PDZ-binding motif
TEAD	Transcriptional enhanced associate domain
TGF- $\beta$	Transforming growth factor $\beta$
TMA	Tissue microarray
TME	Tumour microenvironment
TNBC	Triple-negative breast cancer
VFC	Vocal fold cancer
VEGF	Vascular endothelial growth factor
WT	Wild-type
YAP	Yes-associated protein 1

# List of Original Publications

This dissertation is based on the following original publications, which are referred to in the text by their roman numerals:

- I Kaivola J, Punovuori K, Chastney MR, Miroshnikova YA, Abdo H, Bertillot F, Krautgasser F, Di Franco J, Conway JRW, Follain G, Hagström J, Mäkitie A, Irjala H, Ventelä S, Hamidi H, Scita G, Cerbino R, Wickström SA and Ivaska J. Restoring mechanophenotype reverts malignant properties of ECM-enriched vocal fold cancer. *Manuscript*
- II Lilja J\*, Kaivola J\*, Conway JRW, Vuorio J, Parkkola H, Roivas P, Dibus M, Chastney MR, Varila T, Jacquemet G, Peuhu E, Wang E, Pentikäinen U, Posada IMD, Hamidi H, Najumudeen AK, Sansom OJ, Barsukov IL, Abankwa D, Vattulainen I, Salmi M and Ivaska J. SHANK3 depletion leads to ERK signalling overdose and cell death in KRAS-mutant cancers. *Nature Communications*, 2024; 15(1):8002
- III Conway JRW, Dinç DD, Follain G, Paavolainen O, Kaivola J, Boström P, Hartiala P, Peuhu E and Ivaska J. IGFBP2 secretion by mammary adipocytes limits breast cancer invasion. *Science Advances*, 2023; 9(28):eadg1840

\*These authors contributed equally.

The original publications have been reproduced with the permission of the copyright holders.

# 1 Introduction

Cells adhere to other cells and to the extracellular matrix (ECM) through adhesion molecules at the cell surface. These adhesion molecules are essential for the formation of larger structures such as tissues and organs. Direct and indirect cell-cell and cell-ECM contact enables interaction with other cell surface molecules that regulate cellular functions, including cell proliferation and migration (Gumbiner, 1996). This regulation is highly controlled, as cells need to sense and respond to the changes in their microenvironment to ensure correct and effective signalling to maintain homeostasis. In response to cues from the microenvironment, cells modulate biochemical signalling pathways, which can lead to changes in adhesion capability and strength. Alterations in the way cells respond to these changes in their microenvironment contribute to different steps of cancer progression (Beri et al., 2020; Ungai-Salánki et al., 2021).

Not only do cells sense and respond to biochemical cues, but also mechanical cues play an important role in homeostasis (Wickström & Niessen, 2018). Cells are subjected to internal and external mechanical forces. These mechanical forces are sensed through specialized proteins, mechanosensors, that convert physical information into biochemical signalling cascades (Di et al., 2023). Cells experience a variety of mechanical stimuli, such as stretching, vibration, sheer stress, substrate stiffness, compression and hydrostatic pressure. Cells adapt to these mechanical cues by reinforcing their force-bearing structures, which are located at the cell-cell boundaries and cell-ECM boundaries, by shielding their nuclei through remodelling their cytoskeleton or by nucleocytoplasmic shuttling of mechanoresponsive transcription factors (Andreu et al., 2021; Kechagia et al., 2019a; Kirby & Lammerding, 2018; Yap et al., 2018).

Cells do not merely passively adhere to the ECM, as adhesion is essential for cell growth and modulating signalling pathways. Therefore, the architecture and composition of the ECM must be tightly regulated, as changes in the biophysical properties of the ECM lead to altered responses to mechanical cues. In a variety of pathological conditions, such as fibrosis and cancer, the aberrant ECM composition that frequently results in tissue stiffening, provides cancer cells an effective base for cell growth, which ultimately can give rise to a tumour (Winkler et al., 2020).

Research on ECM mechanics and its influence on cancer biology has revealed that mechanical stress within the ECM can activate signalling pathways that drive tumour progression. Activation of signalling pathways can lead to changes in gene expression, cytoskeletal organization and other cellular functions, affecting the mechanical properties of cells (Di et al., 2023). Moreover, mechanical cues from the ECM can influence cancer therapy efficacy, for tumours with a stiffer ECM exhibit enhanced drug resistance (Kalli et al., 2023; Mai et al., 2024). Therefore, it is crucial to understand the mechanical properties of the ECM in homeostasis and in pathology, and its crosstalk with force-sensing molecules. Recent advances in mechanobiology have brought the field forward, especially regarding changes in tissue stiffness in pathology. However, the fundamental differences in mechanical properties between different tissue types in homeostasis have been overlooked. Therefore, rather than simply focusing on the pathological outcome, it is necessary to consider the imbalance that has led to changes in the mechanical properties of tissues and how it differs from homeostasis. Moreover, the tumour matrix and the other cell types within the tumour microenvironment (TME), such as fibroblasts, immune cells and adipocytes, are pivotal in tumorigenesis (de Visser & Joyce, 2023).

The purpose of this thesis is to explore the biomechanical tumour matrix, by studying how the vocal folds, an organ that is normally under constant mechanical tension, respond to external mechanical stimulus which is lost in vocal fold cancer, and how normal healthy adipocytes influence breast cancer progression. Additionally, I have investigated how cell signalling pathway hyperactivation can be utilized for targeted cell death in KRAS-mutant cancers. The results presented in this thesis will expand our knowledge on biomechanics by providing a new view on how mechanobiology can differ depending on the tissue type and provide insights on the co-operation of normal adipocytes and cancer cells in the TME.

## 2 Review of the Literature

### 2.1 Biomechanics in the tumour matrix

Cells exist within a complex and dynamic microenvironment where mechanical forces have a substantial impact on regulating their behaviour and function (Ladoux & Mège, 2017). Under normal conditions, cells are tightly regulated and respond to signals in a coordinated manner, leading to outcomes such as growth, differentiation and programmed cell death (apoptosis). This regulation is part of a broader mechanism ensuring homeostasis, that allows cells to maintain cellular stability. However, normal cells can acquire mutations that grant them the capability to bypass these regulatory controls, leading to unrestricted growth and tumorigenesis (Hanahan, 2022). In addition to normal cells gaining these advantageous characteristics, changes in the cell microenvironment, such as in the ECM and the surrounding cells, further incite the onset of tumorigenesis and metastasis (de Visser & Joyce, 2023).

Solid tumours are embedded in the ECM, a complex network that occupies the spaces in tissues lacking cells, supporting their structure and function through components like glycosaminoglycans, proteoglycans, glycoproteins and fibrous proteins. Consequently, the cell-ECM connection is essential for regulating cell growth, proliferation and differentiation. This regulation mediates changes in cell behaviour by directly tuning gene and protein expression patterns and indirectly modifying the environmental cues, such as the levels and organization of ECM components (Humphrey et al., 2014). The biochemical and biomechanical properties of the tumour ECM are often altered, leading to changes in tissue architecture, topography and biomechanics, which significantly impact cancer progression. These changes are driven both by cancer cells and cancer-associated-fibroblasts (CAFs), often resulting in stiffening of the pathological tissue (Najafi et al., 2019; Sahai et al., 2020). Furthermore, mechanosensing is essential for homeostatic control of the ECM in healthy tissues. For instance, the ECM provides an optimal substrate rigidity for controlled cell proliferation and migration (Pally & Naba, 2024; Winkler et al., 2020). In addition to permitting proliferation, sensing substrate rigidity serves as a means to induce apoptosis: normal cells on soft matrices undergo apoptosis, whereas those on stiffer ones proliferate. However, cancer cells can exploit this system, being able to grow on softer matrices due to their decrease in rigidity sensing (B. Yang et



al., 2020). This substrate stiffness-dependent apoptosis, owing to failure in reinforcing cell-ECM adhesions, is normally mediated by two established mechanosensors, Yes-associated protein (YAP) and integrins (Shi et al., 2024).

Though the importance of tissue rigidity in tumorigenesis is undeniable, the biomechanical properties of the tumour matrix are not limited to it, as cells and tissues are subjected to a variety of intrinsic and external physical forces. Physical forces, including stretching, hydrostatic pressure and shear stress, remodel the cytoskeleton of cancer cells, affecting their mechanosensing properties and mechanotransduction pathways (Coban et al., 2021; Nia et al., 2020). Therefore, cellular mechanosensing in pathologies is of great interest, with emerging technologies, including dynamic micropatterns, hydrogels, nanoparticles, mechanical vibration and stretching paving the way for studying the key biomechanical regulatory mechanisms altered in cancer cells and in the tumour matrix (Cruz-Acuña et al., 2021; Di et al., 2023). Together these changes in the interactions between cells and the tumour matrix, highlight the complexity of the TME and the importance of the ECM in tumorigenesis.

## 2.2 Integrin-adhesion complexes (IAC's) in the tumour matrix

Cells adhere to the ECM through a group of transmembrane receptors, integrins, that are specialized in cell adhesion. Integrins, along with associated proteins, form integrin-adhesion complexes (IACs) that connect the ECM to the cell cytoskeleton (Chastney et al., 2021). IACs regulate multiple cellular processes, including adhesion, migration, proliferation and survival. IACs are essential components of the cell microenvironment, facilitating interactions between cells and the ECM, as well as between neighbouring cells. Alterations in IAC expression and localization can significantly influence tumour growth and the dissemination of cancer cells, leading to metastasis (Cooper & Giancotti, 2019).

Integrins interact with various ECM proteins, such as fibronectin, collagens and laminins, physically linking cells to the ECM (Kanchanawong & Calderwood, 2023). This linkage allows integrins to function as mechanosensors; cells sense their surroundings and adjust their functions based on the signals they receive through IACs. One of the most important functions of integrins being mechanosensors and binding to the ECM, is their ability to provide the traction required for cancer cell invasion (Kechagia et al., 2019b; Tan et al., 2020). Integrins transmit bidirectional signals across the plasma membrane in a process that is tightly regulated in homeostasis. Thus, changes in the composition of the ECM or IACs can profoundly affect signalling cascades mediated by integrins.

To ensure controlled signalling, integrins need to be activated for signalling to occur. Integrins contribute to the dynamic and reciprocal communication between cancer cells and their microenvironment, for example through association to major signalling molecules, such as growth factors, that are established regulators of tumorigenesis (Sarker et al., 2020). This communication is essential for remodelling of the ECM, which further supports tumorigenesis. The impact of dysregulated IACs extends beyond the tumour matrix to affect tumour vascularization and metastatic colonization, demonstrating that IACs play a crucial role in each step of the metastatic cascade (Hamidi & Ivaska, 2018). Therefore, by influencing the physical and biochemical properties of the ECM, integrins can support the creation of a microenvironment favourable for cancer progression.

Although targeting integrins in solid tumours has shown promise in preclinical studies, clinical trials have not yet achieved the desired efficacy, as challenges such as therapy resistance and variable patient outcomes persist (Pang et al., 2023). The complexity of integrin signalling and its integration with other cellular pathways highlights the need for a comprehensive understanding of IAC biology. Future therapeutic strategies may benefit from a more multidisciplinary approach that considers the diverse roles and co-operation of integrins, the ECM and biomechanics in cancer. This could involve combination therapies that target integrins along with other key regulators of the TME, aiming to overcome resistance mechanisms and improve patient outcomes.

### 2.2.1 IAC structure

IACs are multi-protein complexes that connect cells to the ECM and the cytoskeleton. IACs can roughly be split into two categories, actin-linked adhesions such as focal adhesions (FAs) and intermediated-filament network coupled hemidesmosomes (**Figure 1**). FAs are highly dynamic structures that rapidly respond to extracellular signals and mechanical forces. Hemidesmosomes form more stable adhesions that are crucial for the structural integrity of epithelial tissues. The assembly and regulation of both IAC types are critical for various cellular processes, including cell proliferation and migration. IACs comprise multiple adaptor proteins that link integrins to the cytoskeleton and mediate signalling from the ECM to the cell (Kanchanawong et al., 2010; Nahidiazar et al., 2015).

The core components in IACs, integrins, are transmembrane receptors that mediate the attachment between a cell and the ECM. Integrins were discovered in the 1970s and recognised as a family of cell surface receptors in 1987 (Hynes, 1987). Integrins are formed by single transmembrane helices, and in mammals, they give rise to 24 heterodimeric complexes. These complexes consist of  $\alpha\beta$ -heterodimers that bind to their ligands via a large extracellular domain. The specific combinations of  $\alpha$ - and

$\beta$ -subunits give rise to heterodimers capable of engaging and becoming activated by a subgroup of ligands, such as fibronectin, collagen, vitronectin, tenascin-c and laminin (**Table 1**). Integrin subunits have large extracellular domains which interact non-covalently at their head. In addition, both subunits have a single transmembrane domain and a short cytoplasmic tail. The cytoplasmic tails contain shared conserved motifs found in all integrins as well as subunit-specific amino acid sequences. Both are essential for signalling, and the subunit-specific segments provide a means for integrin heterodimer specific signalling upon binding to different ligands. The cytoplasmic tails of integrins mediate signalling with various intracellular adaptor proteins in IACs (Chastney et al., 2021; Kadry & Calderwood, 2020).

**Table 1.** Integrin heterodimers and their ECM ligands.

ECM ligand	Integrin heterodimer
Fibronectin	$\alpha 4\beta 1$ , $\alpha 5\beta 1$ , $\alpha 8\beta 1$ , $\alpha 11\beta 1$ , $\alpha \nu\beta 3$ , $\alpha \nu\beta 6$ and $\alpha \nu\beta 8$
Collagen	$\alpha 1\beta 1$ , $\alpha 2\beta 1$ , $\alpha 10\beta 1$ and $\alpha 11\beta 1$
Vitronectin	$\alpha \nu\beta 1$ , $\alpha \nu\beta 3$ , $\alpha \nu\beta 5$ and $\alpha 11\beta 3$
Tenascin-C	$\alpha 9\beta 1$ , $\alpha 8\beta 1$ , $\alpha \nu\beta 1$ and $\alpha \nu\beta 6$
Laminin	$\alpha 3\beta 1$ , $\alpha 6\beta 1$ , $\alpha 6\beta 4$ and $\alpha 7\beta 1$

In FAs the main adaptor proteins include talin, kindlin, paxillin and vinculin. Talin binds to the integrin  $\beta$ -tail to activate integrins, in addition to linking them to the actin cytoskeleton (**Figure 1**). Kindlin binds to integrins and assists in integrin activation, whereas vinculin binds to talin and actin, stabilizing the link between integrins and the cytoskeleton (Aretz et al., 2023; Boujemaa-Paterski et al., 2020; Franz et al., 2023). Paxillin is a scaffolding protein that further recruits additional signalling and adaptor proteins to the complex (Efimov et al., 2008; Webb et al., 2004). The most important signalling proteins in FAs include focal adhesion kinase (FAK), a non-receptor tyrosine kinase, and src family of tyrosine kinases that are activated upon integrin engagement (Arias-Salgado et al., 2003; J.-C. Wu et al., 2015). As FAs are linked to the actin cytoskeleton, they also recruit other cytoskeletal proteins such as  $\alpha$ -actinin, that cross-links actin filaments and connects them to integrins. Other regulatory proteins, such as parvin and integrin-linked kinase (ILK), are associated to FAs for example to regulate the assembly and disassembly of FAs, thus controlling cell adhesion and migration (Kanchanawong et al., 2010; Kanchanawong & Calderwood, 2023).

Hemidesmosomes anchor epithelial cells to the basement membrane (BM), providing mechanical stability and structural integrity to tissues. These structures are primarily composed of the  $\alpha 6\beta 4$ -integrin heterodimer (**Figure 1**), whereas FAs can

be made up of variety of different heterodimers. In addition to the difference in the core integrin component, hemidesmosomes connect cells directly to the keratin intermediate filament cytoskeleton instead of actin (Krausova et al., 2021; Walko et al., 2015). In hemidesmosomes,  $\alpha 6\beta 4$ -integrin adheres to the ECM through binding laminin-332, which is a major glycoprotein in the BM. Similar to integrins, collagen XVII (BP180) is a transmembrane protein, that links the ECM to the intracellular

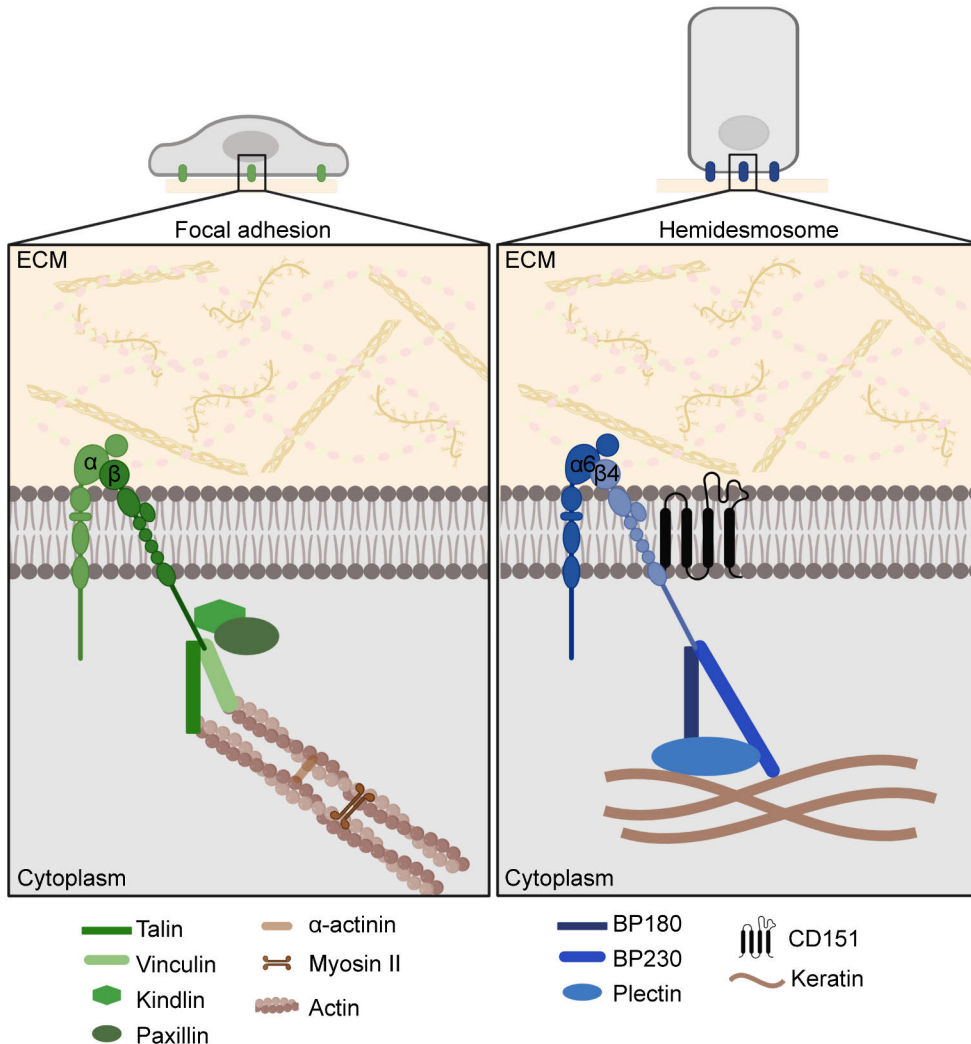


**Figure 1. Focal adhesion (FA) and hemidesmosome composition.** FAs comprise various integrin heterodimers and are connected to the actomyosin cytoskeleton via talin and vinculin. In hemidesmosomes adhesion is mediated by  $\alpha 6\beta 4$ -integrin and they are linked to the keratin intermediate filament cytoskeleton via plectin and BP180.

plaque in hemidesmosomes, and these intracellular plaques interact with the intermediate filament cytoskeleton. Moreover, another membrane spanning protein, tetraspanin CD151, functions as a scaffolding protein to associate  $\alpha 6\beta 4$ -integrins to intracellular proteins. Plectin is a cytoskeletal adaptor protein that connects the intermediate filaments to the intracellular plaque and interacts with Bullous Pemphigoid Antigen 1 (BP230) and  $\beta 4$ -integrin, linking the cytoplasmic plaque to the intermediate filament cytoskeleton. The intermediate filament cytoskeleton comprises of keratins 5 and 14, providing hemidesmosomes tensile strength and mechanical resistance (Molder et al., 2021; Nahidiazar et al., 2015).

## 2.2.2 IAC formation and regulation

IAC formation and regulation are highly controlled and dynamic processes involving multiple steps, including integrin activation, recruitment of adaptor and signalling proteins, and interaction with the cytoskeleton (Hynes, 2002). IAC regulation ensures that cells can respond appropriately to changes in their environment and perform functions such as differentiation, proliferation and migration. This regulation involves transcriptional control, post-translational modifications and interactions with various structural and regulatory components in addition to growth factors (Gahmberg et al., 2019; Gahmberg & Grönholm, 2022; Legerstee et al., 2021). Moreover, mechanical forces are also transmitted through IACs and these forces can influence the size and stability of FAs, as well as activate signalling pathways (Nardone et al., 2017; Yao et al., 2022).

IAC formation begins with integrin activation, which is dependent on their conformation as conformational changes enable activation and signalling (**Figure 2**). Integrin signalling is bi-directional meaning that integrins can be activated through intracellular signals or ligand binding. In their resting state, integrins are typically in a low-affinity (inactive) conformation for their ligands in the ECM. In this state, the extracellular domains are bent and the cytoplasmic tails are close together. Ligand binding or binding of intracellular adaptor proteins leads to integrin activation through a transitional extended closed intermediate state, before becoming fully activated in an extended open conformation (**Figure 2**) (Kolasangiani et al., 2022). Integrin inactivators interfere with the activation and function of integrins. Allosteric integrin inhibitors bind to sites other than the ligand-binding site, stabilizing the inactive conformation of integrins and preventing them from adopting the active conformation (**Figure 2**). SHARPIN (SHANK-associated RH domain-interacting protein) and LRP12 (Low-density lipoprotein receptor-related protein 12) indirectly inhibit integrin activation by binding to cytoplasmic integrin  $\alpha$ -tails and therefore inhibit talin binding (Gao et al., 2019; M. Huang et al., 2023; Rantala et al., 2011). Some integrin inactivators, such as ICAP1 (integrin cytoplasmic domain-

associated protein 1) and filamin, prevent activation by competitively binding to overlapping residues on the cytoplasmic  $\beta$ -tail, thus preventing binding of integrin activators, such as talin (Bouin et al., 2017; Bouvard et al., 2003; Calderwood et al., 2001; J. Liu et al., 2015). Another integrin inactivator protein, SHANK3 (SH3 and multiple ankyrin repeat domains 3), functions as a scaffolding protein. Though SHANK3 is primarily known for its role in neuronal synapses, where it regulates signalling and plasticity, it can also influence integrin activity in non-neuronal cells. SHANK3 can indirectly affect the activation and function of integrins by sequestering active RAP1 (Ras proximity 1), thus limiting talin recruitment to the plasma membrane. SHANK3 can also influence the organization and dynamics of the actin cytoskeleton, potentially altering the mechanical forces and signals that regulate integrin activation (Salomaa et al., 2021). Moreover, SHANK3 SPN domain has a Ras-association domain with a high affinity for GTP-bound Ras, indicating a possible relevance in regulating KRAS-mediated cancer cell migration and invasion (Lilja et al., 2017).

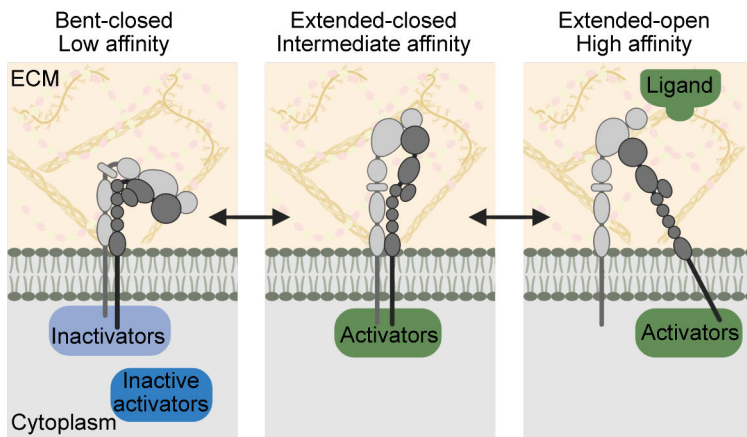


**Figure 2. Conformational activation of integrins.** Integrins are inactive in a bent closed conformation with low affinity, and activation is further inhibited by intracellular integrin inactivators. The intermediate primed conformation can be activated by recruitment of intracellular activators to the cytoplasmic integrin tails. High affinity integrins are in an extended-open conformation with activators binding to the cytoplasmic  $\beta$ -tails.

In FAs the cytoplasmic integrin tails interact with intracellular adaptor proteins such as talin. Talin binding to the integrin  $\beta$ -tail induces a conformational change that separates the  $\alpha$  and  $\beta$  subunits, extending the extracellular domain into an active conformation that can bind ECM ligands with high affinity. Though integrin signalling is bi-directional, a recent study implies that the ligand-integrin-talin-actomyosin cytoskeleton complex is required, as talin does not induce integrin extension or

opening, and the main activation initiating event would be extracellular ligand binding (J. Li et al., 2024). Talin binds to the integrin  $\beta$ -tail and to actin filaments, linking integrins to the cytoskeleton. Vinculin, another adaptor protein, binds to talin and further reinforces this connection (Atherton et al., 2019; Franz et al., 2023). Additional proteins such as paxillin, kindlin and focal adhesion kinase (FAK) are recruited to the developing FA, aiding in the organization and stability of the complex. These adaptor proteins, such as kindlin and talin, also interact together to activate integrins (Lu et al., 2022). Once activated, integrins bind to specific ECM proteins leading to integrin clustering, which enhances the strength of the cell-ECM adhesion (Cheng et al., 2020; Mana et al., 2023). In signal transduction, proteins such as FAK and src are activated in response to integrin engagement, initiating downstream signalling cascades that regulate changes in gene expression, cell survival, proliferation and migration without affecting IAC composition (Horton et al., 2016). Linkage to the actin cytoskeleton is formed through some of these adaptor proteins, such as talin, vinculin, tropomyosins and  $\alpha$ -actinin, and this connection is needed for mechanical stability of FAs and for the transmission of mechanical forces across the cell membrane (Kumari et al., 2024; Roca-Cusachs et al., 2013). Additionally, the linkage also enables cells to exert traction forces on the ECM (Atherton et al., 2019). FA regulation and turnover are tightly regulated by phosphorylation, dephosphorylation, endocytic recycling, proteolysis and mechanical forces. Phosphorylation and dephosphorylation modify the activity of IAC components to modulate FA assembly and disassembly (S. Kumar et al., 2023). Many components of FAs, including integrins, FAK, paxillin and src, are regulated by phosphorylation, modifying their activity, localization and interactions with other proteins. FA disassembly is a critical aspect of their regulation, allowing cells to detach from the ECM, which is essential for processes like cell migration and tissue remodelling (Mavrakis & Juanes, 2023). Proteolytic degradation of ECM components or adhesion proteins can trigger FA disassembly, modulating the strength and duration of cell-ECM adhesions. IAC degradation is regulated by ubiquitination and proteolysis, facilitating the disassembly of adhesions when needed (Teckchandani & Cooper, 2016). Moreover, local changes in pH and ion concentrations can also influence protein interactions and signalling within IACs. For example, changes in intracellular calcium ( $\text{Ca}^+$ ) levels can affect the activity of enzymes like calpains, which are involved in the disassembly of focal adhesions (Tiwari et al., 2011).

Integrins are synthesized in the endoplasmic reticulum and then trafficked and sorted at the Golgi apparatus. Integrin trafficking is a crucial regulator of cell migration. Integrin trafficking is a dynamic process that includes the internalization, recycling and delivery of integrins to distinct cellular compartments. Studies have emphasized the importance of integrin trafficking in coordinating the delivery of integrins and effectors, driving tissue formation through dynamic remodelling of adhesions via rapid endocytic and exocytic trafficking (Moreno-Layseca et al.,

2019). The rapid turnover of integrins through endocytic and exocytic trafficking mechanisms allows cells to modulate their interactions with the ECM and responses to environmental changes. Integrins can be transported to endosomal compartments in both inactive and active conformations and recycled back to the cell surface through distinct routes and with different kinetics (Arjonen et al., Traffic). This trafficking is essential for maintaining cellular dynamics and ensuring that integrins are appropriately positioned to mediate cell adhesion and migration. Moreover, FA signalling overlaps with other signalling pathways, such as MAPK/ERK, PI3K/AKT and Rho GTPase pathways, that are involved in the regulation of cytoskeletal dynamics, cell cycle progression and other cellular processes.

Since FAs and hemidesmosomes differ structurally, they also have differences in their formation and regulation. Most hemidesmosome components, including  $\alpha 6\beta 4$ -integrin, plectin, BP180 and BP230, are synthesized at the endoplasmic reticulum and transported to the plasma membrane. Integrin  $\alpha 6\beta 4$  at the plasma membrane binds to the BM via laminin-332, which is secreted by epithelial cells. Additionally,  $\alpha 6\beta 4$ -integrin recruits intracellular linker proteins such as plectin and BP230 to connect the integrin complex to the keratin cytoskeleton, providing stability to the forming hemidesmosome. BP180 further stabilizes the structure by linking to both laminin-332 and the integrin complex (Molder et al., 2021; Walko et al., 2015). The regulation of hemidesmosomes and FAs share several common mechanisms, such as post-translational modifications, proteolysis and ECM composition. Changes in the ECM, including alterations in the laminin content or structure in the BM, can regulate hemidesmosome formation as cells respond to these changes by adjusting the assembly or turnover of hemidesmosomes. Various signalling pathways, including those triggered by growth factors and cytokines can also influence the assembly and disassembly of hemidesmosomes. For example, signalling through the epidermal growth factor receptor (EGFR) can lead to phosphorylation of  $\beta 4$ -integrin, causing hemidesmosome disassembly during cell migration (Frijns et al., 2010). Hemidesmosome components can also be cleaved by proteases (Walko et al., 2011; M. E. Werner et al., 2007). Moreover, as hemidesmosomes and FAs are linked to the same signalling pathways, they can also regulate each other's functions in mechanosensing, where lack of  $\alpha 6\beta 4$ -integrin in hemidesmosomes results in increased FA formation and consequent traction forces (W. Wang et al., 2020).

### 2.2.3 IAC function

The primary function of IACs is to anchor cells to the ECM via integrins, providing structural and mechanical stability. In addition to adhesion, IACs transmit signals from the ECM into the cell and from the cell to the ECM. This bidirectional



signalling modulates various cellular processes, including proliferation, migration, survival and invasion. Integrin-mediated signalling activates pathways that promote cell growth and prevent apoptosis through the MAPK/ERK and PI3K/AKT pathways. As biomechanical sensors, integrin signalling guide cell differentiation depending on the composition and mechanical properties of the ECM. The dynamic FA formation and disassembly at the leading edges of migrating cells provides traction forces essential for cell movement. Integrins mediate directed migration based on ECM and signalling cues in wound healing, immune responses and cancer metastasis (Green & Brown, 2019; Kechagia et al., 2019b). Along with FAs, hemidesmosomes participate in migration as these stable adhesions can be dismantled through phosphorylation, permitting cell movement. In cancer progression, hemidesmosomes can be switched to another laminin-binding integrin adhesion, the  $\alpha6\beta1$  heterodimer. This switch changes the linkage from keratins to the actin cytoskeleton, facilitating increased cell motility and invasion, thereby promoting cancer progression (Schmidt et al., 2022; Wenta et al., 2022). Hemidesmosomes are particularly essential in dermal keratinocytes, where mutations in genes encoding hemidesmosome proteins cause a blistering skin disease known as epidermolysis bullosa, highlighting the importance of hemidesmosomes in maintaining epithelial tissue integrity and their potential role in disease when disrupted (Bardhan et al., 2020).

Functional IACs maintain cell position and tissue architecture as they enable cells to adhere to the ECM, transmit signals between cells and the ECM and this contact allows the formation of traction forces, enabling cell movement. Therefore, IACs are needed from development to homeostasis (Molè et al., 2021) and they can facilitate cancer progression. IACs in various cell types in the TME adjust their function to meet different cellular needs and respond to environmental cues by interacting with multiple factors in their microenvironment, such as the ECM and soluble factors. Notably, integrins are involved in mechanotransduction, the process by which cells sense and respond to mechanical cues from the ECM. IACs are sensitive to mechanical forces and changes in the ECM's mechanical properties. Through mechanotransduction, integrins can convert mechanical signals from the ECM into biochemical signals within the cell. This ability allows cells to sense and respond to the stiffness, composition and architecture of their environment, playing a critical role in processes like tissue morphogenesis, homeostasis and disease (Kechagia et al., 2019b; Mathieu et al., 2024a). Integrins participate in organization of the cytoskeleton, which maintains cell shape, polarity and mechanical integrity by linking ECM components to intracellular actin filaments. In outside-in signalling integrin binding to ECM components triggers signalling pathways inside the cell. Conversely, intracellular signals can modify integrin affinity, thus regulating cell adhesion to the ECM and the subsequent organization of the ECM. However,

adhesion to the ECM must be tightly regulated and dynamically controlled, as it must provide attachment while permitting movement. Accordingly, integrins can weaken their adhesion strength and contact to the ECM and strengthen cell-cell adhesion, an essential adhesion interplay in for example mitosis (Huber et al., 2023; Ungai-Salánki et al., 2021). As cells migrate, integrins are endocytosed and recycled facilitating adhesion turnover and generation of new adhesion in areas such as from adhesion sites to the leading protrusions where these newly formed adhesion sites generate traction, essential for cell movement.

As well as generating traction forces for movement, cells deposit ECM into the extracellular space through a process involving integrins. During this process integrin to become activated and engagement with the ECM upon receiving intracellular signals or binding to ECM components like fibronectin, collagen, or laminin, which in turn increases their affinity for ECM proteins. Once integrins are activated, they cluster together and aid in the assembly and crosslinking of ECM components. Crosslinking enzymes such as lysyl oxidases (LOXs) covalently crosslink ECM components, stabilizing and strengthening the matrix and integrins, such as  $\alpha 5\beta 1$ -integrin, interact with LOXs (Vallet et al., 2020). Activated integrins that have undergone a conformational change, can bind their ECM ligands. However, ECM ligand binding is not exclusively dependent on conformation. For example, manganese ions ( $Mn^{2+}$ ) increase  $\alpha 5\beta 1$ -integrin affinity for fibronectin in its half-bent conformation (Schumacher et al., 2021), whereas  $\alpha v$ -integrin binding to fibronectin is solely mediated by the RGD-domain (Benito-Jardón et al., 2020). Cells secrete soluble fibronectin, which integrins can bind to at the cell surface. Integrins (notably,  $\alpha 5\beta 1$ ,  $\alpha IIb\beta 3$  and  $\alpha v\beta 3$ ) are involved in the initiation, formation and activation of fibronectin fibrillogenesis (Filla et al., 2019; Lickert et al., 2024; Melamed et al., 2023). The interaction between fibronectin and integrins, coupled with the contractile forces generated by the actomyosin cytoskeleton, pulls and stretches fibronectin molecule thus exposing additional binding sites on fibronectin. This further promotes fibril formation and subsequent ECM assembly to a highly organized structure.

In cancer, IAC signalling contributes to the invasive and metastatic potential of cancer cells by altering their adhesive properties and enhancing their ability to migrate and invade surrounding tissues (Haake et al., 2024). By interacting with ECM proteins in the tumour matrix and activating proteolytic enzymes such as matrix-metalloproteinases (MMPs), integrins help cancer cells degrade ECM components facilitating invasion (Niland et al., 2021). IACs regulate ECM composition and stiffness, which impact the mechanical properties of the tumour matrix. This remodelling is crucial for creating a permissive environment for tumorigenesis and metastasis. IACs mediate interactions between the ECM and the various cell types in the TME, such as cancer cells, fibroblasts, adipocytes, endothelial cells and immune

cells. Moreover, IACs mediate endothelial cell interaction to immune cells and cancer cells, and cancer cells to immune cells (Sökeland & Schumacher, 2019). These interactions further support cancer progression by promoting angiogenesis, suppressing immune responses and facilitating immune cell recruitment (Malenica et al., 2021). Integrins, particularly  $\alpha\beta3$  and  $\alpha\beta5$ , are involved in the regulation of angiogenesis, the formation of new blood vessels (Beauvais et al., 2009; Nisato et al., 2003). By interacting with ECM components like vitronectin and fibronectin, integrins promote the migration and survival of endothelial cells, supporting tumour angiogenesis and the supply of nutrients to the growing tumour. Moreover, IAC-mediated adhesion to the ECM activates several signalling pathways, including the MAPK/ERK, PI3K/AKT, FAK/Src and YAP/TAZ pathways. These pathways promote cell proliferation, survival and resistance to apoptosis (Cooper & Giancotti, 2019). Together these functions provide insight to how IACs can contribute to all of the different hallmarks of cancer.

## 2.3 Tumour – Tumour matrix interaction

The composition and physical properties of the TME are dynamically altered during cancer progression, significantly impacting invasion and metastasis. Cancer cells actively interact with stromal cells, including fibroblasts, adipocytes, vascular endothelial cells and smooth muscle cells. As this interaction is essential for providing structural support and signalling cues to cells, cancer cells can modify the ECM and activate fibroblasts and adipocytes to produce and remodel the ECM, providing a microenvironment that supports cancer cell growth and dissemination (**Figure 3**). Disruption of ECM integrity facilitates cancer cell invasion by breaking down ECM barriers and providing migratory tracks that enable metastasis (Gaggioli et al., 2007; Page-McCaw et al., 2007).

The physical properties of the tumour ECM, particularly its stiffness, have been linked to cancer progression in several cancer types. In tumours, fibroblasts and cancer cells confined tumours generate mechanical compressive forces that stimulate cancer cell migration (Barbazan et al., 2023; Tse et al., 2012). This stiffening activates mechanotransduction signals that promote pro-carcinogenic responses, such as increased cell proliferation, invasion and metastasis in multiple cancers (Berger et al., 2020; Dong et al., 2019; Fattet et al., 2020; Grasset et al., 2018; Pankova et al., 2019; Watson et al., 2021). Tissue stiffening can occur, for example, when collagen is crosslinked in the tumour matrix (X. Liu et al., 2023; Maller et al., 2021) and inhibition of this crosslinking can improve drug response by increased drug penetration (Nicolas-Boluda et al., 2021). EMC crosslinking further impacts focal adhesion formation and growth factor signalling, creating a feedback loop that enhances tumour progression (Levental et al., 2009). Moreover, increased matrix

stiffness correlates with poor patient survival outcomes and can drive epithelial-mesenchymal transition (EMT), a process where epithelial cells acquire mesenchymal, migratory properties that enhance their invasive potential (Denis et al., 2016; W. Huang et al., 2021; Koorman et al., 2022; Morkunas et al., 2021; Rice et al., 2017; Sharma et al., 2019; S. C. Wei et al., 2015). EMT has been implicated as a critical step in the metastatic cascade, enabling cancer cells to detach from the primary tumour, invade surrounding tissues and eventually colonize distant organs (Bornes et al., 2021). However, this remains somewhat debated and in many instances disseminating cancer cells have been shown to adopt intermediate states retaining epithelial properties while gaining mesenchymal features. This is referred to as hybrid EMT (Bornes et al., 2021; Jolly et al., 2019). Alterations in the expression of ECM molecules can lead to significant changes in cancer cell-ECM adhesion, affecting how cancer cells interact with their surrounding environment, their ability to migrate, invade and survive.

Normal stromal fibroblasts modify the ECM to maintain homeostasis. To maintain homeostasis, normal fibroblasts inhibit the growth of adjacent abnormal or transformed cells through growth suppression. The growth suppression of neighbouring cells is dependent on both contact and soluble factors, including transforming growth factor beta (TGF $\beta$ ) (Alkasalias et al., 2014; Kaukonen et al., 2016). Quiescent normal fibroblasts respond to tissue injury and become reversibly activated. Activated fibroblasts have enhanced contractility, ECM production and secretion of inflammatory proteins that initiate regenerative repair in wound healing, making them an interesting ally for cancer cells. Cancer cells activate normal fibroblasts by growth factors and as a result perpetually activated cancer-associated fibroblast (CAFs) are formed. CAFs exhibit increased deposition of ECM components, enhanced cross-linking of collagen fibres and changes in ECM stiffness in breast, colorectal and pancreatic cancer (**Figure 3**) (Hanley et al., 2016; X. Liu et al., 2023; Rice et al., 2017; B. Wei et al., 2017). Altering the composition and structure of the ECM promotes cancer progression and therapy resistance.

Normal adipocytes can be differentiated by the canonical wnt signalling pathway and tumour exosomes, resulting in dedifferentiation and formation of cancer-associated adipocytes (CAAs). CAAs have been mainly studied in breast cancer, since adipose tissue is the main component of the breast. CAAs exhibit delipidation and decreased expression of adipocyte markers, in addition to overexpression of matrix-degrading proteinases and proinflammatory cytokines (**Figure 3**) (Bouche & Quail, 2023). Breast, colorectal and endometrial tumours comprise largely of adipose tissue, making them interesting tissues to study the role of CAAs (Pallegar & Christian, 2020). Though CAAs have not been studied regarding tissues stiffness, dysfunctional adipocytes promote tumour progression through YAP/TAZ, indicating a possible role in mechanical signalling (Y. Song et al., 2024).

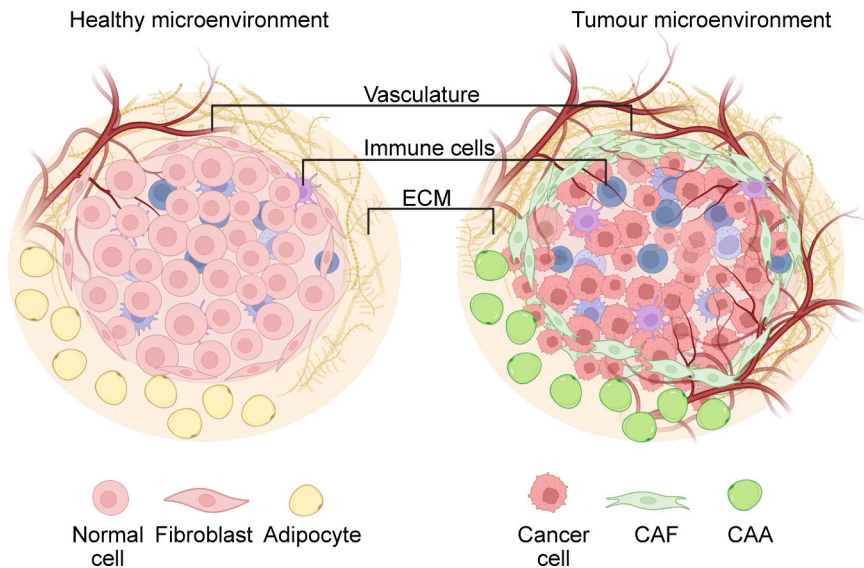


**Figure 3. A healthy microenvironment and a tumour microenvironment (TME).** A healthy microenvironment supports normal cell function through controlled interactions with neighboring cells, including immune cells, fibroblasts and adipocytes, in addition to providing a homeostatic ECM composition. In the TME fibroblasts are transformed into CAFs, normal adipocytes into CAAs, tumour vasculature and ECM composition are increased and an immunosuppressive environment is formed, together supporting cancer progression and metastasis.

### 2.3.1 Extracellular matrix (ECM)

The ECM in the TME has multiple roles, providing cells with structural support, regulating cell signalling and mediating cell adhesion and migration. Alterations in ECM organization and composition in the tumour matrix are associated with increased tumour aggressiveness (Kai et al., 2019; Winkler et al., 2020). The stiffness, topography, and dimensionality of the ECM, along with mechanical stimuli are key mechanical properties that influence cell behaviour. Cancer cells proliferate more on stiffer matrices and preferentially migrate toward stiffer areas, a process known as durotaxis (Mathieu et al., 2024a; Sunyer et al., 2016). Many solid tumours exhibit increased stiffness, creating an ideal environment for cancer cell growth and proliferation. This stiffening can be driven by CAFs remodelling the ECM by upregulating ECM components and downregulating ECM-degrading enzymes. Fibronectin, collagens and laminins are abundant in multiple tissues and are essential components of the ECM (Kai et al., 2019; McKee et al., 2019). Integrins bind to ECM proteins like fibronectin and laminins, transmitting mechanical signals from the ECM to the cell interior, thereby regulating cellular responses and contributing to cancer progression (Cox, 2021). Cell engagement with the ECM permits directed cell movement, which can occur through durotaxis or haptotaxis (SenGupta et al.,

2021). Durotaxis refers to cell movement in response to stiffness gradients in the ECM; cells are inclined to migrate from softer to stiffer environments and cancer cells can exploit durotaxis to invade stiffer areas (DuChez et al., 2019; Mathieu et al., 2024b). In haptotaxis cells respond to gradients of adhesive molecules in the ECM to direct their movement; cells migrate towards areas with higher concentrations of ECM molecules (King et al., 2016). In metastasis, haptotaxis guides cancer cells toward areas rich in specific ECM components (Zimmerman et al., 2017). Thus, in the TME, gradients of both stiffness and ECM molecules coordinate cell movement, enabling cancer cells to invade surrounding tissues, enter the vasculature and establish metastases in distant organs.

Collagens are the most abundant ECM proteins in the stroma, constituting approximately 30% of the body's proteins, with 28 different types found in humans. Five subtypes of collagen can be categorized based on its location; Type I makes up 90% the body's collagen providing structure to the skin, bones, tendons and ligaments, type II is found in elastic cartilage supporting joints, type III is found in muscles, arteries and organs, type IV in the skin and type V in the cornea of eyes, skin, hair and placenta (Bella, 2016; Makareeva & Leikin, 2014). Collagen contributes to the mechanical properties of tissues, providing structural support, strength, and elasticity. Collagens form fibrillar and microfibrillar networks that contribute to tissue organization and function. This hierarchical organization of collagen structure allows collagen to withstand tensile forces and provide structural integrity and maintaining tissue architecture (Gachon & Mesquida, 2022; Quigley et al., 2018; Rennekamp et al., 2023). Collagen plays a role in development and pathologies. For instance, the mechanical properties and distinct expression patterns of collagen drive branching morphogenesis and mammary gland development (Buchmann et al., 2021; Tsutsui et al., 2020), while increased stromal collagen in mammary tissue drives tumour formation and metastasis (Papanicolaou et al., 2022; Sharp et al., 2024; Wishart et al., 2024; H. Zhang et al., 2018). Upregulation of collagen synthesis and its cross-linkers, such as LOXs, causes tissue stiffening, promoting cell proliferation and contributing to cancer progression (X. Liu et al., 2023; Maller et al., 2021; Rosell-Garcia & Rodriguez-Pascual, 2018; Sato et al., 2021)

Fibronectin is a crucial mediator of cell-ECM adhesion, binding to integrin receptors on the cell surface through an RGD motif (Chastney et al., 2021). The ubiquitous expression of this glycoprotein is essential for mammalian development and tissue repair. Fibronectin exists in two forms: a soluble form in the blood plasma and an insoluble matrix form in tissues. It is made of repeating units, including type I, II and III domains, which mediate interactions with other ECM components, cell surface receptors and growth factors (Früh et al., 2015; Singh et al., 2010). The functional role of fibronectin is closely linked to its ability to bind

to other ECM components and form a fibrillar matrix through these interactions. Fibronectin and collagen assembly are tightly linked, multiple studies providing evidence on their interdependent function in cells and tissues. For instance, fibronectin along with heparan sulfate act as scaffolds for procollagen processing (Saunders & Schwarzbauer, 2019). Relaxed fibronectin fibrils also act as templates for collagen assembly, and assembled collagen fibres shield fibronectin fibres from cellular force-induced stretching (Kubow et al., 2015). Fibronectin expression and assembly facilitates tumour initiation and affects cancer progression and invasion by modulating the tumour matrix (Spada et al., 2021; C. Wu et al., 2023). For instance, upregulation of fibronectin facilitates cancer cell spreading in 3D cell cultures (Park & Helfman, 2019). Moreover, lysyl oxidase-like-3 (LOXL3) can bind and oxidize fibronectin, initiating fibrillogenesis in a force-independent manner that increases cell adhesion and mechanosensing, thereby promoting features essential for cancer cells (Melamed et al., 2023). An organized fibrillar matrix is formed in cancer cells that can undergo dormancy and exiting and growth after dormancy requires MMP-mediated fibronectin degradation (Barney et al., 2024). Additionally, pharmacologic and genetic inhibition of fibronectin suppresses tumour growth (Ghura et al., 2021).

Laminin is a large, multidomain glycoprotein composed of  $\alpha$ -,  $\beta$ -, and  $\gamma$ -chains that assemble into a cross-shaped structure. These heterotrimers can weigh up to 900 kDa. The modular structure of laminin provides binding sites for integrins, proteoglycans and other ECM proteins (Arimori et al., 2021; Aumailley, 2021). Laminins assemble into a fibrillar matrix and are involved in promoting cancer invasion, metastasis and tissue vascularization by modulating gene and protein expression of cancer cells and endothelial cells (Patarroyo et al., 2002). Laminin-mediated cell adhesion to the ECM is essential for tissue development as they are key components of the BM (Hohenester, 2019). The involvement of laminins in cancer is not surprising, as their receptors, such as integrins, are well recognized in the metastatic cascade. Aberrant laminin expression is observed in various cancers, including breast, pancreatic, ovarian and colorectal cancer, as its expression can enhance cell motility (Akhavan et al., 2012; Galatenko et al., 2018; H. Li et al., 2022; van der Zee et al., 2012). For example, local laminin expression in breast cancer cells sustains integrin activity in leader cells and controls collective cell migration (P. Y. Hwang et al., 2023). In addition, collective invasion of breast cancer cells increases laminin accumulation in the BM around the breaching site, as cells induce local contractile forces and an expansion in cell volume mediates invasion (J. Chang et al., 2024).

### 2.3.2 Cancer-associated fibroblasts (CAFs)

Fibroblasts are stromal cells found in connective tissue, responsible for the synthesis of ECM components and the maintenance of structural tissue integrity. As implied by their name, upon interaction with cancer cells, quiescent normal fibroblasts are activated and recruited to orchestrate interactions between the cancer cells and the tumour matrix. CAFs remodelling the ECM results in changes in tissue mechanics that promote cancer cell migration, invasion and affect cellular signalling pathways that enhance malignancy and promote chemoresistance (Ireland & Mielgo, 2018; Sahai et al., 2020).

CAF activation is driven by factors secreted by cancer cells, such as TGF- $\beta$ , platelet-derived growth factor (PDGF) and fibroblast growth factor (FGF). These signalling molecules induce the expression of  $\alpha$ -smooth muscle actin ( $\alpha$ -SMA), fibroblast activation protein (FAP), tenascin-C and other markers, characterizing the activated CAF phenotype (Nurmik et al., 2020). CAFs differ from normal fibroblasts in their function, adopting a more proliferative and secretory profile that supports tumorigenesis. In addition, activated CAFs are highly contractile, a characteristic that is essential for their role in wound healing and that can be exploited in cancer invasion. Moreover, CAFs support enhanced migratory capacity by inducing EMT in cancer cells through paracrine secretion of TGF- $\beta$  and interleukin 6 (IL-6) (Erdogan et al., 2017).

In addition to their altered phenotype and ability to reinforce mesenchymal characteristics in cancer cells, CAFs modify the tumour matrix architecture by producing ECM proteins and reorganizing the ECM, which together alter the mechanical properties of the matrix and provide tracks for cancer cell invasion. (Najafi et al., 2019; Sahai et al., 2020; D. Yang et al., 2023). CAFs are heavily involved in remodelling the ECM by producing and reorganizing its components, such as fibronectin, collagen and hyaluronan (Erdogan et al., 2017; Kay et al., 2022; Z. Zhang et al., 2016). Remodelling of the ECM creates a scaffold for tumour growth and alters the physical properties of the TME, for instance by increasing tissue stiffness (García-Palmero et al., 2016; J.-Y. Zhang et al., 2021). CAFs function itself is dependent on mechanotransduction; YAP activation is a signature CAF feature and YAP-induced matrix stiffening further enhances YAP activation through actomyosin contractility, creating a mechanically self-reinforced feed-forward loop that maintains CAF phenotype (Calvo et al., 2013). CAFs can further create a supportive microenvironment for tumorigenesis by altering the metabolic landscape of the TME, through secreting metabolic intermediates and enzymes and promoting angiogenesis. CAFs undergo aerobic glycolysis and provide lactate and other metabolites to cancer cells, which then utilize these metabolites for energy production and biosynthesis (Gong et al., 2020; X. Gu et al., 2024; Ippolito et al., 2019; D. Kumar et al., 2018). To support vascularization, CAFs secrete and



exosomally transfer pro-angiogenic factors, such as vascular endothelial growth factor (VEGF), that stimulate formation of new blood vessels, supplying the growing tumour with oxygen and nutrients (De Francesco et al., 2013; J. Li et al., 2020; Miaomiao et al., 2023; Tang et al., 2016). CAFs can also recruit endothelial cells to aid in the formation of a stable vascular network (Pape et al., 2020; Sewell-Loftin et al., 2017).

Researchers have tried multiple approaches to target signalling pathways involved in CAF activation to prevent the recruitment and activation of fibroblasts. CAFs have high and stable expression of FAP, therefore FAP inhibitors have been used to selectively kill CAFs (Akai et al., 2024; Privé et al., 2023). Another approach has been to convert CAFs back to a quiescent state or altering their secretory profile to be less supportive of cancer growth (Chauhan et al., 2019; Dauer et al., 2018; Yasuda et al., 2021). Inhibiting ECM components or ECM-degrading enzymes involved in ECM remodelling, such as collagen and MMPs, or modifying the ECM to reduce its stiffness, it may be possible to disrupt the supportive scaffold and hinder cancer progression and metastasis (Cruz-Acuña et al., 2021; Glentis et al., 2017). However, targeting CAFs has been faced with many challenges regarding heterogeneity. Systematic characterization of CAFs in various cancer types revealed CAFs to originate not only from normal fibroblasts, but from tumour endothelial cells, tumour-associated macrophages and peripheral nerve cells. All four CAF groups exhibiting three differential states that may contribute to outcomes in immunotherapy (H. Luo et al., 2022). Moreover, some CAFs may have tumour-suppressive roles, thus targeting them without distinguishing between different CAF subtypes could result in unwanted outcomes (Gieniec et al., 2019). For instance, depleting CAFs in pancreatic cancer mouse models leads to invasive and undifferentiated tumours with increased EMT properties. Additionally, loss of myofibroblasts correlated with poor patient survival (Özdemir et al., 2014). Clinical trials targeting CAFs have largely failed despite multiple studies suggesting therapeutic potential in their immune suppressive functions (Y. Chen, McAndrews, et al., 2021). Due to the heterogeneity and dual nature of CAFs, targeting them could lead to unintended effects on normal fibroblasts and other cells or accelerate cancer progression. Therefore, strategies to target CAFs need to be specific and carefully controlled. Targeting distinct CAF subtypes rather than a pan-CAF target, while also accounting for differences in cancer subtypes may be necessary.

### 2.3.3 Cancer-associated adipocytes (CAAs)

Adipocytes in the TME that undergo phenotypic changes due to signals from cancer cells are called cancer-associated adipocytes (CAAs). These transformed and dysregulated adipocytes support tumour growth by metabolic reprogramming,

secretion of pro-tumorigenic factors, ECM alteration and immune modulation (Bouche & Quail, 2023; Q. Wu et al., 2019). In some cancers, such as breast, pancreatic, colorectal and ovarian cancer, a fibrotic environment created by increased ECM deposition and remodelling promotes cancer cell invasion and correlates with poor patient outcomes (Acerbi et al., 2015; Mascharak et al., 2023; Ueno et al., 2021; Wolf et al., 2023). These desmoplastic cancers are characterized by growth of fibrous tissue in a normally adipocyte-rich environment. For instance, breast cancer progression is directly linked to desmoplasia and loss of adjacent adipocytes (Bochet et al., 2013). Moreover, adipocytes in the TME can undergo de-differentiation gaining phenotypic characteristics that resemble myofibroblasts and macrophages, and promote tumour growth through inflammation and ECM remodelling (Mukherjee et al., 2023). Adipose tissue inflammation and dysregulation is present in CAAs and is also associated with obesity. Increased adipose tissue due to obesity is an independent risk factor for cancer progression, as the adipose tissue in obese individuals is altered and inflamed, contributing to the dysregulation of normal processes (Abarca-Gómez et al., 2017; Rask-Andersen et al., 2023).

The metabolic support and pro-inflammatory signals provided by CAAs are crucial for the survival and growth of metastatic cells. CAAs release various secreted factors, such as adipokines, cytokines and chemokines, that promote inflammation and ECM remodelling. Especially in mammary tissues, CAAs stimulate breast cancer invasion through metabolic remodelling of tumour cells. In triple-negative breast cancer (TNBC) CAAs secrete interleukin-6 (IL-6) that activates the JAK/STAT3 and PI3K/AKT pathways, inducing migration and invasion of cancer cells (He et al., 2018; C. Zhao et al., 2023). C-C motif chemokine ligand 5 (CCL5) secreted by CAAs activate AKT pathway that induces EMT, in addition to contributing to ECM remodelling by upregulating MMP-2 and MMP-9 expression in TNBC (X. Song et al., 2018). In addition to increasing MMP expression, CAAs can influence the cross-linking of collagen fibers, altering the mechanical properties of the ECM (M. Kim et al., 2022; X. Wei et al., 2019). Activation of the mechanically sensitive YAP/TAZ signalling pathway in CAAs supports dedifferentiation, an inflammatory phenotype and tumour growth, all of which can be reversed by pharmacological inhibition of YAP/TAZ (Y. Song et al., 2024). Moreover, CAAs can produce chemokines that recruit immune cells to the TME. For example, CC-chemokine ligand 2 (CCL2) secretion causes abundant M2 macrophage infiltration and decreases activation of T-cell infiltration, thereby creating an immunosuppressive TME (Y. Liu et al., 2021). CAAs can indirectly affect ECM remodelling by modulating the immune landscape. For example, they can promote the polarization of macrophage polarization towards a tumour-promoting M2-

phenotype through STAT3 activation (C. Zhao et al., 2023). The M2-phenotype is associated with increased ECM remodelling (Witherel et al., 2021).

CAAs regulate the availability and synthesis of macronutrients, such as carbohydrates, lipids and amino acids. For instance, CAAs secrete lipid metabolites, such as free fatty acids (FFAs), through lipolysis and breast cancer cells utilize these FFAs as fuel for fatty acid oxidation (FAO) that facilitates their proliferation and survival under nutrient-poor conditions in the TME (Balaban et al., 2017; Y. Y. Wang et al., 2017). In colon cancer carnitine palmitoyltransferase I (CPT1A)-dependent FAO promotes acetylation and nuclear translocation of  $\beta$ -catenin, thereby advancing proliferation and tumour growth (Xiong et al., 2020). Moreover, upregulation of autophagy and mitochondrial FAO via AMPK promotes colon cancer cell migration and EMT (Wen et al., 2017). CAAs also support pancreatic cancer progression by promoting the invasion capability and EMT properties of pancreatic cancer cells through serum amyloid A1 (SAA1) expression (Takehara et al., 2020).

## 2.4 Cellular mechanosensing

Cells perceive and respond to intrinsic and extrinsic mechanical cues in their microenvironment (**Figure 4**). Sensing and adapting to the biophysical changes in their surroundings is essential for cellular homeostasis and tissue integrity. To transduce mechanical signals into biochemical ones, cells assess changes in cell-cell boundaries, cell-ECM attachment and matrix mechanics, predominantly through integrins and the connected actomyosin cytoskeleton. In addition to gauging the surrounding matrix, mechano-regulation includes the deposition, rearrangement and removal of ECM to maintain its overall form and function (Di et al., 2023; Humphrey et al., 2014). Moreover, the actomyosin cytoskeleton is directly connected to the nucleus through transmembrane LINC complex proteins, transmitting mechanical stimuli from the cell surface to the nucleus (Davidson & Cadot, 2021).

Intrinsic mechanical stimuli originate from within the cell and include nuclear deformation, cytoskeletal tension and membrane tension (**Figure 4**). Nuclear deformation takes place when the nucleus is exposed to mechanical forces transmitted through the actomyosin cytoskeleton (Kalukula et al., 2022). Deformation of the nuclear envelope alters chromatin organization, thereby affecting gene expression, cell cycle and cellular differentiation (Aureille et al., 2019; Chi et al., 2022; Ghagre et al., 2024; Nava et al., 2020; Sen et al., 2024). Furthermore, changes in membrane tension can regulate the activity of mechanosensitive ion channels, such as Piezo1, and membrane trafficking (Lachowski et al., 2022; Loh et al., 2019; Lüchtfeld et al., 2024; H. J. Wang et al., 2024). To the contrary, extrinsic mechanical stimuli originate from the cells' external environment and include forces

exerted by the ECM, neighbouring cells and mechanical loads such as shear stress, stretching, substrate rigidity and compression (**Figure 4**) (Y. Li et al., 2022). Cells sense and respond to external forces primarily through focal adhesions, where integrin receptors connect the ECM to the actomyosin cytoskeleton (Kechagia et al., 2019b).

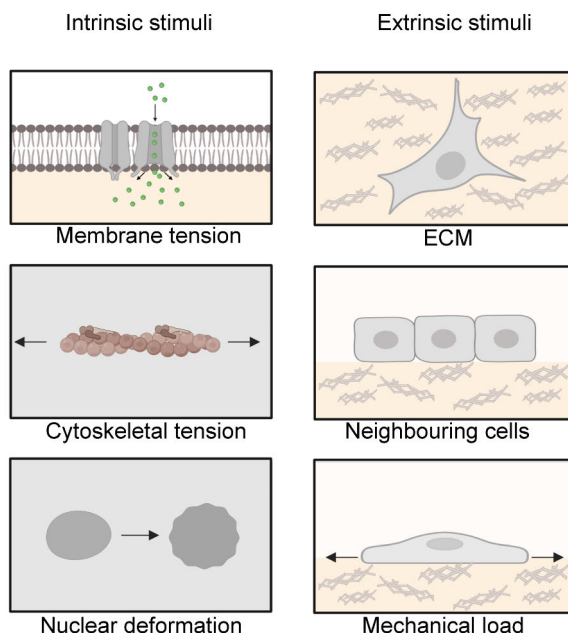


**Figure 4. Intrinsic and extrinsic mechanical cues.** Cells sense intrinsic (membrane tension, cytoskeletal tension and nuclear deformation and extrinsic (ECM rigidity, forces transmitted by neighbouring cells and mechanical loads such as stretching) mechanical cues in their microenvironment, guiding their behaviour.

The cell cytoskeleton is a core component of cellular mechanosensing, for intrinsic mechanical tension is predominantly generated by the cytoskeleton and cells adapt to the extrinsic stimuli by cytoskeletal reorganization. The cytoskeleton is a dynamic network of protein filaments, including actin filaments, microtubules and intermediate filaments such as keratins. These filaments provide structural support and drive cellular movement (Laly et al., 2021; Moujaber & Stochaj, 2020; Pora et al., 2020). Cytoskeletal tension arises as actin filaments and myosin motors generate contractile forces within the cell and it is essential for maintaining cell shape, enabling motility and facilitating cellular processes such as cytokinesis during cell division and patterned actomyosin contractility in organogenesis (Gupta et al., 2021; Nematbakhsh et al., 2020; Taneja et al., 2020). However, it is important to note that though many proteins will undergo changes under mechanical tension, they

are not considered mechanosensors. Proteins that alter their function due to mechanical load and that can mediate mechanotransduction mediate cellular mechanosensing.

### 2.4.1 Mechanical forces in homeostasis and cancer

Mechanical forces are essential for development and normal physiological function. In development, coordinated mechanical forces guide tissue morphogenesis, ensuring proper formation of organs and organisms through controlled cell differentiation and tissue patterning (Hallou & Brunet, 2020; Villeneuve et al., 2024). For example, mesenchymal stem cell (MSC) differentiation is guided by matrix stiffness, as MSCs differentiate into osteoblasts or adipocytes depending on substrate rigidity (M. Sun et al., 2018; Takata et al., 2020). In wound healing, contractile forces generated by migrating fibroblasts, help to repair and close the wound (Knoedler et al., 2023). This function can be exploited as mechanically reprogrammed fibroblast have potential to be utilized in cell-based therapies in tissue regeneration (Roy et al., 2024). During apoptosis, the apoptotic cell forms a contractile ring, exerting tension on neighbouring cells to push out the apoptotic cell from the tissue monolayer (Matamoro-Vidal & Levayer, 2019; Monier et al., 2015).

Similarly, in cardiovascular function mechanical forces such as shear stress and cyclic stretching influence the behaviour of endothelial cells, contributing to vascular homeostasis and function. Endothelial cells in the blood flow that are exposed to these mechanical forces produce anti-inflammatory and anti-thrombotic factors, while disturbed flow patterns lead to atherosclerosis. Moreover, mechanical stimuli can be used to reprogram endothelial cells in atherosclerosis by inducing flow (Dessalles et al., 2021; Warboys et al., 2011). Cells in tissues such as cartilage and bone experience compressive and tensile forces: chondrocytes in cartilage respond to compression by altering matrix synthesis (Fahy et al., 2018; Ouyang et al., 2019; Petitjean et al., 2023) and osteoblasts in bone respond to mechanical loading by promoting bone formation through increased migration, cell division and regulation of mechanosensitive ion channels (W. Sun et al., 2019, 2023; Takemoto et al., 2023).

In addition to their role in development and homeostasis, mechanical forces are implicated in cancer progression. While the consequence of increased matrix stiffness has gained general consensus (discussed in sections 2.1 and 2.3), the outcomes of other mechanical stimuli remain inconclusive. For example, stretching cancer cells have raised multiple different views. While stretching can reduce tumour growth and cause selective killing of cancer cells (Berrueta et al., 2018; Tijore et al., 2021), it can also promote invasion and expression of two Rho GTPases, RhoA and Rac1, that are implemented in increasing cancer cell motility (L.-K. Chen et al., 2023; Yadav et al., 2020). Some of the conflicting views can be partially explained

by cells experiencing multiply mechanical stimuli simultaneously. For instance, normally cells are unable to adhere to soft surfaces, but combining cyclic stretching on soft substrates results in stiffness-insensitivity (Cui et al., 2015). This insensitivity is also dependent on ECM composition, as it can be induced by specific ECM compositions (Conway et al., 2023).

## 2.4.2 Cell-cell and ECM mediated mechanotransduction

Cells can migrate within a tissue in a coordinated manner, maintaining cell-cell junctions throughout the process. This collective migration requires robust intercellular adhesion, primarily facilitated by molecules like cadherins and catenins. Cadherins are a class of transmembrane proteins that mediate calcium-dependent cell-cell adhesion (S. A. Kim et al., 2011). These cell adhesions are stabilized by catenins as they bind to the intracellular domain of cadherins, linking them to the actin cytoskeleton and contributing to junctional stability (**Figure 5.**) (Stepniak et al., 2009). Cadherin/catenin ectodomains bind to other cadherins/catenins in adjacent cells, while their cytoplasmic tails interact with intracellular proteins such as integrins (Hadjisavva et al., 2022). Cadherins, comprising of E-, N-, P- and VE-cadherin, and catenins, including  $\alpha$ -,  $\beta$ -,  $\gamma$ - and  $\delta$ -catenin, are critical for maintaining tissue integrity, as they are coupled to the actomyosin structures of neighbouring cells, functioning as force-bearing proteins that provide resistance to external mechanical stimuli (Angulo-Urarte et al., 2020; Charras & Yap, 2018).

Cadherin-based adherens junctions are force-sensitive, the amount of force applied influences the composition and strength of these junctions, with cadherins being recruited to the junctions in response to mechanical stress (Borghi et al., 2012; Buckley et al., 2014; Y. Chen, Brasch, et al., 2021; Le Duc et al., 2010). The ectodomains of cadherins form transmembrane dimers with cadherins on opposing cells and undergo clustering, which strengthens the junctions by increasing their density and coordinating rearrangement of traction forces. The activation of the Rho-ROCK pathway can reinforce the actomyosin structures linked to cell-cell adhesion sites, enhancing the mechanical integrity of the tissue (Mertz et al., 2013). In endothelial monolayers, VE-cadherin is crucial for maintaining junctional integrity, with shear forces impacting monolayer dynamics and junction stability (Jin et al., 2022).

Various cell-cell junctions, including tight junctions, adherens junctions and desmosomes, participate in tissue integrity, though mechanotransduction has primarily been studied in adherens junctions (AJs). In adherens junctions, cadherins are physically linked to F-actin, allowing them to sense mechanical force through actomyosin contraction. Cadherins typically form homotypic junctions, though heterotypic junctions are also formed (Arbore et al., 2022; Viji Babu et al.,

2021). AJs can be categorized into five types: linear, focal, zonula, tricellular and fascia. Linear AJs are stable and mature, aligning parallel to the actin cytoskeleton (J. Zhang et al., 2005). In contrast, focal junctions run perpendicularly to the actin cytoskeleton and are thought to be more tensile due to their association with pulling actin bundles where vinculin is recruited to  $\alpha$ -catenin.  $\alpha$ -catenin is a well-characterized force sensor in AJs; under tension, it undergoes conformational changes that reveal a vinculin binding site (Yao et al., 2014). Though it is known that  $\alpha$ -catenin can refold with tension, it is not entirely understood whether it requires other processing (Le et al., 2024).  $\alpha$ -catenin also modulates cortical F-actin dynamics, linking adherens junctions to the actin cytoskeleton and actomyosin contractility (**Figure 5**) (Mei et al., 2020). Vinculin binding to the open conformation of  $\alpha$ -catenin stabilizes the structure, reinforcing adhesion strength by recruiting additional vinculin molecules (**Figure 5**) (Bejar-Padilla et al., 2022; Seddiki et al., 2018). Zonula adherens junctions (ZAs) form puncta in epithelial cells, before maturing into linear AJs. ZAs attach to thick actomyosin bundles and coordinate polarization through actomyosin remodelling (J. Zhang et al., 2005). Tricellular junctions, where three cells converge, are known tension hotspots. Tricellulin is the main component of tricellular junctions, maintaining epithelial barrier function by interacting with actomyosin and orienting mitosis (Bosveld et al., 2016; Cho et al., 2022). Fascia AJs connect to myofibrils and are found in cardiomyocytes. The linkage to actin bundles in myofibrils allows exertion of high contractile forces (Mezzano & Sheikh, 2012).

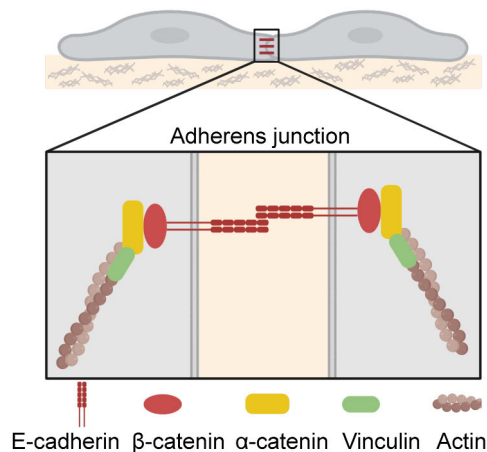


**Figure 5. Adherens junction (AJ) composition.** Cells are connected to each other through Ajs composed of cadherins,  $\alpha$ -catenin and  $\beta$ -catenin. Additionally,  $\alpha$ -catenin binds to vinculin, bridging the junctions to the actin cytoskeleton.

Recent advancements, such as fluorescence resonance energy transfer (FRET) biosensors, have been used to measure forces at junctions within cells and tissues (Haas et al., 2020; J. Wang et al., 2023). Additionally, customized cell–cell interactions can be studied with synthetic cell adhesion molecules with adhesion properties similar to native interactions. It will be interesting to see how coupling synthetic cadherins or catenins to integrins changes tension and mechanotransduction signalling pathways, providing insights into the dynamic nature of cell-cell junctions and cell-ECM adhesions (Stevens et al., 2023). Recently, it has been shown that force transmission can also occur via  $\beta$ -catenin. In the absence of  $\alpha$ -catenin,  $\beta$ -catenin can directly interact with vinculin in its open conformation, bearing physiological forces. Furthermore, force-transmission at AJs can occur alternatively through  $\alpha$ -catenin and  $\beta$ -catenin, since both cooperatively interact with vinculin and  $\beta$ -catenin can prevent vinculin autoinhibition in the presence of  $\alpha$ -catenin, by occupying vinculin’s head-tail interaction site (Morales-Camilo et al., 2024). ECM mediated mechanotransduction occurs via FAs respond to mechanical stimuli by the force-sensitive proteins, such as talin and vinculin, undergoing structural rearrangements or enzymatic modifications (Franz et al., 2023; Gough et al., 2021; Rothenberg et al., 2018). In addition to sensing tension, integrins are in a mechanically reserved state that provides mechanical integrity to tissues. This mechanically reserved state has a mechanical load of 2–7 pN, which is below the peak capacity of integrin heterodimers (A. C. Chang et al., 2016; Tan et al., 2020). Mechanical stimuli can further strengthen mechanotransduction, as for example mechanical stretching of cells leads to FA and cytoskeleton reinforcement (Andreu et al., 2021). Moreover, physical pulling on FAs that leads to the activation of integrin signaling exhibits high specificity in ligand binding, allowing cells to respond distinctively to mechanical stimuli based on the integrins present on their surface. For example, both  $\alpha 5\beta 1$ - and  $\alpha v\beta 1$ -integrin bind ECM ligands with an RGD motif, such as fibronectin, but with different tension thresholds (Jo et al., 2022). This mechanical specificity ensures that cells can finely tune their responses to the unique mechanical environments they encounter. Molecular tension is also required for FA maturation and nuclear translocation of the mechanosensor YAP, at a threshold of 50 pN–54 pN (Chang Chien et al., 2022; Cooper & Giancotti, 2019). In addition to mechanical stimuli, the geometric organization of FAs regulates mechanotransduction. Dynamic changes in the orientational order of FAs can fine-tune cell sensitivity to the ECM. For instance,  $\alpha v$ -integrins and actin exhibit precise changes in the orientational order mediated by ECM-activated integrins and these changes are sensitive to ECM density but myosin-II-independent (Grudtsyna et al., 2023).

The crosstalk between cell-ECM- and cell-cell-mechanotransducers allows cells to integrate mechanical and biochemical cues, ensuring coordinated responses to environmental changes. Integrin- and cadherin-based adhesions are very similar to each other and together form an integrated network via shared binding partners such



as vinculin. For instance, vinculin can directly bind talin,  $\alpha$ -actinin and actin, all of which are part of focal adhesions and also part of AJs (Hadjisavva et al., 2022; Humphries et al., 2007; Peng et al., 2010). The diversity in integrin subtypes contributes to cell-type-specific mechanical responses in addition to crosstalk between integrins and cadherins. This crosstalk is necessary for collective migration in morphogenesis. During development and wound healing, cells need to rearrange, migrate and form stratified epithelia while maintaining connections with neighboring cells and the ECM. Integrins and cadherins work together to balance adhesion and movement, enabling cells to move in a coordinated manner while sensing mechanical stimuli (Ly et al., 2024; S. Wang et al., 2021).

### 2.4.3 Oncogenic functions of mechanosensitive transcriptional mediators

Mechanosensitive transcription factors demonstrate the importance of being in the correct place at the right time. These mechanosensors have been shown to shuttle between cellular compartments, such as the nucleus and the cytoplasm to regulate gene transcription. This dynamic localization initiates complex signalling pathways through transcription in response to mechanical cues. In addition to changes in localization, transcription can be prevented by degradation of the mechanosensitive transcriptional mediators at distinct subcellular localizations. Transcriptional mediators like YAP/TAZ, MRTFs and  $\beta$ -catenin exemplify how cells convert mechanical signals into biochemical responses, thereby influencing cell behavior through regulation of gene expression (Wagh et al., 2021).

YAP (Yes-associated protein) and TAZ (transcriptional coactivator with PDZ-binding motif) are the most well recognized examples of mechanically regulated transcriptional co-activators. The YAP/TAZ complex is part of the Hippo-signalling pathway and it converts mechanical stimuli into biochemical responses by activating downstream signalling pathways in the nucleus, affecting cell proliferation, survival and differentiation. The Hippo pathway is a highly conserved signalling cascade (Y. Chen et al., 2020; Gerri et al., 2023). It is activated by various upstream signals, including mechanical cues, polarity, and receptors/scaffolding molecules such as  $\alpha$ -catenin, G-protein-coupled receptors (GPCRs) and neurofibromin 2 (NF2) (Dupont et al., 2011; Hamaratoglu et al., 2006; Schlegelmilch et al., 2011; F.-X. Yu et al., 2012). The key kinases in the Hippo pathway are MST1/2 (Mammalian sterile 20-like kinase 1/2), which upon activation phosphorylate and activate LATS1/2 (Large tumor suppressor kinase 1/2). Activated LATS1/2 kinases therein phosphorylate and inhibit the downstream effectors, YAP and TAZ. YAP/TAZ are inhibited by their retention in the cytoplasm and degradation (Zhong et al., 2024). When the pathway is inactive and YAP/TAZ are not phosphorylated, they translocate to the nucleus,

where they interact with transcription factors, such as TEADs (Transcriptional enhanced associate domain), to promote gene expression. TEADs are a family of transcription factors that bind to specific DNA sequences, MCAT elements, in the promoters of target genes, driving their transcription (Currey et al., 2021). TEADs require coactivators like YAP /TAZ to effectively initiate gene transcription, as TEADs alone have limited transcriptional activity (Chan et al., 2009).

YAP activation by external physical forces such as mechanical loading and substrate stiffness, drives its nuclear translocation and subsequent transcription of target genes, such as AXL, CTGF, CYR61, THBS1 and TEAD (Pocaterra et al., 2020; Scott et al., 2021). YAP target gene transcription is partly regulated by liquid-liquid phase separation (LLPS). YAP forms nuclear and cytoplasmic condensates with a distinct set of proteins, which contribute to both its ability to redistribute into the nucleus and its role in transcriptional control. Furthermore, nuclear YAP droplets reorganize the genome, driving long-term expression of YAP target genes (Cai et al., 2019). YAP activity depends on its localization, which is modulated by mechanical stimuli (**Figure 6**). Active YAP is found in the nucleus under conditions of a stiff ECM, stretched cells and large cell areas without contact inhibition. Whereas it is inactive and located in the cytoplasm on soft ECM, small surface areas and in cell crowding (**Figure 6**). However, YAP is not found to be in one explicit localization at a time, rather the ratio on nuclear to cytoplasmic levels determine gene activity. Cell-ECM adhesions and cell-cell contacts in crowded monolayers regulate this ratio and can result in contact inhibition and the nuclear exit of YAP (Dupont et al., 2011). For instance, mechanical stretching of E-cadherin-based cell-cell junctions leads to YAP nuclear accumulation and cell cycle re-entry (Benham-Pyle et al., 2015). The Rho family GTPases have been identified as regulators of YAP, essential for its activation and downstream effects on cellular responses to mechanical cues. Moreover, upregulation and overactivation of YAP has been reported in multiple cancer, in addition to its interaction with the TEAD/TEF family of transcription factors, which is crucial for its role in tumor growth and metastasis (Zanconato et al., 2016). YAP expression is essential for development, double knockdown of YAP leads to failed embryonic axis assembly (Sousa-Ortega et al., 2023) and live-imaging of mouse embryos exhibit nuclear YAP expression patterns in pre- and post-implantation (B. Gu et al., 2022). In pluripotent stem cells (PSCs) YAP-TEAD pathway controls PSCs mechanics independently of cell-cell contacts. PSC cell colonies on micropatterned surfaces sustain transcriptional activity of YAP target genes regardless of cell density. However, contact inhibition can be restored by a negative upstream regulator of YAP, angiomin (AMOT) (Pagliari et al., 2021). Though YAP has been studied in many different tissues and settings, all research has not been uniform. There are encounters with differing findings from the general

consensus, most likely owing to the fact that YAP/TAZ can function as a tumour suppressor in addition to its role as an oncogene (Baroja et al., 2024).

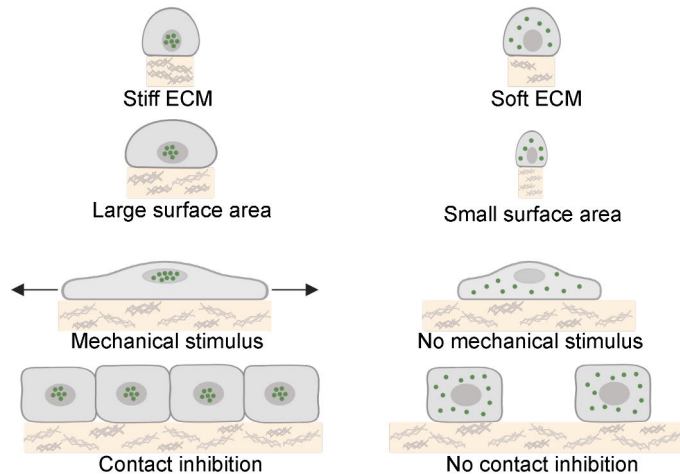


**Figure 6. Regulation of YAP/TAZ activity via mechanical and topological cues.** YAP is inactive on soft substrates, small surfaces, under contact inhibition and in the absence of mechanical stimuli. YAP translocates to the nucleus and is active on stiff substrates, large surfaces, in sparse spacing and under mechanical stimulation. Modified from <https://www.mbi.nus.edu.sg/mbinfo/what-is-the-hippo-yap-taz-tumor-suppressor-pathway/>

The serum response factor (SRF) and myocardin-related transcription factor (MRTF) are transcription factors that regulate genes involved in actin dynamics, thus impacting cytoskeletal structure and function. MRTFs, such as MRTF-A and MRTF-B, act as coactivators of SRF by enhancing its transcriptional activity (Gau & Roy, 2018). The SRF-MRTF pathway is regulated by actin polymerisation; under conditions where actin is predominantly in its monomeric G-actin form, MRTFs are sequestered in the cytoplasm. Activation of RhoA leads to changes in the actin cytoskeleton, promoting actin polymerization into filamentous F-actin and thus reducing G-actin availability. As G-actin levels drop, MRTFs are released from G-actin and translocate to the nucleus, binding to SRF. The SRF-MRTF complex binds to CA<sub>2</sub>G boxes in the promoters of target genes, initiating their transcription (Miralles et al., 2003; D.-Z. Wang et al., 2001).

MRTFs also signal through the Hippo pathway and consequently, cellular signalling of these transcription factors and YAP/TAZ is co-dependent. MRTFs can bind the YAP WW domain via a conserved PPXY motif, allowing MRTF to regulate YAP transcriptional activity (T. Kim et al., 2017). In addition, indirect crosstalk takes place through changes in cytoskeletal dynamics as MRTFs are critical regulators of the actin cytoskeleton by controlling the expression of actin and actin-

associated proteins (Foster et al., 2017; Sidorenko & Vartiainen, 2019). In cancer cells, MRTFs enhance cell motility and invasive capabilities largely through the transcriptional activation of genes such as RhoA and RhoC, which are involved in cytoskeletal reorganization (Lawson & Ridley, 2018). These Rho family GTPases in addition to the TEAD family of transcription factors are some of the regulators shared with YAP/TAZ (O. M. Yu et al., 2016). MRTFs can also increase YAP activity through regulating TAZ transcription (C.-Y. Liu et al., 2016). In addition, MRTFs control the cytoskeletal gene  $\alpha$ -SMA, which is highly expressed in CAFs, further supporting their oncogenic functions (S. Werner et al., 2019). MRTFs interact with various signaling pathways that are highly involved in uncontrolled cell growth leading to tumorigenesis, such as the TGF- $\beta$ - and MAPK/ERK-signalling pathways (Du et al., 2021; Girard et al., 2020; Miranda et al., 2017). MRTF mechanotransduction is activated by various stimuli, for example, external physical forces such as mechanical stretching and matrix stiffness, leading to its nuclear accumulation and subsequent activation and transcription of target genes (Dai et al., 2019; Hoffman et al., 2020; Melcher et al., 2022). The SRF-MRTF pathway is implemented in lung fibrosis, as it promotes the expression of genes involved in ECM production and cell migration (Sisson et al., 2015). Moreover, MRTF acts as a crucial regulator of matrix stiffness-mediated EMT (Dai et al., 2019).

$\beta$ -catenin has a dual role, function as a junctional protein in adherens junctions and as a transcription factor in the nucleus, where it activates the canonical Wnt-signalling pathway. The canonical Wnt-signalling pathway is dependent on  $\beta$ -catenin activity, while its activity is determined by nuclear to cytoplasmic shuttling (Qin et al., 2024). In the absence of Wnt-signaling, cytoplasmic  $\beta$ -catenin is short-lived as it is kept at low levels through a destruction complex consisting of adenomatous polyposis coli (APC), Axin, glycogen synthase kinase 3 beta (GSK-3 $\beta$ ) and casein kinase 1(CK1). This complex phosphorylates  $\beta$ -catenin in the cytoplasm, targeting it for ubiquitination and subsequent proteasomal degradation (Lybrand et al., 2019; Nong et al., 2021). Otherwise, Wnt-ligand binding to the Frizzled and LRP5/6 receptors activates Wnt-signalling, leading to inhibition of the destruction complex. Consequently,  $\beta$ -catenin is stabilized and accumulates in the cytoplasm.  $\beta$ -Catenin then translocates to the nucleus, where it interacts with T-cell factor/lymphoid enhancer factor (TCF/LEF) transcription factors to activate the expression of target genes (J. Liu et al., 2022). In cancer, the nuclear localization of  $\beta$ -catenin and subsequent gene transcription activation is what makes it function as an oncoprotein (Shang et al., 2017). Mutations in the APC gene prevent  $\beta$ -catenin degradation, leading to  $\beta$ -catenin nuclear accumulation and transcription activation. This aberrant activation results in the overexpression of oncogenic target genes such as c-MYC and cyclin D1 (D. Zhang et al., 2024).  $\beta$ -catenin activation is one of the primary causes of colorectal cancer, particularly in cases of familial adenomatous

polyposis (FAP), where APC mutations are inherited (Talseth-Palmer, 2017). The nuclear-cytoplasmic shuttling of  $\beta$ -catenin is also mediated by mechanical stimuli, making it a mechanosensitive protein. Increasing  $\beta$ -catenin activity in normal canine kidney cells (MDCK cells) combined with stretching triggers cells in S/G2- phase to divide (Benham-Pyle et al., 2016). In colon cancer, mechanical stimulation of APC deficient mouse colon tissue leads to  $\beta$ -catenin phosphorylation and increased nuclear localization (Whitehead et al., 2008). In addition, fluid shear stress on colon cancer cells increases nuclear  $\beta$ -catenin levels without affecting total levels (Avvisato et al., 2007). Ongoing research is exploring various strategies to inhibit  $\beta$ -catenin signaling in colorectal cancer, including small molecules, antibodies and (proteolysis-targeting chimeras (PROTACs) that degrade  $\beta$ -catenin (S.-Y. Hwang et al., 2016; Liao et al., 2020; Röth et al., 2023).

# 3 Aims

Biomechanical research has primarily focused on non-motile tissues, such as the breast, prostate, liver and pancreas, where aberrant ECM in cancer leads to tissue stiffening that further supports tumour growth. However, a variety of other mechanical properties present in homeostasis can be lost in cancer. Biomechanics in tissues under continuous mechanical stress in homeostasis, might differ in their mechanosensing properties compared to non-motile tissues. By investigating the loss of mechanical stimuli in vocal fold cancer, this thesis seeks to elucidate the diverse mechanisms through which mechanical forces influence cancer progression. The insights gained will contribute to a broader understanding of how different biomechanical TMEs impact cancer development. In addition to cancer cells interacting with the extracellular tumour matrix, other cell types in the TME, such as CAFs and CAAs, can regulate cancer cell signalling. CAFs remodel the ECM and secrete growth factors that can enhance tumorigenesis. Moreover, CAAs and dysregulated adipocytes secrete cytokines and other bioactive molecules that influence cancer cell metabolism and growth. Here, I have investigated the mechanism by which normal mammary adipocytes provide a barrier to breast cancer invasion. Additionally, I have explored a new strategy for selectively targeting and killing a broad spectrum of KRAS-mutant cancers using hyperactivation-induced cell death.

The specific aims of the thesis were:

- I. Characterization of external mechanical stimuli and ECM mechanics in vocal fold tissue homeostasis and cancer progression.
- II. Investigation of hyperactivation-induced cell death to treat KRAS-mutant cancers by disrupting the interaction between SHANK3 and KRAS.
- III. Uncovering the protective role of mammary adipocytes in the TME.

## 4 Materials and Methods

The experimental procedures in which I have been highly involved in are described. This includes conceptualizing, designing and performing the experiments. Detailed description of methodology is available in the original publications (I–III).

### 4.1 Cell culture (I, II, III)

Cell lines and their culture media are listed in Table 2. All cell lines were maintained in a humidified incubator (37 °C, 5% CO<sub>2</sub>) and regularly tested for mycoplasma (MycoAlert<sup>TM</sup> Mycoplasma Detection Kit, LT07-418 Lonza; MycoAlert<sup>TM</sup> Assay Control Set, LT07-518 Lonza). Cells were enzymatically detached with 0.25% trypsin-EDTA solution (L0932, Biowest). Cell lines were acquired from the American Type Culture Collection (ATCC) excluding patient-derived UT-SCC-11 and UT-SCC-103 cell lines, which were acquired from Auria Biobank (AB22-7195). Cell lines used in original publication II were authenticated by the Leibniz Institute DSMZ.

**Table 2.** Cell lines and culture media used in the original publications (I-III). DMEM = Dulbecco's Modified Eagle's Medium; RPMI = Roswell Park Memorial Institute; FBS = Fetal bovine serum; NEAA = non-essential amino acid.

Cell line	Culture medium	Original publication
A549	DMEM (high-glucose) supplemented with 10% FBS and 2 mM L-glutamine.	II
ARPE-19	DMEM: F12 supplemented with 10% FBS and 2 mM L-glutamine	II
AsPC-1	DMEM (high-glucose) supplemented with 10% FBS and 2 mM L-glutamine.	II
BXPC-3	RPMI-1640 supplemented with 10% FBS and 2 mM L-glutamine	II
H441	RPMI-1640 supplemented with 10% FBS and 2 mM L-glutamine	II
HaCat	DMEM (high-glucose) supplemented with 10% FBS and 2 mM L-glutamine.	I
HCT-116	DMEM (high-glucose) supplemented with 10% FBS and 2 mM L-glutamine.	II
HT-29	DMEM (high-glucose) supplemented with 10% FBS and 2 mM L-glutamine.	II
MDA-MB-231	DMEM (high-glucose) supplemented with 10% FBS and 100 mM L-glutamine.	III
MIA PaCa-2	DMEM (high-glucose) supplemented with 10% FBS and 2 mM L-glutamine.	II
PANC-1	DMEM (high-glucose) supplemented with 10% FBS and 2 mM L-glutamine.	II
Panc10.05	RPMI-1640 supplemented with 10% FBS, 10 Units/ml human recombinant insulin and 2 mM L-glutamine	II
TIF	DMEM (high-glucose) supplemented with 10% FBS and 100 mM L-glutamine.	III
UT-SCC-11	DMEM (high-glucose) supplemented with 10% FBS, 1% NEAA and 2 mM L-glutamine.	I
UT-SCC-103	DMEM (high-glucose) supplemented with 10% FBS, 1% NEAA and 2 mM L-glutamine.	I

## 4.2 Plasmid DNA and siRNA transfections (II)

A cationic lipid-based transfection was used to introduce 500 ng of plasmid DNA (Lipofectamine 3000; L3000001, Thermo Fisher Scientific) and 30–67 nM siRNA (Lipofectamine RNAiMAX Reagent, Thermo Fisher Scientific) into cells as per manufacturer’s instructions in serum-reduced conditions (Opti-MEM™; 31985054, Gibco). Transfection medium was changed to culture medium one day post-transfection and cells were used in experiments 24–96 h post-transfection.

**Table 3.** Plasmid DNA and siRNA oligonucleotides used in the original publication II.

Target	Catalog number	Source
Negative control PmCherry-C1	N/A	Gift from Jeroen Pouwels
mCherry-SHANK3-SPN A01 nanobody	N/A	Hybrigenics
mCherry-SHANK3-SPN-E01 nanobody	N/A	Hybrigenics
Negative control siRNA	1027281	Qiagen
Human KRAS siRNA SMARTpool	L-005069-00-0010	Dharmacon, Horizon Discovery
Human SHANK3 siRNA_2	S100717710	Qiagen
Human SHANK3 siRNA_7	J-024645-07	Dharmacon, Horizon Discovery
Human SHANK3 siRNA SMARTpool	L-024645-00-0010	Dharmacon, Horizon Discovery

## 4.3 Antibodies and antibody detection (I, II, III)

Antibody-based detection was used in immunofluorescence, western blotting and immunohistochemistry. Moreover, blocking antibodies were used to study integrin function. Primary antibodies used in original publications (I–III) are listed in Table 4. Target antigens were labelled in western blot assays with AzureSpectra-650 and AzureSpectra-800 antibodies (Azure) against mouse, rabbit, rat and guinea pig. Target antigens were visualized in immunofluorescence microscopy with AlexaFluor-488, AlexaFluor-568 and AlexaFluor-647 antibodies (Invitrogen) against mouse, rabbit, rat and guinea pig. In addition, DNA and filamentous actin were visualized with DAPI (4',6-diamidino-2-phenylindole), AlexaFluor-488 phalloidin (Invitrogen), phalloidinAtto-647 (Invitrogen) and SiR-actin (Spirochrome).



**Table 4.** Primary antibodies used in the original publications I–III. WB = western blotting assay; IF = Immunofluorescence; IHC = Immunohistochemistry.

Antigen	Application	Catalog number	Source	Original publication
AKT	WB	9272	Cell Signaling Technology	II
AKT (phospho-S473)	WB	9271	Cell Signaling Technology	II
Amotl2	IF, WB	23351-1-AP	Proteintech	I
$\beta$ -catenin (E247)	IF, WB	ab32572	Abcam	I
CD151	IF	ab33315	Abcam	I
COLXVII (EPR18614)	IF, WB	ab184996	Abcam	I
E-cadherin (24E10)	IF, WB	3195	Cell Signaling Technology	I
ERK1/2	WB	91025	Cell Signaling Technology	II
ERK1/2 (phospho-T202/Y204)	WB	4370	Cell Signaling Technology	II
FAK	WB	610088	BD Biosciences	II
FAK (phospho-Y397)	WB	8556	Cell Signaling Technology	II
Fibronectin	WB	F3648	Sigma-Aldrich	I
GAPDH	WB	5G4-6C5	Hyttest	I, II
HSP70	WB	ADI-SPA-815	Enzo	I, II
IgG	Integrin blocking control	12-371	Millipore	I
ILK (EPR1592)	IF, WB	ab76468	Abcam	I
Integrin $\alpha$ 3 (ASC-1)	IF	ab228425	Abcam	I
Integrin $\alpha$ 3	WB	ab131055	Abcam	I
Integrin $\alpha$ 3 (clone P1B5)	Integrin $\alpha$ 3 blocking	N/A	In-house	I
Integrin $\alpha$ 6 (CD49F, clone GOH3)	IF	MCA699	Serotec	I
Integrin $\alpha$ 6	WB	ab97760	Abcam	II
Integrin $\alpha$ 6 (clone P5G10)	Integrin $\alpha$ 6 blocking	N/A	In-house	I
Integrin $\beta$ 1 (active, clone 12G10)	Integrin $\beta$ 1 blocking	N/A	In-house	I
Integrin $\beta$ 1 (inactive, clone mAb13)	Integrin $\beta$ 1 blocking	N/A	In-house	I
Integrin $\beta$ 4	IF, WB	MAB1964	Millipore	I
Keratin 14	IF, WB	PRB-155P	Covance	I
KI67	IHC	M7240	Dako	II, III
KRAS	WB	WH0003845M1	Sigma-Aldrich	II
MLC2 (phospho-T18/S19)	IF	3674	Cell Signaling Technology	I
PARP1 (cleaved)	WB, IHC	ab4830	Abcam	II
SHANK3	WB	HPA003446	Atlas antibodies	II
SHANK3	WB	sc-30193	Santa Cruz	II
Vinculin	IF, WB	V9131	Sigma-Aldrich	I
YAP	IF, WB	sc-101199	Santa Cruz	I

## 4.4 Gene and protein expression (I, II)

### 4.4.1 Quantitative real-time PCR (II)

RNA was extracted from cells using NucleoSpin RNA -kit (#740955.250, Macherey-Nagel) and from CAM and mouse tumours using TRIsure (BIO-38032, Bioline Ltd) as per the manufacturer's instructions. Total RNA concentration was measured with Nanodrop (Thermo Fischer Scientific) and complementary DNA was synthesized by reverse transcription as per the manufacturer's instructions (high capacity cDNA Reverse Transcription Kit, Thermo Fisher Scientific). Target gene expression levels were measured with QuantStudio™ 12K Flex Real-Time PCR System (Thermo Fisher Scientific) and normalized to GAPDH levels.

### 4.4.2 RNA sequencing (I)

RNA was extracted from cells seeded on coated BioFlex® plates using NucleoSpin RNA -kit (#740955.250, Macherey-Nagel) as per the manufacturer's instructions. RNA quality was verified using Agilent Bioanalyzer 2100, and final concentrations were measured using Qubit®/Quant-IT® Fluorometric Quantitation (Life Technologies). Illumina stranded total RNA prep library was prepared using 100 ng of RNA as per the manufacturer's instructions (Illumina Stranded mRNA Preparation and Ligation kit, Illumina) and sequenced with Novaseq 6000 (S4 instrument, Illumina, v1.5).

### 4.4.3 Western blot assay (I, II)

Cells were kept on ice for a wash with cold PBS and lysed with +90 °C TX- lysis buffer (50 mM Tris-HCl, pH 7.5, 150 mM NaCl, 0.5% Triton-X, 0.5% glycerol, 1% SDS, complete protease inhibitor (SigmaAldrich), and phos-stop tablet (Sigma-Aldrich)). Lysed cells were boiled for 5 min at +90 °C, followed by a 10 min sonication and a 10 min centrifugation at 13000 rpm at +4 °C. Protein concentrations were determined from the supernatant with the DC Protein assay (Bio-Rad) as per the manufacturer's instructions. Samples were boiled at +90 °C for 5 min prior to protein separation using precast SDS-PAGE gradient gels (4–20% Mini-PROTEAN TGX, Bio-Rad) and transferred onto nitrocellulose membranes with a semi-dry Trans-Blot Turbo Transfer System (Bio-Rad). Membranes were blocked with AdvanceBlock-Fluor blocking solution (AH Diagnostics) diluted 1:1 in PBS for 1 h at room temperature and incubated over night at +4 °C with primary antibodies (see **Table 4**) diluted in AdvanBlock-Fluor blocking solution. Membranes were washed for 5 min three times with TBST (Tris-buffered saline and 0.1% Tween 20) and

incubated 1:2500 with fluorophore-conjugated Azure secondary antibodies (Azure) in AdvanBlock-Fluor blocking solution for 1 h at room temperature. Membranes were washed three times with TBST for 5 min at room temperature and scanned using an infrared imaging system (Azure Sapphire RGBNIR Biomolecular Imager). Band intensities were analysed using Image Studio Lite (Licor) by normalizing target signal to GAPDH or HSP70.

## 4.5 Methods to study cell growth (I, II)

### 4.5.1 Proliferation assay (I, II)

Softwell® Easy Coat (Matrigen) or plastic (Corning) 24-well plates were coated with 10 µg/ml collagen I (C8919, Sigma) and 10 µg/ml fibronectin (341631, Sigma) diluted in PBS or 10 µg/ml growth factor reduced Matrigel (354230, Corning®) diluted in PBS, and incubated in a humidified incubator for 1 h (37 °C, 5% CO<sub>2</sub>). Coated plates were washed three times with PBS prior to seeding cells (10 000 cells per well) in culture medium (original publication I). In addition, cells were seeded on a 96-well plate (5000 cells per well) and transfected with siRNAs on the following day, as described above (original publication II). Time-lapse live-imaging was performed using IncuCyte S3 or ZOOM Live-Cell Analysis System for 96 h with 2 h imaging intervals (10× objective), changing the medium every second day. Relative proliferation was analysed with IncuCyte S3 or ZOOM software.

### 4.5.2 Viability assay (I, II)

Cell viability was measured with CCK8 cell counting kit (ab228554, abcam) as per manufacturer's instructions. Cells were seeded on a 96-well plate (5000 cells per well) in culture medium. DMSO (D265, Sigma), YAP-TAZ-TEAD inhibitors K-975 (HY-138565, MedChemExpress) or IK-930 (HY-153585, MedChemExpress) were added at different concentrations the following day. Cells were incubated with CCK8 reagent for 2 h at +37 °C prior to measuring viability, 48 h after inhibitor treatment, as absorbance at 450 nm (original publication I). Additionally, 3D spheroid formation assay cell viability was measured with CCK8 at the final timepoint (original publication II).

### 4.5.3 Flow cytometry (II)

Cells were cultured to 70% confluence and stained with Annexin V apoptosis kit (BMS500FI-300, Thermo Fisher Scientific Inc) as per manufacturer's instructions. Annexin V-FITC/propidium iodide labelling was used to evaluate proportion of

apoptotic and necrotic cell death in cells transfected with plasmid DNA or siRNA. Labelled cells were detected 1–4 days post-transfection using BD LSR Fortessa™ analyser (BD Biosciences). Live and apoptotic/necrotic cell populations were quantified using Flowing software.

#### 4.5.4 3D spheroid formation assay (I, II)

3D spheroid formation was assessed by embedding cells between two layers of Matrigel (Corning, 354230) in an angiogenesis 96-well  $\mu$ -plate (89646, Ibidi GmbH). The bottom of the well was coated with 10  $\mu$ l of 50% Matrigel diluted in culture medium and centrifuged at +4 °C (200 g for 20 min). The centrifuged Matrigel layer was incubated for 1 hour in a humidified incubator (37 °C, 5% CO<sub>2</sub>). Next, 20  $\mu$ l of single-cell suspension in 25% Matrigel diluted in culture medium (500–1000 cells/well) was added to each well, centrifuged at +4 °C (100 g for 10 min) and incubated for 4 h in a humidified incubator (37 °C, 5% CO<sub>2</sub>). Next, wells were filled with culture medium supplemented with 10  $\mu$ g/ml function blocking antibodies or IgG control; mouse anti-IgG (31903, Invitrogen), mouse anti-human  $\alpha$ 3 integrin (P1B5, In-house hybridoma), mouse anti-human  $\alpha$ 6 integrin (P5G10, In-house hybridoma) and rat anti-human  $\beta$ 1 integrin (mAb13, In-house hybridoma) (original publication I) or unsupplemented culture medium (original publication II). Spheroid formation was monitored for 10–12 days with IncuCyte S3 Live-Cell Analysis system (10 $\times$  objective), changing culture medium every 2–3 days. Analysis of spheroid growth was performed using OrganoSeg software and ImageJ software.

### 4.6 Methods to study cell migration and invasion (I)

#### 4.6.1 Migration assay (I)

50 kPa Softwell Easy Coat (Matrigen) 24-well plates were coated with PBS-diluted 10  $\mu$ g/ml fibronectin (341631, Sigma) and 10  $\mu$ g/ml collagen I (C8919, Sigma) for 1 h in a humidified incubator (37 °C, 5% CO<sub>2</sub>). Next, plates were washed three times with PBS prior to seeding 1000 cells in culture medium. Time-lapse live-imaging was performed using Nikon Eclipse Ti2-E (10 $\times$ / 0.3 objective) for 24 h with 10 min imaging intervals. Single-cell tracking was performed using TrackMate plugin in ImageJ software.

#### 4.6.2 Wound healing assay (I)

Cells were seeded (100 000 cells per well) on IncuCyte ImageLock 96-well plates (Essen BioScience). The following day a scratch wound was made with the IncuCyte

WoundMaker (Essen BioScience). Wells were washed with PBS to remove detached cells and culture medium was added. Time-lapse live-imaging was performed to monitor wound closure using IncuCyte ZOOM Live-Cell Analysis System for 96 h with 2 h imaging intervals (10× objective). Wound closure was analysed with the IncuCyte ZOOM software.

### 4.6.3 Invasion assay (I)

Cells were seeded (200 000 cells per well) in serum free medium on Matrigel transwell inserts (354480, Corning) and placed in culture medium. After 45 h of invasion, uninvaded cells in the inner well were wiped off with cotton buds and invaded cells were fixed with 4% PFA (diluted in PBS) for 10 min at room temperature. Inserts were washed 3 times with PBS and stained overnight with DAPI. Invaded cells were assessed by confocal imaging (3i Marianas CSU-W1; 20×/0.8 objective) and quantifying the number of invaded cells per field of view in ImageJ software.

## 4.7 In vivo methods (I, II, III)

### 4.7.1 Chick embryo chorioallantoic membrane assay (II)

Fertilised chicken eggs were washed with 70% ethanol and placed in a humidified incubator (37 °C, 5% CO<sub>2</sub>). On day three, a small hole was made in the eggshell to detach the chorioallantoic membrane (CAM) from the shell. On day 7 a plastic ring was placed on the CAM and one million cells were implanted inside the ring in 20 µl of 50% Matrigel (354230, Corning) diluted in PBS. After 4–5 days, the formed tumours were dissected, weighed and fixed in 10% formalin.

### 4.7.2 Subcutaneous tumour xenograft (II, III)

Subcutaneous xenografts were performed using six- to eight-week-old athymic nude mice (Foxn1nu; Envigo, UK/France) by injecting five million PANC-1 cells, expressing dox-inducible SHANK3 shRNA (pool of clones 4S and 1C) resuspended in 100 µl 50% Matrigel (Cat. no. 354230, Corning) diluted in PBS (original publication II) or by co-injecting six million mT2-TIFs or TIFs IGFBP2-TIFs and two million MDA-MM231 cells in PBS (original publication III). Mice were housed in standard conditions (12-hour light/12-hour dark cycle) with food and water available ad libitum. PANC-1 SHANK3 tumours were blindly randomized into two groups, once tumour volume reached 100 mm<sup>3</sup>. Mice with PANC-1 SHANK3 tumours were fed either a normal chow (control group; Teklad 2914 diet, Envigo) or

dox-containing chow (SHANK3-depleted group; Teklad doxycycline-diet, 625 mg/kg, in 2014 diet base, irradiated (2914), colour red, Envigo). Additionally, the mice received two intraperitoneal (i.p) injections of PBS or doxycycline (80 mg/kg of body weight) on day one and two of doxycycline induction. Successful induction of SHANK3 shRNA expression was confirmed using IVIS live-imaging. PANC-1 SHANK3 tumour growth was monitored by palpation twice a week and mice were sacrificed when tumour volume reached  $>500 \text{ mm}^3$  (original publication II). TIF mT2/IGFBP2 and MDA-MM231 tumour growth was tracked by palpation until the tumour volume reached  $>300 \text{ mm}^3$  (original publication III). After reaching final tumour volume the mice were euthanized and tumours were dissected, weighed and snap-frozen in liquid nitrogen for RNA extraction. Quantification of local invasion was performed in QuPath by quantifying the percentage of local invasion in the xenograft (invaded cell areas divided by the total tumour area). All animal experiments were performed in accordance with the Finnish Act on Animal Experimentation (animal license numbers ESAVI/9339/2016, ESAVI/37571/2019 and ESAVI/12558/2021)

### 4.7.3 Patient samples (I)

Patient samples were obtained under the Finnish Biobank Act with written informed consent from the sample donors (§279, 9/2001) at Turku University Hospital. Patient samples were given an arbitrary identifier and no patient information, excluding age and histopathological information were available or recorded. For further processing, obtained tissue samples were snap frozen with liquid nitrogen and stored at  $-80 \text{ }^\circ\text{C}$ .

## 4.8 Methods to study cell mechanics (I)

### 4.8.1 Cell stretching (I)

Polydimethylsiloxane (PDMS) stretch chambers (STB-CH-4W, STREX Cell Stretching Systems) coated with  $10 \text{ }\mu\text{g/ml}$  fibronectin (341631, Sigma) and  $10 \text{ }\mu\text{g/ml}$  collagen I (C8919, Sigma) diluted in PBS for 2 hours in a humidified incubator ( $37 \text{ }^\circ\text{C}$ ,  $5\% \text{ CO}_2$ ). Coated chambers were washed three times with PBS prior to seeding 200 000 cells per well in culture medium. Cells were stretched the following day with STREX cell stretching system (STB-140-10) with 20% stretch (6.40 mm), 1 Hz frequency for varying periods (5 min, 30 min 1 h). Stretched cells were fixed with 4% PFA for 10 min, washed three times with PBS at room temperature and stored at  $+4 \text{ }^\circ\text{C}$ .

## 4.8.2 Cell vibration (I)

Flexible-bottomed silicone elastomer plates (BF-3001U, BioFlex®) were coated with 10 µg/ml fibronectin (341631, Sigma) and 10 µg/ml collagen I (C8919, Sigma) diluted in PBS for 2 hours in a humidified incubator (37 °C, 5% CO<sub>2</sub>). Coated chambers were washed three times at room temperature with PBS prior to seeding cells (500 000–900 000 cells per well) in culture medium. Cells were vibrated the following day with a phonomimetic bioreactor (Kirsch et al., 2019) connected to a Crown XLS 1502 amplifier. Stimulating sound files were played for varying periods (5 min, 30 min 1 h, 6 h) with 1 min intervals (1 min on /1 min off) at a frequency range of 50–250 Hz. Vibrated cells were fixed with 4% PFA for 10 min, washed three times with PBS at room temperature and stored at +4 °C.

## 4.8.3 Cell growth on elastic surfaces (I)

Hydrogels (Softwell Easy Coat, Matrigen) of varying rigidities were coated with 10 µg/ ml fibronectin (341631, Sigma) and 10 µg/ ml collagen I (C8919, Sigma) diluted in PBS for 2 hours in a humidified incubator (37 °C, 5% CO<sub>2</sub>). Coated hydrogels were washed three times with PBS prior to seeding 200 000 cells per well in culture medium and cell growth was monitored for 72–96 hours. Cells were fixed with 4% PFA for 10 min, washed three times with PBS at room temperature and stored at +4 °C.

## 4.9 Imaging techniques (I, II)

### 4.9.1 Immunolabeling (I, II)

Fixed cells were permeabilized and blocked for nonspecific antibody-binding using 0.3% Triton-X-100 in 10% normal horse serum diluted in PBS for 20 min at room temperature. Target proteins in cells were labelled with primary antibodies diluted in 10% normal horse serum overnight at 4 °C. The following day cells were washed three times for 5 min with PBS and incubated with secondary fluorescence-conjugated antibodies diluted in PBS for 1 h at room temperature, followed by three 5-min washes with PBS. Samples were either imaged right away or stored at 4 °C protected from light until imaging. Antibodies used for immunolabeling are listed in Table 4.

## 4.9.2 Imaging fixed samples (I)

Fixed samples were imaged with a 3i spinning disk confocal microscope (Marianas spinning disk imaging system with a Yokogawa CSU-W1 scanning unit on an inverted Carl Zeiss Axio Observer Z1 microscope, Intelligent Imaging Innovations, Inc., Denver, USA). Objectives used for imaging: 10× Zeiss Plan-Apochromat objective (without immersion, 2mm working distance, 0.45 numerical aperture), 40× Zeiss LD C-Apochromat objective (water immersion, 0.62 mm working distance, 1.1 numerical aperture) and 63× Zeiss Plan-Apochromat objective (oil immersion, 0.19 mm working distance, 1.4 numerical aperture). Image analysis was performed using ImageJ software.

## 4.9.3 Live imaging (I, II)

Live imaging was performed using Nikon Eclipse Ti2-E (Hamamatsu sCMOS Orca Flash4.0, Lumencor Spectra X LED excitation) with a 20x objective (Nikon CFI S Plan Fluor ELWD, NA 0.45, WD 8,200 µm) or the IncuCyte Live-Cell Analysis System (S3 and ZOOM). Image analysis was performed using ImageJ software or IncuCyte software.

## 4.10 Genomic databases (I)

### 4.10.1 The Cancer Genome Atlas (TCGA) (I)

TCGA head and neck squamous cell carcinoma (HNSCC) dataset was retrieved and filtered for patient IDs with laryngeal cancer as primary tumour site. Pathology reports were reviewed to assess tumour subsite (glottic larynx) and vocal fold involvement. Raw files were downloaded from xena browser (<https://xenabrowser.net/>). Differentially expressed genes (FDR < 0.05) were determined using Bioconductor R package ROTS (v.1.14.0).

### 4.10.2 Cancer Dependency Map (DepMap) (I)

A pan cancer search identifying the top 20 co-dependencies in the CRISPR DepMap Public 23Q2+Score Chronos dataset was performed to survey YAP dependency hits (Pearson's correlation,  $r$ ). Data files were downloaded from DepMap (<https://depmap.org/portal/>).



## 4.11 Statistical analysis (I, II)

Statistical analyses and data visualization were performed using GraphPad Prism. Outliers were identified with 0.1% ROTS and distribution was determined with D'Agostino-Pearson normality test. Two-sample testing was performed using Student's t-test with Welch's correction (normally distributed data) or nonparametric Mann-Whitney U-test (non-normally distributed data). Multiple comparisons were performed using ANOVA with Holm-Sidak's post hoc test for normally distributed data and Dunnett's post hoc test for non-normally distributed data. Data are presented as dot plots or column graphs (mean $\pm$ s.d.) with p-values less than 0.05 considered to be statistically significant.

## 5 Results

### 5.1 Tumour reversion by mechanical stimuli in vocal fold cancer (I)

The vocal folds are a biomechanically interesting tissue for in homeostasis they are under regular mechanical stimulation; phonation is induced by vibration and the vocal folds open as one breathes and close when swallowing and speaking. The vocal folds are made up of the vocalis muscle, the BM, lamina propria and the epithelial layer. Each layer is characterized by its ECM composition (Gray, 2000). In vocal fold cancer, a squamous cell carcinoma arises in the epithelial layer. Early stages of cancer (T1–T2) are confined by the BM, but in later stages (T3–T4) the cancer cells breach the BM invading the surrounding tissues. In addition to invasion to the underlying muscle and tissues of the neck, VFC progression is characterized by its mobility status based on TNM-status; T1–T2 vocal folds move normally, whereas in T3–T4 are mechanical fixed (I, Fig. 1A and B). Despite the interesting mechanical homeostasis that is lost in cancer as the tissue becomes immobile (Knudsen et al., 2019), biomechanics in the vocal folds remain underexplored. Here using patient-derived VFC cell lines, we uncover a mechanophenotype that can revert its oncogenic properties in response to external mechanical stimuli. Moreover, VFC patient samples reveal an increase in tissue stiffness as well as extensive tumour matrix remodelling. Finally, vulnerability to YAP-TEAD inhibition *in vitro* uncovers a promising therapeutic pathway to explore for cancer intervention.

#### 5.1.1 ECM remodelling and increased rigidity supports migration and invasion in VFC

Intrigued by the immobility in VFC, we aspired to investigate a possible role for the ECM. We analysed vocal fold RNA-sequencing data generated by The Cancer Genome Atlas (TCGA), comparing normal (n=12) and cancer (T1–T4, n=54) samples to identify differentially expressed genes (false discovery rate, FDR < 0.05). The analysis revealed upregulation of 2041 genes and downregulation of 1629 genes in cancer samples compared to normal tissue. ECM and collagen-related GO-terms (Gene ontology) were enriched among the upregulated genes in cancer (I, Fig. 1C).

Furthermore, Matrisome AnalyzeR identified all differentially expressed collagens to be upregulated, such as collagens I, III, IV and V that are present in the different vocal fold layers (I, Fig. 1E). Moreover, 53 ECM glycoprotein genes were upregulated (I, Fig. 1F), including fibronectin (FN) and laminin-332 chains (LAMA3, LAMB3 and LAMC2). Additionally, 59 ECM regulator genes were upregulated (I, Fig. 1G), such as lysyl oxidases (LOXs) and metalloproteinases. Next, we sought to investigate whether the increased ECM production impacted tissue stiffness. Atomic force microscopy (AFM) on non-cancerous (NC) (n=3) and cancer (n=2) patient samples (obtained from vocal fold surgery) confirmed a 3.2-fold increase in the cancerous tissue stiffness ( $2.441 \pm 1.479$  kPa) compared to normal tissue ( $0.751 \pm 0.341$  kPa) (I, Fig. 1H and I).

As increased ECM production and stiffness can promote cell proliferation, we next aimed to explore whether the changes seen in vocal fold patient tissue samples influence VFC on the cellular level. For the *in vitro* experiments, we compared T1 (UT-SCC-11) and T3 (UT-SCC-103) patient-derived VFC cell lines, generated at the University of Turku, to non-cancerous (NC) (HaCaT) cells. Live-cell imaging of T1 and T3 cell proliferation for 4 days on hydrogels of varying stiffnesses and on plastic (coated with collagen I and fibronectin or Matrigel) exhibited significantly higher proliferation of T3 cells compared to T1 cells (I, Fig. 3A–C; Fig. S3A–C). Additionally, single-cell migration of T3 cells demonstrated increased speed, accumulated distance and directionality compared to T1 cells on 50 kPa hydrogels (I, Fig. 3D and E). Collective cell migration of T3 cells was significantly greater in speed compared to T1 cells (I, Fig. S3F and G) as was invasion efficiency (I, Fig. 3F and G). Taken together, these results demonstrate increased ECM composition and stiffness in VFC and consequent elevated VFC proliferation, migration and invasion.

### 5.1.2 Laminin-binding integrins modulate VFC monolayer dynamics and cell clustering

Following our findings on the ECM, we next explored the role of IACs in VFC, as they mediate adhesion to the ECM in addition to functioning as mechanosensors. The afore mentioned TCGA results indicated upregulation of several genes encoding IACs, notably the laminin-binding integrins  $\alpha 3$ ,  $\alpha 6$ ,  $\beta 1$  and  $\beta 4$ . These integrins are found either in hemidesmosomes as a  $\alpha 6\beta 4$  heterodimer or in FAs as a dimer with integrin  $\beta 1$  (I, Fig. 2A and B). To determine integrin expression in our cell model, we used mass cytometry for high-dimensional phenotypic analysis of the cell-surface expression of 19 integrins, revealing a heterogeneous single-cell surface expression of integrins  $\alpha 6$  and  $\beta 4$  in cancer cells compared to NC cells (I, Fig. 2C) The observation was further confirmed by confocal immunofluorescence imaging (I, Fig.

2D). Expression of hemidesmosome components BP180 (COLXVII) and keratin 14 reflected a similar heterogeneity and loss of hemidesmosome structures in T3 cells. Single-cell surface expression of FA integrins  $\alpha 3$  and  $\beta 1$  was also heterogeneous in both T1 and T3 cells (I, Fig. 2E). Confocal immunofluorescence imaging affirmed that the changes in surface expression levels were likely due to a difference in subcellular integrin localization (I, Fig. 2F), as integrin  $\alpha 3$  localized in cell-cell junctions in NC and T1 cells (I, Fig. 2G). However, integrin  $\alpha 3$  was predominantly localized in endosome-like intracellular structures in T3 cancer cells (I, Fig. 2G). We observed similar changes in CD151 localization, a tetraspanin present in both FAs and hemidesmosomes (I, Fig. 2H). Furthermore, T1 and T3 cells exhibited an increased number of smaller vinculin- and active integrin  $\beta 1$  (12G10)-positive cell-ECM adhesions compared to NC cells (I, Fig. 2I and J).

The aforementioned changes in cell-cell and cell-ECM adhesion, led us to investigate the functional role of laminin-binding integrins in VFC. We treated sparse cell clusters with integrin  $\alpha 3$ - (P1B5),  $\alpha 6$ - (P5G10) and  $\beta 1$  (mAb13)-blocking antibodies and performed live-cell imaging. Dual inhibition of integrins  $\alpha 3$  and  $\alpha 6$  resulted in slowing cell movement in addition to retraction of junctional and cell-edge lamellipodia (Videos 13-15). Inhibition of E-cadherin had an opposing effect as the weakened cell-cell adhesions caused cell scattering and elongation (Videos 16-18). Inhibiting the laminin-binding integrins ( $\alpha 3 + \alpha 6$  and  $\beta 1$ ) in 3D-spheroids increased growth of NC and T1 cells (spheroid area) compared to IgG control treatment (I, Fig. 4A and B), likely due to reduced spheroid compaction and increased cell dissociation (I, Fig. S4a). While integrin inhibition had clear effects on NC and T1 cells, T3 cells grew rapidly into large spheroids regardless of treatment and did not show increased cell dissociation compared to IgG control (I, Fig. 4A and B). These findings are concordant with the differences in cellular localization of laminin-binding integrins.

To further investigate the role of cell-cell junctions in VFC, we analysed junction morphology based on confocal immunofluorescence staining of E-cadherin and  $\beta$ -catenin. T3 cell junctions were linear, indicating low junctional tension, whereas NC and T1 cells had protrusive finger-like junctions that are linked to higher junctional tension (I, Fig. 4C). Analysis of junction morphology (straight, reticular and finger-like) confirmed presence of reticular junctions in all cells, whereas finger-like-junctions were lost in T3 cells in addition to a larger proportion of straight junctions in T3 cells (I, Fig. 4C). Overall, these data demonstrate that laminin-binding integrins contribute to cell-ECM and cell-cell adhesion dynamics in VFC.

### 5.1.3 Uncovering a previously unobserved motility state in VFC cells

In homeostasis, cells cease and undergo a jamming phase transition (PT) when reaching a critical cell density. This is regulated by cell-cell and cell-ECM adhesion mechanics and functions as a tumour-suppressive mechanism. However, cancer cells can undergo unjamming and flocking PTs to promote collective invasion (Ilina et al., 2020; Oswald et al., 2017). In fluid-like flocking, cells move in a coordinated manner without being tightly bound to each other, allowing them to rearrange and adapt their movements. Contrarily, in solid-like flocking, cells stick closely to one another, forming a more rigid structure as cells move as a whole. To explore PTs in VFC monolayer dynamics treated with integrin inhibitors, we performed PIV (Particle image velocimetry) analysis on live-cell movies. While untreated NC cells exhibited a progressive reduction in cell motility (I, Fig. 4C), inhibiting integrins  $\alpha 3$ ,  $\alpha 6$  and  $\beta 1$  significantly reduced their collective motion; the inhibitor treatments accelerated the transition towards a jamming state (I, Fig. S4B). Cell motility in untreated T1 and T3 cells remained constant, and greater than the final velocity of NC cells (I, Fig. 4F and M). Though inhibition of integrin  $\beta 1$  or integrins  $\alpha 3$  and  $\alpha 6$  together reduced T1 cell velocity, T3 cell motility was insensitive to integrin inhibition; T3 cells exhibited a complete loss of correlation in motility and T1 cells an intermediate loss, suggesting that T1 and T3 monolayers are far from reaching a jammed state (I, Fig. 4J and M). Moreover, T1 cells had cohesive and coordinated movement with aligned cell velocities and maintained long-range coordinated motion despite anti-integrin treatments (I, Fig. 4K). Similar motion was detected in T3 cells to a lesser extent (I, Fig. 4N). These data imply a solid-like flocking PT in VFC, characterized by long-range coordinated motility and absence of local cell rearrangements. Interestingly, solid-like flocking has not yet been observed experimentally in mammalian cells. These findings suggest that VFC cells exploit a solid-like flocking state to enhance long-distance collective motion and thus advancing cancer invasion and metastasis.

Next, we set out to mimic the early step of local dissemination by spreading of 3D spheroids onto ECM-coated substrate in a “wetting” transition. This transition is dependent on the cohesive cell-cell tensional state and viscoelastic properties of the spheroids, in addition to the cell-ECM interactions. Both T1 and T3 spheroids showed a significant increase in wetting velocity compared to NC cells: T1 spheroids rapidly and uniformly wetted the surface, consistent with the solid-like flocking motion and elevated monolayer velocity (I, Fig. 4G and I), while T3 spheroids wetted the surface by extending protruding clusters with contractile local regions, consistent with their high contractility and reduced monolayer velocity (I, Fig. S4C and D). In NC spheroids, inhibition of integrins  $\alpha 3$ ,  $\alpha 6$  and  $\beta 1$  caused an evident reduction in wetting velocity. Conversely, no marked effects were observed in T1 and T3 wetting

spheroids treated with integrin inhibitors (I, Fig. 4J and K; Fig S4. E and F), suggesting that VFC wetting is independent of cell-ECM adhesion receptors and directed by the bulk mechanical properties of the 3D spheroids.

#### 5.1.4 Mimicking mechanical stimuli in the vocal folds induces cytoskeletal changes, junctional alterations and cell extrusion

We next sought to determine differences in response to mechanical stimuli. To mimic the mechanical forces in the vocal folds, we subjected the cells to stretching and vibration. Uniaxial cyclic cell stretching (1 Hz, 20% stretch) for 1 h induced perpendicular actin cytoskeleton alignment (coherency) to the stretch direction in NC and T1 cells (I, Fig. 5A and B). T3 cells did not exhibit visible actin alignment, though alignment analysis showed a significant increase (I, Fig. 5B). Similarly, vibration stimulus matching the frequency of human adult vocal folds during normal phonation (50-250 Hz, 1 min off/on) induced visible formation of actin stress fibers (I, Fig. 5C) and monolayer remodelling in NC and T1 cells. Furthermore, 6-hours of vibration of T3 cells induced a significant increase in extrusion of contractile, pMLC-positive cells (I, Fig. 5E–G; Fig. S5C). Thus, reintroducing mobility in T3 cells causes cell extrusion likely as a means to ensure homeostasis.

Next, we explored the outcomes of mechanical manipulation on cell-cell junctions. We firstly noticed that  $\beta$ -catenin was not only located at cell-cell junctions, but present in the nucleus in T1 and T3 cells, where it acts as a transcription factor promoting tumorigenesis (I, Fig. 5F and G). Uniaxial cyclic stretching (1 Hz, 20% stretch) for 1 hour resulted in junction alignment in NC and T1 cells (I, Fig. S5D). Interestingly, stretching caused a significant reduction in nuclear and total  $\beta$ -catenin levels in T1 and T3 cells (I, Fig. 5H and I; Fig. S5E). This reduction in oncogenic nuclear  $\beta$ -catenin expression occurred also in vibrated cells (I, Fig. 5J and K; Fig. S5F). Together these data demonstrate that NC and VFC cells differ in their response to mechanical stimuli, notably in the regulation of oncogenic nuclear  $\beta$ -catenin (**Figure 7**).

#### 5.1.5 Mimicking mechanical stimuli in the vocal folds decreases nuclear and total YAP levels

In addition to  $\beta$ -catenin, YAP is another oncoprotein that shuttles between the cytoplasm and nucleus, activating oncogenic signalling cascades in the nucleus. Total YAP RNA and protein expression levels (I, Fig. 6A–C) did not show significant changes in VFC cells compared to NC cells. However, RNA expression levels of YAP downstream targets Ankyrin Repeat Domain 1 (ANKRD1), AXL,

macrophage colony stimulating factor (CSF1) and Cysteine-rich angiogenic inducer 61 (CYR61) were increased in VFC cells (I, Fig. 6D) indicative of pathway activity. We next assessed the effect of vibration on YAP levels, showing that vibration decreased total and nuclear YAP levels in a time-dependent manner in all cell lines (I, Fig. 6E–G). Intrigued by our results implying that vibration primarily regulates YAP levels rather than its nucleocytoplasmic shuttling, we next conducted a YAP pan cancer search identifying the top 20 co-dependencies in the CRISPR DepMap Public 23Q2+Score Chronos dataset in DepMap. We found the strongest dependency hits (Pearson’s correlation,  $r$ ) with Angiomotin-like protein 2 (AMOTL2,  $r = -0.28$ ), Rho Guanine Nucleotide Exchange Factor 7 (ARHGEF7,  $r = 0.29$ ), TEA Domain Transcription Factor 3 (TEAD3,  $r = 0.29$ ), TEA Domain Transcription Factor 1 (TEAD1,  $r = 0.29$ ) and Tankyrase 2 (TNKS2,  $r = 0.28$ ) (I, Fig. 6H). As AMOTL2 has a strong negative co-dependency to YAP based on the survey, we next investigated the relationship between YAP and AMOTL2 in VFC. AMOTL2 has previously been shown to retain YAP within the cytoplasm by direct interaction (B. Zhao et al., 2011). AMOTL2 RNA levels showed no changes between the cell lines (I, Fig. 6I). However, AMOTL protein levels were significantly lower in VFC cells compared to NC cells (I, Fig. 6 J and K). Moreover, vibration significantly increased AMOTL2 total and nuclear levels in VFC cells (I, Fig. 6L–N; Fig. S6B), which coincides with the decrease in YAP levels (I, Fig. 6F–G). Collectively, these results demonstrate that mechanical forces support tissue homeostasis by decrease oncogenic nuclear YAP levels in VFC cells (**Figure 7**).

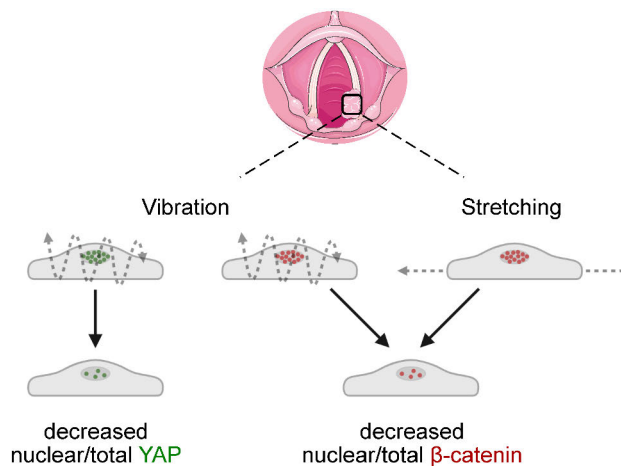


**Figure 7. Mechanical stimuli downregulates oncogenic YAP and β-catenin signalling in vocal fold cancer.** Vibrating and stretching vocal fold cancer cells reverts cellular oncogenic properties by decreasing nuclear and total YAP and β-catenin expression.

### 5.1.6 Therapeutic potential of YAP-TEAD inhibition

To explore our *in vitro* findings in patient samples, we built a laryngeal cancer tumour microarray (TMA) with cancer patient samples from T1 to T4 (n=218). Analysis of multiplex immunohistochemistry staining revealed a high correlation between ECM related proteins (FN, Col I, SMA, laminin and vinculin) (I, Fig. S7A). We assigned an ECM score (median values of stromal ECM related proteins in the patient cohort) and applied it to each patient; ECM-scores ranged from zero to five based on how many of the five ECM proteins were expressed above average level. Thus, ECM score 0 indicates that all ECM proteins are expressed below average, and ECM score 5 indicates that all ECM proteins are expressed above average. These scores were further divided into two groups; ECM-low (ECM scores 0–2) and ECM-high (ECM score 3–5). Analysis of the implemented ECM score and patient data revealed a significant correlation between ECM score and T-status, with lower ECM scores being associated with lower T-status (I, Fig. 7A). Similar scoring regarding above and below average expression was applied to YAP to determine whether YAP expression correlates with T-status and the ECM score. Interestingly, we discovered that patients with higher T-status (T3–4) expressed high levels of YAP in tumours in addition to increased nuclear YAP levels in tumours correlating with higher ECM scores (I, Fig. 7B–D). Moreover, nuclear YAP was predictive of disease-specific survival (I, Fig. 7E). Based on our TMA findings on YAP, we next investigated whether inhibition of YAP/TAZ/TEAD pathway would impair VFC viability by treating NC and VFC cells with two YAP-TAZ-TEAD inhibitors; K-975 and IK-930. Both inhibitors caused a significant and dose-dependent decrease in cell viability, notably in T3 VFC cells (I, Fig. 7F–I). Together, these findings imply clinical potential for YAP/TAZ/TEAD inhibition as a targeted treatment option for VFC.

## 5.2 Signalling overdose to target KRAS-mutant cancers (II)

Mutations in the KRAS (Kirsten rat sarcoma viral oncogene homolog) oncogene are prevalent in a significant number of cancers, such as pancreatic, lung and colorectal cancers (L. Huang et al., 2021). These mutations result in continuous activation of proliferative signalling pathways, leading to uncontrolled cell growth and resistance to standard therapies. Despite recent advancements in developing mutation-specific inhibitors, there remains a substantial gap in effective treatments for most KRAS-mutant cancers. As SHANK3 was discovered to have a Ras-association domain (Lilja et al., 2017), we sought to explore whether expression and signalling of the scaffolding protein SHANK3 could modulate KRAS activity. We focused on



KRAS-mutant cancers that have been particularly hard to target, though having great interest as a potential target for cancer therapies (Punekar et al., 2022).

### 5.2.1 SHANK3's interaction with active KRAS and modulation of MAPK/ERK signalling

Previous research has shown that the SHANK3 N-terminus, containing a Ras-association (RA) domain-like SPN structure, interacts with active (GTP-bound) KRAS mutants (Lilja et al., 2017). Microscale thermophoresis (MST) and isothermal titration calorimetry (ITC) confirmed this interaction with low micromolar affinity, while no interaction occurred with inactive (GDP-bound) KRAS (II, Fig. 2B–D). Co-immunoprecipitation and FLIM-FRET (Fluorescence lifetime microscopy and fluorescence resonance energy transfer) experiments in cells demonstrated that SHANK3 specifically binds to KRAS through conserved R12 and K22 residues (II, Fig. 2E and F). Mutations in these residues disrupted the interaction, confirming their importance (II, Fig. 2G). Additionally, re-expression of wild-type (WT) SHANK3, but not a KRAS-binding-deficient mutant, restored cell viability in SHANK3-silenced KRAS-mutant cancer cells, highlighting the crucial role of SHANK3-KRAS interaction in supporting cell survival (II, Fig. 2 H).

KRAS must associate with the plasma membrane and recruit effector proteins such as RAF for active signalling (Simanshu et al., 2017). GFP-SHANK3 and endogenous SHANK3 both localize to the plasma membrane and overlap with mutant mCherry-KRASG12V, suggesting an interaction (II, Fig. 3A). Simulations showed that SHANK3 SPN and ARR domains interact with the negatively charged plasma membrane, similar to RAF's Ras-binding domain (RBD) (II, Fig. 3B–E). Structural analysis indicated that SHANK3 competes with RAF for KRAS binding on the membrane, potentially limiting KRAS signalling (II, Fig. 3B and C). *In vitro* competition assays confirmed that increasing SHANK3 SPN concentrations reduced KRAS binding to RAF-RBD (II, Fig. 3D). Isothermal titration calorimetry (ITC) measurements showed SHANK3 and RAF-RBD have similar affinities for KRAS, supporting the competition hypothesis (II, Extended Data Fig. 3F). In cells, SHANK3 silencing enhanced RAF-KRAS interaction, indicating SHANK3 competes with RAF for KRAS binding and influences downstream signalling. SHANK3's ability to compete with RAF was tested in KRAS-mutant cells. Overexpression of SHANK3 SPN WT reduced ERK1/2 phosphorylation and nuclear translocation, while a KRAS-binding-deficient mutant did not (II, Fig. 3F and G). Furthermore, SHANK3 SPN WT restrained KRAS-driven tumour growth in xenografts (II, Fig. 3H). Together these findings demonstrate that SHANK3 competes with RAF for active KRAS binding, thereby limiting MAPK/ERK signalling and oncogenic activity.

## 5.2.2 SHANK3 in KRAS-mutant cancer cell viability

As we established that SHANK3 interacts with active KRAS, we next sought out to understand SHANK3's role in cancer cell viability using RNA interference (RNAi) to deplete SHANK3 in various KRAS-mutant cancer cell lines, including pancreatic ductal adenocarcinoma (PDAC), non-small cell lung cancer (NSCLC) and colorectal cancer (CRC). SHANK3 depletion significantly impaired proliferation in all 12 tested KRAS-mutant cell lines, with inhibition rates ranging from 38% to 81% (II, Fig. 1A). In contrast, cancer cell lines with WT KRAS showed no significant reduction in proliferation (II, Fig. 1A). Further, SHANK3 silencing reduced colony growth by about 90% in KRAS-mutant pancreatic (PANC-1) and lung cancer (A549) cells (II, Extended Data Fig. 1B). In 3D cultures, growth inhibition was also evident in KRAS-mutant pancreatic and lung cancer spheroids (II, Fig. 1B). Furthermore, we generated PANC-1 cell clones with doxycycline (dox)-inducible shRNA against SHANK3 (II, Fig. 5A), and dox-induced SHANK3 depletion halted the growth of 3D spheroids (II, Fig. 5C–D). These findings demonstrate that SHANK3 depletion effectively blocks cell proliferation in KRAS-mutant cancers.

## 5.2.3 SHANK3 depletion leads to tumour suppression *in vivo*

Prompted by our *in vitro* findings, we performed *in vivo* experiments using xenograft models to assess SHANK3's role in tumour growth. Firstly, SHANK3 depletion in KRAS-mutant PANC-1 and A549 xenografts on chick embryo chorioallantoic membranes (CAMs) led to reduced tumour weight and fewer proliferating cells, while WT KRAS tumours remained unaffected (II, Fig. 1C–E). We next evaluated whether SHANK3 is essential in maintaining tumour growth. Dox-inducible PANC-1 cells were implanted into flanks of athymic nude mice (Foxn1nu) and dox-induced SHANK3 depletion was initiated once tumours of 100 mm<sup>3</sup> in volume were established. SHANK3 depletion significantly inhibited tumour growth compared to controls (II, Fig. 5I and J). Moreover, the tumours showed sustained suppression of SHANK3 mRNA and reduced mass by the end of the experiment (II, Fig. 5K and L). These findings suggest that targeting SHANK3 could be an effective anti-cancer strategy for KRAS-mutant tumours.

## 5.2.4 SHANK3-induced cell death via RAS-MAPK pathway hyperactivation

Recent studies suggest that MAPK/ERK activity must be precisely balanced in tumour cells to promote growth without triggering apoptosis (Leung et al., 2019; Unni et al., 2018). SHANK3 depletion in KRAS-mutant pancreatic (PANC-1) and

lung (A549) cancer cells led to a marked increase in ERK1/2 phosphorylation, without significantly affecting AKT activity (II, Fig. 4A; Fig. 5B; Extended Data Fig. 4A). This hyperactivation was not observed in KRAS WT cells (II, Extended Data Fig. 4B and C). Using an ERK kinase translocation reporter (ERK-KTR), increased ERK activity was confirmed in SHANK3-silenced PANC-1 cells (II, Fig. 4B). SHANK3 depletion also elevated cleaved-PARP1 levels and the number of Annexin V/PI-positive apoptotic cells, specifically in KRAS-mutant cells (II, Fig. 4C and D, Fig. 5B and F), while impairing PANC-1 spheroid formation and increasing apoptosis in 3D models and *in vivo* (II, Fig. 4E; Fig. 5C–E). Further, higher cleaved caspase-3 levels were detected in SHANK3 depleted A549 tumours and PANC-1 cells (II, Fig. 4F; Fig. 5F). To determine whether these effects were due to MAPK/ERK hyperactivation, PANC-1 cells were treated with MEK inhibitors trametinib and selumetinib, as well as the ERK inhibitor SCH772984. These inhibitors reduced ERK activity and partially rescued the proliferation defect caused by SHANK3 silencing (II, Fig. G–K). KRAS silencing partially reduced ERK activation and modestly improved cell viability (Extended Data Fig. 6D–F). These findings indicate that the loss of SHANK3 in KRAS-mutant cells leads to dysregulated MAPK/ERK activity, resulting in reduced cell viability and increased apoptosis (**Figure 8**).

### 5.2.5 Therapeutic potential of targeting the SHANK3-KRAS interaction

To explore SHANK3 as a therapeutic target, we developed nanobodies that disrupt the SHANK3-KRAS interaction and tested their effects on KRAS-mutant cancer cells. From a phage display library, two nanobodies (A01 and E01) targeting the SHANK3 SPN domain were identified; E01 exhibited strong binding affinity to SHANK3 ( $138 \pm 1.2$  nM), while A01 also bound SHANK3 but with lower affinity (II, Extended Data Fig. 11). Both nanobodies effectively inhibited the SHANK3-KRAS interaction *in vitro* (II, Fig. 6A and B). When expressed in KRAS-mutant pancreatic and lung cancer cells, the nanobodies co-precipitated endogenous SHANK3 and significantly increased apoptosis, as indicated by higher Annexin V staining (II, Fig. 6C–D). In a CAM xenograft model, nanobody overexpression reduced KRAS-driven tumour growth (II, Fig. 6F). Together these results suggest that disrupting the SHANK3-KRAS interaction, thereby hyperactivating the RAS-MAPK pathway, could be a promising therapeutic approach for KRAS-mutant cancers (II, Fig. 6G) (**Figure 8**).

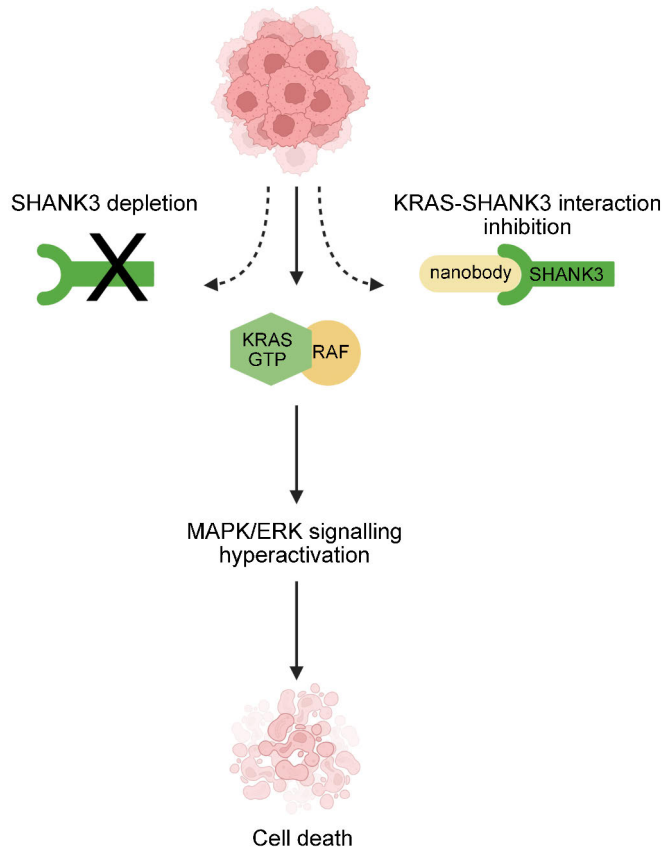


**Figure 8. SHANK3 depletion induces cell death in KRAS-mutant cancers.** SHANK3 depletion and inhibition of KRAS-SHANK3 SPN interaction with anti-SHANK3 SPN nanobodies enables active KRAS interaction with RAF, leading to hyperactivation of the MAPK/ERK signalling pathway. Modified from original publication II.

### 5.3 Mammary adipocytes restrict breast cancer invasion (III)

In breast cancer, metastasis starts with a switch from non-invasive ductal carcinoma (DCIS) to an invasive phenotype, driven by both intrinsic and extrinsic factors through signalling between the tumour and its extracellular microenvironment (J. Wang et al., 2024). Healthy mammary stroma, rich in adipocytes, contrasts with the breast cancer microenvironment, characterized by high desmoplasia (Risom et al., 2022). Dysregulated adipocytes and cancer-associated adipocytes have been shown to contribute to breast cancer invasion and metastasis (Q. Wu et al., 2019). However, the role of normal adipocytes in breast cancer remains poorly understood. Here we reveal how normal mammary adipocytes can limit breast cancer invasion.

### 5.3.1 IGFBP2 secretion inhibits cancer cell invasion

As cancer cells invade into adjacent blood and lymphatic vessels eventually leading to metastasis, we set out to investigate cancer cell invasion into fibroblast-contracted collagen I matrices toward human endothelial cells (from umbilical vein; HUVEC). Surprisingly, co-culture of HUVECs and triple-negative breast cancer (TNBC) MDA-MB-231 cells significantly inhibited cancer cell invasion without affecting their proliferation (III, Fig. 1A–C), insinuating secretion of an anti-invasive factor by HUVECs. This was affirmed by treating MDA-MB-231 cells with HUVEC-derived medium in inverted invasion assays (III, Fig. 1D–F). To identify the anti-invasive factor, published HUVEC secretomes were filtered against the tumour suppressor gene database (TSGene 2.0) leading us to identify IGFBP2 as a strong candidate. Specificity of IGFBP2-mediated inhibition of invasion was confirmed by silencing IGFBP2 in HUVECs and treating MDA-MB-231 cells with silenced conditioned medium (III, Fig. 2A and B). Further experiments with telomerase-immortalized fibroblasts (TIFs) engineered to overexpress IGFBP2 showed that IGFBP2 secretion significantly hindered cancer cell invasion into collagen I matrices compared to the control cells expressing mT2 (fluorescent protein construct mTurquoise2) (III, Fig. 2C–F).

### 5.3.2 IGFBP2 mechanism of action

To determine the IGFBP2 mechanism of action in inhibiting cancer invasion, we first explored whether IGFBP2 binds to the surface of cancer cells or the ECM. Flow cytometry confirmed no exogenous IGFBP2 binding in MDA-MB-231 cells treated with concentrated IGFBP2 medium from TIFs, as fluorescence signal in clover-tagged or untagged (negative control) IGFBP2 MDA-MB-231 cells compared to MDA-MB-231s stably expressing IGFBP2-Clover (positive control) did not show an increase in signal (III, Fig. S3E and F). IGFBP2 has previously been shown to bind to collagen IV, fibronectin, heparin, laminin and vitronectin in the ECM (Arai et al., 1996; Russo et al., 2005). However, cell-derived matrices using TIFs stably expressing IGFBP2-Clover or mT2 as a control indicated that IGFBP2-Clover does not bind to collagen or laminin fibers, nor did it affect ECM organization or fibronectin deposition (III, Fig. S3G–J). Next, we sought to investigate the interaction partners of soluble IGFBP2 in an unbiased mass spectrometry; MDA-MB-231 cells were incubated with IGFBP2-Clover produced by TIFs or recombinant green fluorescent protein (rGFP; negative control) to isolate IGFBP2-binding proteins using GFP-trap. Here we identified IGF-II as an IGFBP2-binding partner (III, Fig. 4A and data S3) with anti-invasive capability when silenced in MDA-MB-231 cells (III, Fig. 4D and E). Moreover, blocking secreted IGF-II with an anti-IGF-II antibody recapitulated the IGFBP2 anti-invasive effect (III, Fig. 4F and G). A clear

reduction in MM-MB-231 cell invasion was observed when cells were treated with the anti-IGF-II blocking antibody and IGFBP2 (III, Fig. 4K). Together these data imply that IGFBP2 binds to IGF-II, preventing it from interacting with its receptor on the surface of breast cancer cells (**Figure 9**). Therefore, by sequestering IGF-II, IGFBP2 blocks pathways supporting cancer cell invasion.

### 5.3.3 IGFBP2 expression limits invasion *in vivo*

To explore the role in IGFBP2 *in vivo*, we co-injected MDA-MB-231 cells and TIFs expressing either control mT2 or IGFBP2 into athymic nude mice (Foxn1<sup>nu</sup>) and monitored tumour growth by palpation. Tumours were collected as their volume reached >300 mm<sup>3</sup> to assess invasion to the surrounding stroma. As in the *in vitro* experiments (III, Fig. S1A and B; Fig. S1G and H), we did not observe changes in cancer cell proliferation (III, Fig. S2E). However, there was a clear reduction in cancer cell invasion into the surrounding stroma in the TIF IGFBP2 co-xenografts (III, Fig. 2G–H). This results further supports aforementioned findings of IGFBP2 having a protective role in the TME.

### 5.3.4 IGFBP2 secretion by mammary adipocytes and its therapeutic implications

To validate the physiological relevance of IGFBP2 in breast cancer invasion, IGFBP2 expression was assessed in a patient sample cohort of healthy mammary gland, DCIS and IDC samples. Additionally, its expression was determined in patient-derived stromal cells which were differentiated into mature adipocytes. Staining of the cohort and differentiated mature adipocytes demonstrated that IGFBP2 expression is prominently observed in adipocytes (III, Fig. 3A and B). To investigate whether IGFBP2 is secreted into the breast microenvironment by adipocytes, we assessed invasion of breast cancer cells when treated with medium derived from primary adipocytes differentiated from healthy reduction mammoplasty samples. These adipocytes exhibited high levels of IGFBP2 expression (III, Fig. 3D) and inhibited breast cancer cell invasion in comparison to control medium (adipocyte growth medium or complete medium) (III, Fig. 3E and F). Additionally, coculture of cancer cells with the IGFBP2-secreting adipocytes significantly reduced cancer cell invasion into fibroblast-contracted collagen I matrices (III, Fig. 3G and H).

We also examined the relationship between IGFBP2 levels and mammary density, a known risk factor for breast cancer (Huo et al., 2015; Yaghjian et al., 2011). As mammary density increases, the number of adipocytes in the breast tissue decreases (III; Fig. 5A and B), leading to lower IGFBP2 levels (III; Fig. 5C–F). This

reduction in IGFBP2 creates an environment that is more conducive to cancer invasion, providing a potential explanation for why women with dense breast tissue are at a higher risk of developing invasive breast cancer. The *in vivo* findings were corroborated by observations in human breast cancer tissues, where lower levels of IGFBP2 were associated with more invasive and aggressive forms of the disease (III, Fig. 5C–F). Together these results suggest that the secretion of IGFBP2 by normal adipocytes serves as a barrier against invasive breast cancer progression, indicating potential for therapeutic interventions that reintroduce the IGFBP2-mediated protective mechanism into clinical settings (**Figure 9**).

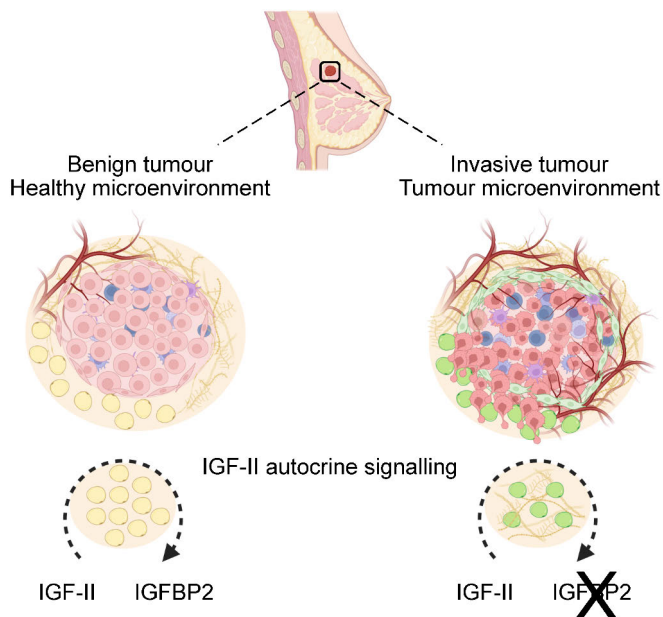


**Figure 9. IGFBP2 secretion in the breast microenvironment limits cancer invasion.** IGFBP2 secreted by mammary adipocytes inhibits breast cancer invasion by disrupting proinvasive IGF-II autocrine signaling in the breast microenvironment.

## 6 Discussion

### 6.1 Mechanical intervention as a therapeutic approach (I)

Recent advancements in cancer research have shed light on the crucial role that mechanical forces and their associated signalling pathways play in cancer progression. The emerging understanding of these processes has opened up new avenues for therapeutic interventions targeting the biomechanical properties of tumours (Streibel et al., 2024). Mechanical forces within the TME are largely dictated by the ECM stiffness, interstitial fluid pressure, and the physical interactions between cells and their surrounding environment. Increased matrix stiffness is a hallmark of many solid tumours and is associated with aggressive cancer phenotypes (Mancini et al., 2024). Given the significant impact of mechanical forces on cancer progression, targeting these forces and their downstream signalling pathways presents a promising therapeutic strategy. Therapies aimed at modulating the ECM to reduce stiffness have shown potential in preclinical studies (Liang & Song, 2023; Mai et al., 2024). Enzymatic degradation of ECM components or inhibition of ECM cross-linking enzymes such as LOX can decrease tissue stiffness, thus impairing the mechanotransduction signals that promote cancer growth and metastasis (Saatci et al., 2020). Directly targeting key components of mechanotransduction pathways offers another therapeutic angle. Inhibitors of integrins, FAK, and ROCK have been explored for their ability to disrupt the transmission of mechanical signals that support cancer progression. For instance, FAK inhibitors have demonstrated the ability to reduce tumour growth and sensitize tumours to chemotherapy by impairing cell adhesion and survival signals (Tiede et al., 2018; Timbrell et al., 2021; B. Zhang et al., 2021). Small molecules targeting YAP/TAZ or their upstream regulators are currently under investigation in both preclinical and clinical settings (M. Luo et al., 2022). Despite the promise of targeting mechanical forces in cancer therapy, several challenges remain. One major hurdle is the heterogeneity of mechanical properties within and between tumours, which complicates the development of universally effective treatments. Additionally, the redundancy and adaptability of mechanotransduction pathways may lead to resistance mechanisms, necessitating combination therapies that target multiple pathways simultaneously. Furthermore,



translating these findings into clinical practice requires a deeper understanding of the interplay between mechanical forces and other tumorigenic factors, such as immune responses and metabolic reprogramming. Therefore, future research should also focus on identifying biomarkers that can predict tumour responsiveness to mechanotherapy, enabling personalized treatment strategies.

Our research on vocal fold cancer biomechanics can serve to pave the way in mechanotherapy as there are multiple tissues in the body that undergo involuntary movements, such as peristalsis in the oesophagus, reflexes in the oropharynx and movement of the tongue and lungs. Our finding of restoring a mechanophenotype to revert malignant properties of cancer cells, may be a general phenotype in other tissues under sustained mechanical stimuli that is lost in cancer. Integrins and YAP/TAZ are the most well-known mechanoregulators (Kechagia et al., 2019a; Piccolo et al., 2022). Nonetheless, there are presumable multiple other proteins with mechanosensing properties yet to be discovered. For instance, AMOTL2 has been primarily researched in endothelial junctions and has been implied to have mechanosensitive properties (Hildebrand et al., 2017; Hultin et al., 2017; Y. Zhang et al., 2023). However, here we see AMOTL2 located in the nucleus and exhibiting sensitivity to mechanical stimulation by changes in its localization when subjected to vibration. Further research is needed to establish the role of AMOTL2 in mechanosensing, nevertheless, it is an interesting candidate due to it being a negative regulator of YAP (W. Wang et al., 2011). Moreover, a recent study observed downregulation of AMOTL2 in high-grade glioma tissues and high levels of AMOTL2 expressing patients having a higher survival rate (X. Chen et al., 2021). Additionally, the study showed that AMOTL2 can directly bind to  $\beta$ -catenin and induce its nuclear translocation. This finding insinuates AMOTL2 as a regulator of two important nucleocytoplasmic shuttling oncogenic transcription factors and making it an interesting protein to study in tissue biomechanics.

Besides the importance of nucleocytoplasmic shuttling, such as with YAP/TAZ and  $\beta$ -catenin (Shang et al., 2017; Zanconato et al., 2016), protein localisation in other cellular compartments can be crucial for distinction of normal function and oncogenic activity. Reduced tension in epithelial cells can lead to endocytosis (Thottacherry et al., 2018). In our study, we saw an increase in endosomal localisation of mechanoregulators, integrin  $\alpha$ 3 and CD151, as well as junctional proteins E-cadherin and  $\beta$ -catenin in VFC cells. Though we did not thoroughly investigate or quantify all these changes (such as in the case of E-cadherin and  $\beta$ -catenin), their endosomal compartmentalization might be an outcome of tissue immobility in VFC. Both endosomal integrin and E-cadherin can enhance the oncogenic properties of cells. Endosomal integrins have been shown to support anchorage independent growth, MMP production and metastasis, while dismantled adherens junctions due to internalized E-cadherin promote EMT (Alanko et al.,

2015; Miao et al., 2023; Miyashita & Ozawa, 2007; Palacios et al., 2005). Further research on these proteins that exhibit endosomal localisation in T3 cancers, could serve to discover novel biomarkers that indicate potential for biomechanical intervention as a treatment option.

In the study we noticed a loss of hemidesmosome structures in VFC cells along with an increase in FA count, which may account for the altered responses seen in their biomechanics. Integrin  $\beta$ 4-mutants have been shown to have increased traction forces, elevated YAP-expression and increased FA count (W. Wang et al., 2020). Additionally, cells can switch from hemidesmosomes to focal contact in order to acquire a more invasive phenotype in cancer (Schmidt et al., 2022; Wenta et al., 2022). In our study we reveal an increase in LOX gene expression as well as an increased FA count in VFC, insinuating a possibility of a positive feedback loop between tissue remodelling and FAs. LOX-inhibition could serve to reduce both cancer-driving changes in ECM architecture and FA dynamics. However, we cannot conclude based on these interesting changes in the biomechanical properties of VFC cells whether loss of mechanical stimuli is their driver that promotes tissue stiffening and thereby gives rise to cancer, or whether tissue stiffening leads to lost mechanical stimuli and further promotes tumorigenesis by altering mechanoresponsive pathways.

The hallmarks of cancer have demonstrated the need to tackle multiple cancer drivers for effective treatment, thus increasing the interest in researching the combination of two or more therapeutic agents (Hanahan, 2022; Mokhtari et al., 2017). Tissues with a mechanophenotype could benefit from combination treatment targeting the afore mentioned pathways, such as YAP/TAZ, AMOTL2, integrins, LOXs and  $\beta$ -catenin. In addition to combining treatment agents, other means to benefit from the changes in the biomechanics could be used. For instance, it would be intriguing to develop nanotechnology-based drug delivery systems that respond to the mechanical environment of tumours. These systems could release therapeutic agents in response to specific mechanical cues within the TME, providing targeted treatment while minimizing side effects.

Solid tumours are primarily treated by operation, radiation therapy and chemotherapy. For multiple under researched cancer types there is a lack of targeted treatment options. However, it is important to also assess the negative outcomes of standard patient care as changes in biomechanics can be due to treatments rather than cancer progression. For instance, chemotherapy is used to treat pancreatic and breast cancer, though it has been shown to induce changes in ECM composition, resulting in resistance and recurrence (Fatherree et al., 2022; Guarin et al., 2022). Thus, it would be interesting to follow-up on the study by staining TMA-patient samples or retrieving TCGA-patient data and comparing chemotherapy treated vs non-treated patients and their survival and changes in ECM component expression. Additionally,

as chemotherapy in breast cancer mouse and patient samples resulted in increased collagen IV expression, it would be intriguing to assess whether the changes in our study are linked to chemotherapy since all the 28 collagens in our VFC TCGA-data were upregulated.

Currently early stage laryngeal cancers can be treated with Cetuximab, a monoclonal antibody that inhibits EGFR activity, in combination with radiotherapy (Bonner et al., 2016). Combining Cetuximab with an inhibitor targeting mechanical pathways may present an interesting path to venture. Though in this study we did not explore the role of EGF and EGFR, there are some hints that indicate it playing a role in VFC. For instance, epithelial cells have linear stable adherens junctions and EGF treatment was shown to cause dot-like adherens junctions or strands perpendicular to cell boundaries (Zhitnyak et al., 2020). We see a shift from linear adherens junctions in the non-cancerous cells and T1 VFC cells, to dot-like structures in T3 VFC cells. EGF has been linked to EMT and partial EMT has been indicated to play a role in head and neck cancers, which includes cancer of the vocal folds (J. Kim et al., 2016; Pal et al., 2021; Sheng et al., 2017). However, both T1 and T3 VFC cells showed no vimentin expression, which is an established EMT-marker (data not included in publication). Nonetheless, our study suggested other possible EMT-linked changes as the loss of classical looking hemidesmosome structures in T3 cells, could be due to changes in  $\beta$ -catenin expression (Xue et al., 2024). Inhibition of the wnt/ $\beta$ -catenin pathway disrupts hemidesmosome formation (Kosumi et al., 2022).

As in any research, ours presented some limitations. For instance, due to a lack of the availability of a normal vocal fold cell line, we chose to work with a non-cancerous squamous epithelial cell line (HaCat) that originates from the skin. The skin is subjected to mechanical forces throughout one's lifetime, as are the vocal folds (Biggs et al., 2020). Nevertheless, cell line models are used to simplify research and provide a tool to easily engineer and manipulate signalling pathways, *in vitro* data must be validated *in vivo* as the enormous failure rate in clinical trials underscore the importance of more complex study settings (D. Sun et al., 2022). The role of the TME, as highlighted in this thesis, is crucial in cancer progression, and therefore should be taken into consideration when designing a study. Additionally, due to a limited access to fresh laryngeal cancer patient samples, our AFM measurements would benefit from additional measurements. The heterogeneous nature of cancer can easily skew results in a certain direction when samples size is not sufficient. However, the increase in ECM component expression in the TCGA-data and multiplex staining of our TMA patient cohort, provides strong evidence to support the increase in tissue stiffness that we see in patient tissues. However, the absolute elastic modulus values might show more variability in a bigger samples size. The primary idea behind our study was to mimic mechanical cues present in homeostasis that are lost in cancer to identify their role in VFC progression. Our study

demonstrates the importance of focusing research on the shift from homeostasis to pathology. The general consensus in cancer mechanobiology has been that mechanical forces enhance tumorigenesis (S. Kumar & Weaver, 2009; Northcott et al., 2018; Shieh, 2011). However, as most of these studies have been conducted in non-motile tissues in homeostasis, they differ fundamentally to motile ones. Here, the study set-up was the key component to investigating the shift from homeostasis to pathology, focusing on the role of mechanical forces. We discover mechanical restoration to be anti-oncogenic, and hopefully inspiring further research to focus on mechanical stimuli in motile tissues.

In conclusion, targeting mechanical forces, the ECM and their associated signalling pathways represents a novel and promising therapeutic approach in cancer treatment. By disrupting the mechanical cues that drive cancer progression, it may be possible to slow down cancer growth and enhance the efficacy of existing therapies.

## 6.2 Exploiting targeted signalling overdose (II)

We uncover a novel vulnerability in KRAS-mutant cancers by identifying SHANK3 as a critical modulator of KRAS signalling. Our findings suggest that targeting the SHANK3-KRAS interaction could serve as a broad-spectrum therapeutic strategy for various KRAS-mutant cancers. We explore a novel approach to targeting KRAS-mutant cancers by inducing hyperactivation-induced cell death. Several recent studies have reported hyperactivation-induced cell death, particularly in the MAP/ERK pathway, demonstrating that this may be a broader mechanism in various cancers, not limited to KRAS signalling (Leung et al., 2019; Unni et al., 2018; Wood, 2023). The identification of SHANK3 as a binding partner for KRAS is a significant finding as it adds a new layer to our understanding of KRAS signalling regulation. Our study demonstrates that SHANK3 directly interacts with active KRAS and plays a crucial role in maintaining KRAS activity at levels that promote cell survival rather than cell death. This interaction is particularly important in the context of KRAS-mutant cancers, where KRAS is constitutively active and drives tumorigenesis (L. Huang et al., 2021). The finding that SHANK3 limits excessive KRAS signalling suggests that SHANK3 acts as a buffer to prevent the hyperactivation of KRAS pathways that would otherwise trigger cell death.

The therapeutic potential of targeting SHANK3 in KRAS-mutant cancers is highlighted by our results showing that SHANK3 depletion leads to hyperactivation of KRAS signalling and subsequent cell death in multiple KRAS-mutant cancer cell lines. The broad spectrum of KRAS mutations affected by SHANK3 depletion, as observed across different cancer types, underscores the potential universality of this approach. Additionally, our *in vivo* experiments demonstrate that SHANK3

depletion significantly impairs tumour growth, further supporting the viability of this strategy as a therapeutic intervention. The development of nanobodies that disrupt the SHANK3-KRAS interaction is particularly promising. These nanobodies provide proof-of-concept that pharmacological targeting of the SHANK3-KRAS interaction can selectively induce apoptosis in KRAS-mutant cells. This strategy could potentially overcome the limitations of current KRAS inhibitors, which are often mutation-specific and prone to resistance (Johnson et al., 2022). Moreover, our study contributes to the broader field of cancer research by identifying a new vulnerability in KRAS-mutant cancers. The concept of inducing hyperactivation-induced cell death by disrupting critical protein-protein interactions offers a novel approach that could be applied beyond KRAS-mutant cancers. Additionally, the research highlights the importance of exploring the functional roles of scaffold proteins like SHANK3, which have traditionally been studied in the context of neuronal function due to their abundance in the postsynaptic density, but are now shown to play critical roles in cancer (Grasso et al., 2017; Hebert et al., 2020; Serwe et al., 2023; Verpelli et al., 2012).

KRAS signalling has been extensively researched to develop inhibitors, as KRAS mutations are the most common mutation type in cancer (L. Huang et al., 2021). As with most signalling pathways linked to cancer, excessive signalling is thought to be oncogenic by default (Lemmon et al., 2016). Our research showing that signalling pathway hyperactivation can have the opposing effect, resulting in selected cell-death, is highly against the general view, where research focuses on shutting down KRAS signalling (Punekar et al., 2022). However, though initially met with doubts, there are other studies arising with similar findings, providing evidence that rather than halting signalling, an excess in signalling pathway activity can be exploited as a therapeutic approach (Gutierrez-Prat et al., 2022; Ito et al., 2021; Leung et al., 2019).

While the findings are compelling, there are limitations to our study that should be addressed in future research. The reliance on *in vitro* and *in vivo* models does not fully recapitulate the complexity of human tumours, such as involvement of other cells in the TME. Additionally, the long-term effects of SHANK3 depletion on normal tissues were not extensively studied, raising potential concerns about toxicity. However, SHANK3 knockout (KO) mice are viable, exhibiting neurological challenges such as symptoms of autism spectrum disorders likely owing to the absence of SHANK3 in development. No major brain abnormality is associated with SHANK3 KO mice (Peça et al., 2011). Therefore, future studies should explore the potential emergence of resistance mechanisms in response to SHANK3-targeting therapies. Future research may focus on refining the nanobody approach, exploring its efficacy in combination with existing therapies and further elucidating the mechanisms by which SHANK3 regulates KRAS activity. Our study

opens the door to potential new treatments that could significantly impact patient outcomes in cancers driven by KRAS mutations. Overall, our research provides a strong foundation for the development of new therapeutic strategies targeting KRAS-mutant cancers by exploiting the regulatory role of SHANK3. Further investigations into the safety, efficacy and resistance profiles of SHANK3-targeting therapies will be crucial for advancing this promising approach toward clinical application.

### 6.3 Secretion of barrier-reinforcing factors in cancer (III)

The results of our study shed light on the broader implications of the stroma's composition in cancer biology, particularly in maintaining tissue homeostasis and preventing malignancy. Our findings highlight IGFBP2 as a key adipocrine factor that limits breast cancer invasion, contrasting with the previously established notion that adipocytes in the microenvironment predominantly support cancer progression (Bernard & Wellberg, 2021). However, these studies have mainly investigated adipocytes in the TME, and it is plausible that these adipocytes are in fact dysregulated cancer-associated adipocytes, exhibiting altered metabolic reprogramming in comparison to adipocytes in a healthy microenvironment. The discovery that IGFBP2 acts by binding to and sequestering IGF-II, a known promoter of cancer cell invasion, underscores the importance of adipocyte-secreted factors in maintaining tissue homeostasis and preventing cancer invasion. Moreover, our study demonstrates that IGFBP2 secretion by both endothelial cells and fibroblasts also contributes to its anti-invasive effects, suggesting a broader role for IGFBP2 in various stromal compartments.

As the adipocyte population is diminished, such as in conditions of increased mammary density, the levels of IGFBP2 are correspondingly reduced. This reduction creates a permissive environment for the invasion and progression of breast cancer cells, suggesting that IGFBP2 levels are directly linked to the aggressiveness of the disease. Additionally, we observed IGFBP2 levels being linked to age, older patients having decreased IGFBP2 expression. The risk of developing breast cancer increases with age as for instance older people with an inherited BRCA1 or BRCA2 gene mutation are at higher risk of developing cancer (Metcalf et al., 2023). The observed reduction in cancer cell invasion when IGFBP2 is reintroduced into the TME presents a potential therapeutic avenue. By reactivating or mimicking the protective effects of IGFBP2, it might be possible to develop treatments that slow or prevent the transition of breast cancer from a non-invasive DCIS to an invasive IDC state. Application of anti-IGF-II antibody has already shown promising efficacy as an anticancer agent in breast cancer xenografts (Tominaga et al., 2017). Moreover,

strategies that aim to enhance IGFBP2 levels in the breast stroma could potentially prevent the progression of DCIS to IDC, thereby reducing the risk of metastasis and improving patient outcomes. Conversion of invasive breast cancer cells into adipocytes has been shown to inhibit metastasis, arising an interesting option to explore IGFBP2 secretion in these reprogrammed cells and a possible therapeutic exploitation (Ishay-Ronen et al., 2019). Another option for utilizing our findings is to assess whether IGFBP2 levels in breast tissue could serve as a biomarker for predicting the risk of invasive breast cancer, as women with lower levels of IGFBP2 may be at a higher risk and could benefit from closer monitoring and preventative interventions. Furthermore, the study highlights the potential for developing therapies that mimic or enhance the function of IGFBP2, either through direct supplementation or by targeting the pathways that regulate its secretion. Our findings emphasize the importance of the breast adipose tissue microenvironment in cancer progression and suggest that therapies enhancing IGFBP2 activity could be a novel approach to prevent the invasive progression of breast cancer. Our study also raises interesting questions about the relationship between mammary density and breast cancer risk. While increased mammary density is typically associated with a higher risk of breast cancer (Bodewes et al., 2022), the presence of IGFBP2 in healthy adipocytes might offer a counterbalance, containing the invasive potential of emerging tumours.

The use of *in vitro* models, while powerful, may not fully capture the complexity of tumour-stroma interactions *in vivo*. Additionally, the focus on IGFBP2 and IGF-II interactions leaves open questions about other potential mechanisms through which normal healthy mammary adipocytes might influence cancer progression. Future studies could explore these mechanisms and assess the therapeutic potential of targeting IGFBP2 and other secreted factors in more detail.

# 7 Conclusions

The purpose of this thesis was to explore the biomechanical tumour matrix in tissues where homeostatic mechanical forces are lost in cancer, and to investigate the role of normal, healthy adipocytes in breast cancer progression. Additionally, we sought to unravel the functional consequences of the interaction between SHANK3 and KRAS in KRAS-mutant cancers. Our findings demonstrate that restoring a mechanophenotype in vocal fold cancer through mechanical stimulation reduces oncogenic signalling activity. In breast cancer, we identified IGFBP2 as an anti-invasive factor secreted by normal adipocytes. Finally, we propose a novel approach to targeting KRAS-mutant cancers by disrupting the interaction between SHANK3 and KRAS.

## Original publication I

The findings of this study discover restoring a mechanophenotype in vocal fold cancer to promote tumour reversion. By comparing cancerous and normal vocal fold tissue samples, an upregulation of multiple ECM components, including fibronectin and collagens, was observed in cancerous tissues. Atomic force microscopy measurements further confirmed a marked increase in tissue stiffness in vocal fold cancer. The study also examined the effects of mechanical manipulation on non-cancerous and patient-derived cancer cells, uncovering that cell stretching and vibration leads to a reduction in oncogenic nuclear  $\beta$ -catenin levels in vocal fold cancer cells. Additionally, vibration resulted in the downregulation of oncogenic nuclear YAP levels. Furthermore, an analysis of a large cohort of vocal fold cancer patients revealed a correlation between increased ECM content and advanced cancer stage. High ECM content was positively associated with elevated nuclear YAP levels, which, in turn, were linked to significantly lower disease-specific survival. Collectively, this research demonstrates that mechanical stimulation can promote reversion of vocal fold cancer cells toward a less malignant state.



### Original publication II

This research identifies SHANK3 as a critical regulator of KRAS-mutant cancer cell survival. The study demonstrates that SHANK3 interacts directly with active KRAS, particularly in its GTP-bound state, to limit excessive oncogenic signalling, thus maintaining it at non-lethal levels. Depleting SHANK3 leads to hyperactivation of KRAS/ERK signalling, which in turn selectively induces cell death in KRAS-mutant cancer cells. Importantly, the disruption of the SHANK3-KRAS interaction, either through genetic silencing or pharmacological means, significantly impairs tumour growth in various *in vitro* and *in vivo* models. This work suggests that targeting the SHANK3-KRAS interaction offers a promising new therapeutic strategy that could be applicable across a broad range of KRAS-mutant cancers, addressing the limitations of current mutation-specific treatments. The findings open new avenues for the development of pan-KRAS-targeted therapies, particularly for cancers resistant to existing treatments.

### Original publication III

This study reveals that HUVEC-derived angiocrine factor IGFBP2 plays a crucial role in inhibiting breast cancer cell invasion. The anti-invasive effect of IGFBP2 was demonstrated through *in vitro* models, where its secretion by HUVECs and mammary adipocytes significantly reduced cancer cell invasion without affecting cell proliferation. IGFBP2 exerts this effect by sequestering pro-invasive IGF-II, disrupting its autocrine signalling pathway. Furthermore, IGFBP2 expression is notably decreased in breast cancer patient samples, particularly in older individuals and those with invasive ductal carcinoma. This reduction is linked to age-related cancer progression, suggesting that maintaining stromal IGFBP2 levels could be protective against breast cancer invasion. The findings highlight the importance of stromal cells in maintaining tissue homeostasis and the potential of IGFBP2 as a therapeutic target for preventing cancer progression or a biomarker to predict disease progression.

# Acknowledgements

This thesis work was carried out at the Faculty of Medicine, Department of Medical Biochemistry and Genetics, University of Turku and Turku Bioscience Centre. I would sincerely like to thank Riitta Lahesmaa and John Eriksson, the current and previous directors of Turku Bioscience Centre. I am grateful for the inspiring research environment with excellent facilities, and the supportive technical and administrative personnel.

I had the privilege to be supervised by an outstanding group leader and researcher Professor Johanna Ivaska. First, I would like to thank Johanna for all the advice and support you have given me during these years. You are truly an inspiring scientist and group leader. I deeply appreciate the effort you make to have time for each of your students, even with a busy schedule. Thank you for giving me the opportunity to be part of your research group. Your enthusiasm for science and determination are characteristics that make you a great role model for any young scientist. During my PhD you have challenged me to step out of my comfort zone and grow as an independent scientist.

I would like to thank Professor Klaus Elenius for accepting me as a doctoral researcher at the Department of Medical Biochemistry and Genetics at the University of Turku. I would like to especially thank the Turku Doctoral Programme of Molecular Medicine director Noora Kotaja and coordinator Eeva Valve for maintaining an interesting and supportive doctoral programme. TuDMM organized multiple fun and exciting scientific and social events through which I have met wonderful people. Furthermore, I am thankful for the chief academic officer of the Faculty of Medicine, Outi Irjala, for the support throughout the thesis submission. I would like to express my gratitude towards my doctoral thesis supervision committee members, Same Ventelä and Sara Wickström. I looked forward to our annual meetings as I got such great feedback and ideas for my PhD projects, the support from you have helped me take my projects forward.

I would like to express my gratitude to my thesis pre-examiners Anniina Färkkilä and Valerio Izzi. I sincerely thank you both for evaluating my work. I sincerely thank Rachel Lennon for accepting the invitation to be my opponent and I look forward to discussing my thesis with you.

I would like to thank the current and past members of the Ivaska lab, without your support I would not have been able to finish my PhD work. Thank you Aki, Aleksi, Camilo, David, Elisa, Emmi, Eva, Gautier, Guillaume, Hanna, Hellyeh, Huayi, Hussein, Ilkka, Iman, James, Jaroslav, Jenni, Johanna L., Maria, Martina, Mathilde, Max, Megan, Meri, Michal, Michalis, Mitro, Monika, Nicolas, Niklas, Omkar, Paula, Paulina, Petra, Sanskriti, Siiri, Sonja, Taru, Trinh, Valentijn and Veli-Matti. I have learned a lot from all of you and I have made wonderful memories with you. I am especially deeply grateful for the friendship I have built with Maria and Nicolas, our time in the lab and outside has been truly amazing. I would like to express my warmest thanks to our amazing technicians Jenni and Petra for all the help, laughs, therapy sessions and support during the past years. Furthermore, I sincerely thank our coordinator Hellyeh for always being so helpful.

I would especially like to thank Sanni for having multiple meltdowns with me and our daily emotional support lunch breaks. We have supported each other throughout our studies and you are truly one of my greatest friends. I would also like to thank Emil for sharing our PhD struggles and overcoming them together. You created a safe space to voice any concern or accomplishment.

Finally I would like to express my deepest gratitude to my mother Angelina and my brother Oliver. Thank you for always supporting me even while not fully understanding what I am doing. My PhD studies have taken a lot of my time and I have not been able to spend as much time with you as I would have wanted to, yet you have always been understanding of the situation. I am privileged to have such a loving mother and brother. Your encouraging messages have meant a lot to me and kept me going.

This work has been financially supported by Turku Doctoral Programme of Molecular Medicine, the Finnish Cultural Foundation and the Ida Montin Foundation.

Turku, November 2024

*Jasmin Kaivola*

# References

- Abarca-Gómez, L., Abdeen, Z. A., Hamid, Z. A., Abu-Rmeileh, N. M., Acosta-Cazares, B., Acuin, C., Adams, R. J., Aekplakorn, W., Afsana, K., Aguilar-Salinas, C. A., Agyemang, C., Ahmadvand, A., Ahrens, W., Ajlouni, K., Akhtaeva, N., Al-Hazzaa, H. M., Al-Othman, A. R., Al-Raddadi, R., Al Buhairan, F., ... Ezzati, M. (2017). Worldwide trends in body-mass index, underweight, overweight, and obesity from 1975 to 2016: a pooled analysis of 2416 population-based measurement studies in 128·9 million children, adolescents, and adults. *The Lancet*, *390*(10113), 2627–2642. [https://doi.org/10.1016/S0140-6736\(17\)32129-3](https://doi.org/10.1016/S0140-6736(17)32129-3)
- Acerbi, I., Cassereau, L., Dean, I., Shi, Q., Au, A., Park, C., Chen, Y. Y., Liphardt, J., Hwang, E. S., & Weaver, V. M. (2015). Human breast cancer invasion and aggression correlates with ECM stiffening and immune cell infiltration. *Integrative Biology*, *7*(10), 1120–1134. <https://doi.org/10.1039/c5ib00040h>
- Akai, M., Noma, K., Kato, T., Nishimura, S., Matsumoto, H., Kawasaki, K., Kunitomo, T., Kobayashi, T., Nishiwaki, N., Kashima, H., Kikuchi, S., Ohara, T., Tazawa, H., Choyke, P. L., Kobayashi, H., & Fujiwara, T. (2024). Fibroblast activation protein-targeted near-infrared photoimmunotherapy depletes immunosuppressive cancer-associated fibroblasts and remodels local tumor immunity. *British Journal of Cancer*, *130*(10), 1647–1658. <https://doi.org/10.1038/s41416-024-02639-1>
- Akhavan, A., Griffith, O. L., Sorocceanu, L., Leonoudakis, D., Luciani-Torres, M. G., Daemen, A., Gray, J. W., & Muschler, J. L. (2012). Loss of Cell-Surface Laminin Anchoring Promotes Tumor Growth and Is Associated with Poor Clinical Outcomes. *Cancer Research*, *72*(10), 2578–2588. <https://doi.org/10.1158/0008-5472.CAN-11-3732>
- Alanko, J., Mai, A., Jacquemet, G., Schauer, K., Kaukonen, R., Saari, M., Goud, B., & Ivaska, J. (2015). Integrin endosomal signalling suppresses anoikis. *Nature Cell Biology*, *17*(11), 1412–1421. <https://doi.org/10.1038/ncb3250>
- Alkasalias, T., Flaberg, E., Kashuba, V., Alexeyenko, A., Pavlova, T., Savchenko, A., Szekely, L., Klein, G., & Guven, H. (2014). Inhibition of tumor cell proliferation and motility by fibroblasts is both contact and soluble factor dependent. *Proceedings of the National Academy of Sciences*, *111*(48), 17188–17193. <https://doi.org/10.1073/pnas.1419554111>
- Andreu, I., Falcones, B., Hurst, S., Chahare, N., Quiroga, X., Le Roux, A.-L., Kechagia, Z., Beedle, A. E. M., Elosegui-Artola, A., Trepas, X., Farré, R., Betz, T., Almendros, I., & Roca-Cusachs, P. (2021). The force loading rate drives cell mechanosensing through both reinforcement and cytoskeletal softening. *Nature Communications*, *12*(1), 4229. <https://doi.org/10.1038/s41467-021-24383-3>
- Angulo-Urarte, A., van der Wal, T., & Huvencers, S. (2020). Cell-cell junctions as sensors and transducers of mechanical forces. *Biochimica et Biophysica Acta - Biomembranes*, *1862*(9), 183316. <https://doi.org/10.1016/j.bbamem.2020.183316>
- Arai, T., Busby, W., & Clemmons, D. R. (1996). Binding of insulin-like growth factor (IGF) I or II to IGF-binding protein-2 enables it to bind to heparin and extracellular matrix. *Endocrinology*, *137*(11), 4571–4575. <https://doi.org/10.1210/endo.137.11.8895319>
- Arbore, C., Sergides, M., Gardini, L., Bianchi, G., Kashchuk, A. V., Pertici, I., Bianco, P., Pavone, F. S., & Capitanio, M. (2022).  $\alpha$ -catenin switches between a slip and an asymmetric catch bond with

- F-actin to cooperatively regulate cell junction fluidity. *Nature Communications*, 13(1), 1146. <https://doi.org/10.1038/s41467-022-28779-7>
- Aretz, J., Aziz, M., Strohmeyer, N., Sattler, M., & Fässler, R. (2023). Talin and kindlin use integrin tail allosterism and direct binding to activate integrins. *Nature Structural & Molecular Biology*, 30(12), 1913–1924. <https://doi.org/10.1038/s41594-023-01139-9>
- Arias-Salgado, E. G., Lizano, S., Sarkar, S., Brugge, J. S., Ginsberg, M. H., & Shattil, S. J. (2003). Src kinase activation by direct interaction with the integrin  $\beta$  cytoplasmic domain. *Proceedings of the National Academy of Sciences*, 100(23), 13298–13302. <https://doi.org/10.1073/pnas.2336149100>
- Arimori, T., Miyazaki, N., Mihara, E., Takizawa, M., Taniguchi, Y., Cabañas, C., Sekiguchi, K., & Takagi, J. (2021). Structural mechanism of laminin recognition by integrin. *Nature Communications*, 12(1), 4012. <https://doi.org/10.1038/s41467-021-24184-8>
- Atherton, P., Lausecker, F., Carisey, A., Gilmore, A., Critchley, D., Barsukov, I., & Ballestrem, C. (2019). Relief of talin autoinhibition triggers a force-independent association with vinculin. *Journal of Cell Biology*, 219(1), e201903134. <https://doi.org/10.1083/jcb.201903134>
- Aumailley, M. (2021). Laminins and interaction partners in the architecture of the basement membrane at the dermal-epidermal junction. *Experimental Dermatology*, 30(1), 17–24. <https://doi.org/10.1111/exd.14239>
- Aureille, J., Buffière-Ribot, V., Harvey, B. E., Boyault, C., Pernet, L., Andersen, T., Bacola, G., Balland, M., Fraboulet, S., Van Landeghem, L., & Guilluy, C. (2019). Nuclear envelope deformation controls cell cycle progression in response to mechanical force. *EMBO Reports*, 20(9), e48084. <https://doi.org/https://doi.org/10.15252/embr.201948084>
- Avvisato, C. L., Yang, X., Shah, S., Hoxter, B., Li, W., Gaynor, R., Pestell, R., Tozeren, A., & Byers, S. W. (2007). Mechanical force modulates global gene expression and  $\beta$ -catenin signaling in colon cancer cells. *Journal of Cell Science*, 120(15), 2672–2682. <https://doi.org/10.1242/jcs.03476>
- Balaban, S., Shearer, R. F., Lee, L. S., van Geldermalsen, M., Schreuder, M., Shtein, H. C., Cairns, R., Thomas, K. C., Fazakerley, D. J., Grewal, T., Holst, J., Saunders, D. N., & Hoy, A. J. (2017). Adipocyte lipolysis links obesity to breast cancer growth: adipocyte-derived fatty acids drive breast cancer cell proliferation and migration. *Cancer & Metabolism*, 5(1), 1. <https://doi.org/10.1186/s40170-016-0163-7>
- Barbazan, J., Pérez-González, C., Gómez-González, M., Dedenon, M., Richon, S., Latorre, E., Serra, M., Mariani, P., Descroix, S., Sens, P., Trepast, X., & Vignjevic, D. M. (2023). Cancer-associated fibroblasts actively compress cancer cells and modulate mechanotransduction. *Nature Communications*, 14(1). <https://doi.org/10.1038/s41467-023-42382-4>
- Bardhan, A., Bruckner-Tuderman, L., Chapple, I. L. C., Fine, J.-D., Harper, N., Has, C., Magin, T. M., Marinkovich, M. P., Marshall, J. F., McGrath, J. A., Mellerio, J. E., Polson, R., & Heagerty, A. H. (2020). Epidermolysis bullosa. *Nature Reviews Disease Primers*, 6(1), 78. <https://doi.org/10.1038/s41572-020-0210-0>
- Barney, L. E., Hall, C. L., Schwartz, A. D., Parks, A. N., Sparages, C., Galarza, S., Platt, M. O., Mercurio, A. M., & Peyton, S. R. (2024). Tumor cell-organized fibronectin maintenance of a dormant breast cancer population. *Science Advances*, 6(11), eaaz4157. <https://doi.org/10.1126/sciadv.aaz4157>
- Baroja, I., Kyriakidis, N. C., Halder, G., & Moya, I. M. (2024). Expected and unexpected effects after systemic inhibition of Hippo transcriptional output in cancer. *Nature Communications*, 15(1). <https://doi.org/10.1038/s41467-024-46531-1>
- Beauvais, D. M., Ell, B. J., McWhorter, A. R., & Rapraeger, A. C. (2009). Syndecan-1 regulates  $\alpha$ v $\beta$ 3 and  $\alpha$ v $\beta$ 5 integrin activation during angiogenesis and is blocked by synstatin, a novel peptide inhibitor. *Journal of Experimental Medicine*, 206(3), 691–705. <https://doi.org/10.1084/jem.20081278>
- Bejar-Padilla, V., Cabe, J. I., Lopez, S., Narayanan, V., Mezher, M., Maruthamuthu, V., & Conway, D. E. (2022).  $\alpha$ -Catenin-dependent vinculin recruitment to adherens junctions is antagonistic to focal adhesions. *Molecular Biology of the Cell*, 33(11), 1–9. <https://doi.org/10.1091/mbc.E22-02-0071>

- Bella, J. (2016). Collagen structure: new tricks from a very old dog. *Biochemical Journal*, 473(8), 1001–1025. <https://doi.org/10.1042/BJ20151169>
- Benham-Pyle, B. W., Pruitt, B. L., & Nelson, W. J. (2015). Mechanical strain induces E-cadherin-dependent Yap1 and  $\beta$ -catenin activation to drive cell cycle entry. *Science*, 348(6238), 1024–1027. <https://doi.org/10.1126/science.aaa4559>
- Benham-Pyle, B. W., Sim, J. Y., Hart, K. C., Pruitt, B. L., & Nelson, W. J. (2016). Increasing  $\beta$ -catenin/Wnt3A activity levels drive mechanical strain-induced cell cycle progression through mitosis. *ELife*, 5(OCTOBER2016), 1–28. <https://doi.org/10.7554/eLife.19799>
- Berger, A. J., Renner, C. M., Hale, I., Yang, X., Ponik, S. M., Weisman, P. S., Masters, K. S., & Kreeger, P. K. (2020). Scaffold stiffness influences breast cancer cell invasion via EGFR-linked Mena upregulation and matrix remodeling. *Matrix Biology*, 85–86, 80–93. <https://doi.org/10.1016/j.matbio.2019.07.006>
- Beri, P., Popravko, A., Yeoman, B., Kumar, A., Chen, K., Hodzic, E., Chiang, A., Banisadr, A., Placone, J. K., Carter, H., Fraley, S. I., Katira, P., & Engler, A. J. (2020). Cell Adhesiveness Serves as a Biophysical Marker for Metastatic Potential. *Cancer Research*, 80(4), 901–911. <https://doi.org/10.1158/0008-5472.CAN-19-1794>
- Bernard, J. J., & Wellberg, E. A. (2021). The Tumor Promotional Role of Adipocytes in the Breast Cancer Microenvironment and Macroenvironment. *The American Journal of Pathology*, 191(8), 1342–1352. <https://doi.org/10.1016/j.ajpath.2021.02.006>
- Berrueta, L., Bergholz, J., Munoz, D., Muskaj, I., Badger, G. J., Shukla, A., Kim, H. J., Zhao, J. J., & Langevin, H. M. (2018). Stretching Reduces Tumor Growth in a Mouse Breast Cancer Model. *Scientific Reports*, 8(1), 7864. <https://doi.org/10.1038/s41598-018-26198-7>
- Biggs, L. C., Kim, C. S., Miroshnikova, Y. A., & Wickström, S. A. (2020). Mechanical Forces in the Skin: Roles in Tissue Architecture, Stability, and Function. *Journal of Investigative Dermatology*, 140(2), 284–290. <https://doi.org/https://doi.org/10.1016/j.jid.2019.06.137>
- Bochet, L., Lehuédé, C., Dauvillier, S., Wang, Y. Y., Dirat, B., Laurent, V., Dray, C., Guiet, R., Maridonneau-Parini, I., Le Gonidec, S., Couderc, B., Escourrou, G., Valet, P., & Muller, C. (2013). Adipocyte-Derived Fibroblasts Promote Tumor Progression and Contribute to the Desmoplastic Reaction in Breast Cancer. *Cancer Research*, 73(18), 5657–5668. <https://doi.org/10.1158/0008-5472.CAN-13-0530>
- Bodewes, F. T. H., van Asselt, A. A., Dorrius, M. D., Greuter, M. J. W., & de Bock, G. H. (2022). Mammographic breast density and the risk of breast cancer: A systematic review and meta-analysis. *The Breast*, 66, 62–68. <https://doi.org/10.1016/j.breast.2022.09.007>
- Bonner, J., Giralt, J., Harari, P., Spencer, S., Schulten, J., Hossain, A., Chang, S.-C., Chin, S., & Baselga, J. (2016). Cetuximab and Radiotherapy in Laryngeal Preservation for Cancers of the Larynx and Hypopharynx. *JAMA Otolaryngology–Head & Neck Surgery*, 142(9), 842. <https://doi.org/10.1001/jamaoto.2016.1228>
- Borghgi, N., Sorokina, M., Shcherbakova, O. G., Weis, W. I., Pruitt, B. L., Nelson, W. J., & Dunn, A. R. (2012). E-cadherin is under constitutive actomyosin-generated tension that is increased at cell-cell contacts upon externally applied stretch. *Proceedings of the National Academy of Sciences of the United States of America*, 109(31), 12568–12573. <https://doi.org/10.1073/pnas.1204390109>
- Bornes, L., Belthier, G., & van Rheenen, J. (2021). Epithelial-to-Mesenchymal Transition in the Light of Plasticity and Hybrid E/M States. *Journal of Clinical Medicine*, 10(11), 2403. <https://doi.org/10.3390/jcm10112403>
- Bosveld, F., Markova, O., Guirao, B., Martin, C., Wang, Z., Pierre, A., Balakireva, M., Gaugue, I., Ainslie, A., Christophorou, N., Lubensky, D. K., Minc, N., & Bellaïche, Y. (2016). Epithelial tricellular junctions act as interphase cell shape sensors to orient mitosis. *Nature*, 530(7591), 495–498. <https://doi.org/10.1038/nature16970>
- Bouche, C., & Quail, D. F. (2023). Fueling the Tumor Microenvironment with Cancer-Associated Adipocytes. *Cancer Research*, 83(8), 1170–1172. <https://doi.org/10.1158/0008-5472.CAN-23-0505>

- Bouin, A.-P., Kyurmurkov, A., Régent-Kloeckner, M., Ribba, A.-S., Faurobert, E., Fournier, H.-N., Bourrin-Reynard, I., Manet-Dupé, S., Oddou, C., Baland, M., Planus, E., & Albiges-Rizo, C. (2017). ICAP-1 monoubiquitylation coordinates matrix density and rigidity sensing for cell migration through ROCK2–MRCK $\alpha$  balance. *Journal of Cell Science*, *130*(3), 626–636. <https://doi.org/10.1242/jcs.200139>
- Boujemaa-Paterski, R., Martins, B., Eibauer, M., Beales, C. T., Geiger, B., & Medalia, O. (2020). Talin-activated vinculin interacts with branched actin networks to initiate bundles. *ELife*, *9*, e53990. <https://doi.org/10.7554/eLife.53990>
- Bouvard, D., Vignoud, L., Dupé-Manet, S., Abed, N., Fournier, H.-N., Vincent-Monegat, C., Retta, S. F., Fässler, R., & Block, M. R. (2003). Disruption of Focal Adhesions by Integrin Cytoplasmic Domain-associated Protein-1 $\alpha$ . *Journal of Biological Chemistry*, *278*(8), 6567–6574. <https://doi.org/10.1074/jbc.M211258200>
- Buchmann, B., Engelbrecht, L. K., Fernandez, P., Hutterer, F. P., Raich, M. K., Scheel, C. H., & Bausch, A. R. (2021). Mechanical plasticity of collagen directs branch elongation in human mammary gland organoids. *Nature Communications*, *12*(1), 2759. <https://doi.org/10.1038/s41467-021-22988-2>
- Buckley, C. D., Tan, J., Anderson, K. L., Hanein, D., Volkman, N., Weis, W. I., Nelson, W. J., & Dunn, A. R. (2014). The minimal cadherin-catenin complex binds to actin filaments under force. *Science*, *346*(6209). <https://doi.org/10.1126/science.1254211>
- Cai, D., Feliciano, D., Dong, P., Flores, E., Gruebele, M., Porat-Shliom, N., Sukenik, S., Liu, Z., & Lippincott-Schwartz, J. (2019). Phase separation of YAP reorganizes genome topology for long-term YAP target gene expression. *Nature Cell Biology*, *21*(12), 1578–1589. <https://doi.org/10.1038/s41556-019-0433-z>
- Calderwood, D. A., Huttenlocher, A., Kiosses, W. B., Rose, D. M., Woodside, D. G., Schwartz, M. A., & Ginsberg, M. H. (2001). Increased filamin binding to  $\beta$ -integrin cytoplasmic domains inhibits cell migration. *Nature Cell Biology*, *3*(12), 1060–1068. <https://doi.org/10.1038/ncb1201-1060>
- Calvo, F., Ege, N., Grande-Garcia, A., Hooper, S., Jenkins, R. P., Chaudhry, S. I., Harrington, K., Williamson, P., Moecdarbary, E., Charras, G., & Sahai, E. (2013). Mechanotransduction and YAP-dependent matrix remodelling is required for the generation and maintenance of cancer-associated fibroblasts. *Nature Cell Biology*, *15*(6), 637–646. <https://doi.org/10.1038/ncb2756>
- Chan, S. W., Lim, C. J., Loo, L. S., Chong, Y. F., Huang, C., & Hong, W. (2009). TEADs Mediate Nuclear Retention of TAZ to Promote Oncogenic Transformation. *Journal of Biological Chemistry*, *284*(21), 14347–14358. <https://doi.org/10.1074/jbc.M901568200>
- Chang, A. C., Mekhdjian, A. H., Morimatsu, M., Denisin, A. K., Pruitt, B. L., & Dunn, A. R. (2016). Single Molecule Force Measurements in Living Cells Reveal a Minimally Tensioned Integrin State. *ACS Nano*, *10*(12), 10745–10752. <https://doi.org/10.1021/acs.nano.6b03314>
- Chang Chien, C.-Y., Chou, S.-H., & Lee, H.-H. (2022). Integrin molecular tension required for focal adhesion maturation and YAP nuclear translocation. *Biochemistry and Biophysics Reports*, *31*, 101287. <https://doi.org/10.1016/j.bbrep.2022.101287>
- Chang, J., Saraswathibhatla, A., Song, Z., Varma, S., Sanchez, C., Alyafei, N. H. K., Indana, D., Slyman, R., Srivastava, S., Liu, K., Bassik, M. C., Marinkovich, M. P., Hodgson, L., Shenoy, V., West, R. B., & Chaudhuri, O. (2024). Cell volume expansion and local contractility drive collective invasion of the basement membrane in breast cancer. *Nature Materials*, *23*(5), 711–722. <https://doi.org/10.1038/s41563-023-01716-9>
- Charras, G., & Yap, A. S. (2018). Tensile Forces and Mechanotransduction at Cell–Cell Junctions. In *Current Biology* (Vol. 28, Issue 8, pp. R445–R457). Cell Press. <https://doi.org/10.1016/j.cub.2018.02.003>
- Chastney, M. R., Conway, J. R. W., & Ivaska, J. (2021). Integrin adhesion complexes. *Current Biology*, *31*(10), R536–R542. <https://doi.org/10.1016/j.cub.2021.01.038>
- Chauhan, V. P., Chen, I. X., Tong, R., Ng, M. R., Martin, J. D., Naxerova, K., Wu, M. W., Huang, P., Boucher, Y., Kohane, D. S., Langer, R., & Jain, R. K. (2019). Reprogramming the

- microenvironment with tumor-selective angiotensin blockers enhances cancer immunotherapy. *Proceedings of the National Academy of Sciences*, 116(22), 10674–10680. <https://doi.org/10.1073/pnas.1819889116>
- Chen, L.-K., Hsieh, C.-C., Huang, Y.-C., Huang, Y.-J., Lung, C.-F., Hsu, W.-E., Yao, C.-L., Tseng, T.-Y., Wang, C.-C., & Hsu, Y.-C. (2023). Mechanical Stretch Promotes Invasion of Lung Cancer Cells via Activation of Tumor Necrosis Factor- $\alpha$ . *Biotechnology and Bioprocess Engineering*, 28(3), 467–472. <https://doi.org/10.1007/s12257-022-0260-0>
- Chen, X., Lu, Y., Guo, G., Zhang, Y., Sun, Y., Guo, L., Li, R., Nan, Y., Yang, X., Dong, J., Jin, X., & Huang, Q. (2021). AMOTL2-knockdown promotes the proliferation, migration and invasion of glioma by regulating  $\beta$ -catenin nuclear localization. *Oncology Reports*, 46(1), 139. <https://doi.org/10.3892/or.2021.8090>
- Chen, Y., Brasch, J., Harrison, O. J., & Bidone, T. C. (2021). Computational model of E-cadherin clustering under force. *Biophysical Journal*, 120(22), 4944–4954. <https://doi.org/10.1016/j.bpj.2021.10.018>
- Chen, Y., Han, H., Seo, G., Vargas, R. E., Yang, B., Chuc, K., Zhao, H., & Wang, W. (2020). Systematic analysis of the Hippo pathway organization and oncogenic alteration in evolution. *Scientific Reports*, 10(1), 3173. <https://doi.org/10.1038/s41598-020-60120-4>
- Chen, Y., McAndrews, K. M., & Kalluri, R. (2021). Clinical and therapeutic relevance of cancer-associated fibroblasts. *Nature Reviews Clinical Oncology*, 18(12), 792–804. <https://doi.org/10.1038/s41571-021-00546-5>
- Cheng, B., Wan, W., Huang, G., Li, Y., Genin, G. M., Mofrad, M. R. K., Lu, T. J., Xu, F., & Lin, M. (2020). Nanoscale integrin cluster dynamics controls cellular mechanosensing via FAKY397 phosphorylation. *Science Advances*, 6(10), eaax1909. <https://doi.org/10.1126/sciadv.aax1909>
- Chi, Y.-H., Wang, W.-P., Hung, M.-C., Liou, G.-G., Wang, J.-Y., & Chao, P.-H. G. (2022). Deformation of the nucleus by TGF $\beta$ 1 via the remodeling of nuclear envelope and histone isoforms. *Epigenetics & Chromatin*, 15(1), 1. <https://doi.org/10.1186/s13072-021-00434-3>
- Cho, Y., Haraguchi, D., Shigetomi, K., Matsuzawa, K., Uchida, S., & Ikenouchi, J. (2022). Tricellulin secures the epithelial barrier at tricellular junctions by interacting with actomyosin. *Journal of Cell Biology*, 221(4), e202009037. <https://doi.org/10.1083/jcb.202009037>
- Coban, B., Bergonzini, C., Zweemer, A. J. M., & Danen, E. H. J. (2021). Metastasis: crosstalk between tissue mechanics and tumour cell plasticity. *British Journal of Cancer*, 124(1), 49–57. <https://doi.org/10.1038/s41416-020-01150-7>
- Conway, J. R. W., Isomursu, A., Follain, G., Härmä, V., Jou-Ollé, E., Pasquier, N., Välimäki, E. P. O., Rantala, J. K., & Ivaska, J. (2023). Defined extracellular matrix compositions support stiffness-insensitive cell spreading and adhesion signaling. *Proceedings of the National Academy of Sciences of the United States of America*, 120(43). <https://doi.org/10.1073/pnas.2304288120>
- Cooper, J., & Giancotti, F. G. (2019). Integrin Signaling in Cancer: Mechanotransduction, Stemness, Epithelial Plasticity, and Therapeutic Resistance. *Cancer Cell*, 35(3), 347–367. <https://doi.org/10.1016/j.ccell.2019.01.007>
- Cox, T. R. (2021). The matrix in cancer. *Nature Reviews Cancer*, 21(4), 217–238. <https://doi.org/10.1038/s41568-020-00329-7>
- Cruz-Acuña, R., Vunjak-Novakovic, G., Burdick, J. A., & Rustgi, A. K. (2021). Emerging technologies provide insights on cancer extracellular matrix biology and therapeutics. *iScience*, 24(5), 102475. <https://doi.org/10.1016/j.isci.2021.102475>
- Cui, Y., Hameed, F. M., Yang, B., Lee, K., Pan, C. Q., Park, S., & Sheetz, M. (2015). Cyclic stretching of soft substrates induces spreading and growth. *Nature Communications*, 6, 1–8. <https://doi.org/10.1038/ncomms7333>
- Currey, L., Thor, S., & Piper, M. (2021). TEAD family transcription factors in development and disease. *Development*, 148(12), dev196675. <https://doi.org/10.1242/dev.196675>
- Dai, J., Qin, L., Chen, Y., Wang, H., Lin, G., Li, X., Liao, H., & Fang, H. (2019). Matrix stiffness regulates epithelial-mesenchymal transition via cytoskeletal remodeling and MRTF-A



- translocation in osteosarcoma cells. *Journal of the Mechanical Behavior of Biomedical Materials*, *90*, 226–238. <https://doi.org/10.1016/j.jmbbm.2018.10.012>
- Dauer, P., Zhao, X., Gupta, V. K., Sharma, N., Kesh, K., Gnamlin, P., Dudeja, V., Vickers, S. M., Banerjee, S., & Saluja, A. (2018). Inactivation of Cancer-Associated-Fibroblasts Disrupts Oncogenic Signaling in Pancreatic Cancer Cells and Promotes Its Regression. *Cancer Research*, *78*(5), 1321–1333. <https://doi.org/10.1158/0008-5472.CAN-17-2320>
- Davidson, P. M., & Cadot, B. (2021). Actin on and around the Nucleus. *Trends in Cell Biology*, *31*(3), 211–223. <https://doi.org/10.1016/j.tcb.2020.11.009>
- De Francesco, E. M., Lappano, R., Santolla, M. F., Marsico, S., Caruso, A., & Maggiolini, M. (2013). HIF-1 $\alpha$ /GPER signaling mediates the expression of VEGF induced by hypoxia in breast cancer associated fibroblasts (CAFs). *Breast Cancer Research*, *15*(4), R64. <https://doi.org/10.1186/bcr3458>
- de Visser, K. E., & Joyce, J. A. (2023). The evolving tumor microenvironment: From cancer initiation to metastatic outgrowth. *Cancer Cell*, *41*(3), 374–403. <https://doi.org/10.1016/j.ccell.2023.02.016>
- Denis, M., Gregory, A., Bayat, M., Fazzio, R. T., Whaley, D. H., Ghosh, K., Shah, S., Fatemi, M., & Alizad, A. (2016). Correlating Tumor Stiffness with Immunohistochemical Subtypes of Breast Cancers: Prognostic Value of Comb-Push Ultrasound Shear Elastography for Differentiating Luminal Subtypes. *PLOS ONE*, *11*(10), e0165003. <https://doi.org/10.1371/journal.pone.0165003>
- Dessalles, C. A., Leclech, C., Castagnino, A., & Barakat, A. I. (2021). Integration of substrate- and flow-derived stresses in endothelial cell mechanobiology. *Communications Biology*, *4*(1), 764. <https://doi.org/10.1038/s42003-021-02285-w>
- Di, X., Gao, X., Peng, L., Ai, J., Jin, X., Qi, S., Li, H., Wang, K., & Luo, D. (2023). Cellular mechanotransduction in health and diseases: from molecular mechanism to therapeutic targets. *Signal Transduction and Targeted Therapy*, *8*(1), 282. <https://doi.org/10.1038/s41392-023-01501-9>
- Dong, Y., Zheng, Q., Wang, Z., Lin, X., You, Y., Wu, S., Wang, Y., Hu, C., Xie, X., Chen, J., Gao, D., Zhao, Y., Wu, W., Liu, Y., Ren, Z., Chen, R., & Cui, J. (2019). Higher matrix stiffness as an independent initiator triggers epithelial-mesenchymal transition and facilitates HCC metastasis. *Journal of Hematology & Oncology*, *12*(1), 112. <https://doi.org/10.1186/s13045-019-0795-5>
- Du, F., Qi, X., Zhang, A., Sui, F., Wang, X., Proud, C. G., Lin, C., Fan, X., & Li, J. (2021). MRTF-A-NF- $\kappa$ B/p65 axis-mediated PDL1 transcription and expression contributes to immune evasion of non-small-cell lung cancer via TGF- $\beta$ . *Experimental & Molecular Medicine*, *53*(9), 1366–1378. <https://doi.org/10.1038/s12276-021-00670-3>
- DuChez, B. J., Doyle, A. D., Dimitriadis, E. K., & Yamada, K. M. (2019). Durotaxis by Human Cancer Cells. *Biophysical Journal*, *116*(4), 670–683. <https://doi.org/10.1016/j.bpj.2019.01.009>
- Dupont, S., Morsut, L., Aragona, M., Enzo, E., Giulitti, S., Cordenonsi, M., Zanconato, F., Le Digabel, J., Forcato, M., Bicciato, S., Elvassore, N., & Piccolo, S. (2011). Role of YAP/TAZ in mechanotransduction. *Nature*, *474*(7350), 179–183. <https://doi.org/10.1038/nature10137>
- Efimov, A., Schiefermeier, N., Grigoriev, I., Brown, M. C., Turner, C. E., Small, J. V., & Kaverina, I. (2008). Paxillin-dependent stimulation of microtubule catastrophes at focal adhesion sites. *Journal of Cell Science*, *121*(2), 196–204. <https://doi.org/10.1242/jcs.012666>
- Erdogan, B., Ao, M., White, L. M., Means, A. L., Brewer, B. M., Yang, L., Washington, M. K., Shi, C., Franco, O. E., Weaver, A. M., Hayward, S. W., Li, D., & Webb, D. J. (2017). Cancer-associated fibroblasts promote directional cancer cell migration by aligning fibronectin. *Journal of Cell Biology*, *216*(11), 3799–3816. <https://doi.org/10.1083/jcb.201704053>
- Fahy, N., Alini, M., & Stoddart, M. J. (2018). Mechanical stimulation of mesenchymal stem cells: Implications for cartilage tissue engineering. *Journal of Orthopaedic Research*, *36*(1), 52–63. <https://doi.org/https://doi.org/10.1002/jor.23670>
- Fatherree, J. P., Guarin, J. R., McGinn, R. A., Naber, S. P., & Oudin, M. J. (2022). Chemotherapy-Induced Collagen IV Drives Cancer Cell Motility through Activation of Src and Focal Adhesion Kinase. *Cancer Research*, *82*(10), 2031–2044. <https://doi.org/10.1158/0008-5472.CAN-21-1823>

- Fattet, L., Jung, H.-Y., Matsumoto, M. W., Aubol, B. E., Kumar, A., Adams, J. A., Chen, A. C., Sah, R. L., Engler, A. J., Pasquale, E. B., & Yang, J. (2020). Matrix Rigidity Controls Epithelial-Mesenchymal Plasticity and Tumor Metastasis via a Mechanoresponsive EPHA2/LYN Complex. *Developmental Cell*, *54*(3), 302-316.e7. <https://doi.org/10.1016/j.devcel.2020.05.031>
- Filla, M. S., Faralli, J. A., Desikan, H., Peotter, J. L., Wannow, A. C., & Peters, D. M. (2019). Activation of  $\alpha\beta 3$  Integrin Alters Fibronectin Fibril Formation in Human Trabecular Meshwork Cells in a ROCK-Independent Manner. *Investigative Ophthalmology & Visual Science*, *60*(12), 3897. <https://doi.org/10.1167/iovs.19-27171>
- Foster, C. T., Gualdrini, F., & Treisman, R. (2017). Mutual dependence of the MRTF-SRF and YAP-TEAD pathways in cancer-associated fibroblasts is indirect and mediated by cytoskeletal dynamics. *Genes & Development*, *31*(23-24), 2361-2375. <https://doi.org/10.1101/gad.304501.117>
- Franz, F., Tapia-Rojo, R., Winograd-Katz, S., Boujemaa-Paterski, R., Li, W., Unger, T., Albeck, S., Aponte-Santamaria, C., Garcia-Manyes, S., Medalia, O., Geiger, B., & Gräter, F. (2023). Allosteric activation of vinculin by talin. *Nature Communications*, *14*(1), 4311. <https://doi.org/10.1038/s41467-023-39646-4>
- Frijns, E., Sachs, N., Kreft, M., Wilhelmson, K., & Sonnenberg, A. (2010). EGF-induced MAPK Signaling Inhibits Hemidesmosome Formation through Phosphorylation of the Integrin  $\beta 4$ . *Journal of Biological Chemistry*, *285*(48), 37650-37662. <https://doi.org/10.1074/jbc.M110.138818>
- Früh, S. M., Schoen, I., Ries, J., & Vogel, V. (2015). Molecular architecture of native fibronectin fibrils. *Nature Communications*, *6*(1), 7275. <https://doi.org/10.1038/ncomms8275>
- Gachon, E., & Mesquida, P. (2022). Mechanical properties of collagen fibrils determined by buckling analysis. *Acta Biomaterialia*, *149*, 60-68. <https://doi.org/10.1016/j.actbio.2022.06.044>
- Gaggioli, C., Hooper, S., Hidalgo-Carcedo, C., Grosse, R., Marshall, J. F., Harrington, K., & Sahai, E. (2007). Fibroblast-led collective invasion of carcinoma cells with differing roles for RhoGTPases in leading and following cells. *Nature Cell Biology*, *9*(12), 1392-1400. <https://doi.org/10.1038/ncb1658>
- Gahmberg, C. G., & Grönholm, M. (2022). How integrin phosphorylations regulate cell adhesion and signaling. *Trends in Biochemical Sciences*, *47*(3), 265-278. <https://doi.org/10.1016/j.tibs.2021.11.003>
- Gahmberg, C. G., Grönholm, M., Madhavan, S., Jahan, F., Mikkola, E., Viazmina, L., & Koivunen, E. (2019). Regulation of cell adhesion: a collaborative effort of integrins, their ligands, cytoplasmic actors, and phosphorylation. *Quarterly Reviews of Biophysics*, *52*, e10. <https://doi.org/DOI:10.1017/S0033583519000088>
- Galatenko, V. V., Maltseva, D. V., Galatenko, A. V., Rodin, S., & Tonevitsky, A. G. (2018). Cumulative prognostic power of laminin genes in colorectal cancer. *BMC Medical Genomics*, *11*(S1), 9. <https://doi.org/10.1186/s12920-018-0332-3>
- Gao, J., Bao, Y., Ge, S., Sun, P., Sun, J., Liu, J., Chen, F., Han, L., Cao, Z., Qin, J., White, G. C., Xu, Z., & Ma, Y.-Q. (2019). Sharpin suppresses  $\beta 1$ -integrin activation by complexing with the  $\beta 1$  tail and kindlin-1. *Cell Communication and Signaling*, *17*(1), 101. <https://doi.org/10.1186/s12964-019-0407-6>
- García-Palmero, I., Torres, S., Bartolomé, R. A., Peláez-García, A., Larriba, M. J., Lopez-Lucendo, M., Peña, C., Escudero-Paniagua, B., Muñoz, A., & Casal, J. I. (2016). Twist1-induced activation of human fibroblasts promotes matrix stiffness by upregulating palladin and collagen  $\alpha 1$ (VI). *Oncogene*, *35*(40), 5224-5236. <https://doi.org/10.1038/onc.2016.57>
- Gau, D., & Roy, P. (2018). SRF'ing and SAP'ing – the role of MRTF proteins in cell migration. *Journal of Cell Science*, *131*(19). <https://doi.org/10.1242/jcs.218222>
- Gerri, C., McCarthy, A., Mei Scott, G., Regin, M., Stamatiadis, P., Brumm, S., Simon, C. S., Lee, J., Montesinos, C., Hassitt, C., Hockenhull, S., Hampshire, D., Elder, K., Snell, P., Christie, L., Fouladi-Nashta, A. A., Van de Velde, H., & Niakan, K. K. (2023). A conserved role of the Hippo

- signalling pathway in initiation of the first lineage specification event across mammals. *Development*, 150(8). <https://doi.org/10.1242/dev.201112>
- Ghagre, A., Delarue, A., Srivastava, L. K., Koushki, N., & Ehrlicher, A. (2024). Nuclear curvature determines Yes-associated protein localization and differentiation of mesenchymal stem cells. *Biophysical Journal*, 123(10), 1222–1239. <https://doi.org/10.1016/j.bpj.2024.04.008>
- Ghura, H., Keimer, M., von Au, A., Hackl, N., Klemis, V., & Nakchbandi, I. A. (2021). Inhibition of fibronectin accumulation suppresses tumor growth. *Neoplasia*, 23(9), 837–850. <https://doi.org/10.1016/j.neo.2021.06.012>
- Gieniec, K. A., Butler, L. M., Worthley, D. L., & Woods, S. L. (2019). Cancer-associated fibroblasts—heroes or villains? *British Journal of Cancer*, 121(4), 293–302. <https://doi.org/10.1038/s41416-019-0509-3>
- Girard, C. A., Lecacheur, M., Ben Jouira, R., Berestjuk, I., Diazzi, S., Prod’homme, V., Mallavialle, A., Larbret, F., Gesson, M., Schaub, S., Pisano, S., Audebert, S., Mari, B., Gaggioli, C., Leucci, E., Marine, J.-C., Deckert, M., & Tartare-Deckert, S. (2020). A Feed-Forward Mechanosignaling Loop Confers Resistance to Therapies Targeting the MAPK Pathway in BRAF-Mutant Melanoma. *Cancer Research*, 80(10), 1927–1941. <https://doi.org/10.1158/0008-5472.CAN-19-2914>
- Glentis, A., Oertle, P., Mariani, P., Chikina, A., El Marjou, F., Attieh, Y., Zaccarini, F., Lae, M., Loew, D., Dingli, F., Sirven, P., Schoumacher, M., Gurchenkov, B. G., Plodinec, M., & Vignjevic, D. M. (2017). Cancer-associated fibroblasts induce metalloprotease-independent cancer cell invasion of the basement membrane. *Nature Communications*, 8(1), 924. <https://doi.org/10.1038/s41467-017-00985-8>
- Gong, J., Lin, Y., Zhang, H., Liu, C., Cheng, Z., Yang, X., Zhang, J., Xiao, Y., Sang, N., Qian, X., Wang, L., Cen, X., Du, X., & Zhao, Y. (2020). Reprogramming of lipid metabolism in cancer-associated fibroblasts potentiates migration of colorectal cancer cells. *Cell Death & Disease*, 11(4), 267. <https://doi.org/10.1038/s41419-020-2434-z>
- Gough, R. E., Jones, M. C., Zacharchenko, T., Le, S., Yu, M., Jacquemet, G., Muench, S. P., Yan, J., Humphries, J. D., Jørgensen, C., Humphries, M. J., & Goult, B. T. (2021). Talin mechanosensitivity is modulated by a direct interaction with cyclin-dependent kinase-1. *Journal of Biological Chemistry*, 297(1), 100837. <https://doi.org/10.1016/j.jbc.2021.100837>
- Grasset, E. M., Bertero, T., Bozec, A., Friard, J., Bourget, I., Pisano, S., Lecacheur, M., Maiel, M., Bailleux, C., Emelyanov, A., Ilie, M., Hofman, P., Meneguzzi, G., Duranton, C., Bulavin, D. V., & Gaggioli, C. (2018). Matrix Stiffening and EGFR cooperate to promote the collective invasion of cancer cells. *Cancer Research*, 78(18), 5229–5242. <https://doi.org/10.1158/0008-5472.CAN-18-0601>
- Grasso, S., Chapelle, J., Salemme, V., Aramu, S., Russo, I., Vitale, N., Verdun di Cantogno, L., Dallaglio, K., Castellano, I., Amici, A., Centonze, G., Sharma, N., Lunardi, S., Cabodi, S., Cavallo, F., Lamolinara, A., Stramucci, L., Moiso, E., Provero, P., ... Defilippi, P. (2017). The scaffold protein p140Cap limits ERBB2-mediated breast cancer progression interfering with Rac GTPase-controlled circuitries. *Nature Communications*, 8(1), 14797. <https://doi.org/10.1038/ncomms14797>
- Gray, S. D. (2000). CELLULAR PHYSIOLOGY OF THE VOCAL FOLDS. *Otolaryngologic Clinics of North America*, 33(4), 679–697. [https://doi.org/10.1016/S0030-6665\(05\)70237-1](https://doi.org/10.1016/S0030-6665(05)70237-1)
- Green, H. J., & Brown, N. H. (2019). Integrin intracellular machinery in action. *Experimental Cell Research*, 378(2), 226–231. <https://doi.org/10.1016/j.yexcr.2019.03.011>
- Grudtsyna, V., Packirisamy, S., Bidone, T. C., & Swaminathan, V. (2023). Extracellular matrix sensing via modulation of orientational order of integrins and F-actin in focal adhesions. *Life Science Alliance*, 6(10), e202301898. <https://doi.org/10.26508/lsa.202301898>
- Gu, B., Bradshaw, B., Zhu, M., Sun, Y., Hopyan, S., & Rossant, J. (2022). Live imaging YAP signalling in mouse embryo development. *Open Biology*, 12(1), 210335. <https://doi.org/10.1098/rsob.210335>
- Gu, X., Zhu, Y., Su, J., Wang, S., Su, X., Ding, X., Jiang, L., Fei, X., & Zhang, W. (2024). Lactate-induced activation of tumor-associated fibroblasts and IL-8-mediated macrophage recruitment

- promote lung cancer progression. *Redox Biology*, 74, 103209. <https://doi.org/https://doi.org/10.1016/j.redox.2024.103209>
- Guarin, J. R., Fatherree, J. P., & Oudin, M. J. (2022). Chemotherapy treatment induces pro-invasive changes in liver ECM composition. *Matrix Biology*, 112, 20–38. <https://doi.org/10.1016/j.matbio.2022.08.002>
- Gumbiner, B. M. (1996). Cell Adhesion: The Molecular Basis of Tissue Architecture and Morphogenesis. *Cell*, 84(3), 345–357. [https://doi.org/10.1016/S0092-8674\(00\)81279-9](https://doi.org/10.1016/S0092-8674(00)81279-9)
- Gupta, V. K., Nam, S., Yim, D., Camuglia, J., Martin, J. L., Sanders, E. N., O'Brien, L. E., Martin, A. C., Kim, T., & Chaudhuri, O. (2021). The nature of cell division forces in epithelial monolayers. *Journal of Cell Biology*, 220(8), e202011106. <https://doi.org/10.1083/jcb.202011106>
- Gutierrez-Prat, N., Zuberer, H. L., Mangano, L., Karimaddini, Z., Wolf, L., Tyanova, S., Wellinger, L. C., Marbach, D., Griesser, V., Pettazoni, P., Bischoff, J. R., Rohle, D., Palladino, C., & Vivanco, I. (2022). DUSP4 protects BRAF- and NRAS-mutant melanoma from oncogene overdose through modulation of MITF. *Life Science Alliance*, 5(9), e202101235. <https://doi.org/10.26508/lsa.202101235>
- Haake, S. M., Rios, B. L., Pozzi, A., & Zent, R. (2024). Integrating integrins with the hallmarks of cancer. *Matrix Biology*, 130(April), 20–35. <https://doi.org/10.1016/j.matbio.2024.04.003>
- Haas, A. J., Zihni, C., Ruppel, A., Hartmann, C., Ebnet, K., Tada, M., Balda, M. S., & Matter, K. (2020). Interplay between Extracellular Matrix Stiffness and JAM-A Regulates Mechanical Load on ZO-1 and Tight Junction Assembly. *Cell Reports*, 32(3), 107924. <https://doi.org/10.1016/j.celrep.2020.107924>
- Hadjisavva, R., Anastasiou, O., Ioannou, P. S., Zheltkova, M., & Skourides, P. A. (2022). Adherens junctions stimulate and spatially guide integrin activation and extracellular matrix deposition. *Cell Reports*, 40(3), 111091. <https://doi.org/10.1016/j.celrep.2022.111091>
- Hallou, A., & Brunet, T. (2020). On growth and force: mechanical forces in development. *Development*, 147(4), dev187302. <https://doi.org/10.1242/dev.187302>
- Hamaratoglu, F., Willecke, M., Kango-Singh, M., Nolo, R., Hyun, E., Tao, C., Jafar-Nejad, H., & Halder, G. (2006). The tumour-suppressor genes NF2/Merlin and Expanded act through Hippo signalling to regulate cell proliferation and apoptosis. *Nature Cell Biology*, 8(1), 27–36. <https://doi.org/10.1038/ncb1339>
- Hamidi, H., & Ivaska, J. (2018). Every step of the way: integrins in cancer progression and metastasis. *Nature Reviews Cancer*, 18(9), 533–548. <https://doi.org/10.1038/s41568-018-0038-z>
- Hanahan, D. (2022). Hallmarks of Cancer: New Dimensions. *Cancer Discovery*, 12(1), 31–46. <https://doi.org/10.1158/2159-8290.CD-21-1059>
- Hanley, C. J., Noble, F., Ward, M., Bullock, M., Drifka, C., Mellone, M., Manousopoulou, A., Johnston, H. E., Hayden, A., Thirdborough, S., Liu, Y., Smith, D. M., Mellows, T., Kao, W. J., Garbis, S. D., Mirnezami, A., Underwood, T. J., Eliceiri, K. W., & Thomas, G. J. (2016). A subset of myofibroblastic cancer-associated fibroblasts regulate collagen fiber elongation, which is prognostic in multiple cancers. *Oncotarget*, 7(5), 6159–6174. <https://doi.org/10.18632/oncotarget.6740>
- He, J.-Y., Wei, X.-H., Li, S.-J., Liu, Y., Hu, H.-L., Li, Z.-Z., Kuang, X.-H., Wang, L., Shi, X., Yuan, S.-T., & Sun, L. (2018). Adipocyte-derived IL-6 and leptin promote breast Cancer metastasis via upregulation of Lysyl Hydroxylase-2 expression. *Cell Communication and Signaling*, 16(1), 100. <https://doi.org/10.1186/s12964-018-0309-z>
- Hebert, J. D., Tian, C., Lamar, J. M., Rickelt, S., Abbruzzese, G., Liu, X., & Hynes, R. O. (2020). The scaffold protein IQGAP1 is crucial for extravasation and metastasis. *Scientific Reports*, 10(1), 2439. <https://doi.org/10.1038/s41598-020-59438-w>
- Hildebrand, S., Hultin, S., Subramani, A., Petropoulos, S., Zhang, Y., Cao, X., Mpindi, J., Kalloniemi, O., Johansson, S., Majumdar, A., Lanner, F., & Holmgren, L. (2017). The E-cadherin/AmotL2 complex organizes actin filaments required for epithelial hexagonal packing and blastocyst hatching. *Scientific Reports*, 7(1), 9540. <https://doi.org/10.1038/s41598-017-10102-w>

- Hoffman, L. M., Smith, M. A., Jensen, C. C., Yoshigi, M., Blankman, E., Ullman, K. S., & Beckerle, M. C. (2020). Mechanical stress triggers nuclear remodeling and the formation of transmembrane actin nuclear lines with associated nuclear pore complexes. *Molecular Biology of the Cell*, *31*(16), 1774–1787. <https://doi.org/10.1091/mbc.E19-01-0027>
- Hohenester, E. (2019). Structural biology of laminins. *Essays in Biochemistry*, *63*(3), 285–295. <https://doi.org/10.1042/EBC20180075>
- Horton, E. R., Humphries, J. D., Stutchbury, B., Jacquemet, G., Ballestrem, C., Barry, S. T., & Humphries, M. J. (2016). Modulation of FAK and Src adhesion signaling occurs independently of adhesion complex composition. *Journal of Cell Biology*, *212*(3), 349–364. <https://doi.org/10.1083/jcb.201508080>
- Huang, L., Guo, Z., Wang, F., & Fu, L. (2021). KRAS mutation: from undruggable to druggable in cancer. *Signal Transduction and Targeted Therapy*, *6*(1), 386. <https://doi.org/10.1038/s41392-021-00780-4>
- Huang, M., Lu, L., Lin, C., Zheng, Y., Pan, X., Wang, S., Chen, S., Zhang, Y., Liu, C., Ge, G., Zeng, Y. A., & Chen, J. (2023). LRP12 is an endogenous transmembrane inactivator of  $\alpha 4$  integrins. *Cell Reports*, *42*(6), 112667. <https://doi.org/10.1016/j.celrep.2023.112667>
- Huang, W., Zhu, J., Shi, H., Wu, Q., & Zhang, C. (2021). ITGA2 Overexpression Promotes Esophageal Squamous Cell Carcinoma Aggression via FAK/AKT Signaling Pathway. *OncoTargets and Therapy*, *Volume 14*, 3583–3596. <https://doi.org/10.2147/OTT.S302028>
- Huber, M., Casares-Arias, J., Fässler, R., Müller, D. J., & Strohmeyer, N. (2023). In mitosis integrins reduce adhesion to extracellular matrix and strengthen adhesion to adjacent cells. *Nature Communications*, *14*(1). <https://doi.org/10.1038/s41467-023-37760-x>
- Hultin, S., Subramani, A., Hildebrand, S., Zheng, Y., Majumdar, A., & Holmgren, L. (2017). AmotL2 integrates polarity and junctional cues to modulate cell shape. *Scientific Reports*, *7*(1), 7548. <https://doi.org/10.1038/s41598-017-07968-1>
- Humphrey, J. D., Dufresne, E. R., & Schwartz, M. A. (2014). Mechanotransduction and extracellular matrix homeostasis. *Nature Reviews Molecular Cell Biology*, *15*(12), 802–812. <https://doi.org/10.1038/nrm3896>
- Humphries, J. D., Wang, P., Streuli, C., Geiger, B., Humphries, M. J., & Ballestrem, C. (2007). Vinculin controls focal adhesion formation by direct interactions with talin and actin. *Journal of Cell Biology*, *179*(5), 1043–1057. <https://doi.org/10.1083/jcb.200703036>
- Huo, C. W., Chew, G., Hill, P., Huang, D., Ingman, W., Hodson, L., Brown, K. A., Magenau, A., Allam, A. H., McGhee, E., Timpson, P., Henderson, M. A., Thompson, E. W., & Britt, K. (2015). High mammographic density is associated with an increase in stromal collagen and immune cells within the mammary epithelium. *Breast Cancer Research*, *17*(1), 79. <https://doi.org/10.1186/s13058-015-0592-1>
- Hwang, P. Y., Mathur, J., Cao, Y., Almeida, J., Ye, J., Morikis, V., Cornish, D., Clarke, M., Stewart, S. A., Pathak, A., & Longmore, G. D. (2023). A Cdh3- $\beta$ -catenin-laminin signaling axis in a subset of breast tumor leader cells control leader cell polarization and directional collective migration. *Developmental Cell*, *58*(1), 34–50.e9. <https://doi.org/10.1016/j.devcel.2022.12.005>
- Hwang, S.-Y., Deng, X., Byun, S., Lee, C., Lee, S.-J., Suh, H., Zhang, J., Kang, Q., Zhang, T., Westover, K. D., Mandinova, A., & Lee, S. W. (2016). Direct Targeting of  $\beta$ -Catenin by a Small Molecule Stimulates Proteasomal Degradation and Suppresses Oncogenic Wnt/ $\beta$ -Catenin Signaling. *Cell Reports*, *16*(1), 28–36. <https://doi.org/10.1016/j.celrep.2016.05.071>
- Hynes, R. O. (1987). Integrins: a family of cell surface receptors. *Cell*, *48*(4), 549–554. [https://doi.org/10.1016/0092-8674\(87\)90233-9](https://doi.org/10.1016/0092-8674(87)90233-9)
- Hynes, R. O. (2002). Integrins. *Cell*, *110*(6), 673–687. [https://doi.org/10.1016/S0092-8674\(02\)00971-6](https://doi.org/10.1016/S0092-8674(02)00971-6)
- Ilna, O., Gritsenko, P. G., Syga, S., Lippoldt, J., La Porta, C. A. M., Chepizhko, O., Grosser, S., Vullings, M., Bakker, G.-J., Starruß, J., Bult, P., Zapperi, S., Käs, J. A., Deutsch, A., & Friedl, P. (2020). Cell–cell adhesion and 3D matrix confinement determine jamming transitions in breast

- cancer invasion. *Nature Cell Biology*, 22(9), 1103–1115. <https://doi.org/10.1038/s41556-020-0552-6>
- Ippolito, L., Morandi, A., Taddei, M. L., Parri, M., Comito, G., Iscaro, A., Raspollini, M. R., Magherini, F., Rapizzi, E., Masquelier, J., Muccioli, G. G., Sonveaux, P., Chiarugi, P., & Giannoni, E. (2019). Cancer-associated fibroblasts promote prostate cancer malignancy via metabolic rewiring and mitochondrial transfer. *Oncogene*, 38(27), 5339–5355. <https://doi.org/10.1038/s41388-019-0805-7>
- Ireland, L. V., & Mielgo, A. (2018). Macrophages and Fibroblasts, Key Players in Cancer Chemoresistance. *Frontiers in Cell and Developmental Biology*, 6, 131. <https://doi.org/10.3389/fcell.2018.00131>
- Ishay-Ronen, D., Diepenbruck, M., Kalathur, R. K. R., Sugiyama, N., Tiede, S., Ivanek, R., Bantug, G., Morini, M. F., Wang, J., Hess, C., & Christofori, G. (2019). Gain Fat—Lose Metastasis: Converting Invasive Breast Cancer Cells into Adipocytes Inhibits Cancer Metastasis. *Cancer Cell*, 35(1), 17–32.e6. <https://doi.org/10.1016/j.ccell.2018.12.002>
- Ito, T., Young, M. J., Li, R., Jain, S., Wernitznig, A., Krill-Burger, J. M., Lemke, C. T., Monducci, D., Rodriguez, D. J., Chang, L., Dutta, S., Pal, D., Paoletta, B. R., Rothberg, M. V., Root, D. E., Johannessen, C. M., Parida, L., Getz, G., Vazquez, F., ... Sellers, W. R. (2021). Paralog knockout profiling identifies DUSP4 and DUSP6 as a digenic dependence in MAPK pathway-driven cancers. *Nature Genetics*, 53(12), 1664–1672. <https://doi.org/10.1038/s41588-021-00967-z>
- Jin, Y., Ding, Y., Richards, M., Kaakinen, M., Giese, W., Baumann, E., Szymborska, A., Rosa, A., Nordling, S., Schimmel, L., Akmeriç, E. B., Pena, A., Nwadozi, E., Jamalpour, M., Holstein, K., Sáinz-Jaspeado, M., Bernabeu, M. O., Welsh, M., Gordon, E., ... Claesson-Welsh, L. (2022). Tyrosine-protein kinase Yes controls endothelial junctional plasticity and barrier integrity by regulating VE-cadherin phosphorylation and endocytosis. *Nature Cardiovascular Research*, 1(12), 1156–1173. <https://doi.org/10.1038/s44161-022-00172-z>
- Jo, M. H., Li, J., Jaumouillé, V., Hao, Y., Coppola, J., Yan, J., Waterman, C. M., Springer, T. A., & Ha, T. (2022). Single-molecule characterization of subtype-specific  $\beta 1$  integrin mechanics. *Nature Communications*, 13(1), 7471. <https://doi.org/10.1038/s41467-022-35173-w>
- Johnson, C., Burkhart, D. L., & Haigis, K. M. (2022). Classification of KRAS -Activating Mutations and the Implications for Therapeutic Intervention. *Cancer Discovery*, 12(4), 913–923. <https://doi.org/10.1158/2159-8290.CD-22-0035>
- Jolly, M. K., Somarelli, J. A., Sheth, M., Biddle, A., Tripathi, S. C., Armstrong, A. J., Hanash, S. M., Bapat, S. A., Rangarajan, A., & Levine, H. (2019). Hybrid epithelial/mesenchymal phenotypes promote metastasis and therapy resistance across carcinomas. *Pharmacology and Therapeutics*, 194, 161–184. <https://doi.org/10.1016/j.pharmthera.2018.09.007>
- Kadry, Y. A., & Calderwood, D. A. (2020). Chapter 22: Structural and signaling functions of integrins. *Biochimica et Biophysica Acta - Biomembranes*, 1862(5), 183206. <https://doi.org/10.1016/j.bbmem.2020.183206>
- Kai, F., Drain, A. P., & Weaver, V. M. (2019). The Extracellular Matrix Modulates the Metastatic Journey. *Developmental Cell*, 49(3), 332–346. <https://doi.org/10.1016/j.devcel.2019.03.026>
- Kalli, M., Poskus, M. D., Stylianopoulos, T., & Zervantonakis, I. K. (2023). Beyond matrix stiffness: targeting force-induced cancer drug resistance. *Trends in Cancer*, 9(11), 937–954. <https://doi.org/10.1016/j.trecan.2023.07.006>
- Kalukula, Y., Stephens, A. D., Lammerding, J., & Gabriele, S. (2022). Mechanics and functional consequences of nuclear deformations. *Nature Reviews Molecular Cell Biology*, 23(9), 583–602. <https://doi.org/10.1038/s41580-022-00480-z>
- Kanchanawong, P., & Calderwood, D. A. (2023). Organization, dynamics and mechanoregulation of integrin-mediated cell–ECM adhesions. *Nature Reviews Molecular Cell Biology*, 24(2), 142–161. <https://doi.org/10.1038/s41580-022-00531-5>

- Kanchanawong, P., Shtengel, G., Pasapera, A. M., Ramko, E. B., Davidson, M. W., Hess, H. F., & Waterman, C. M. (2010). Nanoscale architecture of integrin-based cell adhesions. *Nature*, *468*(7323), 580–584. <https://doi.org/10.1038/nature09621>
- Kaukonen, R., Mai, A., Georgiadou, M., Saari, M., De Franceschi, N., Betz, T., Sihto, H., Ventelä, S., Elo, L., Jokitalo, E., Westermark, J., Kellokumpu-Lehtinen, P.-L., Joensuu, H., Grenman, R., & Ivaska, J. (2016). Normal stroma suppresses cancer cell proliferation via mechanosensitive regulation of JMJD1a-mediated transcription. *Nature Communications*, *7*(1), 12237. <https://doi.org/10.1038/ncomms12237>
- Kay, E. J., Paterson, K., Riera-Domingo, C., Sumpton, D., Däbritz, J. H. M., Tardito, S., Boldrini, C., Hernandez-Fernaud, J. R., Athineos, D., Dhayade, S., Stepanova, E., Gjerga, E., Neilson, L. J., Lilla, S., Hedley, A., Koulouras, G., McGregor, G., Jamieson, C., Johnson, R. M., ... Zanivan, S. (2022). Cancer-associated fibroblasts require proline synthesis by PYCR1 for the deposition of pro-tumorigenic extracellular matrix. *Nature Metabolism*, *4*(6), 693–710. <https://doi.org/10.1038/s42255-022-00582-0>
- Kechagia, J. Z., Ivaska, J., & Roca-Cusachs, P. (2019a). Integrins as biomechanical sensors of the microenvironment. *Nature Reviews Molecular Cell Biology*, *20*(8), 457–473. <https://doi.org/10.1038/s41580-019-0134-2>
- Kechagia, J. Z., Ivaska, J., & Roca-Cusachs, P. (2019b). Integrins as biomechanical sensors of the microenvironment. *Nature Reviews Molecular Cell Biology*, *20*(8), 457–473. <https://doi.org/10.1038/s41580-019-0134-2>
- Kim, J., Kong, J., Chang, H., Kim, H., & Kim, A. (2016). EGF induces epithelial-mesenchymal transition through phospho-Smad2/3-Snail signaling pathway in breast cancer cells. *Oncotarget*, *7*(51), 85021–85032. <https://doi.org/10.18632/oncotarget.13116>
- Kim, M., Lee, C., & Park, J. (2022). Extracellular matrix remodeling facilitates obesity-associated cancer progression. *Trends in Cell Biology*, *32*(10), 825–834. <https://doi.org/10.1016/j.tcb.2022.02.008>
- Kim, S. A., Tai, C.-Y., Mok, L.-P., Mosser, E. A., & Schuman, E. M. (2011). Calcium-dependent dynamics of cadherin interactions at cell–cell junctions. *Proceedings of the National Academy of Sciences*, *108*(24), 9857–9862. <https://doi.org/10.1073/pnas.1019003108>
- Kim, T., Hwang, D., Lee, D., Kim, J., Kim, S., & Lim, D. (2017). MRTF potentiates TEAD - YAP transcriptional activity causing metastasis . *The EMBO Journal*, *36*(4), 520–535. <https://doi.org/10.15252/embj.201695137>
- King, S. J., Asokan, S. B., Haynes, E. M., Zimmerman, S. P., Rotty, J. D., Alb, J. G., Tagliatela, A., Blake, D. R., Lebedeva, I. P., Marston, D., Johnson, H. E., Parsons, M., Sharpless, N. E., Kuhlman, B., Haugh, J. M., & Bear, J. E. (2016). Lamellipodia are crucial for haptotactic sensing and response. *Journal of Cell Science*, *129*(12), 2329–2342. <https://doi.org/10.1242/jcs.184507>
- Kirby, T. J., & Lammerding, J. (2018). Emerging views of the nucleus as a cellular mechanosensor. *Nature Cell Biology*, *20*(4), 373–381. <https://doi.org/10.1038/s41556-018-0038-y>
- Kirsch, A., Hortobagyi, D., Stachl, T., Karbiener, M., Grossmann, T., Gerstenberger, C., & Gugatschka, M. (2019). Development and validation of a novel phonomimetic bioreactor. *PLoS One*, *14*(3), e0213788. <https://doi.org/10.1371/journal.pone.0213788>
- Knoedler, S., Broichhausen, S., Guo, R., Dai, R., Knoedler, L., Kauke-Navarro, M., Diatta, F., Pomahac, B., Machens, H.-G., Jiang, D., & Rinkevich, Y. (2023). Fibroblasts – the cellular choreographers of wound healing. *Frontiers in Immunology*, *14*, 1233800. <https://doi.org/10.3389/fimmu.2023.1233800>
- Knudsen, R., Gaunsbaek, M. Q., Schultz, J. H., Nilsson, A. C., Madsen, J. S., & Asgari, N. (2019). Vocal cord paralysis as primary and secondary results of malignancy. A prospective descriptive study. *Laryngoscope Investigative Otolaryngology*, *4*(2), 241–245. <https://doi.org/10.1002/lio.2.251>
- Kolasangiani, R., Bidone, T. C., & Schwartz, M. A. (2022). Integrin Conformational Dynamics and Mechanotransduction. *Cells*, *11*(22), 3584. <https://doi.org/10.3390/cells11223584>

- Koorman, T., Jansen, K. A., Khalil, A., Haughton, P. D., Visser, D., Rätze, M. A. K., Haakma, W. E., Sakalauskaite, G., van Diest, P. J., de Rooij, J., & Derksen, P. W. B. (2022). Spatial collagen stiffening promotes collective breast cancer cell invasion by reinforcing extracellular matrix alignment. *Oncogene*, *41*(17), 2458–2469. <https://doi.org/10.1038/s41388-022-02258-1>
- Kosumi, H., Watanabe, M., Shinkuma, S., Nohara, T., Fujimura, Y., Tsukiyama, T., Donati, G., Iwata, H., Nakamura, H., Ujiie, H., & Natsuga, K. (2022). Wnt/ $\beta$ -Catenin Signaling Stabilizes Hemidesmosomes in Keratinocytes. *Journal of Investigative Dermatology*, *142*(6), 1576–1586.e2. <https://doi.org/10.1016/j.jid.2021.10.018>
- Krausova, A., Buresova, P., Sarnova, L., Oyman-Eyrimelmez, G., Skarda, J., Wohl, P., Bajec, L., Sticova, E., Bartonova, L., Pacha, J., Koubkova, G., Prochazka, J., Spörrer, M., Dürrbeck, C., Stehlikova, Z., Vit, M., Ziolkowska, N., Sedlacek, R., Jirak, D., ... Gregor, M. (2021). Plectin ensures intestinal epithelial integrity and protects colon against colitis. *Mucosal Immunology*, *14*(3), 691–702. <https://doi.org/10.1038/s41385-021-00380-z>
- Kubow, K. E., Vukmirovic, R., Zhe, L., Klotzsch, E., Smith, M. L., Gourdon, D., Luna, S., & Vogel, V. (2015). Mechanical forces regulate the interactions of fibronectin and collagen I in extracellular matrix. *Nature Communications*, *6*(1), 8026. <https://doi.org/10.1038/ncomms9026>
- Kumar, D., New, J., Vishwakarma, V., Joshi, R., Enders, J., Lin, F., Dasari, S., Gutierrez, W. R., Leef, G., Ponnurangam, S., Chavan, H., Ganaden, L., Thornton, M. M., Dai, H., Tawfik, O., Straub, J., Shnyder, Y., Kakarala, K., Tsue, T. T., ... Thomas, S. M. (2018). Cancer-Associated Fibroblasts Drive Glycolysis in a Targetable Signaling Loop Implicated in Head and Neck Squamous Cell Carcinoma Progression. *Cancer Research*, *78*(14), 3769–3782. <https://doi.org/10.1158/0008-5472.CAN-17-1076>
- Kumar, S., Stainer, A., Dubrulle, J., Simpkins, C., & Cooper, J. A. (2023). Cas phosphorylation regulates focal adhesion assembly. *ELife*, *12*, e90234. <https://doi.org/10.7554/eLife.90234>
- Kumar, S., & Weaver, V. M. (2009). Mechanics, malignancy, and metastasis: The force journey of a tumor cell. *Cancer and Metastasis Reviews*, *28*(1–2), 113–127. <https://doi.org/10.1007/s10555-008-9173-4>
- Kumari, R., Ven, K., Chastney, M., Kokate, S. B., Peränen, J., Aaron, J., Kogan, K., Almeida-Souza, L., Kremneva, E., Poincloux, R., Chew, T.-L., Gunning, P. W., Ivaska, J., & Lappalainen, P. (2024). Focal adhesions contain three specialized actin nanoscale layers. *Nature Communications*, *15*(1), 2547. <https://doi.org/10.1038/s41467-024-46868-7>
- Lachowski, D., Matellan, C., Gopal, S., Cortes, E., Robinson, B. K., Saiani, A., Miller, A. F., Stevens, M. M., & del Río Hernández, A. E. (2022). Substrate Stiffness-Driven Membrane Tension Modulates Vesicular Trafficking via Caveolin-1. *ACS Nano*, *16*(3), 4322–4337. <https://doi.org/10.1021/acsnano.1c10534>
- Ladoux, B., & Mège, R.-M. (2017). Mechanobiology of collective cell behaviours. *Nature Reviews Molecular Cell Biology*, *18*(12), 743–757. <https://doi.org/10.1038/nrm.2017.98>
- Laly, A. C., Sliogeryte, K., Pundel, O. J., Ross, R., Keeling, M. C., Avisetti, D., Waseem, A., Gavara, N., & Connelly, J. T. (2021). The keratin network of intermediate filaments regulates keratinocyte rigidity sensing and nuclear mechanotransduction. *Science Advances*, *7*(5), 1–12. <https://doi.org/10.1126/sciadv.abd6187>
- Lawson, C. D., & Ridley, A. J. (2018). Rho GTPase signaling complexes in cell migration and invasion. *Journal of Cell Biology*, *217*(2), 447–457. <https://doi.org/10.1083/jcb.201612069>
- Le Duc, Q., Shi, Q., Blonk, I., Sonnenberg, A., Wang, N., Leckband, D., & De Rooij, J. (2010). Vinculin potentiates E-cadherin mechanosensing and is recruited to actin-anchored sites within adherens junctions in a myosin II-dependent manner. *Journal of Cell Biology*, *189*(7), 1107–1115. <https://doi.org/10.1083/jcb.201001149>
- Le, S., Yu, M., & Yan, J. (2024). Direct single-molecule quantification reveals unexpectedly high mechanical stability of vinculin—talin/ $\alpha$ -catenin linkages. *Science Advances*, *5*(12), eaav2720. <https://doi.org/10.1126/sciadv.aav2720>



- Legerstee, K., Abraham, T. E., van Cappellen, W. A., Nigg, A. L., Slotman, J. A., & Houtsmuller, A. B. (2021). Growth factor dependent changes in nanoscale architecture of focal adhesions. *Scientific Reports*, *11*(1), 2315. <https://doi.org/10.1038/s41598-021-81898-x>
- Lemmon, M. A., Freed, D. M., Schlessinger, J., & Kiyatkin, A. (2016). The Dark Side of Cell Signaling: Positive Roles for Negative Regulators. *Cell*, *164*(6), 1172–1184. <https://doi.org/10.1016/j.cell.2016.02.047>
- Leung, G. P., Feng, T., Sigoillot, F. D., Geyer, F. C., Shirley, M. D., Ruddy, D. A., Rakiec, D. P., Freeman, A. K., Engelman, J. A., Jaskelioff, M., & Stuart, D. D. (2019). Hyperactivation of MAPK Signaling Is Deleterious to RAS/RAF-mutant Melanoma. *Molecular Cancer Research*, *17*(1), 199–211. <https://doi.org/10.1158/1541-7786.MCR-18-0327>
- Levental, K. R., Yu, H., Kass, L., Lakins, J. N., Egeblad, M., Erler, J. T., Fong, S. F. T., Csiszar, K., Giaccia, A., Weninger, W., Yamauchi, M., Gasser, D. L., & Weaver, V. M. (2009). Matrix crosslinking forces tumor progression by enhancing integrin signaling. *Cell*, *139*(5), 891–906. <https://doi.org/10.1016/j.cell.2009.10.027>
- Li, H., Zeng, C., Shu, C., Cao, Y., Shao, W., Zhang, M., Cao, H., & Zhao, S. (2022). Laminins in tumor-derived exosomes upregulated by ETS1 reprogram omental macrophages to promote omental metastasis of ovarian cancer. *Cell Death & Disease*, *13*(12), 1028. <https://doi.org/10.1038/s41419-022-05472-7>
- Li, J., Jo, M. H., Yan, J., Hall, T., Lee, J., López-Sánchez, U., Yan, S., Ha, T., & Springer, T. A. (2024). Ligand binding initiates single-molecule integrin conformational activation. *Cell*, *187*(12), 2990–3005.e17. <https://doi.org/10.1016/j.cell.2024.04.049>
- Li, J., Liu, X., Zang, S., Zhou, J., Zhang, F., Sun, B., Qi, D., Li, X., Kong, J., Jin, D., Yang, X., Luo, Y., Lu, Y., Lin, B., Niu, W., & Liu, T. (2020). Small extracellular vesicle-bound vascular endothelial growth factor secreted by carcinoma-associated fibroblasts promotes angiogenesis in a bevacizumab-resistant manner. *Cancer Letters*, *492*, 71–83. <https://doi.org/10.1016/j.canlet.2020.08.030>
- Li, Y., Wong, I. Y., & Guo, M. (2022). Reciprocity of Cell Mechanics with Extracellular Stimuli: Emerging Opportunities for Translational Medicine. *Small*, *18*(36), e2107305. <https://doi.org/10.1002/sml.202107305>
- Liang, R., & Song, G. (2023). Matrix stiffness-driven cancer progression and the targeted therapeutic strategy. *Mechanobiology in Medicine*, *1*(2), 100013. <https://doi.org/10.1016/j.mbm.2023.100013>
- Liao, H., Li, X., Zhao, L., Wang, Y., Wang, X., Wu, Y., Zhou, X., Fu, W., Liu, L., Hu, H.-G., & Chen, Y.-G. (2020). A PROTAC peptide induces durable  $\beta$ -catenin degradation and suppresses Wnt-dependent intestinal cancer. *Cell Discovery*, *6*(1), 35. <https://doi.org/10.1038/s41421-020-0171-1>
- Lickert, S., Kenny, M., Selcuk, K., Mehl, J. L., Bender, M., Früh, S. M., Burkhardt, M. A., Studt, J.-D., Nieswandt, B., Schoen, I., & Vogel, V. (2024). Platelets drive fibronectin fibrillogenesis using integrin  $\alpha$ IIb $\beta$ 3. *Science Advances*, *8*(10), eabj8331. <https://doi.org/10.1126/sciadv.abj8331>
- Lilja, J., Zacharchenko, T., Georgiadou, M., Jacquemet, G., Franceschi, N. De, Peuhu, E., Hamidi, H., Pouwels, J., Martens, V., Nia, F. H., Beifuss, M., Boeckers, T., Kreienkamp, H.-J., Barsukov, I. L., & Ivaska, J. (2017). SHANK proteins limit integrin activation by directly interacting with Rap1 and R-Ras. *Nature Cell Biology*, *19*(4), 292–305. <https://doi.org/10.1038/ncb3487>
- Liu, C.-Y., Chan, S. W., Guo, F., Toloczko, A., Cui, L., & Hong, W. (2016). MRTF/SRF dependent transcriptional regulation of TAZ in breast cancer cells. *Oncotarget*, *7*(12), 13706–13716. <https://doi.org/10.18632/oncotarget.7333>
- Liu, J., Das, M., Yang, J., Ithychanda, S. S., Yakubenko, V. P., Plow, E. F., & Qin, J. (2015). Structural mechanism of integrin inactivation by filamin. *Nature Structural & Molecular Biology*, *22*(5), 383–389. <https://doi.org/10.1038/nsmb.2999>
- Liu, J., Xiao, Q., Xiao, J., Niu, C., Li, Y., Zhang, X., Zhou, Z., Shu, G., & Yin, G. (2022). Wnt/ $\beta$ -catenin signalling: function, biological mechanisms, and therapeutic opportunities. *Signal Transduction and Targeted Therapy*, *7*(1). <https://doi.org/10.1038/s41392-021-00762-6>

- Liu, X., Li, J., Yang, X., Li, X., Kong, J., Qi, D., Zhang, F., Sun, B., Liu, Y., & Liu, T. (2023). Carcinoma-associated fibroblast-derived lysyl oxidase-rich extracellular vesicles mediate collagen crosslinking and promote epithelial-mesenchymal transition via p-FAK/p-paxillin/YAP signaling. *International Journal of Oral Science*, *15*(1), 32. <https://doi.org/10.1038/s41368-023-00236-1>
- Liu, Y., Tiruthani, K., Wang, M., Zhou, X., Qiu, N., Xiong, Y., Pecot, C. V., Liu, R., & Huang, L. (2021). Tumor-targeted gene therapy with lipid nanoparticles inhibits tumor-associated adipocytes and remodels the immunosuppressive tumor microenvironment in triple-negative breast cancer. *Nanoscale Horizons*, *6*(4), 319–329. <https://doi.org/10.1039/D0NH00588F>
- Loh, J., Chuang, M.-C., Lin, S.-S., Joseph, J., Su, Y.-A., Hsieh, T.-L., Chang, Y.-C., Liu, A. P., & Liu, Y.-W. (2019). An acute decrease in plasma membrane tension induces macropinocytosis via PLD2 activation. *Journal of Cell Science*, *132*(17), jcs232579. <https://doi.org/10.1242/jcs.232579>
- Lu, F., Zhu, L., Bromberger, T., Yang, J., Yang, Q., Liu, J., Plow, E. F., Moser, M., & Qin, J. (2022). Mechanism of integrin activation by talin and its cooperation with kindlin. *Nature Communications*, *13*(1). <https://doi.org/10.1038/s41467-022-30117-w>
- Lüchtfeld, I., Pivkin, I. V., Gardini, L., Zare-Eelanjegh, E., Gäbelein, C., Ihle, S. J., Reichmuth, A. M., Capitanio, M., Martinac, B., Zambelli, T., & Vassalli, M. (2024). Dissecting cell membrane tension dynamics and its effect on Piezo1-mediated cellular mechanosensitivity using force-controlled nanopipettes. *Nature Methods*, *21*(6), 1063–1073. <https://doi.org/10.1038/s41592-024-02277-8>
- Luo, H., Xia, X., Huang, L.-B., An, H., Cao, M., Kim, G. D., Chen, H.-N., Zhang, W.-H., Shu, Y., Kong, X., Ren, Z., Li, P.-H., Liu, Y., Tang, H., Sun, R., Li, C., Bai, B., Jia, W., Liu, Y., ... Xu, H. (2022). Pan-cancer single-cell analysis reveals the heterogeneity and plasticity of cancer-associated fibroblasts in the tumor microenvironment. *Nature Communications*, *13*(1), 6619. <https://doi.org/10.1038/s41467-022-34395-2>
- Luo, M., Xu, Y., Chen, H., Wu, Y., Pang, A., Hu, J., Dong, X., Che, J., & Yang, H. (2022). Advances of targeting the YAP/TAZ-TEAD complex in the hippo pathway for the treatment of cancers. *European Journal of Medicinal Chemistry*, *244*, 114847. <https://doi.org/10.1016/j.ejmech.2022.114847>
- Ly, M., Schimmer, C., Hawkins, R., E. Rothenberg, K., & Fernandez-Gonzalez, R. (2024). Integrin-based adhesions promote cell–cell junction and cytoskeletal remodelling to drive embryonic wound healing. *Journal of Cell Science*, *137*(5), 1–9. <https://doi.org/10.1242/jcs.261138>
- Lybrand, D. B., Naiman, M., Laumann, J. M., Boardman, M., Petshow, S., Hansen, K., Scott, G., & Wehrli, M. (2019). Destruction complex dynamics: Wnt/ $\beta$ -catenin signaling alters Axin-GSK3 $\beta$  interactions in in vivo. *Development*, *146*(13), dev164145. <https://doi.org/10.1242/dev.164145>
- Mai, Z., Lin, Y., Lin, P., Zhao, X., & Cui, L. (2024). Modulating extracellular matrix stiffness: a strategic approach to boost cancer immunotherapy. *Cell Death & Disease*, *15*(5), 307. <https://doi.org/10.1038/s41419-024-06697-4>
- Makareeva, E., & Leikin, S. (2014). Collagen Structure, Folding and Function. In J. R. Shapiro, P. H. Byers, F. H. Glorieux, & P. D. B. T.-O. I. Sponseller (Eds.), *Osteogenesis Imperfecta* (pp. 71–84). Elsevier. <https://doi.org/10.1016/B978-0-12-397165-4.00007-1>
- Malenica, I., Adam, J., Corgnac, S., Mezquita, L., Auclin, E., Damei, I., Grynszpan, L., Gros, G., de Montpréville, V., Planchard, D., Théret, N., Besse, B., & Mami-Chouaib, F. (2021). Integrin- $\alpha$ V-mediated activation of TGF- $\beta$  regulates anti-tumour CD8 T cell immunity and response to PD-1 blockade. *Nature Communications*, *12*(1), 5209. <https://doi.org/10.1038/s41467-021-25322-y>
- Maller, O., Drain, A. P., Barrett, A. S., Borgquist, S., Ruffell, B., Zakharevich, I., Pham, T. T., Gruosso, T., Kuasne, H., Lakins, J. N., Acerbi, I., Barnes, J. M., Nemkov, T., Chauhan, A., Gruenberg, J., Nasir, A., Bjarnadottir, O., Werb, Z., Kabos, P., ... Weaver, V. M. (2021). Tumour-associated macrophages drive stromal cell-dependent collagen crosslinking and stiffening to promote breast cancer aggression. *Nature Materials*, *20*(4), 548–559. <https://doi.org/10.1038/s41563-020-00849-5>

- Mana, G., Valdembri, D., Askari, J. A., Li, Z., Caswell, P., Zhu, C., Humphries, M. J., Ballestrem, C., & Serini, G. (2023). The  $\beta 1$  domain promotes active  $\beta 1$  integrin clustering into mature adhesion sites. *Life Science Alliance*, *6*(2), e202201388. <https://doi.org/10.26508/lsa.202201388>
- Mancini, A., Gentile, M. T., Pentimalli, F., Cortellino, S., Grieco, M., & Giordano, A. (2024). Multiple aspects of matrix stiffness in cancer progression. *Frontiers in Oncology*, *14*, 1406644. <https://doi.org/10.3389/fonc.2024.1406644>
- Mascharak, S., Guo, J. L., Foster, D. S., Khan, A., Davitt, M. F., Nguyen, A. T., Burcham, A. R., Chinta, M. S., Guardino, N. J., Griffin, M., Lopez, D. M., Miller, E., Januszyk, M., Raghavan, S. S., Longacre, T. A., Delitto, D. J., Norton, J. A., & Longaker, M. T. (2023). Desmoplastic stromal signatures predict patient outcomes in pancreatic ductal adenocarcinoma. *Cell Reports Medicine*, *4*(11), 101248. <https://doi.org/10.1016/j.xcrm.2023.101248>
- Matamoro-Vidal, A., & Levayer, R. (2019). Multiple Influences of Mechanical Forces on Cell Competition. *Current Biology*, *29*(15), R762–R774. <https://doi.org/10.1016/j.cub.2019.06.030>
- Mathieu, M., Isomursu, A., & Ivaska, J. (2024a). Positive and negative durotaxis – mechanisms and emerging concepts. *Journal of Cell Science*, *137*(8). <https://doi.org/10.1242/jcs.261919>
- Mathieu, M., Isomursu, A., & Ivaska, J. (2024b). Positive and negative durotaxis – mechanisms and emerging concepts. *Journal of Cell Science*, *137*(8), jcs261919. <https://doi.org/10.1242/jcs.261919>
- Mavrikakis, M., & Juanes, M. A. (2023). The compass to follow: Focal adhesion turnover. *Current Opinion in Cell Biology*, *80*, 102152. <https://doi.org/10.1016/j.ceb.2023.102152>
- McKee, T. J., Perlman, G., Morris, M., & Komarova, S. V. (2019). Extracellular matrix composition of connective tissues: a systematic review and meta-analysis. *Scientific Reports*, *9*(1), 10542. <https://doi.org/10.1038/s41598-019-46896-0>
- Mei, L., Espinosa de los Reyes, S., Reynolds, M. J., Leicher, R., Liu, S., & Alushin, G. M. (2020). Molecular mechanism for direct actin force-sensing by  $\alpha$ -catenin. *ELife*, *9*, e62514. <https://doi.org/10.7554/eLife.62514>
- Melamed, S., Zaffryar-Eilot, S., Nadjar-Boger, E., Aviram, R., Zhao, H., Yaseen-Badarne, W., Kalev-Altman, R., Sela-Donenfeld, D., Lewinson, O., Astrof, S., Hasson, P., & Wolfenson, H. (2023). Initiation of fibronectin fibrillogenesis is an enzyme-dependent process. *Cell Reports*, *42*(5), 112473. <https://doi.org/10.1016/j.celrep.2023.112473>
- Melcher, M.-L., Block, I., Kropf, K., Singh, A. K., & Posern, G. (2022). Interplay of the transcription factor MRTF-A and matrix stiffness controls mammary acinar structure and protrusion formation. *Cell Communication and Signaling*, *20*(1), 158. <https://doi.org/10.1186/s12964-022-00977-2>
- Mertz, A. F., Che, Y., Banerjee, S., Goldstein, J. M., Rosowski, K. A., Revilla, S. F., Niessen, C. M., Marchetti, M. C., Dufresne, E. R., & Horsley, V. (2013). Cadherin-based intercellular adhesions organize epithelial cell-matrix traction forces. *Proceedings of the National Academy of Sciences of the United States of America*, *110*(3), 842–847. <https://doi.org/10.1073/pnas.1217279110>
- Metcalf, K. A., Gronwald, J., Tung, N. M., McCuaig, J. M., Eisen, A., Elser, C., Foulkes, W. D., Neuhausen, S. L., Senter, L., Moller, P., Bordeleau, L., Fruscio, R., Velsher, L., Zakalik, D., Olopade, O. I., Eng, C., Pal, T., Cullinane, C. A., Couch, F. J., ... Narod, S. A. (2023). The risks of cancer in older women with BRCA pathogenic variants: How far have we come? *Cancer*, *129*(6), 901–907. <https://doi.org/10.1002/cncr.34615>
- Mezzano, V., & Sheikh, F. (2012). Cell–cell junction remodeling in the heart: Possible role in cardiac conduction system function and arrhythmias? *Life Sciences*, *90*(9), 313–321. <https://doi.org/https://doi.org/10.1016/j.lfs.2011.12.009>
- Miao, M. Z., Su, Q. P., Cui, Y., Bahnsen, E. M., Li, G., Wang, M., Yang, Y., Collins, J. A., Wu, D., Gu, Q., Chubinskaya, S., Diekmann, B. O., Yamada, K. M., & Loeser, R. F. (2023). Redox-active endosomes mediate  $\alpha 5\beta 1$  integrin signaling and promote chondrocyte matrix metalloproteinase production in osteoarthritis. *Science Signaling*, *16*(809), eadf8299. <https://doi.org/10.1126/scisignal.adf8299>
- Miaomiao, S., Xiaoqian, W., Yuwei, S., Chao, C., Chenbo, Y., Yinghao, L., Yichen, H., Jiao, S., & Kuisheng, C. (2023). Cancer-associated fibroblast-derived exosome microRNA-21 promotes

- angiogenesis in multiple myeloma. *Scientific Reports*, 13(1), 9671. <https://doi.org/10.1038/s41598-023-36092-6>
- Miralles, F., Posern, G., Zaromytidou, A.-I., & Treisman, R. (2003). Actin Dynamics Control SRF Activity by Regulation of Its Coactivator MAL. *Cell*, 113(3), 329–342. [https://doi.org/10.1016/S0092-8674\(03\)00278-2](https://doi.org/10.1016/S0092-8674(03)00278-2)
- Miranda, M. Z., Bialik, J. F., Speight, P., Dan, Q., Yeung, T., Szász, K., Pedersen, S. F., & Kapus, A. (2017). TGF- $\beta$ 1 regulates the expression and transcriptional activity of TAZ protein via a Smad3-independent, myocardin-related transcription factor-mediated mechanism. *Journal of Biological Chemistry*, 292(36), 14902–14920. <https://doi.org/10.1074/jbc.M117.780502>
- Miyashita, Y., & Ozawa, M. (2007). Increased Internalization of p120-uncoupled E-cadherin and a Requirement for a Dileucine Motif in the Cytoplasmic Domain for Endocytosis of the Protein. *Journal of Biological Chemistry*, 282(15), 11540–11548. <https://doi.org/10.1074/jbc.M608351200>
- Mokhtari, R. B., Homayouni, T. S., Baluch, N., Morgatskaya, E., Kumar, S., Das, B., & Yeger, H. (2017). Combination therapy in combating cancer. *Oncotarget*, 8(23), 38022–38043. <https://doi.org/10.18632/oncotarget.16723>
- Molder, L. Te, Pereda, J. M. D., Sonnenberg, A., te Molder, L., de Pereda, J. M., & Sonnenberg, A. (2021). Regulation of hemidesmosome dynamics and cell signaling by integrin  $\alpha$ 6 $\beta$ 4. *Journal of Cell Science*, 134(18). <https://doi.org/10.1242/jcs.259004>
- Molè, M. A., Weberling, A., Fässler, R., Campbell, A., Fishel, S., & Zernicka-Goetz, M. (2021). Integrin  $\beta$ 1 coordinates survival and morphogenesis of the embryonic lineage upon implantation and pluripotency transition. *Cell Reports*, 34(10), 108834. <https://doi.org/10.1016/j.celrep.2021.108834>
- Monier, B., Gettings, M., Gay, G., Mangeat, T., Schott, S., Guarner, A., & Suzanne, M. (2015). Apical-basal forces exerted by apoptotic cells drive epithelium folding. *Nature*, 518(7538), 245–248. <https://doi.org/10.1038/nature14152>
- Morales-Camilo, N., Liu, J., Ramírez, M. J., Canales-Salgado, P., Alegría, J. J., Liu, X., Ong, H. T., Barrera, N. P., Fierro, A., Toyama, Y., Goult, B. T., Wang, Y., Meng, Y., Nishimura, R., Fong-Ngern, K., Low, C. S. L., Kanchanawong, P., Yan, J., Ravasio, A., & Bertocchi, C. (2024). Alternative molecular mechanisms for force transmission at adherens junctions via  $\beta$ -catenin-vinculin interaction. *Nature Communications*, 15(1), 5608. <https://doi.org/10.1038/s41467-024-49850-5>
- Moreno-Layseca, P., Icha, J., Hamidi, H., & Ivaska, J. (2019). Integrin trafficking in cells and tissues. *Nature Cell Biology*, 21(2), 122–132. <https://doi.org/10.1038/s41556-018-0223-z>
- Morkunas, M., Zilenaite, D., Laurinaviciene, A., Treigys, P., & Laurinavicius, A. (2021). Tumor collagen framework from bright-field histology images predicts overall survival of breast carcinoma patients. *Scientific Reports*, 11(1), 15474. <https://doi.org/10.1038/s41598-021-94862-6>
- Moujaber, O., & Stochaj, U. (2020). The Cytoskeleton as Regulator of Cell Signaling Pathways. *Trends in Biochemical Sciences*, 45(2), 96–107. <https://doi.org/10.1016/j.tibs.2019.11.003>
- Mukherjee, A., Bezwada, D., Greco, F., Zandbergen, M., Shen, T., Chiang, C.-Y., Tasdemir, M., Fahrman, J., Grapov, D., La Frano, M. R., Vu, H. S., Faubert, B., Newman, J. W., McDonnell, L. A., Nezi, L., Fiehn, O., DeBerardinis, R. J., & Lengyel, E. (2023). Adipocytes reprogram cancer cell metabolism by diverting glucose towards glycerol-3-phosphate thereby promoting metastasis. *Nature Metabolism*, 5(9), 1563–1577. <https://doi.org/10.1038/s42255-023-00879-8>
- Nahidiazar, L., Kreft, M., van den Broek, B., Secades, P., Manders, E. M. M., Sonnenberg, A., & Jalink, K. (2015). The molecular architecture of hemidesmosomes as revealed by super-resolution microscopy. *Journal of Cell Science*, 128(20), 3714–3719. <https://doi.org/10.1242/jcs.171892>
- Najafi, M., Farhood, B., & Mortezaee, K. (2019). Extracellular matrix (ECM) stiffness and degradation as cancer drivers. *Journal of Cellular Biochemistry*, 120(3), 2782–2790. <https://doi.org/10.1002/jcb.27681>
- Nardone, G., Oliver-De La Cruz, J., Vrbsky, J., Martini, C., Pribyl, J., Skládal, P., Pešl, M., Caluori, G., Pagliari, S., Martino, F., Maceckova, Z., Hajduch, M., Sanz-Garcia, A., Pugno, N. M., Stokin,

- G. B., & Forte, G. (2017). YAP regulates cell mechanics by controlling focal adhesion assembly. *Nature Communications*, 8(1), 15321. <https://doi.org/10.1038/ncomms15321>
- Nava, M. M., Miroshnikova, Y. A., Biggs, L. C., Whitefield, D. B., Metge, F., Boucas, J., Vihinen, H., Jokitalo, E., Li, X., García Arcos, J. M., Hoffmann, B., Merkel, R., Niessen, C. M., Dahl, K. N., & Wickström, S. A. (2020). Heterochromatin-Driven Nuclear Softening Protects the Genome against Mechanical Stress-Induced Damage. *Cell*, 181(4), 800-817.e22. <https://doi.org/10.1016/j.cell.2020.03.052>
- Nematbakhsh, A., Levis, M., Kumar, N., Chen, W., Zartman, J. J., & Alber, M. (2020). Epithelial organ shape is generated by patterned actomyosin contractility and maintained by the extracellular matrix. *PLOS Computational Biology*, 16(8), e1008105. <https://doi.org/10.1371/journal.pcbi.1008105>
- Nia, H. T., Munn, L. L., & Jain, R. K. (2020). Physical traits of cancer. *Science*, 370(6516). <https://doi.org/10.1126/science.aaz0868>
- Nicolas-Boluda, A., Vaquero, J., Vimeux, L., Guilbert, T., Barrin, S., Kantari-Mimoun, C., Ponzo, M., Renault, G., Deptula, P., Pogoda, K., Bucki, R., Cascone, I., Courty, J., Fouassier, L., Gazeau, F., & Donnadieu, E. (2021). Tumor stiffening reversion through collagen crosslinking inhibition improves T cell migration and anti-PD-1 treatment. *ELife*, 10, e58688. <https://doi.org/10.7554/eLife.58688>
- Niland, S., Riscanevo, A. X., & Eble, J. A. (2021). Matrix Metalloproteinases Shape the Tumor Microenvironment in Cancer Progression. *International Journal of Molecular Sciences*, 23(1), 146. <https://doi.org/10.3390/ijms23010146>
- Nisato, R. E., Tille, J.-C., Jonczyk, A., Goodman, S. L., & Pepper, M. S. (2003).  $\alpha 3$  and  $\alpha \beta 5$  integrin antagonists inhibit angiogenesis in vitro. *Angiogenesis*, 6(2), 105-119. <https://doi.org/10.1023/B:AGEN.0000011801.98187.f2>
- Nong, J., Kang, K., Shi, Q., Zhu, X., Tao, Q., & Chen, Y.-G. (2021). Phase separation of Axin organizes the  $\beta$ -catenin destruction complex. *Journal of Cell Biology*, 220(4), e202012112. <https://doi.org/10.1083/jcb.202012112>
- Northcott, J. M., Dean, I. S., Mouw, J. K., & Weaver, V. M. (2018). Feeling Stress: The Mechanics of Cancer Progression and Aggression. *Frontiers in Cell and Developmental Biology*, 6, 17. <https://doi.org/10.3389/fcell.2018.00017>
- Nurmik, M., Ullmann, P., Rodriguez, F., Haan, S., & Letellier, E. (2020). In search of definitions: Cancer-associated fibroblasts and their markers. *International Journal of Cancer*, 146(4), 895-905. <https://doi.org/10.1002/ijc.32193>
- Oswald, L., Grosser, S., Smith, D. M., & Käs, J. A. (2017). Jamming transitions in cancer. *Journal of Physics D: Applied Physics*, 50(48). <https://doi.org/10.1088/1361-6463/aa8e83>
- Ouyang, X., Xie, Y., & Wang, G. (2019). Mechanical stimulation promotes the proliferation and the cartilage phenotype of mesenchymal stem cells and chondrocytes co-cultured in vitro. *Biomedicine & Pharmacotherapy*, 117, 109146. <https://doi.org/https://doi.org/10.1016/j.biopha.2019.109146>
- Özdemir, B. C., Pentcheva-Hoang, T., Carstens, J. L., Zheng, X., Wu, C.-C., Simpson, T. R., Laklai, H., Sugimoto, H., Kahlert, C., Novitskiy, S. V., De Jesus-Acosta, A., Sharma, P., Heidari, P., Mahmood, U., Chin, L., Moses, H. L., Weaver, V. M., Maitra, A., Allison, J. P., ... Kalluri, R. (2014). Depletion of Carcinoma-Associated Fibroblasts and Fibrosis Induces Immunosuppression and Accelerates Pancreas Cancer with Reduced Survival. *Cancer Cell*, 25(6), 719-734. <https://doi.org/10.1016/j.ccr.2014.04.005>
- Page-McCaw, A., Ewald, A. J., & Werb, Z. (2007). Matrix metalloproteinases and the regulation of tissue remodelling. In *Nature Reviews Molecular Cell Biology* (Vol. 8, Issue 3, pp. 221-233). <https://doi.org/10.1038/nrm2125>
- Pagliari, S., Vinarsky, V., Martino, F., Perestrello, A. R., Oliver De La Cruz, J., Caluori, G., Vrbsky, J., Mozetic, P., Pompeiano, A., Zancla, A., Ranjani, S. G., Skladal, P., Kytyr, D., Zdráhal, Z., Grassi, G., Sampaolesi, M., Rainer, A., & Forte, G. (2021). YAP-TEAD1 control of cytoskeleton

- dynamics and intracellular tension guides human pluripotent stem cell mesoderm specification. *Cell Death & Differentiation*, 28(4), 1193–1207. <https://doi.org/10.1038/s41418-020-00643-5>
- Pal, A., Barrett, T. F., Paolini, R., Parikh, A., & Puram, S. V. (2021). Partial EMT in head and neck cancer biology: a spectrum instead of a switch. *Oncogene*, 40(32), 5049–5065. <https://doi.org/10.1038/s41388-021-01868-5>
- Palacios, F., Tushir, J. S., Fujita, Y., & D'Souza-Schorey, C. (2005). Lysosomal Targeting of E-Cadherin: a Unique Mechanism for the Down-Regulation of Cell-Cell Adhesion during Epithelial to Mesenchymal Transitions. *Molecular and Cellular Biology*, 25(1), 389–402. <https://doi.org/10.1128/MCB.25.1.389-402.2005>
- Pallegar, N. K., & Christian, S. L. (2020). Adipocytes in the Tumour Microenvironment. In *Advances in experimental medicine and biology* (Vol. 1234, pp. 1–13). [https://doi.org/10.1007/978-3-030-37184-5\\_1](https://doi.org/10.1007/978-3-030-37184-5_1)
- Pally, D., & Naba, A. (2024). Extracellular matrix dynamics: A key regulator of cell migration across length-scales and systems. *Current Opinion in Cell Biology*, 86, 102309. <https://doi.org/10.1016/j.ceb.2023.102309>
- Pang, X., He, X., Qiu, Z., Zhang, H., Xie, R., Liu, Z., Gu, Y., Zhao, N., Xiang, Q., & Cui, Y. (2023). Targeting integrin pathways: mechanisms and advances in therapy. In *Signal Transduction and Targeted Therapy* (Vol. 8, Issue 1). Springer Nature. <https://doi.org/10.1038/s41392-022-01259-6>
- Pankova, D., Jiang, Y., Chatzifrangkeskou, M., Vendrell, I., Buzzelli, J., Ryan, A., Brown, C., & O'Neill, E. (2019). RASSF1A controls tissue stiffness and cancer stem-like cells in lung adenocarcinoma. *The EMBO Journal*, 38(13), e100532. <https://doi.org/10.15252/embj.2018100532>
- Papanicolaou, M., Parker, A. L., Yam, M., Filipe, E. C., Wu, S. Z., Chitty, J. L., Wyllie, K., Tran, E., Mok, E., Nadalini, A., Skhinas, J. N., Lucas, M. C., Herrmann, D., Nobis, M., Pereira, B. A., Law, A. M. K., Castillo, L., Murphy, K. J., Zaratzian, A., ... Cox, T. R. (2022). Temporal profiling of the breast tumour microenvironment reveals collagen XII as a driver of metastasis. *Nature Communications*, 13(1), 4587. <https://doi.org/10.1038/s41467-022-32255-7>
- Pape, J., Magdeldin, T., Stamati, K., Nyga, A., Loizidou, M., Emberton, M., & Cheema, U. (2020). Cancer-associated fibroblasts mediate cancer progression and remodel the tumour stroma. *British Journal of Cancer*, 123(7), 1178–1190. <https://doi.org/10.1038/s41416-020-0973-9>
- Park, H.-J., & Helfman, D. M. (2019). Up-regulated fibronectin in 3D culture facilitates spreading of triple negative breast cancer cells on 2D through integrin  $\beta$ -5 and Src. *Scientific Reports*, 9(1), 19950. <https://doi.org/10.1038/s41598-019-56276-3>
- Patarroyo, M., Tryggvason, K., & Virtanen, I. (2002). Laminin isoforms in tumor invasion, angiogenesis and metastasis. *Seminars in Cancer Biology*, 12(3), 197–207. [https://doi.org/10.1016/S1044-579X\(02\)00023-8](https://doi.org/10.1016/S1044-579X(02)00023-8)
- Peça, J., Feliciano, C., Ting, J. T., Wang, W., Wells, M. F., Venkatraman, T. N., Lascola, C. D., Fu, Z., & Feng, G. (2011). Shank3 mutant mice display autistic-like behaviours and striatal dysfunction. *Nature*, 472(7344), 437–442. <https://doi.org/10.1038/nature09965>
- Peng, X., Cuff, L. E., Lawton, C. D., & DeMali, K. A. (2010). Vinculin regulates cell-surface E-cadherin expression by binding to  $\beta$ -catenin. *Journal of Cell Science*, 123(4), 567–577. <https://doi.org/10.1242/jcs.056432>
- Petitjean, N., Canadas, P., Jorgensen, C., Royer, P., Le Floc'h, S., & Noël, D. (2023). Complex deformation of cartilage micropellets following mechanical stimulation promotes chondrocyte gene expression. *Stem Cell Research & Therapy*, 14(1), 226. <https://doi.org/10.1186/s13287-023-03459-5>
- Piccolo, S., Panciera, T., Contessotto, P., & Cordenonsi, M. (2022). YAP/TAZ as master regulators in cancer: modulation, function and therapeutic approaches. *Nature Cancer*, 4(1), 9–26. <https://doi.org/10.1038/s43018-022-00473-z>
- Pocaterra, A., Romani, P., & Dupont, S. (2020). YAP/TAZ functions and their regulation at a glance. *Journal of Cell Science*, 133(2). <https://doi.org/10.1242/jcs.230425>

- Pora, A., Yoon, S., Dreissen, G., Hoffmann, B., Merkel, R., Windoffer, R., & Leube, R. E. (2020). Regulation of keratin network dynamics by the mechanical properties of the environment in migrating cells. *Scientific Reports*, *10*(1), 1–17. <https://doi.org/10.1038/s41598-020-61242-5>
- Privé, B. M., Boussihmad, M. A., Timmermans, B., van Gemert, W. A., Peters, S. M. B., Derks, Y. H. W., van Lith, S. A. M., Mehra, N., Nagarajah, J., Heskamp, S., & Westdorp, H. (2023). Fibroblast activation protein-targeted radionuclide therapy: background, opportunities, and challenges of first (pre)clinical studies. *European Journal of Nuclear Medicine and Molecular Imaging*, *50*(7), 1906–1918. <https://doi.org/10.1007/s00259-023-06144-0>
- Punekar, S. R., Velcheti, V., Neel, B. G., & Wong, K.-K. (2022). The current state of the art and future trends in RAS-targeted cancer therapies. *Nature Reviews Clinical Oncology*, *19*(10), 637–655. <https://doi.org/10.1038/s41571-022-00671-9>
- Qin, K., Yu, M., Fan, J., Wang, H., Zhao, P., Zhao, G., Zeng, W., Chen, C., Wang, Y., Wang, A., Schwartz, Z., Hong, J., Song, L., Wagstaff, W., Haydon, R. C., Luu, H. H., Ho, S. H., Strelzow, J., Reid, R. R., ... Shi, L. L. (2024). Canonical and noncanonical Wnt signaling: Multilayered mediators, signaling mechanisms and major signaling crosstalk. *Genes & Diseases*, *11*(1), 103–134. <https://doi.org/10.1016/j.gendis.2023.01.030>
- Quigley, A. S., Bancelin, S., Deska-Gauthier, D., Légaré, F., Veres, S. P., & Kreplak, L. (2018). Combining tensile testing and structural analysis at the single collagen fibril level. *Scientific Data*, *5*(1), 180229. <https://doi.org/10.1038/sdata.2018.229>
- Rantala, J. K., Pouwels, J., Pellinen, T., Veltel, S., Laasola, P., Mattila, E., Potter, C. S., Duffy, T., Sundberg, J. P., Kallioniemi, O., Askari, J. A., Humphries, M. J., Parsons, M., Salmi, M., & Ivaska, J. (2011). SHARPIN is an endogenous inhibitor of  $\beta$ 1-integrin activation. *Nature Cell Biology*, *13*(11), 1315–1324. <https://doi.org/10.1038/ncb2340>
- Rask-Andersen, M., Ivansson, E., Höglund, J., Ek, W. E., Karlsson, T., & Johansson, Å. (2023). Adiposity and sex-specific cancer risk. *Cancer Cell*, *41*(6), 1186–1197.e4. <https://doi.org/10.1016/j.ccell.2023.05.010>
- Rennekamp, B., Karfusehr, C., Kurth, M., Ünal, A., Monego, D., Riedmiller, K., Gryn'ova, G., Hudson, D. M., & Gräter, F. (2023). Collagen breaks at weak sacrificial bonds taming its mechanoradicals. *Nature Communications*, *14*(1), 2075. <https://doi.org/10.1038/s41467-023-37726-z>
- Rice, A. J., Cortes, E., Lachowski, D., Cheung, B. C. H., Karim, S. A., Morton, J. P., & del Rio Hernández, A. (2017). Matrix stiffness induces epithelial–mesenchymal transition and promotes chemoresistance in pancreatic cancer cells. *Oncogenesis*, *6*(7), e352–e352. <https://doi.org/10.1038/oncsis.2017.54>
- Risom, T., Glass, D. R., Averbukh, I., Liu, C. C., Baranski, A., Kagel, A., McCaffrey, E. F., Greenwald, N. F., Rivero-Gutiérrez, B., Strand, S. H., Varma, S., Kong, A., Keren, L., Srivastava, S., Zhu, C., Khair, Z., Veis, D. J., Deschryver, K., Vennam, S., ... Angelo, M. (2022). Transition to invasive breast cancer is associated with progressive changes in the structure and composition of tumor stroma. *Cell*, *185*(2), 299–310.e18. <https://doi.org/10.1016/j.cell.2021.12.023>
- Roca-Cusachs, P., del Rio, A., Puklin-Faucher, E., Gauthier, N. C., Biais, N., & Sheetz, M. P. (2013). Integrin-dependent force transmission to the extracellular matrix by  $\alpha$ -actinin triggers adhesion maturation. *Proceedings of the National Academy of Sciences*, *110*(15), E1361–70. <https://doi.org/10.1073/pnas.1220723110>
- Rosell-García, T., & Rodríguez-Pascual, F. (2018). Enhancement of collagen deposition and cross-linking by coupling lysyl oxidase with bone morphogenetic protein-1 and its application in tissue engineering. *Scientific Reports*, *8*(1), 10780. <https://doi.org/10.1038/s41598-018-29236-6>
- Röth, S., Kocaturk, N. M., Sathyamurthi, P. S., Carton, B., Watt, M., Macartney, T. J., Chan, K.-H., Isidro-Llobet, A., Konopacka, A., Queisser, M. A., & Sapkota, G. P. (2023). Identification of KLHDC2 as an efficient proximity-induced degrader of K-RAS, STK33,  $\beta$ -catenin, and FoxP3. *Cell Chemical Biology*, *30*(10), 1261–1276.e7. <https://doi.org/10.1016/j.chembiol.2023.07.006>

- Rothenberg, K. E., Scott, D. W., Christoforou, N., & Hoffman, B. D. (2018). Vinculin Force-Sensitive Dynamics at Focal Adhesions Enable Effective Directed Cell Migration. *Biophysical Journal*, *114*(7), 1680–1694. <https://doi.org/10.1016/j.bpj.2018.02.019>
- Roy, B., Pekec, T., Yuan, L., & Shivashankar, G. V. (2024). Implanting mechanically reprogrammed fibroblasts for aged tissue regeneration and wound healing. *Aging Cell*, *23*(2), e14032. <https://doi.org/https://doi.org/10.1111/acel.14032>
- Russo, V. C., Schütt, B. S., Andaloro, E., Ymer, S. I., Hoefflich, A., Ranke, M. B., Bach, L. A., & Werther, G. A. (2005). Insulin-Like Growth Factor Binding Protein-2 Binding to Extracellular Matrix Plays a Critical Role in Neuroblastoma Cell Proliferation, Migration, and Invasion. *Endocrinology*, *146*(10), 4445–4455. <https://doi.org/10.1210/en.2005-0467>
- Saatci, O., Kaymak, A., Raza, U., Ersan, P. G., Akbulut, O., Banister, C. E., Sikirzhyski, V., Tokat, U. M., Aykut, G., Ansari, S. A., Dogan, H. T., Dogan, M., Jandaghi, P., Isik, A., Gundogdu, F., Kosemehmetoglu, K., Dizdar, O., Aksoy, S., Akyol, A., ... Sahin, O. (2020). Targeting lysyl oxidase (LOX) overcomes chemotherapy resistance in triple negative breast cancer. *Nature Communications*, *11*(1), 1–17. <https://doi.org/10.1038/s41467-020-16199-4>
- Sahai, E., Atsaturuv, I., Cukierman, E., DeNardo, D. G., Egeblad, M., Evans, R. M., Fearon, D., Greten, F. R., Hingorani, S. R., Hunter, T., Hynes, R. O., Jain, R. K., Janowitz, T., Jorgensen, C., Kimmelman, A. C., Kolonin, M. G., Maki, R. G., Powers, R. S., Puré, E., ... Werb, Z. (2020). A framework for advancing our understanding of cancer-associated fibroblasts. *Nature Reviews Cancer*, *20*(3), 174–186. <https://doi.org/10.1038/s41568-019-0238-1>
- Salomaa, S. I., Miihkinen, M., Kremneva, E., Paatero, I., Lilja, J., Jacquemet, G., Vuorio, J., Antenucci, L., Kogan, K., Hassani Nia, F., Hollos, P., Isomursu, A., Vattulainen, I., Coffey, E. T., Kreienkamp, H.-J., Lappalainen, P., & Ivaska, J. (2021). SHANK3 conformation regulates direct actin binding and crosstalk with Rap1 signaling. *Current Biology*, *31*(22), 4956-4970.e9. <https://doi.org/10.1016/j.cub.2021.09.022>
- Sarker, F. A., Prior, V. G., Bax, S., & O'Neill, G. M. (2020). Forcing a growth factor response – tissue-stiffness modulation of integrin signaling and crosstalk with growth factor receptors. *Journal of Cell Science*, *133*(23). <https://doi.org/10.1242/jcs.242461>
- Sato, K., Parag-Sharma, K., Terajima, M., Musicant, A. M., Murphy, R. M., Ramsey, M. R., Hibi, H., Yamauchi, M., & Amelio, A. L. (2021). Lysyl hydroxylase 2-induced collagen cross-link switching promotes metastasis in head and neck squamous cell carcinomas. *Neoplasia*, *23*(6), 594–606. <https://doi.org/10.1016/j.neo.2021.05.014>
- Saunders, J. T., & Schwarzbauer, J. E. (2019). Fibronectin matrix as a scaffold for procollagen proteinase binding and collagen processing. *Molecular Biology of the Cell*, *30*(17), 2218–2226. <https://doi.org/10.1091/mbc.E19-03-0140>
- Schlegelmilch, K., Mohseni, M., Kirak, O., Pruszek, J., Rodriguez, J. R., Zhou, D., Kreger, B. T., Vasioukhin, V., Avruch, J., Brummelkamp, T. R., & Camargo, F. D. (2011). Yap1 Acts Downstream of  $\alpha$ -Catenin to Control Epidermal Proliferation. *Cell*, *144*(5), 782–795. <https://doi.org/10.1016/j.cell.2011.02.031>
- Schmidt, A., Kaakinen, M., Wenta, T., & Manninen, A. (2022). Loss of  $\alpha 6 \beta 4$  Integrin-Mediated Hemidesmosomes Promotes Prostate Epithelial Cell Migration by Stimulating Focal Adhesion Dynamics. *Frontiers in Cell and Developmental Biology*, *10*. <https://doi.org/10.3389/fcell.2022.886569>
- Scott, K. E., Fraley, S. I., & Rangamani, P. (2021). A spatial model of YAP/TAZ signaling reveals how stiffness, dimensionality, and shape contribute to emergent outcomes. *Proceedings of the National Academy of Sciences of the United States of America*, *118*(20), 1–12. <https://doi.org/10.1073/pnas.2021571118>
- Seddiki, R., Narayana, G. H. N. S., Strale, P.-O., Balcioglu, H. E., Peyret, G., Yao, M., Le, A. P., Teck Lim, C., Yan, J., Ladoux, B., & Mège, R. M. (2018). Force-dependent binding of vinculin to  $\alpha$ -catenin regulates cell-cell contact stability and collective cell behavior. *Molecular Biology of the Cell*, *29*(4), 380–388. <https://doi.org/10.1091/mbc.E17-04-0231>



- Sen, B., Xie, Z., Thomas, M. D., Pattenden, S. G., Howard, S., McGrath, C., Styner, M., Uzer, G., Furey, T. S., & Rubin, J. (2024). Nuclear actin structure regulates chromatin accessibility. *Nature Communications*, *15*(1), 4095. <https://doi.org/10.1038/s41467-024-48580-y>
- SenGupta, S., Parent, C. A., & Bear, J. E. (2021). The principles of directed cell migration. *Nature Reviews. Molecular Cell Biology*, *22*(8), 529–547. <https://doi.org/10.1038/s41580-021-00366-6>
- Serwe, G., Kachaner, D., Gagnon, J., Plutoni, C., Lajoie, D., Duramé, E., Sahmi, M., Garrido, D., Lefrançois, M., Arseneault, G., Saba-El-Leil, M. K., Meloche, S., Emery, G., & Therrien, M. (2023). CNK2 promotes cancer cell motility by mediating ARF6 activation downstream of AXL signalling. *Nature Communications*, *14*(1), 3560. <https://doi.org/10.1038/s41467-023-39281-z>
- Sewell-Loftin, M. K., Bayer, S. V. H., Crist, E., Hughes, T., Joison, S. M., Longmore, G. D., & George, S. C. (2017). Cancer-associated fibroblasts support vascular growth through mechanical force. *Scientific Reports*, *7*(1), 12574. <https://doi.org/10.1038/s41598-017-13006-x>
- Shang, S., Hua, F., & Hu, Z. W. (2017). The regulation of  $\beta$ -catenin activity and function in cancer: Therapeutic opportunities. *Oncotarget*, *8*(20), 33972–33989. <https://doi.org/10.18632/oncotarget.15687>
- Sharma, S., Goswami, R., Zhang, D. X., & Rahaman, S. O. (2019). TRPV4 regulates matrix stiffness and TGF $\beta$ 1-induced epithelial-mesenchymal transition. *Journal of Cellular and Molecular Medicine*, *23*(2), 761–774. <https://doi.org/https://doi.org/10.1111/jcmm.13972>
- Sheng, W., Chen, C., Dong, M., Wang, G., Zhou, J., Song, H., Li, Y., Zhang, J., & Ding, S. (2017). Calreticulin promotes EGF-induced EMT in pancreatic cancer cells via Integrin/EGFR-ERK/MAPK signaling pathway. *Cell Death & Disease*, *8*(10), e3147–e3147. <https://doi.org/10.1038/cddis.2017.547>
- Shi, L., Nadjar-Boger, E., Jafarinaia, H., Carlier, A., & Wolfenson, H. (2024). YAP mediates apoptosis through failed integrin adhesion reinforcement. *Cell Reports*, *43*(3), 113811. <https://doi.org/10.1016/j.celrep.2024.113811>
- Shieh, A. C. (2011). Biomechanical Forces Shape the Tumor Microenvironment. *Annals of Biomedical Engineering*, *39*(5), 1379–1389. <https://doi.org/10.1007/s10439-011-0252-2>
- Sidorenko, E., & Vartiainen, M. K. (2019). Nucleoskeletal regulation of transcription: Actin on MRTF. *Experimental Biology and Medicine*, *244*(15), 1372–1381. <https://doi.org/10.1177/1535370219854669>
- Simanshu, D. K., Nissley, D. V., & McCormick, F. (2017). RAS Proteins and Their Regulators in Human Disease. *Cell*, *170*(1), 17–33. <https://doi.org/10.1016/j.cell.2017.06.009>
- Singh, P., Carraher, C., & Schwarzbauer, J. E. (2010). Assembly of Fibronectin Extracellular Matrix. *Annual Review of Cell and Developmental Biology*, *26*(1), 397–419. <https://doi.org/10.1146/annurev-cellbio-100109-104020>
- Sisson, T. H., Ajayi, I. O., Subbotina, N., Dodi, A. E., Rodansky, E. S., Chibucos, L. N., Kim, K. K., Keshamouni, V. G., White, E. S., Zhou, Y., Higgins, P. D. R., Larsen, S. D., Neubig, R. R., & Horowitz, J. C. (2015). Inhibition of Myocardin-Related Transcription Factor/Serum Response Factor Signaling Decreases Lung Fibrosis and Promotes Mesenchymal Cell Apoptosis. *The American Journal of Pathology*, *185*(4), 969–986. <https://doi.org/10.1016/j.ajpath.2014.12.005>
- Sökeland, G., & Schumacher, U. (2019). The functional role of integrins during intra- and extravasation within the metastatic cascade. In *Molecular Cancer* (Vol. 18, Issue 1). BioMed Central Ltd. <https://doi.org/10.1186/s12943-018-0937-3>
- Song, X., Zhou, X., Qin, Y., Yang, J., Wang, Y., Sun, Z., Yu, K., Zhang, S., & Liu, S. (2018). Emodin inhibits epithelial-mesenchymal transition and metastasis of triple negative breast cancer via antagonism of CC-chemokine ligand $_{25}$  secreted from adipocytes. *International Journal of Molecular Medicine*, *42*(1), 579–588. <https://doi.org/10.3892/ijmm.2018.3638>
- Song, Y., Na, H., Lee, S. E., Kim, Y. M., Moon, J., Nam, T. W., Ji, Y., Jin, Y., Park, J. H., Cho, S. C., Lee, J., Hwang, D., Ha, S. J., Park, H. W., Kim, J. B., & Lee, H. W. (2024). Dysfunctional adipocytes promote tumor progression through YAP/TAZ-dependent cancer-associated adipocyte

- transformation. *Nature Communications*, *15*(1), 1–16. <https://doi.org/10.1038/s41467-024-48179-3>
- Sousa-Ortega, A., Vázquez-Marín, J., Sanabria-Reinoso, E., Corbacho, J., Polvillo, R., Campoy-López, A., Buono, L., Loosli, F., Almuedo-Castillo, M., & Martínez-Morales, J. R. (2023). A Yap-dependent mechanoregulatory program sustains cell migration for embryo axis assembly. *Nature Communications*, *14*(1), 2804. <https://doi.org/10.1038/s41467-023-38482-w>
- Spada, S., Tocci, A., Di Modugno, F., & Nisticò, P. (2021). Fibronectin as a multiregulatory molecule crucial in tumor matrixome: from structural and functional features to clinical practice in oncology. *Journal of Experimental & Clinical Cancer Research*, *40*(1), 102. <https://doi.org/10.1186/s13046-021-01908-8>
- Stepniak, E., Radice, G. L., & Vasioukhin, V. (2009). Adhesive and Signaling Functions of Cadherins and Catenins in Vertebrate Development. *Cold Spring Harbor Perspectives in Biology*, *1*(5), a002949–a002949. <https://doi.org/10.1101/cshperspect.a002949>
- Stevens, A. J., Harris, A. R., Gerdtts, J., Kim, K. H., Trentesaux, C., Ramirez, J. T., McKeithan, W. L., Fattahi, F., Klein, O. D., Fletcher, D. A., & Lim, W. A. (2023). Programming multicellular assembly with synthetic cell adhesion molecules. *Nature*, *614*(7946), 144–152. <https://doi.org/10.1038/s41586-022-05622-z>
- Streibel, Y., Breckwoldt, M. O., Hunger, J., Pan, C., Fischer, M., Turco, V., Boztepe, B., Fels-Palesandro, H., Scheck, J. G., Sturm, V., Karimian-Jazi, K., Agardy, D. A., Annio, G., Mustapha, R., Soni, S. S., Alasa, A., Weidenfeld, I., Rodell, C. B., Wick, W., ... Schregel, K. (2024). Tumor biomechanics as a novel imaging biomarker to assess response to immunotherapy in a murine glioma model. *Scientific Reports*, *14*(1), 15613. <https://doi.org/10.1038/s41598-024-66519-7>
- Sun, D., Gao, W., Hu, H., & Zhou, S. (2022). Why 90% of clinical drug development fails and how to improve it? *Acta Pharmaceutica Sinica B*, *12*(7), 3049–3062. <https://doi.org/10.1016/j.apsb.2022.02.002>
- Sun, M., Chi, G., Xu, J., Tan, Y., Xu, J., Lv, S., Xu, Z., Xia, Y., Li, L., & Li, Y. (2018). Extracellular matrix stiffness controls osteogenic differentiation of mesenchymal stem cells mediated by integrin  $\alpha 5$ . *Stem Cell Research & Therapy*, *9*(1), 52. <https://doi.org/10.1186/s13287-018-0798-0>
- Sun, W., Chi, S., Li, Y., Ling, S., Tan, Y., Xu, Y., Jiang, F., Li, J., Liu, C., Zhong, G., Cao, D., Jin, X., Zhao, D., Gao, X., Liu, Z., Xiao, B., & Li, Y. (2019). The mechanosensitive Piezo1 channel is required for bone formation. *ELife*, *8*, e47454. <https://doi.org/10.7554/eLife.47454>
- Sun, W., Li, Y., Li, J., Tan, Y., Yuan, X., Meng, H., Ye, J., Zhong, G., Jin, X., Liu, Z., Du, R., Xing, W., Zhao, D., Song, J., Li, Y., Pan, J., Zhao, Y., Li, Q., Wang, A., ... Li, Y. (2023). Mechanical stimulation controls osteoclast function through the regulation of Ca<sup>2+</sup>-activated Cl<sup>-</sup> channel Anoctamin 1. *Communications Biology*, *6*(1), 407. <https://doi.org/10.1038/s42003-023-04806-1>
- Sunyer, R., Conte, V., Escribano, J., Elosegui-Artola, A., Labernadie, A., Valon, L., Navajas, D., García-Aznar, J. M., Muñoz, J. J., Roca-Cusachs, P., & Trepats, X. (2016). Collective cell durotaxis emerges from long-range intercellular force transmission. *Science*, *353*(6304), 1157–1161. <https://doi.org/10.1126/science.aaf7119>
- Takata, K., Goto, T., Kuroda, M., Kimura, Y., Harada, I., Ueda, K., Kawada, T., & Kioka, N. (2020). Stiffness of the extracellular matrix regulates differentiation into beige adipocytes. *Biochemical and Biophysical Research Communications*, *532*(2), 205–210. <https://doi.org/https://doi.org/10.1016/j.bbrc.2020.08.032>
- Takehara, M., Sato, Y., Kimura, T., Noda, K., Miyamoto, H., Fujino, Y., Miyoshi, J., Nakamura, F., Wada, H., Bando, Y., Ikemoto, T., Shimada, M., Muguruma, N., & Takayama, T. (2020). Cancer-associated adipocytes promote pancreatic cancer progression through SAA1 expression. *Cancer Science*, *111*(8), 2883–2894. <https://doi.org/10.1111/cas.14527>
- Takemoto, F., Uchida-Fukuhara, Y., Kamioka, H., Okamura, H., & Ikegame, M. (2023). Mechanical stretching determines the orientation of osteoblast migration and cell division. *Anatomical Science International*, *98*(4), 521–528. <https://doi.org/10.1007/s12565-023-00716-8>

- Talseth-Palmer, B. A. (2017). The genetic basis of colonic adenomatous polyposis syndromes. *Hereditary Cancer in Clinical Practice*, 15(1), 5. <https://doi.org/10.1186/s13053-017-0065-x>
- Tan, S. J., Chang, A. C., Anderson, S. M., Miller, C. M., Prael, L. S., Odde, D. J., & Dunn, A. R. (2020). Regulation and dynamics of force transmission at individual cell-matrix adhesion bonds. *Science Advances*, 6(20), 1–11. <https://doi.org/10.1126/sciadv.aax0317>
- Taneja, N., Bersi, M. R., Baillargeon, S. M., Fenix, A. M., Cooper, J. A., Ohi, R., Gama, V., Merryman, W. D., & Burnette, D. T. (2020). Precise Tuning of Cortical Contractility Regulates Cell Shape during Cytokinesis. *Cell Reports*, 31(1), 107477. <https://doi.org/10.1016/j.celrep.2020.03.041>
- Tang, D., Gao, J., Wang, S., Ye, N., Chong, Y., Huang, Y., Wang, J., Li, B., Yin, W., & Wang, D. (2016). Cancer-associated fibroblasts promote angiogenesis in gastric cancer through galectin-1 expression. *Tumor Biology*, 37(2), 1889–1899. <https://doi.org/10.1007/s13277-015-3942-9>
- Teckchandani, A., & Cooper, J. A. (2016). The ubiquitin-proteasome system regulates focal adhesions at the leading edge of migrating cells. *ELife*, 5. <https://doi.org/10.7554/eLife.17440>
- Tharp, K. M., Kersten, K., Maller, O., Timblin, G. A., Stashko, C., Canale, F. P., Menjivar, R. E., Hayward, M.-K., Berestjuk, I., ten Hoeve, J., Samad, B., Ironside, A. J., di Magliano, M. P., Muir, A., Geiger, R., Combes, A. J., & Weaver, V. M. (2024). Tumor-associated macrophages restrict CD8<sup>+</sup> T cell function through collagen deposition and metabolic reprogramming of the breast cancer microenvironment. *Nature Cancer*. <https://doi.org/10.1038/s43018-024-00775-4>
- Thottacherry, J. J., Kosmalska, A. J., Kumar, A., Vishen, A. S., Elosegui-Artola, A., Pradhan, S., Sharma, S., Singh, P. P., Guadamillas, M. C., Chaudhary, N., Vishwakarma, R., Trepast, X., del Pozo, M. A., Parton, R. G., Rao, M., Pullarkat, P., Roca-Cusachs, P., & Mayor, S. (2018). Mechanochemical feedback control of dynamin independent endocytosis modulates membrane tension in adherent cells. *Nature Communications*, 9(1), 4217. <https://doi.org/10.1038/s41467-018-06738-5>
- Tiede, S., Meyer-Schaller, N., Kalathur, R. K. R., Ivanek, R., Fagiani, E., Schmassmann, P., Stillhard, P., Häfliger, S., Kraut, N., Schweifer, N., Waizenegger, I. C., Bill, R., & Christofori, G. (2018). The FAK inhibitor BI 853520 exerts anti-tumor effects in breast cancer. *Oncogenesis*, 7(9), 73. <https://doi.org/10.1038/s41389-018-0083-1>
- Tijore, A., Yao, M., Wang, Y.-H., Hariharan, A., Nematbakhsh, Y., Lee Doss, B., Lim, C. T., & Sheetz, M. (2021). Selective killing of transformed cells by mechanical stretch. *Biomaterials*, 275, 120866. <https://doi.org/https://doi.org/10.1016/j.biomaterials.2021.120866>
- Timbrell, S., Aglan, H., Cramer, A., Foden, P., Weaver, D., Pachter, J., Kilgallon, A., Clarke, R. B., Farnie, G., & Bundred, N. J. (2021). FAK inhibition alone or in combination with adjuvant therapies reduces cancer stem cell activity. *Npj Breast Cancer*, 7(1), 65. <https://doi.org/10.1038/s41523-021-00263-3>
- Tiwari, S., Askari, J. A., Humphries, M. J., & Bulleid, N. J. (2011). Divalent cations regulate the folding and activation status of integrins during their intracellular trafficking. *Journal of Cell Science*, 124(10), 1672–1680. <https://doi.org/10.1242/jcs.084483>
- Tominaga, K., Shimamura, T., Kimura, N., Murayama, T., Matsubara, D., Kanauchi, H., Niida, A., Shimizu, S., Nishioka, K., Tsuji, E.-I., Yano, M., Sugano, S., Shimono, Y., Ishii, H., Saya, H., Mori, M., Akashi, K., Tada, K.-I., Ogawa, T., ... Gotoh, N. (2017). Addiction to the IGF2-ID1-IGF2 circuit for maintenance of the breast cancer stem-like cells. *Oncogene*, 36(9), 1276–1286. <https://doi.org/10.1038/onc.2016.293>
- Tse, J. M., Cheng, G., Tyrrell, J. A., Wilcox-Adelman, S. A., Boucher, Y., Jain, R. K., & Munn, L. L. (2012). Mechanical compression drives cancer cells toward invasive phenotype. *Proceedings of the National Academy of Sciences*, 109(3), 911–916. <https://doi.org/10.1073/pnas.1118910109>
- Tsutsui, S., Wakasa, H., Tsugami, Y., Suzuki, T., Nishimura, T., & Kobayashi, K. (2020). Distinct Expression Patterns of Fibrillar Collagen Types I, III, and V in Association with Mammary Gland Remodeling during Pregnancy, Lactation and Weaning. *Journal of Mammary Gland Biology and Neoplasia*, 25(3), 219–232. <https://doi.org/10.1007/s10911-020-09457-0>

- Ueno, H., Ishiguro, M., Nakatani, E., Ishikawa, T., Uetake, H., Murotani, K., Matsui, S., Teramukai, S., Sugai, T., Ajioka, Y., Maruo, H., Kotaka, M., Tsujie, M., Munemoto, Y., Yamaguchi, T., Kuroda, H., Fukunaga, M., Tomita, N., & Sugihara, K. (2021). Prognostic value of desmoplastic reaction characterisation in stage II colon cancer: prospective validation in a Phase 3 study (SACURA Trial). *British Journal of Cancer*, *124*(6), 1088–1097. <https://doi.org/10.1038/s41416-020-01222-8>
- Ungai-Salánki, R., Haty, E., Gerecsei, T., Francz, B., Béres, B., Sztilkovics, M., Székács, I., Szabó, B., & Horvath, R. (2021). Single-cell adhesion strength and contact density drops in the M phase of cancer cells. *Scientific Reports*, *11*(1), 18500. <https://doi.org/10.1038/s41598-021-97734-1>
- Unni, A. M., Harbourne, B., Oh, M. H., Wild, S., Ferrarone, J. R., Lockwood, W. W., & Varmus, H. (2018). Hyperactivation of ERK by multiple mechanisms is toxic to RTK-RAS mutation-driven lung adenocarcinoma cells. *ELife*, *7*. <https://doi.org/10.7554/eLife.33718>
- Vallet, S. D., Berthollier, C., Salza, R., Muller, L., & Ricard-Blum, S. (2020). The Interactome of Cancer-Related Lysyl Oxidase and Lysyl Oxidase-Like Proteins. *Cancers*, *13*(1), 71. <https://doi.org/10.3390/cancers13010071>
- van der Zee, J. A., van Eijck, C. H., Hop, W. C., Biermann, K., Dicheva, B. M., Seynhaeve, A. L., Koning, G. A., Eggermont, A. M., & ten Hagen, T. L. (2012). Tumour basement membrane laminin expression predicts outcome following curative resection of pancreatic head cancer. *British Journal of Cancer*, *107*(7), 1153–1158. <https://doi.org/10.1038/bjc.2012.373>
- Verpelli, C., Schmeisser, M. J., Sala, C., & Boeckers, T. M. (2012). Scaffold Proteins at the Postsynaptic Density. In *Advances in experimental medicine and biology* (Vol. 970, pp. 29–61). [https://doi.org/10.1007/978-3-7091-0932-8\\_2](https://doi.org/10.1007/978-3-7091-0932-8_2)
- Viji Babu, P. K., Mirastschijski, U., Belge, G., & Radmacher, M. (2021). Homophilic and heterophilic cadherin bond rupture forces in homo- or hetero-cellular systems measured by AFM-based single-cell force spectroscopy. *European Biophysics Journal*, *50*(3), 543–559. <https://doi.org/10.1007/s00249-021-01536-2>
- Villeneuve, C., Hashmi, A., Ylivinkka, I., Lawson-Keister, E., Miroshnikova, Y. A., Pérez-González, C., Myllymäki, S.-M., Bertillot, F., Yadav, B., Zhang, T., Matic Vignjevic, D., Mikkola, M. L., Manning, M. L., & Wickström, S. A. (2024). Mechanical forces across compartments coordinate cell shape and fate transitions to generate tissue architecture. *Nature Cell Biology*, *26*(2), 207–218. <https://doi.org/10.1038/s41556-023-01332-4>
- Wagh, K., Ishikawa, M., Garcia, D. A., Stavreva, D. A., Upadhyaya, A., & Hager, G. L. (2021). Mechanical Regulation of Transcription: Recent Advances. *Trends in Cell Biology*, *31*(6), 457–472. <https://doi.org/10.1016/j.tcb.2021.02.008>
- Walko, G., Castañón, M. J., & Wiche, G. (2015). Molecular architecture and function of the hemidesmosome. *Cell and Tissue Research*, *360*(2), 363–378. <https://doi.org/10.1007/s00441-014-2061-z>
- Walko, G., Vukasinovic, N., Gross, K., Fischer, I., Sibitz, S., Fuchs, P., Reipert, S., Jungwirth, U., Berger, W., Salzer, U., Carugo, O., Castañón, M. J., & Wiche, G. (2011). Targeted Proteolysis of Plectin Isoform 1a Accounts for Hemidesmosome Dysfunction in Mice Mimicking the Dominant Skin Blistering Disease EBS-Ogna. *PLoS Genetics*, *7*(12), e1002396. <https://doi.org/10.1371/journal.pgen.1002396>
- Wang, D.-Z., Chang, P. S., Wang, Z., Sutherland, L., Richardson, J. A., Small, E., Krieg, P. A., & Olson, E. N. (2001). Activation of Cardiac Gene Expression by Myocardin, a Transcriptional Cofactor for Serum Response Factor. *Cell*, *105*(7), 851–862. [https://doi.org/10.1016/S0092-8674\(01\)00404-4](https://doi.org/10.1016/S0092-8674(01)00404-4)
- Wang, H. J., Wang, Y., Mirjavadi, S. S., Andersen, T., Moldovan, L., Vatankhah, P., Russell, B., Jin, J., Zhou, Z., Li, Q., Cox, C. D., Su, Q. P., & Ju, L. A. (2024). Microscale geometrical modulation of PIEZO1 mediated mechanosensing through cytoskeletal redistribution. *Nature Communications*, *15*(1), 5521. <https://doi.org/10.1038/s41467-024-49833-6>

- Wang, J., Li, B., Luo, M., Huang, J., Zhang, K., Zheng, S., Zhang, S., & Zhou, J. (2024). Progression from ductal carcinoma in situ to invasive breast cancer: molecular features and clinical significance. *Signal Transduction and Targeted Therapy*, 9(1), 83. <https://doi.org/10.1038/s41392-024-01779-3>
- Wang, J., Maeda, E., Tsujimura, Y., Abe, T., Kiyonari, H., Kitaguchi, T., Yokota, H., & Matsumoto, T. (2023). In situ FRET measurement of cellular tension using conventional confocal laser microscopy in newly established reporter mice expressing actinin tension sensor. *Scientific Reports*, 13(1), 22729. <https://doi.org/10.1038/s41598-023-50142-z>
- Wang, S., Matsumoto, K., Lish, S. R., Cartagena-Rivera, A. X., & Yamada, K. M. (2021). Budding epithelial morphogenesis driven by cell-matrix versus cell-cell adhesion. *Cell*, 184(14), 3702-3716.e30. <https://doi.org/10.1016/j.cell.2021.05.015>
- Wang, W., Huang, J., & Chen, J. (2011). Angiotensin-like proteins associate with and negatively regulate YAP1. *Journal of Biological Chemistry*, 286(6), 4364–4370. <https://doi.org/10.1074/jbc.C110.205401>
- Wang, W., Zuidema, A., te Molder, L., Nahidiazar, L., Hoekman, L., Schmidt, T., Coppola, S., & Sonnenberg, A. (2020). Hemidesmosomes modulate force generation via focal adhesions. *Journal of Cell Biology*, 219(2). <https://doi.org/10.1083/jcb.201904137>
- Wang, Y. Y., Attané, C., Milhas, D., Dirat, B., Dauvillier, S., Guerard, A., Gilhodes, J., Lazar, I., Alet, N., Laurent, V., Le Gonidec, S., Biard, D., Hervé, C., Bost, F., Ren, G. S., Bono, F., Escourrou, G., Prentki, M., Nieto, L., ... Muller, C. (2017). Mammary adipocytes stimulate breast cancer invasion through metabolic remodeling of tumor cells. *JCI Insight*, 2(4), e87489. <https://doi.org/10.1172/jci.insight.87489>
- Warboys, C. M., Amini, N., Luca, A. de, & Evans, P. C. (2011). The role of blood flow in determining the sites of atherosclerotic plaques. *F1000 Medicine Reports*, 3, 5. <https://doi.org/10.3410/M3-5>
- Watson, A. W., Grant, A. D., Parker, S. S., Hill, S., Whalen, M. B., Chakrabarti, J., Harman, M. W., Roman, M. R., Forte, B. L., Gowan, C. C., Castro-Portuguez, R., Stolze, L. K., Franck, C., Cusanovich, D. A., Zavros, Y., Padi, M., Romanoski, C. E., & Mouneimne, G. (2021). Breast tumor stiffness instructs bone metastasis via maintenance of mechanical conditioning. *Cell Reports*, 35(13), 109293. <https://doi.org/10.1016/j.celrep.2021.109293>
- Webb, D. J., Donais, K., Whitmore, L. A., Thomas, S. M., Turner, C. E., Parsons, J. T., & Horwitz, A. F. (2004). FAK–Src signalling through paxillin, ERK and MLCK regulates adhesion disassembly. *Nature Cell Biology*, 6(2), 154–161. <https://doi.org/10.1038/ncb1094>
- Wei, B., Zhou, X., Liang, C., Zheng, X., Lei, P., Fang, J., Han, X., Wang, L., Qi, C., & Wei, H. (2017). Human colorectal cancer progression correlates with LOX-induced ECM stiffening. *International Journal of Biological Sciences*, 13(11), 1450–1457. <https://doi.org/10.7150/ijbs.21230>
- Wei, S. C., Fattet, L., Tsai, J. H., Guo, Y., Pai, V. H., Majeski, H. E., Chen, A. C., Sah, R. L., Taylor, S. S., Engler, A. J., & Yang, J. (2015). Matrix stiffness drives epithelial–mesenchymal transition and tumour metastasis through a TWIST1–G3BP2 mechanotransduction pathway. *Nature Cell Biology*, 17(5), 678–688. <https://doi.org/10.1038/ncb3157>
- Wei, X., Li, S., He, J., Du, H., Liu, Y., Yu, W., Hu, H., Han, L., Wang, C., Li, H., Shi, X., Zhan, M., Lu, L., Yuan, S., & Sun, L. (2019). Tumor-secreted PAI-1 promotes breast cancer metastasis via the induction of adipocyte-derived collagen remodeling. *Cell Communication and Signaling*, 17(1), 58. <https://doi.org/10.1186/s12964-019-0373-z>
- Wen, Y.-A., Xing, X., Harris, J. W., Zaytseva, Y. Y., Mitov, M. I., Napier, D. L., Weiss, H. L., Mark Evers, B., & Gao, T. (2017). Adipocytes activate mitochondrial fatty acid oxidation and autophagy to promote tumor growth in colon cancer. *Cell Death & Disease*, 8(2), e2593–e2593. <https://doi.org/10.1038/cddis.2017.21>
- Wenta, T., Schmidt, A., Zhang, Q., Devarajan, R., Singh, P., Yang, X., Ahtikoski, A., Vaarala, M., Wei, G. H., & Manninen, A. (2022). Disassembly of  $\alpha 6 \beta 4$ -mediated hemidesmosomal adhesions promotes tumorigenesis in PTEN-negative prostate cancer by targeting plectin to focal adhesions. *Oncogene*, 41(30), 3804–3820. <https://doi.org/10.1038/s41388-022-02389-5>

- Werner, M. E., Chen, F., Moyano, J. V., Yehiely, F., Jones, J. C. R., & Cryns, V. L. (2007). Caspase Proteolysis of the Integrin  $\beta 4$  Subunit Disrupts Hemidesmosome Assembly, Promotes Apoptosis, and Inhibits Cell Migration. *Journal of Biological Chemistry*, 282(8), 5560–5569. <https://doi.org/10.1074/jbc.M603669200>
- Werner, S., Lützkendorf, J., Müller, T., Müller, L. P., & Posern, G. (2019). MRTF-A controls myofibroblastic differentiation of human multipotent stromal cells and their tumour-supporting function in xenograft models. *Scientific Reports*, 9(1), 11725. <https://doi.org/10.1038/s41598-019-48142-z>
- Whitehead, J., Vignjevic, D., Fütterer, C., Beaufort, E., Robine, S., & Farge, E. (2008). Mechanical factors activate  $\beta$ -catenin-dependent oncogene expression in APC 1638N/+ mouse colon. *HFSP Journal*, 2(5), 286–294. <https://doi.org/10.2976/1.2955566>
- Wickström, S. A., & Niessen, C. M. (2018). Cell adhesion and mechanics as drivers of tissue organization and differentiation: local cues for large scale organization. *Current Opinion in Cell Biology*, 54, 89–97. <https://doi.org/https://doi.org/10.1016/j.ceb.2018.05.003>
- Winkler, J., Abisoye-Ogunniyan, A., Metcalf, K. J., & Werb, Z. (2020). Concepts of extracellular matrix remodelling in tumour progression and metastasis. *Nature Communications*, 11(1), 5120. <https://doi.org/10.1038/s41467-020-18794-x>
- Wishart, A. L., Conner, S. J., Guarin, J. R., Fatherree, J. P., Peng, Y., McGinn, R. A., Crews, R., Naber, S. P., Hunter, M., Greenberg, A. S., & Oudin, M. J. (2024). Decellularized extracellular matrix scaffolds identify full-length collagen VI as a driver of breast cancer cell invasion in obesity and metastasis. *Science Advances*, 6(43), eabc3175. <https://doi.org/10.1126/sciadv.abc3175>
- Witherel, C. E., Sao, K., Brisson, B. K., Han, B., Volk, S. W., Petrie, R. J., Han, L., & Spiller, K. L. (2021). Regulation of extracellular matrix assembly and structure by hybrid M1/M2 macrophages. *Biomaterials*, 269, 120667. <https://doi.org/10.1016/j.biomaterials.2021.120667>
- Wolf, B., Weydandt, L., Dornhöfer, N., Hiller, G. G. R., Höhn, A. K., Nel, I., Jain, R. K., Horn, L.-C., & Aktas, B. (2023). Desmoplasia in cervical cancer is associated with a more aggressive tumor phenotype. *Scientific Reports*, 13(1), 18946. <https://doi.org/10.1038/s41598-023-46340-4>
- Wood, K. C. (2023). Hyperactivation of oncogenic driver pathways as a precision therapeutic strategy. *Nature Genetics*, 55(10), 1613–1614. <https://doi.org/10.1038/s41588-023-01493-w>
- Wu, C., Weis, S. M., & Cheresch, D. A. (2023). Upregulation of fibronectin and its integrin receptors – an adaptation to isolation stress that facilitates tumor initiation. *Journal of Cell Science*, 136(20), jcs261483. <https://doi.org/10.1242/jcs.261483>
- Wu, J.-C., Chen, Y.-C., Kuo, C.-T., Wenshin Yu, H., Chen, Y.-Q., Chiou, A., & Kuo, J.-C. (2015). Focal adhesion kinase-dependent focal adhesion recruitment of SH2 domains directs SRC into focal adhesions to regulate cell adhesion and migration. *Scientific Reports*, 5, 18476. <https://doi.org/10.1038/srep18476>
- Wu, Q., Li, B., Li, Z., Li, J., Sun, S., & Sun, S. (2019). Cancer-associated adipocytes: key players in breast cancer progression. *Journal of Hematology & Oncology*, 12(1), 95. <https://doi.org/10.1186/s13045-019-0778-6>
- Xiong, X., Wen, Y.-A., Fairchild, R., Zaytseva, Y. Y., Weiss, H. L., Evers, B. M., & Gao, T. (2020). Upregulation of CPT1A is essential for the tumor-promoting effect of adipocytes in colon cancer. *Cell Death & Disease*, 11(9), 736. <https://doi.org/10.1038/s41419-020-02936-6>
- Xue, W., Yang, L., Chen, C., Ashrafizadeh, M., Tian, Y., & Sun, R. (2024). Wnt/ $\beta$ -catenin-driven EMT regulation in human cancers. *Cellular and Molecular Life Sciences*, 81(1), 79. <https://doi.org/10.1007/s00018-023-05099-7>
- Yadav, S., Barton, M., & Nguyen, N.-T. (2020). Stretching Induces Overexpression of RhoA and Rac1 GTPases in Breast Cancer Cells. *Advanced Biosystems*, 4(2), 1900222. <https://doi.org/https://doi.org/10.1002/adbi.201900222>
- Yaghjian, L., Colditz, G. A., Collins, L. C., Schnitt, S. J., Rosner, B., Vachon, C., & Tamimi, R. M. (2011). Mammographic Breast Density and Subsequent Risk of Breast Cancer in Postmenopausal

- Women According to Tumor Characteristics. *JNCI Journal of the National Cancer Institute*, 103(15), 1179–1189. <https://doi.org/10.1093/jnci/djr225>
- Yang, B., Wolfenson, H., Chung, V. Y., Nakazawa, N., Liu, S., Hu, J., Huang, R. Y. J., & Sheetz, M. P. (2020). Stopping transformed cancer cell growth by rigidity sensing. *Nature Materials*, 19(2), 239–250. <https://doi.org/10.1038/s41563-019-0507-0>
- Yang, D., Liu, J., Qian, H., & Zhuang, Q. (2023). Cancer-associated fibroblasts: from basic science to anticancer therapy. *Experimental and Molecular Medicine*, 55(7), 1322–1332. <https://doi.org/10.1038/s12276-023-01013-0>
- Yao, M., Qiu, W., Liu, R., Efremov, A. K., Cong, P., Seddiki, R., Payre, M., Lim, C. T., Ladoux, B., Mège, R.-M., & Yan, J. (2014). Force-dependent conformational switch of  $\alpha$ -catenin controls vinculin binding. *Nature Communications*, 5(1), 4525. <https://doi.org/10.1038/ncomms5525>
- Yao, M., Tijore, A., Cheng, D., Li, J. V., Hariharan, A., Martinac, B., Tran Van Nhieu, G., Cox, C. D., & Sheetz, M. (2022). Force- and cell state-dependent recruitment of Piezo1 drives focal adhesion dynamics and calcium entry. *Science Advances*, 8(45), eabo1461. <https://doi.org/10.1126/sciadv.abo1461>
- Yap, A. S., Duszyk, K., & Viasnoff, V. (2018). Mechanosensing and mechanotransduction at cell–cell junctions. *Cold Spring Harbor Perspectives in Biology*, 10(8). <https://doi.org/10.1101/cshperspect.a028761>
- Yasuda, T., Koiwa, M., Yonemura, A., Miyake, K., Kariya, R., Kubota, S., Yokomizo-Nakano, T., Yasuda-Yoshihara, N., Uchihara, T., Itoyama, R., Bu, L., Fu, L., Arima, K., Izumi, D., Iwagami, S., Eto, K., Iwatsuki, M., Baba, Y., Yoshida, N., ... Ishimoto, T. (2021). Inflammation-driven senescence-associated secretory phenotype in cancer-associated fibroblasts enhances peritoneal dissemination. *Cell Reports*, 34(8), 108779. <https://doi.org/10.1016/j.celrep.2021.108779>
- Yu, F.-X., Zhao, B., Panupinthu, N., Jewell, J. L., Lian, I., Wang, L. H., Zhao, J., Yuan, H., Tumaneng, K., Li, H., Fu, X.-D., Mills, G. B., & Guan, K.-L. (2012). Regulation of the Hippo-YAP Pathway by G-Protein-Coupled Receptor Signaling. *Cell*, 150(4), 780–791. <https://doi.org/10.1016/j.cell.2012.06.037>
- Yu, O. M., Miyamoto, S., & Brown, J. H. (2016). Myocardin-Related Transcription Factor A and Yes-Associated Protein Exert Dual Control in G Protein-Coupled Receptor- and RhoA-Mediated Transcriptional Regulation and Cell Proliferation. *Molecular and Cellular Biology*, 36(1), 39–49. <https://doi.org/10.1128/MCB.00772-15>
- Zanonato, F., Cordenonsi, M., & Piccolo, S. (2016). YAP/TAZ at the Roots of Cancer. *Cancer Cell*, 29(6), 783–803. <https://doi.org/10.1016/j.ccell.2016.05.005>
- Zhang, B., Zhang, Y., Zhang, J., Liu, P., Jiao, B., Wang, Z., & Ren, R. (2021). Focal Adhesion Kinase (FAK) Inhibition Synergizes with KRAS G12C Inhibitors in Treating Cancer through the Regulation of the FAK–YAP Signaling. *Advanced Science*, 8(16), 2100250. <https://doi.org/10.1002/advs.202100250>
- Zhang, D., Ni, Q.-Q., Wang, S.-Y., He, W.-F., Hong, Z.-X., Liu, H.-Y., Chen, X.-H., Chen, L.-J., Han, F.-Y., Zhang, L.-J., Li, X., Ding, Y., Jiao, H., & Ye, Y. (2024). APC mutations disrupt  $\beta$ -catenin destruction complex condensates organized by Axin phase separation. *Cellular and Molecular Life Sciences*, 81(1), 57. <https://doi.org/10.1007/s00018-023-05068-0>
- Zhang, H., Fredericks, T., Xiong, G., Qi, Y., Rychahou, P. G., Li, J.-D., Pihlajaniemi, T., Xu, W., & Xu, R. (2018). Membrane associated collagen XIII promotes cancer metastasis and enhances anoikis resistance. *Breast Cancer Research*, 20(1), 116. <https://doi.org/10.1186/s13058-018-1030-y>
- Zhang, J.-Y., Zhu, W.-W., Wang, M.-Y., Zhai, R.-D., Wang, Q., Shen, W.-L., & Liu, L.-K. (2021). Cancer-associated fibroblasts promote oral squamous cell carcinoma progression through LOX-mediated matrix stiffness. *Journal of Translational Medicine*, 19(1), 513. <https://doi.org/10.1186/s12967-021-03181-x>
- Zhang, J., Betson, M., Erasmus, J., Zeikos, K., Bailly, M., Cramer, L. P., & Braga, V. M. M. (2005). Actin at cell-cell junctions is composed of two dynamic and functional populations. *Journal of Cell Science*, 118(23), 5549–5562. <https://doi.org/10.1242/jcs.02639>

- Zhang, Y., Zhang, Y., Hutterer, E., Hultin, S., Bergman, O., Kolbeinsdottir, S., Jin, H., Forteza, M. J., Ketelhuth, D. F. J., Roy, J., Hedin, U., Enge, M., Matic, L., Eriksson, P., & Holmgren, L. (2023). The VE-cadherin/AmotL2 mechanosensory pathway suppresses aortic inflammation and the formation of abdominal aortic aneurysms. *Nature Cardiovascular Research*, 2(7), 629–644. <https://doi.org/10.1038/s44161-023-00298-8>
- Zhang, Z., Tao, D., Zhang, P., Liu, X., Zhang, Y., Cheng, J., Yuan, H., Liu, L., & Jiang, H. (2016). Hyaluronan synthase 2 expressed by cancer-associated fibroblasts promotes oral cancer invasion. *Journal of Experimental & Clinical Cancer Research*, 35(1), 181. <https://doi.org/10.1186/s13046-016-0458-0>
- Zhao, B., Li, L., Lu, Q., Wang, L. H., Liu, C. Y., Lei, Q., & Guan, K. L. (2011). Angiomotin is a novel Hippo pathway component that inhibits YAP oncoprotein. *Genes and Development*, 25(1), 51–63. <https://doi.org/10.1101/gad.2000111>
- Zhao, C., Zeng, N., Zhou, X., Tan, Y., Wang, Y., Zhang, J., Wu, Y., & Zhang, Q. (2023). CAA-derived IL-6 induced M2 macrophage polarization by activating STAT3. *BMC Cancer*, 23(1), 392. <https://doi.org/10.1186/s12885-023-10826-1>
- Zhitnyak, I. Y., Rubtsova, S. N., Litovka, N. I., & Gloushankova, N. A. (2020). Early Events in Actin Cytoskeleton Dynamics and E-Cadherin-Mediated Cell-Cell Adhesion during Epithelial-Mesenchymal Transition. *Cells*, 9(3), 578. <https://doi.org/10.3390/cells9030578>
- Zhong, Z., Jiao, Z., & Yu, F.-X. (2024). The Hippo signaling pathway in development and regeneration. *Cell Reports*, 43(3), 113926. <https://doi.org/10.1016/j.celrep.2024.113926>
- Zimmerman, S. P., Asokan, S. B., Kuhlman, B., & Bear, J. E. (2017). Cells lay their own tracks – optogenetic Cdc42 activation stimulates fibronectin deposition supporting directed migration. *Journal of Cell Science*, 130(18), 2971–2983. <https://doi.org/10.1242/jcs.205948>



## Original Publications

**Kaivola J, Punovuori K, Chastney MR, Miroshnikova YA, Abdo H, Bertillot F, Krautgasser F, Di Franco J, Conway JRW, Follain G, Hagström J, Mäkitie A, Irjala H, Ventelä S, Hamidi H, Scita G, Cerbino R, Wickström SA & Ivaska J. (2024)  
Restoring mechanophenotype reverts malignant properties of ECM-enriched vocal fold cancer.  
Manuscript**



# Restoring mechanophenotype reverts malignant properties of ECM-enriched vocal fold cancer

Jasmin Kaivola<sup>1</sup>, Karolina Punovuori<sup>2</sup>, Megan R. Chastney<sup>1</sup>, Yekaterina A. Miroshnikova<sup>2,3</sup>, Hind Abdo<sup>4</sup>, Fabien Bertillot<sup>2,5</sup>, Fabian Krautgasser<sup>6</sup>, Jasmin Di Franco<sup>6,7</sup>, James R.W. Conway<sup>1</sup>, Gautier Follain<sup>1</sup>, Jaana Hagström<sup>8,9,10</sup>, Antti Mäkitie<sup>12,13,14</sup>, Heikki Irjala<sup>15</sup>, Sami Ventelä<sup>1,15</sup>, Hellyeh Hamidi<sup>1</sup>, Giorgio Scita<sup>5,16</sup>, Roberto Cerbino<sup>6</sup>, Sara A. Wickström<sup>2,4,17,18</sup> and Johanna Ivaska<sup>1,19,20,21\*</sup>

<sup>1</sup>Turku Bioscience Centre, University of Turku and Åbo Akademi University, Turku, Finland

<sup>2</sup>Stem Cells and Metabolism Research Program, Faculty of Medicine, University of Helsinki, Helsinki Finland

<sup>3</sup> Laboratory of Molecular Biology, National Institute of Diabetes and Digestive and Kidney Diseases, National Institutes of Health, Bethesda, MD, USA

<sup>4</sup>IFOM, the FIRC Institute of Molecular Oncology, Milan, Italy

<sup>5</sup>Department of Cell and Tissue Dynamics, Max Planck Institute for Molecular Biomedicine, Münster, Germany

<sup>6</sup>Faculty of Physics, University of Vienna, Vienna, Austria.

<sup>7</sup>Vienna Doctoral School in Physics, University of Vienna, Vienna, Austria

<sup>8</sup>Institute for Molecular Medicine Finland, Helsinki Institute of Life Science, University of Helsinki, Helsinki, Finland

<sup>9</sup>Department of Oral Pathology and Radiology, University of Turku and Turku University Hospital, Turku, Finland

<sup>10</sup>Research Programs Unit, Translational Cancer Medicine, University of Helsinki, Helsinki, Finland

<sup>11</sup>Department of Pathology, University of Helsinki, FI-00014 Helsinki, Finland

<sup>12</sup>Department of Otorhinolaryngology – Head and Neck Surgery, University of Helsinki and Helsinki University Hospital, Helsinki, Finland

<sup>13</sup>Research Program in Systems Oncology, Faculty of Medicine, University of Helsinki, Helsinki, Finland

<sup>14</sup>Division of Ear, Nose and Throat Diseases, Department of Clinical Sciences, Intervention and Technology, Karolinska Institute and Karolinska University Hospital, Stockholm, Sweden

<sup>15</sup>Department of Otorhinolaryngology-Head and Neck Surgery, University of Turku and Turku University Hospital, Turku, Finland

<sup>16</sup>Department of Oncology and Haemato-Oncology, University of Milan, Milan, Italy

<sup>17</sup>Helsinki Institute of Life Science, Biomedicum Helsinki, University of Helsinki, Helsinki, Finland

<sup>18</sup>Wihuri Research Institute, Biomedicum Helsinki, University of Helsinki, Helsinki, Finland

<sup>19</sup>Department of Life Technologies, University of Turku, Turku, Finland

<sup>20</sup>InFLAMES Research Flagship Center, University of Turku, Turku, Finland

<sup>21</sup>Foundation for the Finnish Cancer Institute, Helsinki, Finland.

\*Correspondence: joivaska@utu.fi

## Abstract

**Increased extracellular matrix (ECM) and matrix stiffness promote solid tumor progression. However, mechanotransduction in cancers arising in mechanically active tissues remains underexplored. Here, we report upregulation of multiple ECM components accompanied by tissue stiffening in vocal fold cancer (VFC). We compare non-cancerous (NC) and patient-derived VFC cells – from early (mobile, T1) to advanced-stage (immobile, T3) cancers – revealing an association between VFC progression and cell-surface receptor heterogeneity,**

**reduced laminin-binding integrin cell-cell junction localization and a flocking mode of collective cell motility. Mimicking physiological movement of healthy vocal fold tissue (stretching/vibration), decreases oncogenic nuclear  $\beta$ -catenin and YAP levels in VFC. Multiplex immunohistochemistry of VFC tumors uncovered a correlation between ECM content, nuclear YAP and patient survival, concordant with VFC sensitivity to YAP-TEAD inhibitors in vitro. Our findings present evidence that VFC is a mechanically sensitive malignancy and restoration of tumor mechanophenotype or YAP/TAZ targeting, represents a tractable anti-oncogenic therapeutic avenue for VFC.**

The human vocal folds are composed of three layers (epithelial layer, basement membrane and lamina propria) with distinct cellular and extracellular matrix (ECM) compositions<sup>1</sup>. Maintaining proper ECM organization is essential for vocal fold epithelium viscoelasticity, as it has been shown that the biomechanical and physiological performance of the vocal folds relies on ECM homeostasis<sup>2,3</sup>. ECM alterations are also linked to numerous pathological conditions, such as cancer<sup>4</sup>. Vocal fold cancer (VFC) remains a major clinical challenge with limited targeted therapy options, and only a 34% 5-year survival rate for advanced T3-T4 disease. VFC arises in the stratified squamous epithelium, and as it progresses, the squamous cells in the epithelial layer breach the underlying basement membrane, invade into the collagen-rich lamina propria and further to the underlying muscle, leading to mechanical fixation<sup>4-7</sup>, characteristic to T3 and T4 disease.

In recent years, there has been a growing appreciation of the role of ECM remodeling and increased ECM deposition in cancer pathogenesis<sup>8,9</sup> as the ensuing increase in tissue rigidity alters tissue mechanics and drives cancer progression<sup>10-13</sup>. Integrins, the main cellular ECM receptors<sup>14</sup>, act as mechanosensors by probing the physical properties of their surroundings and transducing this information via the cytoskeleton into intracellular biochemical signals and transcriptional changes<sup>15-17</sup>. Among the key oncogenic signals triggered by increased tissue rigidity and integrin engagement, is stabilization and nuclear translocation of the hippo-signaling pathway transcription factors YAP and TAZ<sup>18,19</sup>. YAP/TAZ are upregulated in various cancers and influences tumor initiation, progression and therapeutic resistance<sup>20-22</sup>. Importantly, this signaling is reciprocal with YAP positive control of focal adhesion (FA) assembly<sup>23</sup> and integrin adhesion to the ECM regulates YAP/TAZ in the squamous epithelium<sup>24</sup>. However, it remains unknown whether changes in ECM and cell mechanics play a role in VFC. Further, it is not known whether immobility caused by fixation contributes to VFC malignancy or correlates with patient outcome.

The role of ECM and mechanical forces in tumor development, have predominantly been investigated in solid tumors arising from non-motile tissues such as the mammary gland, brain, and pancreas with a focus solely on the outcomes of increased rigidity. Recently, continuous dynamic mechanical challenge to the lung epithelium was shown to increase nuclear YAP in ventilated rat lungs<sup>25</sup> and cell stretching was shown to trigger changes in heterochromatin architecture and nuclear softening<sup>26</sup>. In contrast, the role of mechanical stimuli on cancer progression in mechanically active organs, which are under continuous biomechanical stress, has not been explored. Due to the unique biomechanical properties of the vocal fold, we sought to understand the role of cell-matrix- and cell-cell adhesion and their mechanical regulation in VFC. We predicted that vocal fold epithelial cell responses to dynamic mechanical vibration and stretching, akin to the situation in vivo, would deviate significantly from currently established principles of cell mechanobiology. Moreover, we set out to explore whether mechanical stimuli would be essential not only for phonation but for tissue homeostasis and whether restoration of mechanical stress in advanced mechanically fixed VFC, would reverse the oncogenic properties of these cells.

## Results

### Vocal fold cancer is associated with elevated gene expression of ECM components and stiffening of tissue.

Earlier studies have demonstrated that vocal fold trauma, such as scarring, can lead to fibronectin and collagen accumulation in the tissue<sup>3,27</sup>. Moreover, VFC progression causes vocal fold immobility as the squamous cell carcinoma invades the underlying muscle and tissues of the neck. VFC staging is based on the mobility status of the vocal folds and invasion of surrounding tissues; in T1-T2 the vocal folds move normally, whereas in T3-T4 mechanical fixation renders the vocal fold(s) immobile (**Fig.1a & b**). We aimed to investigate the ECM composition and stiffness of VFC tissue compared to normal tissue in patient samples. First, we analyzed head and neck cancer RNA-sequencing data generated by The Cancer Genome Atlas (TCGA) research<sup>28</sup>, focusing specifically on samples with patient reports mentioning involvement of the vocal fold tissue (glottic larynx). Considering the low number of T1 and T2 cancer samples (n=4), we pooled all cancer samples together. Normal (n=12) and cancer (T1-T4, n=54) samples were compared to determine differentially expressed genes; 2041 genes were upregulated and 1629 downregulated in cancer samples compared to normal tissue (false discovery rate, FDR < 0.05). Gene ontology (GO) enrichment analysis<sup>29,30</sup> revealed ECM and collagen-related GO-terms such as collagen-containing extracellular matrix, basement membrane and protein complex involved in cell adhesion, over-represented in the upregulated genes in cancer (**Fig.1c**). Conversely, over-represented GO-terms in the downregulated genes were linked to cell junctions and apical regions of the cell (**Fig.1d**). We further determined the genes encoding ECM and ECM-associated proteins in the data set using Matrisome AnalyzeR<sup>31,32</sup>. Strikingly, all differentially expressed collagens were upregulated including collagens I, III, IV and V that are abundant in the vocal folds<sup>33</sup> (**Fig.1e**). Among the 76 differentially expressed ECM glycoprotein genes, 53 were upregulated and 23 downregulated (**Fig.1f; Extended data Fig.1a**). The upregulated genes included fibronectin (FN) and laminin-332 chains (LAMA3, LAMB3 and LAMC2), which can function as autocrine tumor promoters in squamous cell carcinoma<sup>34</sup> through laminin-binding integrins  $\alpha 6\beta 4$  and  $\alpha 3\beta 1$ . Moreover, 59 ECM regulator genes were upregulated (**Fig.1g**) and 28 downregulated (**Extended data Fig.1b**). The upregulated lysyl oxidases (LOXs) (LOX, LOXL, LOX2, and LOXL3), which covalently crosslink collagens to elastin, and metalloproteinases (MMP14, MMP2, MMP10, MMP1, MMP7, MMP19, MMP9, MMP12, MMP11, MMP13, MMP3, MMP17, MMP16 and MMP8) collectively allude to extensive ECM remodeling and stiffening in the cancerous tissue compared to normal tissue.

To further investigate the changes in ECM composition on the cellular level, we compared T1 (UT-SCC-11; 58-year old male) and T3 (UT-SCC-103; 51-year old male) patient-derived VFC cell lines, generated at the University of Turku<sup>35-37</sup>, to non-cancerous (NC) (HaCaT) cells. Western blot analysis confirmed fibronectin upregulation in T3 cancer cells in comparison to NC cells and T1 cancer cells (**Extended data Fig.1c & d**). Several collagens were also upregulated in our RNA-sequencing analysis (**Extended data Fig.1e**). To investigate if the altered ECM production impacted tissue stiffness, we performed atomic force microscopy (AFM) on patient NC (n=3) and cancer (n=2) samples (obtained from vocal fold surgery). Measurements of the elastic modulus confirmed a 3.2-fold increase in stiffness in cancer tissue ( $2.441 \pm 1.479$  kPa) in comparison to normal tissue ( $0.751 \pm 0.341$  kPa) (**Fig. 1h & i**). Taken together, these results demonstrate ECM component over-expression and significant tissue stiffening in VFC.

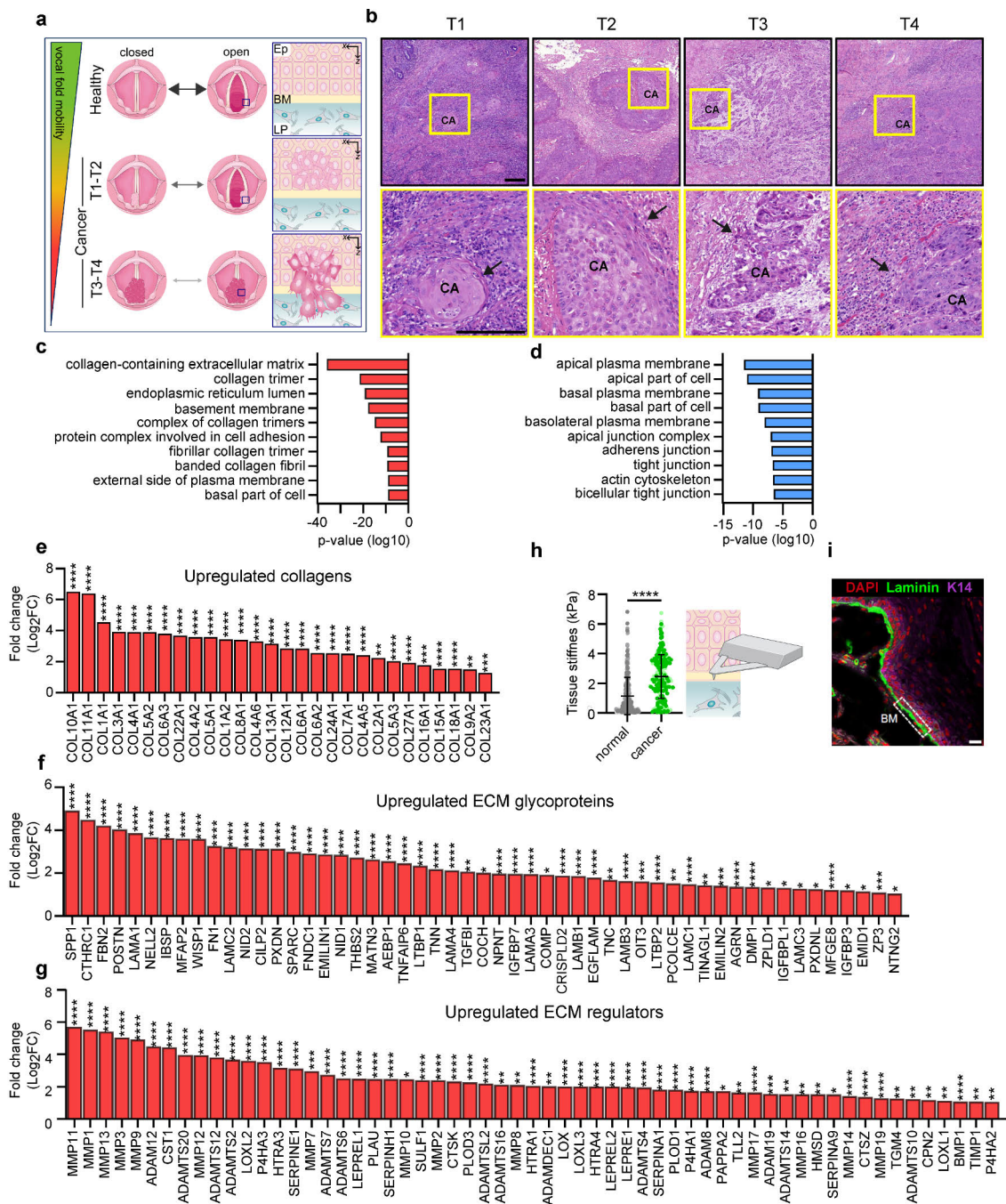


## Fig. 1. | Vocal fold cancer is associated with elevated gene expression of ECM components and stiffening of tissue

**a**, Schematic of changes in vocal fold mobility and invasion of transformed squamous cells through the basement membrane in VFC progression from T1 to T4. Ep= epithelium, BM= basement membrane, LP= lamina propria. **b**, Representative hematoxylin and eosin staining of T1-T4 vocal fold squamous cell carcinoma (CA) in patient tissue with arrows highlighting invasion. Scale bar 0.200 mm **c & d**, Over-represented GO-terms in upregulated (**c**) and downregulated (**d**) differentially expressed genes in VFC (T1-T4, n=54) compared to normal (n=12) patient tissue (TCGA-data, FDR < 0.001). **e-g**, Differentially upregulated (fold change, log<sub>2</sub>) collagens (**e**), ECM glycoproteins (**f**) and ECM regulators (**g**) in VFC (T1-T4,

n=54) compared to normal (n=12) patient tissue (TCGA-data, FDR < 0.05) annotated with Matrisome analyzer<sup>31</sup>. **h**, Tissue stiffness (Pa) of normal (n=3) and cancer (n=2) vocal fold patient tissue measured by AFM. **i**, Representative immunofluorescence staining (dapi, laminin, K14) of normal vocal fold tissue. Scale bar 30  $\mu$ m. Data are mean ( $\pm$  s.d.). FDR was used for assessment of statistical significance for differentially expressed genes and Mann-Whitney U-test for AFM measurements.

### **Expression and subcellular localization of laminin-binding integrins is altered in vocal fold cancer**

Guided by the differentially regulated genes identified in the TCGA-data associated with cell adhesion (**Fig. 1c**), we set out to explore the role of integrin adhesion complexes (IACs) in VFC. The patient data indicated upregulation of several genes encoding integrin adhesome proteins<sup>38,39</sup>, including an increase in laminin-binding integrins  $\alpha$ 3,  $\alpha$ 6 and  $\beta$ 4. Integrin- $\alpha$ 6 $\beta$ 4 heterodimer is found in hemidesmosomes whereas integrins  $\alpha$ 3 and  $\alpha$ 6 form dimers with integrin  $\beta$ 1 in focal contacts<sup>40,41</sup> (**Fig. 2a & b**). To determine whether these changes were recapitulated in the patient-derived cell lines, we used mass cytometry for high-dimensional phenotypic analysis of the cell-surface expression of 42 adhesion and signaling receptors, including 19 integrins, on a single-cell level. The NC cells had largely homogenous expression profiles, whereas the cancer cell lines showed a high degree of variation (**Extended data Fig.2a**). The integrins  $\alpha$ 6 and  $\beta$ 4 cell surface expression levels were heterogenous, ranging from high to very low, in cancer cells compared to NC cells based on mass cytometry analysis (**Fig. 2c; Extended data Fig.2b**) and confocal immunofluorescence imaging (**Fig. 2d**). Staining of  $\alpha$ 6 $\beta$ 4-associated hemidesmosome components BP180 (COLXVII) and keratin 14 reflected a similar heterogeneity and indicated a clear overall loss of hemidesmosomes and their associated intermediate filament cytoskeleton in the T3 cancer cells. Similar changes were also detected on bulk mRNA and protein levels of  $\alpha$ 6,  $\beta$ 4, BP180 and keratin 14 (**Extended data Fig.2c-e**). Cell-surface expression of integrins  $\alpha$ 3 and  $\beta$ 1 was also heterogeneous in cancer cells (**Fig. 2e**) and confocal immunofluorescence imaging demonstrated that this was linked to a striking difference in subcellular integrin localization rather than absolute changes in protein expression (**Fig. 2f**). Integrin  $\alpha$ 3 unexpectedly localized predominantly in cell-cell junctions in NC and T1 cells, whereas junctional localization was significantly decreased, and shifted to endosome-like intracellular structures in T3 cancer cells (**Fig. 2g**). The same was evident for the tetraspanin CD151, which interacts with  $\alpha$ 3 $\beta$ 1 integrin with high affinity, localizing to focal contacts and hemidesmosomes<sup>42,43</sup> (**Fig. 2h**). Furthermore, the cancer cells had an increased number of smaller vinculin-, active integrin  $\beta$ 1 (12G10)- and integrin-linked kinase (ILK)-positive cell-matrix adhesions compared to NC cells (**Fig. 2i & j; Extended data Fig.2g & h**). Intriguingly, in addition to junctional localization, integrin  $\alpha$ 3 also localized in cryptic lamellipodia, which regulate epithelial cell migration<sup>44</sup>, in NC and T1 cells (**Fig.2g**). These marked changes in laminin-binding integrins imply that cell-cell and cell-matrix adhesion are altered in VFC.

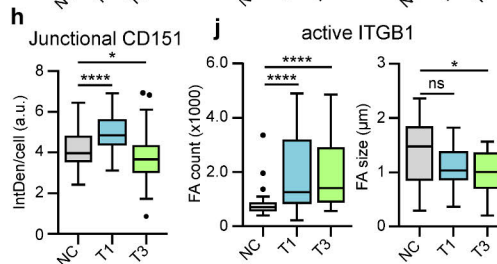
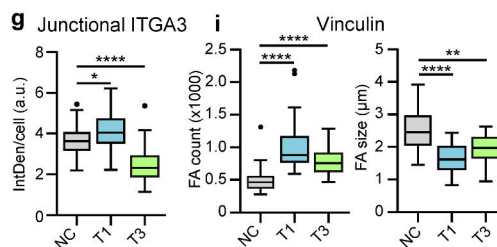
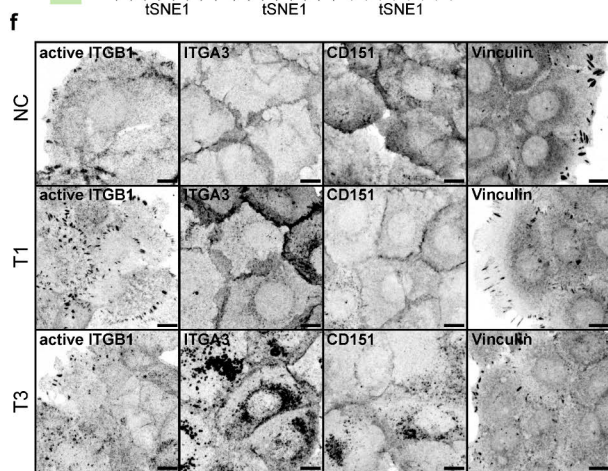
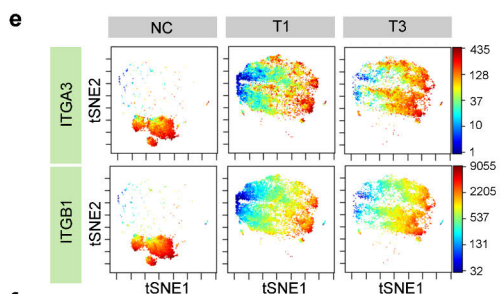
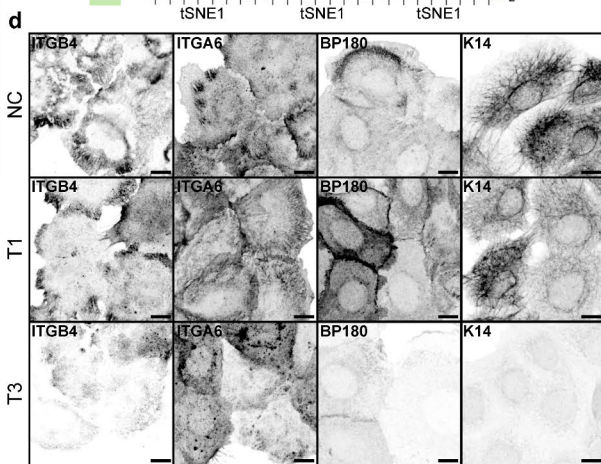
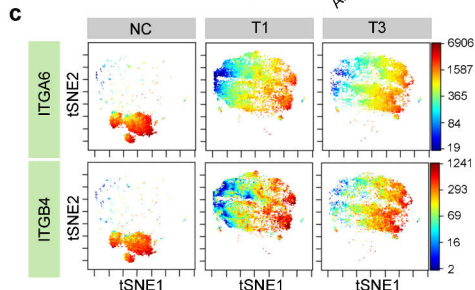
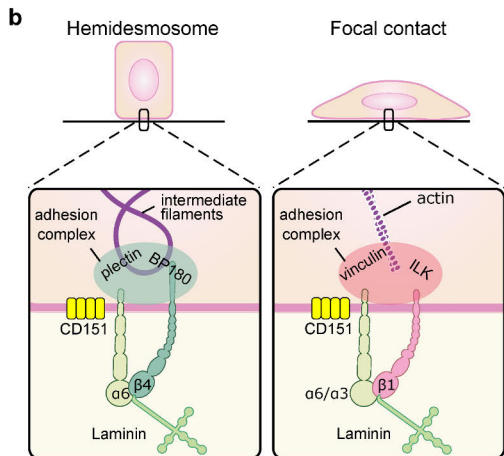
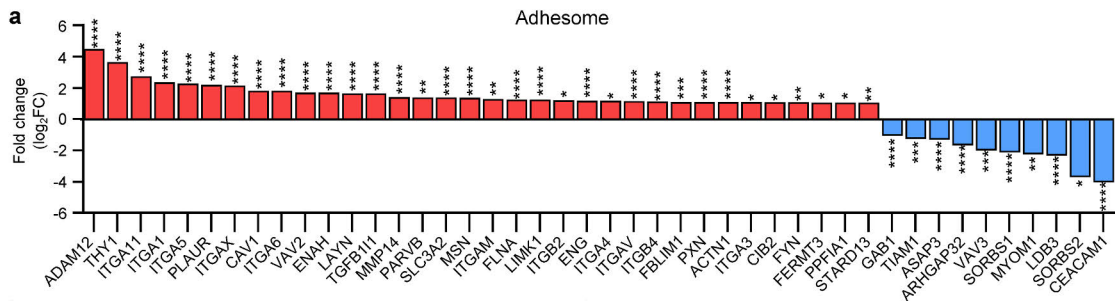




## Fig. 2. | Expression and subcellular localization of laminin-binding integrins is altered in vocal fold cancer

**a**, Differentially upregulated and downregulated (fold change, log<sub>2</sub>) adhesion<sup>38,39</sup> genes in VFC (T1-T4, n=54) compared to normal (n=12) patient tissue (TCGA-data, FDR < 0.05). **b**, Schematic of laminin-binding integrins in hemidesmosomes ( $\alpha6\beta4$ ) and focal contacts ( $\alpha6\beta1$  and  $\alpha3\beta1$ ) connecting epithelial cells to the keratin cytoskeleton via BP180 and plectin or actin cytoskeleton via ILK and vinculin. **c**, t-distributed stochastic neighbor embedding (t-SNE) visualization of ITGA6 and ITGB4 single-cell surface expression (MassCytof) in NC cells and vocal fold T1 and T3 cancer cells. **d**, Representative ITGA6, ITGB4, BP180 and K14 confocal immunofluorescence images of NC cells and VFC T1 and T3 cells (n=3). Scale bar 10  $\mu$ m. **e**, t-SNE visualization of ITGA3 and ITGB1 single-cell surface expression (MassCytof) in NC cells and vocal fold T1 and T3 cancer cells. **f**, Representative ITGA3, active ligand-engaged ITGB1 (12G10), CD151 and vinculin confocal immunofluorescence images of NC cells and vocal fold T1 and T3 cancer cells (n=3). Scale bar 10  $\mu$ m. **g & h**, Quantification of junctional ITGA3 (**g**) and CD151 (**h**) in NC (ITGA3 n=200, CD151 n=209) cells and vocal fold T1 (ITGA3 n=200, CD151 n=199) and T3 (ITGA3 n=199, CD151 n=205) cancer cells. **i & j**, Quantification of FA number (count) (left) and size (right) using vinculin (**i**) and active ITGB1 as markers in NC cells (vinculin n=29-30, ITGB1 n=28-30), and VFC T1 (vinculin n=30, ITGB1 n=30) and T3 (vinculin n=30, ITGB1 n=29-30) cells. Data are mean box plots or tukey mean-difference plots. n is the total number of cells/ average FA count/size per cell in field of view (FOV) pooled from three independent experiments. FDR was used to assess statistical significance of differentially expressed genes and Kruskal-Wallis test followed by post hoc Dunn's multiple comparisons test was used to assess statistical significance of junctional and FA proteins.

### Stiffening of vocal fold tissue supports increased cell proliferation, migration and invasion

As we detected an increase in patient tissue stiffness and ECM expression in cancer, we set out to determine whether changes in stiffness influence VFC cell proliferation. We monitored cell proliferation for 4 days on collagen I and fibronectin- or Matrigel- (mainly composed of laminin and collagen IV) coated hydrogels of varying stiffnesses (0.5 kPa, 25 kPa and 50 kPa) and on plastic. T3 cell proliferation on collagen I and fibronectin-coated plates was significantly higher than those of T1 cells. Both T1 and T3 cells proliferated better on stiffer matrices (**Fig. 3a-b; Videos 1-6**) with more active  $\beta1$ -integrin in adhesions and better cell spreading on stiff (**Extended data Fig.3d**). Similar data were obtained on Matrigel-coated plastic and hydrogels (**Extended data Fig.3a-c; Extended data Fig.3e; Videos 7-12**). As single cells, T3 cells demonstrated increased speed, accumulated distance and directionality compared to T1 cells on collagen I and fibronectin-coated 50 kPa hydrogels (**Fig. 3d & e**). Moreover, T3 collective cell migration (as a sheet in wound healing experiments) was significantly faster compared to T1 cells both on collagen I and fibronectin- (**Extended data Fig.3f-g**) and Matrigel-coated plastic plates (**Extended data Fig. 3h-i**). Accordingly, T3 cells invaded effectively through Matrigel transwell inserts (45h), whereas only a small number of T1 cells were able to invade (**Fig. 3f & g**). Taken together, these data indicate VFC proliferation and migration are positively regulated by increased ECM rigidity.

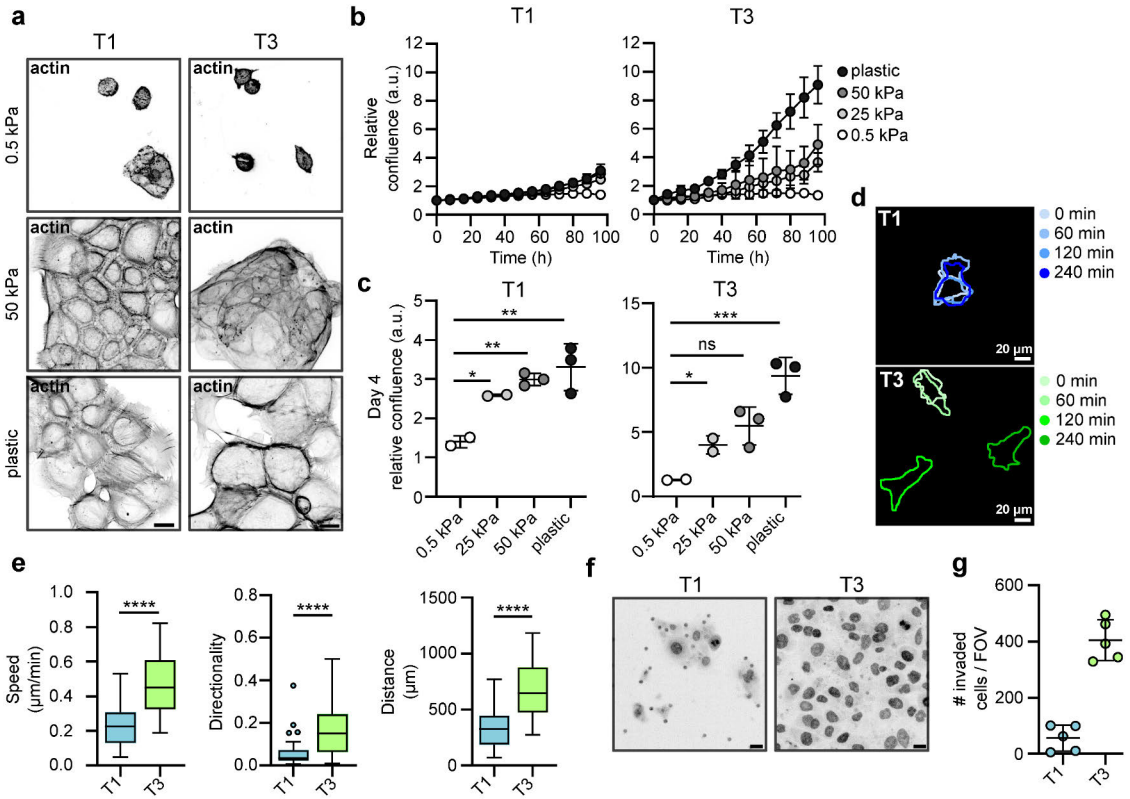


**Fig. 3. | Stiffening of vocal fold tissue supports increased cell proliferation, migration and invasion**

**a**, Representative actin confocal immunofluorescence images of T1 and T3 VFC cells on 0.5 and 50 kPa hydrogels and plastic coated with collagen I and fibronectin ( $n=3$ ). Scale bar 50  $\mu$ m. **b & c**, Proliferation (**b**) of T1 and T3 VFC cells on hydrogels of varying stiffnesses (0.5 kPa, 25 kPa, 50 kPa) and plastic and confluence at end-point (**c**). **d & e**, Representative outlines (**d**) of T1 and T3 VFC single-cell migration on 50 kPa hydrogels at different timepoints (0 min, 60 min, 120 min and 240 min) and quantification (**e**) of speed ( $\mu$ m/min), distance ( $\mu$ m) and directionality ( $n=2$ ). **f**, Representative nuclei (dapi) confocal immunofluorescence images (transwell pores visible in images as dots) and number of invaded T1 and T3 VFC cells per FOV in a Matrigel invasion assay (45h). Scale bar 20  $\mu$ m. ( $n=2$ ). Data are mean ( $\pm$  s.d.) or tukey box plots. Statistical significance was assessed using Kruskal-Wallis test followed by post hoc Dunn's multiple comparisons test or Mann-Whitney test.

### Inhibition of laminin-binding integrins modulates monolayer dynamics and disrupts cell clustering in 3D-spheroids

$\alpha 3 \beta 1$ -integrin localization to cell-cell junctions in normal squamous cells was reported more than two decades ago<sup>45</sup>. While the role of  $\alpha 3 \beta 1$ -integrin in mediating cell-matrix adhesion and controlling cell polarity in stratified epithelia is well-established in vitro and in vivo<sup>46</sup>, the functional role of this receptor in intercellular adhesion of epidermal squamous cells has been controversial and the molecular details remain elusive<sup>47</sup>. To explore the functional role of laminin-binding  $\beta 1$ -integrins in VFC, we treated cells with integrin  $\alpha 3$ - (P1B5),  $\alpha 6$ - (P5G10) and  $\beta 1$  (mAb13)-blocking antibodies. Live-cell imaging of sparse cell clusters revealed retraction of junctional and cell-edge lamellipodia with a concomitant slowing of cell movement in all cell lines, most notably NC cells, after dual inhibition of integrins  $\alpha 3$  and  $\alpha 6$  (**Videos 13-15**). Blocking E-cadherin had the opposite effect;

weakened cell-cell adhesions supported the scattering of cell colonies by reducing cell-cell coordination and increasing cell elongation and movement (**Videos 16-18**).

In a 3D-spheroid model, blocking the subunits of laminin-binding integrins; the common  $\beta 1$  subunit,  $\alpha 3$  alone or in combination with integrin  $\alpha 6$  all resulted in increased spheroid area primarily in NC and T1 cancer cells when compared to IgG control (**Fig. 4a & b**). The observed increase in size was due to reduced spheroid compaction and significantly more dissociated cells (**Extended data Fig.4a**). These data imply a functional role for integrins in the cell-cell junctions in NC and T1 cells (**Fig. 2f & g**). The T3 spheroids grew rapidly into large spheroids and integrin inhibition did not trigger marked spheroid dissociation, concordant with intracellularly localized integrins.

These data prompted us to investigate VFC cell-cell junctions in more detail. T3 cells exhibited straight junctions (E-cadherin and  $\beta$ -catenin immunofluorescence staining), indicative of less tensile adhesions, whereas NC and T1 cells had protrusive finger-like junctions, indicative of more tensile adhesions (**Fig. 4c**). To quantitatively capture these differences, we divided junctions into three categories (straight, reticular and finger-like) based on morphology. Most notably, while reticular adhesions were a prominent feature in all cells, there was a near absence of finger-like-junctions and a larger proportion of straight junctions in T3 cells compared to NC cells and T1 VFC cells (**Fig. 4c**). Overall, these data indicate that cell-cell junctions are altered in VFC cell lines and that integrins contribute to junctional dynamics in NC and T1 VFC.

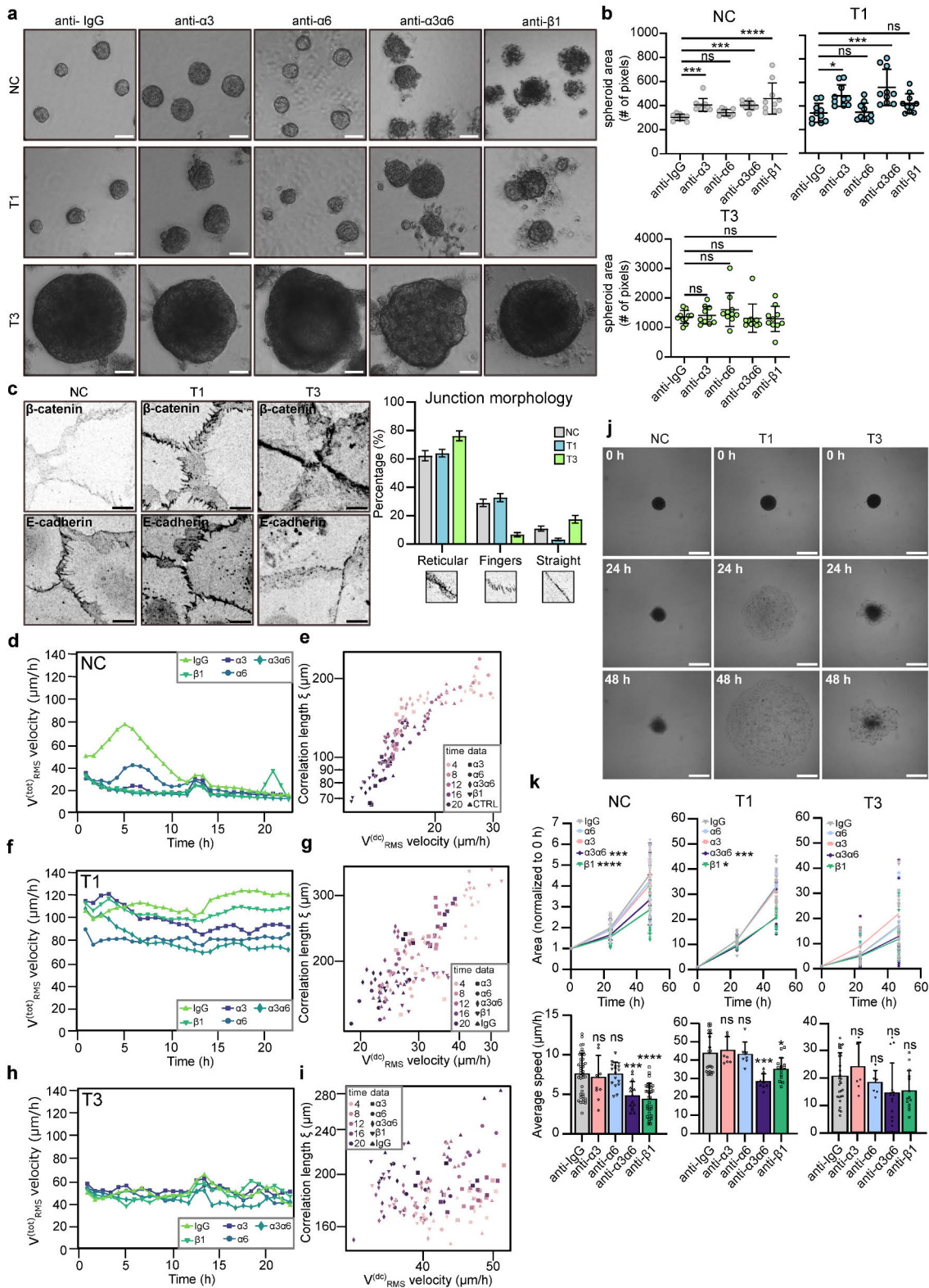


## Fig. 4. | Inhibition of laminin-binding integrins modulates monolayer dynamics and disrupts cell clustering in 3D-spheroids

**a & b**, Representative phase contrast images (**a**) and quantification (**b**) of spheroid size of NC cells and VFC T1 and T3 cells in 3D Matrigel cultures treated with IgG-control or integrin blocking antibodies (anti- $\alpha$ 3, anti- $\alpha$ 6, anti- $\alpha$ 3 $\alpha$ 6 and anti- $\beta$ 1) for 11 days ( $n=3$ ). Scale bar 50  $\mu$ m. **c**, Representative  $\beta$ -catenin and E-cadherin confocal immunofluorescence images and quantification of junction morphology of NC and VFC T1 and T3 cells ( $n=3$ ). Scale bar 10  $\mu$ m. **d-i**, Quantification of total RMS velocity (**d**) and correlation length of NC (**d & e**) and VFC T1 (**f & g**) and T3 (**h & i**) cells treated with IgG-control or integrin blocking antibodies (anti- $\alpha$ 3, anti- $\alpha$ 6, anti- $\alpha$ 3 $\alpha$ 6 and anti- $\beta$ 1) for 24h. **j & k**, Representative phase-contrast images (**j**) and normalized area and average speed ( $\mu$ m/h) (**k**) of NC and VFC T1 and T3 cells treated with IgG-control or integrin blocking antibodies (anti- $\alpha$ 3, anti- $\alpha$ 6, anti- $\alpha$ 3 $\alpha$ 6 and anti- $\beta$ 1) undergoing wetting ( $n=3$ ). Data are mean box plots ( $\pm$  s.d.). Statistical significance was assessed using Kruskal-Wallis test followed by post hoc Dunn's multiple comparisons test.

## VFC cells exhibit a previously unobserved solid-like flocking state ensuring long-range motility

Cell-cell and cell-matrix adhesions are critical determinants of the mechanics and dynamics of multicellular, normal and tumorigenic cell assemblies. At a critical cell density, motility of normal epithelia ceases and cells undergo a jamming phase transition (PT) which is considered a tumor-suppressive mechanism<sup>48,49</sup>, whereas PTs through unjamming and flocking motion, in turn, have been shown to promote collective modes of cancer invasion<sup>50-53</sup>. Thus, we next investigated monolayer dynamics of NC and VFC cells and the impact of integrin inhibition. PIV (Particle Image Velocimetry; see Materials and Methods for details) analysis revealed that untreated NC cells exhibited a progressive reduction in cell motility, quantified by the Root Mean Square velocity  $v_{RMS}^{tot}$ . (Fig. 4d). We also characterized the jamming transition by extracting the velocity correlation length  $\xi$  (expressing the size of a cluster of cells moving together), as well as the drift-corrected total RMS velocity  $v_{RMS}^{dc}(t)$  (**Fig. 4e; Video 19**), used to isolate the disordered velocity component, minimizing the effects of drifts. NC monolayers show for all treatments the expected behavior i.e. initially large  $\xi$  and RMS velocities that simultaneously decrease over time across the jamming transition<sup>54,55</sup>. Inhibiting  $\alpha$ 3 (P1B5),  $\alpha$ 6 (P5G10) and  $\beta$ 1 (mAb13) integrins significantly and robustly reduced the collective motion, resulting in an accelerated transition toward a jamming state, characterized by a progressive loss of degree of alignment in the cell velocity (**Extended data Fig.4b; Videos 20-23**).

Similar analyses were conducted on T1 and T3 cells. In both cases, the total RMS velocity (**Fig. 4f & h; Videos 24 & 29**) remained constant in time with values consistently larger than the final velocity for the NC cells. For T1 cells, inhibition of integrin  $\beta$ 1 or integrins  $\alpha$ 3 and  $\alpha$ 6 together, were most efficient in reducing the total RMS velocity, suggesting a relevant role for these integrins in collective cell motility. In contrast, T3 cell motility was insensitive to integrin inhibition. Plotting the velocity correlation length  $\xi$  vs the drift-corrected total RMS velocity,  $v_{RMS}^{dc}(t)$  (**Fig. 4g & i; Videos 25-28 & 30-33**) revealed a complete loss of correlation for T3 cells, and an intermediate behavior for T1 cells, suggesting that in both cases the tissues are far from a dynamically arrested, jammed state. Consistently, T1 VFC cells displayed cohesive and coordinated movement like bird flocking, with aligned cell velocities spanning the entire field of view (**Extended data Fig.4c**). Interestingly, these cells maintain long-range coordinated motion even when exposed to anti-integrin treatments. Similar flocking behavior was detected in the T3 cells, albeit to a lesser extent (**Extended data Fig.4d**). The absence of mutual cell rearrangements in VFC collective motility point to a mode of PT via a flocking solid transition, characterized by long-range coordinated motility in the absence of local cell rearrangements. Interestingly, flocking solid transition has been predicted by numerical simulation but has thus far not been observed experimentally in mammalian cells<sup>56,57</sup>. Collectively, our data

suggest that VFC cells exploit a solid flocking-state to enhance long-distance collective motion, possibly contributing to invasion and metastasis in the cancer setting<sup>58</sup>. However, this remains to be explored in future studies.

In keeping with this finding, we directly tested the ability of NC and VFC 3D spheroids to spread and diffuse onto ECM-coated substrate by undergoing a “wetting” transition<sup>59–63</sup>. This assay is thought to mimic the early step of local dissemination and depends on both the cohesive tensional state and viscoelastic properties of the cell aggregates and the cell-ECM interactions. Both T1 and T3 spheroids on FN-coated plates displayed a significant increase in wetting velocity compared to NC, but with a notable difference in morpho-dynamics. T1 spheroids rapidly wetted the surface, spreading with an elevated and uniform radial velocity consistent with the flocking solid mode of motion and elevated velocity correlation length  $\xi$  of the monolayer motility (**Fig.4j & k**). T3 spheroids, however, wetted the surface by extending irregular fronts, with protruding clusters and apparently contractile local regions, consistent with their high contractility and the reduced velocity correlation length  $\xi$  of the monolayer motility (**Fig.4j & k**). In NC spheroids, inhibition of  $\alpha 3$  (P1B5),  $\alpha 6$  (P5G10) and  $\beta 1$  (mAb13) integrins caused a notable reduction of wetting velocity. Conversely, only marginal effects on the wetting of both T1 and T3 spheroids were observed under these conditions (**Fig. 4j & k; Extended data Fig. 4e & f**), suggesting that VFC wetting was largely independent of cell-matrix adhesion receptors and likely dominated by the bulk mechanical properties of the 3D spheroids.

### **Mechanical stimuli induce cytoskeletal and junctional alterations and cell extrusion in VFC**

Prompted by the striking cell-intrinsic differences in the adhesive and mechanical properties observed between VFC and NC cells, we sought to determine if these alterations extended to the cellular response to mechanical stimuli. To recapitulate the mechanical forces in the vocal folds, we subjected the cells to two types of mechanical stimuli: stretching to mimic opening and closing of the vocal folds, and vibration, which occurs during phonation. Uniaxial cyclic stretching of cells (1Hz, 20% stretch) for 1 hour induced alignment (coherency) of the NC and T1 cancer cells perpendicularly to the stretch direction as exemplified by the visualization of actin filaments and phosphorylated myosin light chain (pMLC) (**Fig.5a & b, Extended data Fig.5a-b**). The poorly organized T3 cell monolayers did not show visible alignment, albeit their actin alignment (coherency) was significantly increased similarly as in NC and T1 cells (**Fig. 5b**). For the vibration, we chose a stimulus matching the frequency of human adult vocal fold during normal phonation<sup>64</sup> (50-250 Hz, 1 min off/on). This induced actin stress fibers (**Fig.5c**) and caused marked remodeling of the monolayer. Furthermore, continued vibration for 6 hours induced a significant increase in extrusion of highly contractile, pMLC-positive cells in the T3 VFC, but not in the NC or T1 cells (**Fig. 5e-g; Extended data Fig.5c**). This suggests that vocal fold-like mobility in the T3 cell layer induces extrusion of cells akin to ejection of cells from crowded epithelia as a mechanism to ensure epithelial homeostasis and epithelium integrity<sup>65</sup>.

Next, we investigated whether mechanical manipulation would cause changes in cell-cell junctions. Prior to stimulation, we noticed that  $\beta$ -catenin was significantly more nuclear in T1 and T3 cells compared to the NC cells (**Fig.5f-g**). This was particularly interesting, since nuclear  $\beta$ -catenin acts as a transcription factor activating signaling pathways that promote tumor formation<sup>66,67</sup>. Uniaxial cyclic stretching (1 hz, 20% stretch) for 1 hour caused alignment of  $\beta$ -catenin-positive junctions in NC and T1 cells (**Extended data Fig.5d**), and a significant reduction in nuclear and total  $\beta$ -catenin levels in the T1 and T3 cells (**Fig. 5h & i; Extended data Fig.5e**), which was also evident in vibrated cells (**Fig. 5j & k; Extended data Fig.5f**). Collectively, these data indicate that the cellular mechanoresponses under cyclic uniaxial stretch or vibration are different between NC and VFC

cells, and mechanical stimulation of T3 cells, which represent the mechanically immobile stage of VFC *in vivo*, triggers cell extrusion and downregulation of oncogenic nuclear  $\beta$ -catenin.

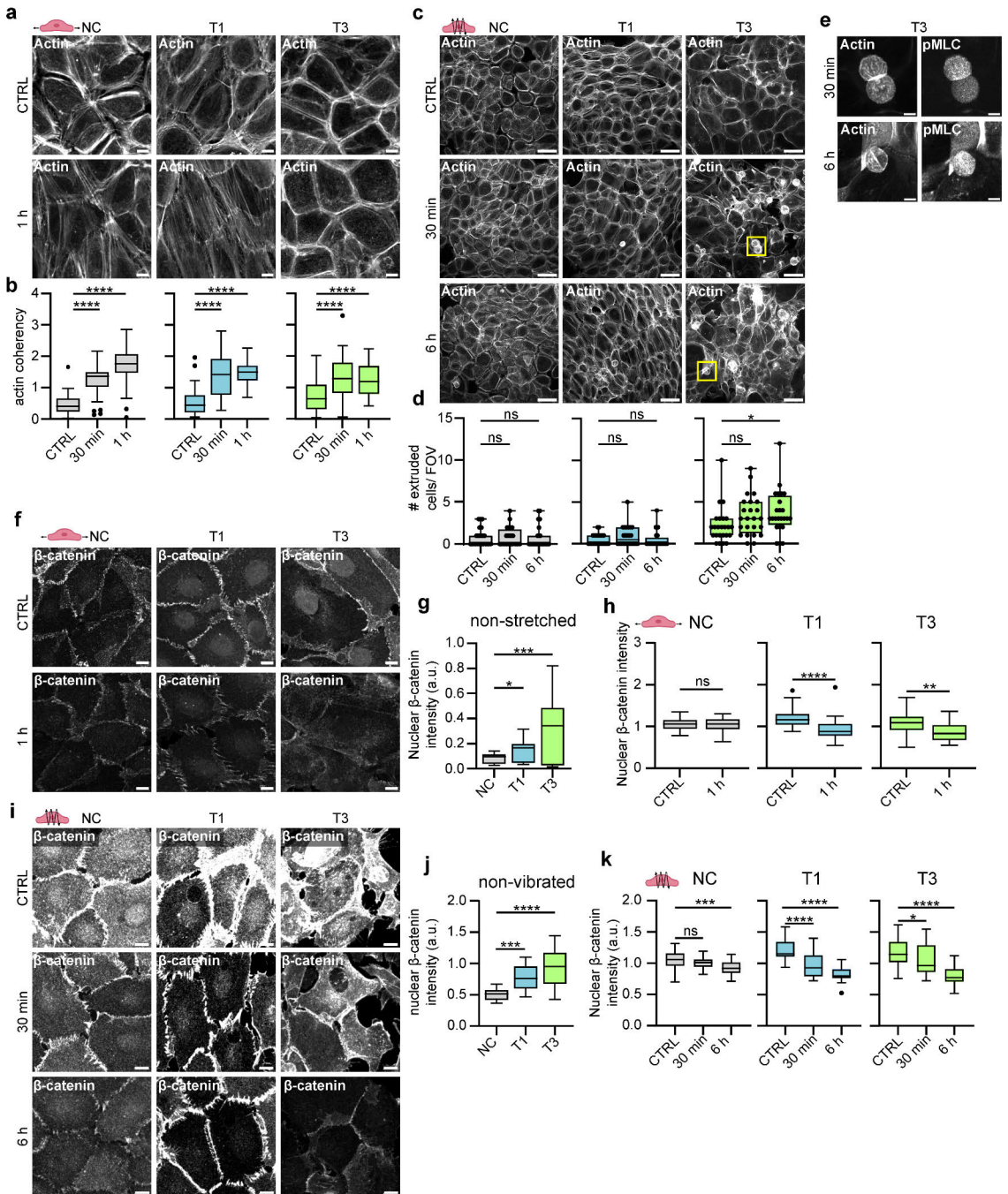


**Fig. 5. | Mechanical stimuli induce cytoskeletal and junctional alterations and cell extrusion in VFC**

**a**, Representative actin confocal immunofluorescence images of NC cells and VFC T1 and T3 cells subjected to stretching (n=3). Scale bar 10  $\mu$ m. **b**, Quantification of actin coherency (alignment) in stretched NC cells and vocal fold T1 and T3 cells (n=3). **c & d**, Representative actin confocal immunofluorescence images (c) and quantification of extruded (d) NC cells and VFC T1 and T3 cells subjected to vibration (n=3). Scale bar 50  $\mu$ m. **e**, Representative actin and pMLC confocal immunofluorescence images of extruded T3 VFC cells

subjected to vibration (n=3). Scale bar Scale bar 10  $\mu\text{m}$ . **f-h**, Representative  $\beta$ -catenin confocal immunofluorescence images (**f**) and quantification of nuclear expression (integrated density per number of nuclei in FOV) of NC cells and VFC T1 and T3 cells in non-stretched conditions (**g**) and subjected to stretching (**h**) (n=3). Scale bar 20  $\mu\text{m}$ . **i-k**, Representative  $\beta$ -catenin confocal immunofluorescence images (**i**) and quantification of nuclear expression (integrated density per number of nuclei in FOV) of NC cells and VFC T1 and T3 cells in non-vibrated conditions (**j**) and subjected to vibration (**k**) (n=3). Scale bar 20  $\mu\text{m}$ .

### **Phonometric mechanical stimuli decreases nuclear and total YAP levels**

In addition to  $\beta$ -catenin, another key mechanosensitive oncoprotein in cancer is Yes-associated protein (YAP), which shuttles between the cytoplasm and nucleus, where it can activate downstream signaling pathways that maintain oncogenic signaling cascades<sup>68</sup>. Total YAP RNA (**Fig.6a**) and protein (**Fig.6b-c**) expression levels showed no significant changes in VFC cell lines compared to NC cells, but RNA expression of YAP downstream targets Cysteine-rich angiogenic inducer 61 (CYR61), Ankyrin Repeat Domain 1 (ANKRD1), AXL and macrophage colony stimulating factor (CSF1) were increased in VFC cells (**Fig.6d**), suggesting elevated pathway activity. Importantly, similarly to  $\beta$ -catenin, vibration decreased total and nuclear YAP levels in a time-dependent manner with prolonged vibration (6 hours) having a more significant effect than the acute 30 min stimulation. Concordant with these kinetics, the effect on the nuclear to cytoplasmic ratio, which is under acute mechanical control in many cell types, was less prominent and not significant in the T3 cells (**Fig. 6e-g and Extended data Fig.6a**). These data imply that cell vibration primarily regulates YAP levels rather than YAP mechanoresponsive shuttling to the nucleus.

To further understand the role of YAP in squamous cell carcinoma, we surveyed YAP1 cancer dependency maps on DepMap<sup>69</sup>. A pan cancer search identifying the top 20 co-dependencies in the CRISPR DepMap Public 23Q2+Score Chronos dataset found the strongest dependency hits (Pearson's correlation,  $r$ ) with Rho Guanine Nucleotide Exchange Factor 7 (ARHGEF7,  $r=0.29$ ), TEA Domain Transcription Factor 3 (TEAD3,  $r=0.29$ ), TEA Domain Transcription Factor 1 (TEAD1,  $r=0.29$ ), Tankyrase 2 (TNKS2,  $r=0.28$ ) and Angiotenin-like protein 2 (AMOTL2,  $r=-0.28$ ) (**Fig.6h**). Moreover, integrin-linked kinase, which had increased FA localization in cancer cells, was one of the top 10 positive dependency hits (ILK,  $r=0.26$ ) (**Extended data Fig.2g & h**).

Intrigued by these findings we sought to investigate the relationship between YAP and AMOTL2 in our cell model. AMOTL2 is a negative YAP regulator and has been shown to directly interact with YAP, retaining it within the cytoplasm<sup>70-73</sup>. AMOTL2 RNA levels were not significantly different between the cell lines (**Fig.6i**). However, AMOTL2 protein levels were significantly lower in VFC cells compared to NC cells (**Fig.6 j & k**). Vibration significantly increased AMOTL2 total and nuclear levels in VFC cells (**Fig.6l-n; Extended data Fig.6b**), coinciding with the decreased YAP levels (**Fig. 6f-g**). In summary, these results suggest that mechanical stimulation may decrease oncogenic nuclear YAP levels through an AMOTL2-dependent regulatory mechanism and the findings further support the notion of vocal fold mechanics contributing to tissue homeostasis, and having anti-oncogenic effects in VFC.



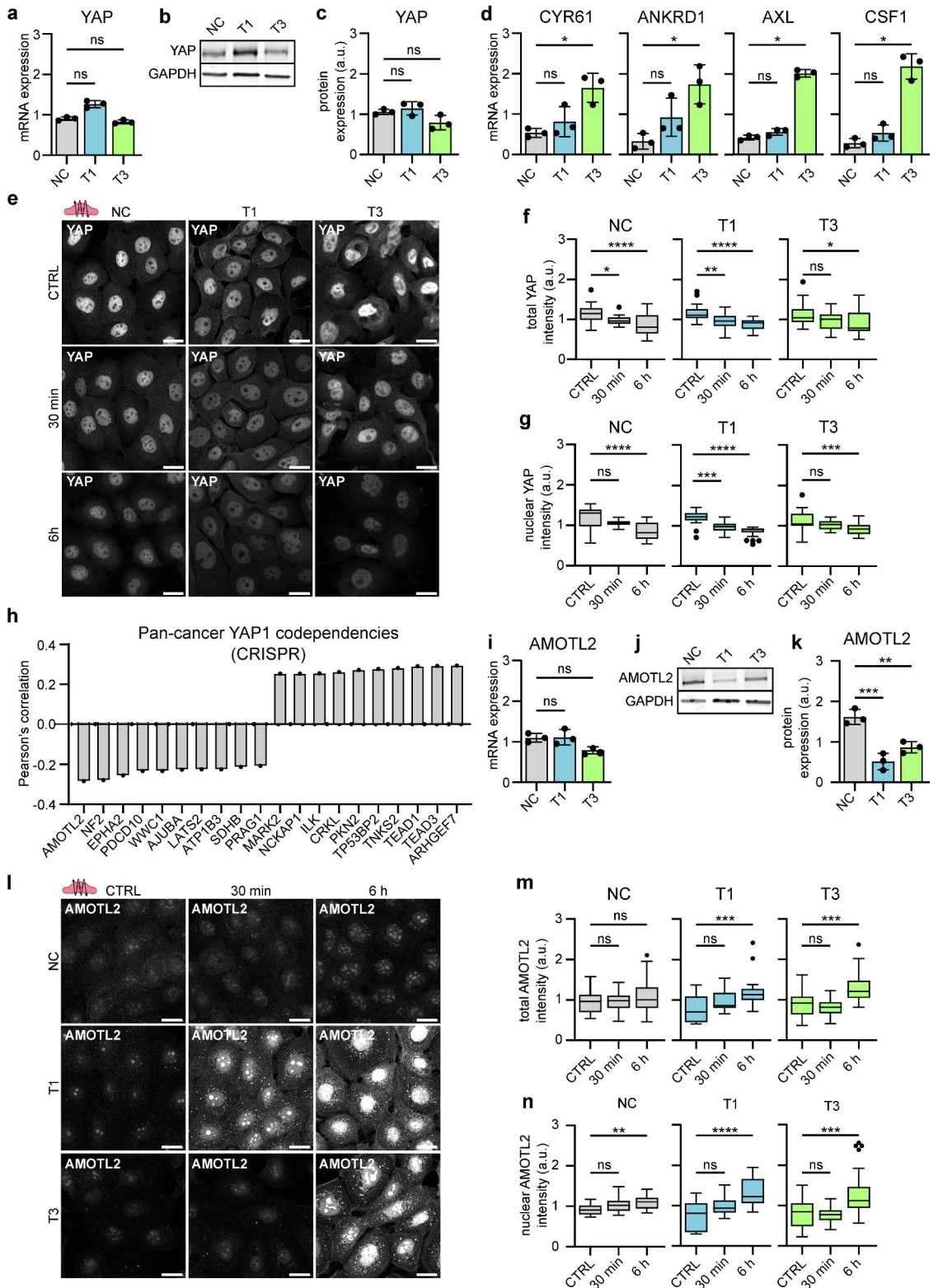


## Fig. 6. | Phonomimetic mechanical stimuli decreases nuclear and total YAP levels

**a**, Quantification of relative YAP mRNA expression (gene count) in NC cells and VFC T1 and T3 cells (n=3). **b & c**, Representative immunoblot (**b**) and quantification (**c**) of relative YAP protein expression in NC cells and VFC T1 and T3 cells (n=3). **d**, Quantification of relative RNA expression of YAP target genes CYR61, ANKRD1, AXL and CSF1 in NC cells and VFC T1 and T3 cells. **e**, Representative YAP confocal immunofluorescence images of NC cells and VFC T1 and T3 cells subjected to vibration (50-250 Hz, 1 min on/off) for 30 min or 6h compared to non-vibrated control (n=3). Scale bar 20  $\mu$ m. **f**, Quantification of total (**f**) and nuclear (**g**) YAP intensity (integrated density) in NC cells and VFC T1 and T3 cells subjected to vibration (50-250 Hz, 1 min on/off) for 30 min or 6h compared to non-vibrated control (n=3). **h**, Quantification of Pan cancer YAP1 CRISPR codependency (DepMap) as Pearson's correlation. **i**, Quantification of relative AMOTL2 mRNA expression (gene count) in NC cells and VFC T1 and T3 cells (n=3). **j & k**, Representative immunoblot (**j**) and quantification (**k**) of relative AMOTL2 protein expression in NC cells and VFC T1 and T3 cells (n=3). **l**, Representative AMOTL2 confocal immunofluorescence images of NC cells and VFC T1 and T3 cells subjected to vibration (50-250 Hz, 1 min on/off) for 30 min or 6h compared to non-vibrated control (n=3). Scale bar 20  $\mu$ m. **m & n**, Quantification of total (**m**) and nuclear (**n**) AMOTL2 intensity (integrated density) in NC cells and VFC T1 and T3 cells subjected to vibration (50-250 Hz, 1 min on/off) for 30 min or 6h compared to non-vibrated control (n=3). Data are illustrated as tukey box plots or mean box plots  $\pm$  s.d. (average of 8 FOV's pooled from three independent experiments). Ordinary one-way Anova followed by post hoc Dunnett's multiple comparisons test or Kruskal-Wallis test followed by post hoc Dunn's multiple comparisons test was used to assess statistical significance.

## High YAP levels correlate with high ECM expression and poor disease specific survival

To translate the in vitro findings into a more clinically relevant setting, we investigated the in vivo relevance of the identified mechanoregulators using multiplex histology and patient sample cohorts. We generated a custom laryngeal cancer tumor microarray (TMA) with cancer patient samples from T1 to T4 (n=218). We first noticed that there is a high correlation between all stromal ECM proteins (**Extended data Fig.7a**) and therefore implemented an ECM score, which considers median values for all the ECM and ECM-related proteins (FN, Col I, SMA, Laminin and Vinculin) in the tumor stroma across the patient cohort. Each patient was assigned an ECM score based on how many of the five ECM proteins were expressed at above-average levels, with scores ranging from 0 (all ECM proteins below average) to 5 (all ECM proteins above average). Scores of 0-2 were then classed as "ECM-low" while scores of 3-5 were classed as "ECM-high". The analysis revealed a significant correlation between ECM score and T-status, with lower ECM scores being associated with lower T-status (**Fig.7a; Extended data Fig.7b-d**), but no significant correlation with patient survival (**Extended data Fig.7f**).

To determine whether YAP expression correlates with T-status (**Extended data Fig.7g&h**) and ECM score (**Extended data Fig.7h&j**) we calculated the median per-patient epithelial YAP-value in the dataset, and classified samples as either YAP-high or YAP-low based on this threshold. We found that YAP-high tumors tended to have higher staging, and patient-level nuclear YAP levels increased with higher ECM scores in tumors (**Fig.7b-d**). Moreover, we observed high YAP expression in T3-4 samples and identified nuclear YAP alone as being predictive of disease-specific survival (**Fig.7e**). Having established that patients with high ECM scores in the stroma have higher nuclear YAP in their tumor and a worse clinical outcome, we set out to explore whether inhibition of YAP-TEAD would affect cell viability. Treating cells with a YAP-TAZ-TEAD inhibitor, K-975, that covalently binds to a palmitate-binding pocket of TEAD and inhibits YAP function<sup>74</sup>, resulted in a significant and dose-dependent decrease in cell viability with the T3 VFC cells showing the highest sensitivity to the drug (**Fig.7f &g**). Another YAP-TAZ-TEAD inhibitor, IK-930, which is in phase I clinical trials for advanced solid tumors<sup>75</sup> also showed increased sensitivity in VFC cells (**Fig.7h & i**). Taken together, these findings reveal clinical potential for YAP-TAZ-TEAD inhibition as a treatment option for VFC (**Fig.7j**).

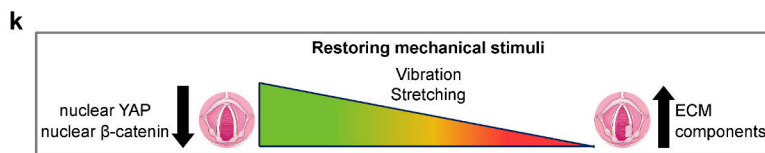
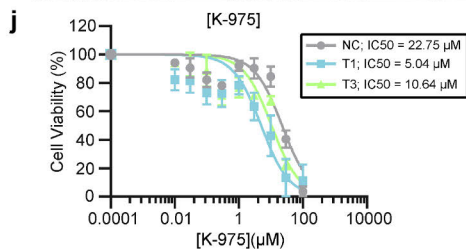
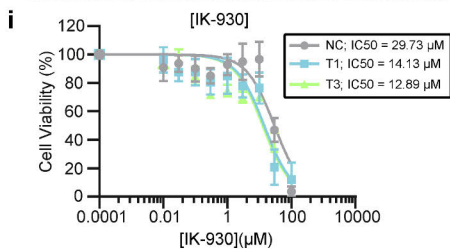
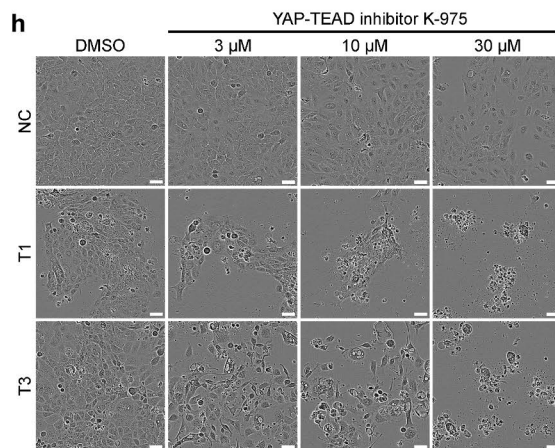
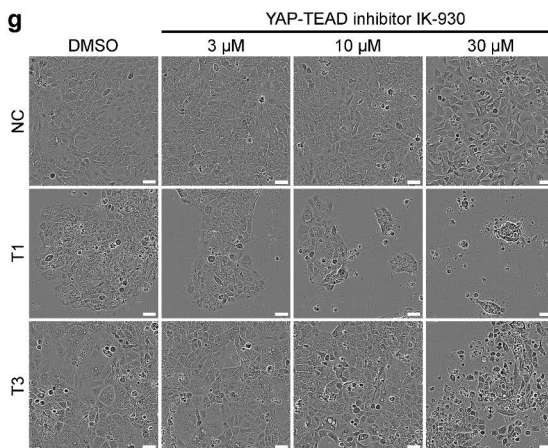
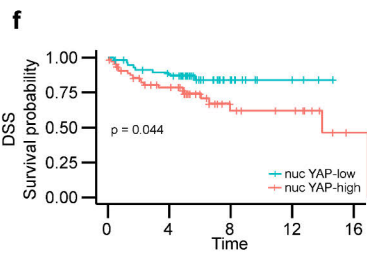
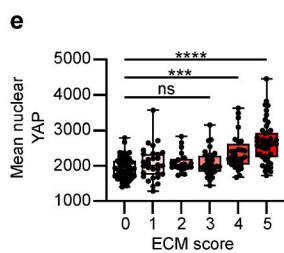
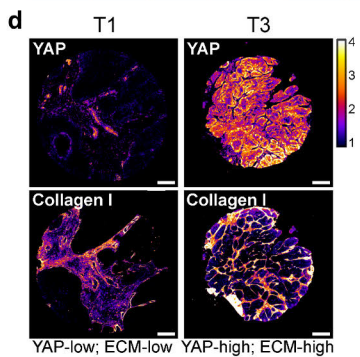
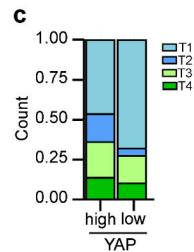
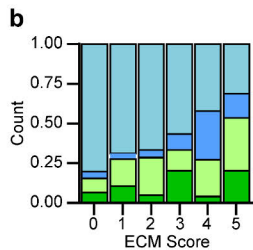
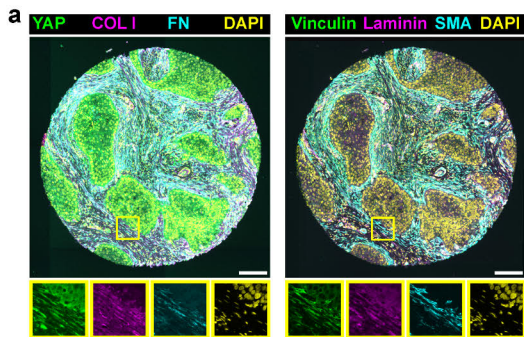


## Fig. 7. | High YAP levels correlate with high ECM expression and poor disease specific survival

**a**, Representative composite immunofluorescence images of TMA core stained for YAP/collagen-I/fibronectin/dapi or vinculin/laminin/SMA/dapi. Scale bar 100  $\mu\text{m}$ . **b**, Quantification of correlation between ECM-score (median patient-level expression of stromal fibronectin, collagen-I, SMA, laminin and vinculin) and T-status in TMA multiplex histology. **c**, Quantification of correlation between YAP-score (median patient-level expression of epithelial YAP) and T-status in TMA multiplex histology. **d**, Representative YAP and collagen I staining of T1 and T3 cancer cells in YAP-low & ECM-low sample and YAP-high and ECM-high sample. Scale bar 100  $\mu\text{m}$ . **e**, Quantification of correlation between ECM-score and mean nuclear YAP expression. **f**, Disease specific survival of YAP-high and YAP-low patients. **g & h**, Representative phase contrast images (**f**) and viability (**g**) of NC cells and vocal fold T1 and T3 cancer cells treated with YAP-TEAD inhibitor IK-930 for 48h. Scale bar 50  $\mu\text{m}$ . **i & j**, Representative phase contrast images (**i**) and viability (**j**) of NC cells and vocal fold T1 and T3 cancer cells treated with YAP-TEAD inhibitor K-975 for 48h. Scale bar 50  $\mu\text{m}$ . **k**, Graphical illustration of mechanical intervention of VFC cells as a therapeutic treatment option. Data are mean box plots ( $\pm$  s.d.). Statistical significance was assessed using Kruskal-Wallis test followed by post hoc Dunn's multiple comparisons test or with Log-rank test for Kaplan-Meier analysis.

## Outlook

Cells sense the biophysical features of their surrounding tissue, and the ensuing biomechanical signaling controls epithelial homeostasis, malignant progression, directed cell migration and drug sensitivity<sup>13,76–78</sup>. The vast majority of research in this area, however, draws from solid carcinomas arising from immobile tissue, such as the mammary gland, and the role of altered tissue mechanics in homeostasis and oncogenic properties of constantly moving epithelia remain poorly understood. Here we used cell culture models recapitulating key features of vocal fold epithelia including ECM rigidity, tissue stretching and vibration. We show that, concordant with the vocal fold epithelia becoming mechanically fixed and invasive with increasing T-status, VFC upregulates expression of multiple ECM components, is stiffer than normal vocal fold and proliferates in a stiffness dependent manner. Unlike kinetically arrested, densely packed (jammed) NC squamous epithelia, patient derived VFC cells are in a flocking, hyper-motile state, similar to the one previously established for invasive breast carcinomas<sup>49,51</sup> in line with their high invasive capacity.

Cell cycle re-entry of arrested epithelia is regulated by nuclear translocation and transcriptional activity of YAP and  $\beta$ -catenin<sup>79</sup>. Malignant HNSCC tissues have higher YAP1 expression in comparison to benign patient samples, and YAP1 activation drives oral SCC tumorigenesis and correlates with poor patient survival<sup>80–83</sup>. However, YAP and  $\beta$ -catenin have not been explored in the molecularly distinct VFC<sup>84</sup>. We find that mechanical stretch and vibration, mimicking normal-like vocal fold mobility, downregulates nuclear  $\beta$ -catenin and nuclear YAP levels with a concomitant induction of the YAP inhibitor AMOTL2 in VFC cells derived from increasingly immobile tumors<sup>85</sup>. Moreover, high YAP correlates with a high ECM signature and poor clinical outcome in patient samples and VFC cells are increasingly sensitive to clinically tested<sup>75</sup> YAP-TEAD small molecule inhibitors. Thus, normal tissue mechanics, mimicked in our cell culture systems by stretching and vibration, downregulate the activity of two relevant and synergistically acting oncogenic pathways<sup>79</sup>. These insights into the role of tissue mobility in maintaining homeostasis and suppression of malignancy may extend to other carcinomas arising from mobile epithelia and broaden our horizon on mechanical control of cancer progression.

## Material and methods

**The Cancer Genome Atlas (TCGA) data acquisition and analysis.** The Cancer Genome Atlas (TCGA) HNSCC dataset was retrieved and filtered for patient ID's with laryngeal cancer as tumor primary site. Pathology reports were then reviewed to assess tumor subsite and involvement of vocal folds. Raw files were downloaded from Xena browser (<https://xenabrowser.net/>). Differentially expressed genes were assessed using Bioconductor R package ROTS (v.1.14.0), defining genes with FDR < 0.05 as differentially expressed<sup>86</sup>. Gene ontology was performed using ClusterProfiler (v. 4.8.3) in R<sup>87</sup>.

**Patient samples.** Patient samples were obtained at the Department of Otorhinolaryngology-Head and Neck Surgery at Turku University Hospital under the Finnish Biobank Act with written informed consent from the sample donors (§279, 9/2001). Upon collection, the samples were given an arbitrary identifier and no patient identifiers, excluding patient age, and histopathological features of were available or recorded. Tissue samples were snap frozen with liquid nitrogen and stored at -80°C until further processing.

**Atomic force microscopy.** Atomic Force Microscopy (AFM) measurements of patient tissues were performed on freshly cut 16 µm snap frozen cryosections with JPK NanoWizard 4 (Bruker Nano) microscope mounted on an Eclipse Ti2 inverted fluorescent microscope (Nikon) and operated via JPK SPM Control Software v.6. Tissue sections were equilibrated in PBS with 1X protease inhibitors and measurements were performed within 30 minutes post thawing the sample. MLCT triangular silicon nitride cantilevers (Bruker) were used to assess basement membrane stiffness. Forces of up to 3 nN were applied at 20 micron per second constant cantilever velocity. All analyses were performed with JPK Data Processing Software v.6 (Bruker Nano) by first removing the offset from the baseline of raw force curves, then identifying the contact point and subtracting cantilever bending before fitting the Hertz model with correct tip geometry to quantify the Young's Modulus.

**Cell lines and culture.** HaCat (human immortalized squamous cells, ATCC), UT-SCC-11 (T1 human glottic laryngeal cancer, Turku University hospital), UT-SCC-103 (T3 human glottic laryngeal cancer, Turku University hospital) cells were cultured in DMEM (Dulbecco's modified Eagle's medium, Sigma-Aldrich) supplemented with 10% FBS (Sigma-Aldrich), 2 mM L-glutamine (Sigma-Aldrich) and 1% MEM nonessential amino acid solution (Sigma-Aldrich) at +37 °C, 5% CO<sub>2</sub>. UT-SCC-11 and UT-SCC-103 cell lines generated at Turku University Hospital have undergone scientific evaluation by Auria Biobank with a positive decision of release (AB22-7195) to be used in the study. All cell lines were regularly tested for mycoplasma with MycoAlert™ Mycoplasma Detection Kit (LT07-418, Lonza) and MycoAlert™ Assay Control Set (LT07-518, Lonza) to ensure mycoplasma-free culturing. Cells were washed with Phosphate-buffered saline (PBS) (Gibco™) and detached enzymatically with 0.25% trypsin-EDTA solution (L0932, Biowest).

**Proliferation assay.** Plastic (Corning) or Softwell® Easy Coat (Matrigen, stiffness range: 0.5 kPa, 25 kPa and 50 kPa) 24-well plates were coated with 10 µg/ml collagen I (C8919, Sigma) and 10 µg/ml fibronectin (341631, Sigma) diluted in PBS or 10 µg/ml growth factor reduced Matrigel (354230, Corning®) diluted in PBS, at +37 °C for 1 h. Coated plates were washed three times with PBS prior to seeding 10 000 cells in culture medium. Time-lapse live-imaging was performed using Incucyte S3® or ZOOM Live-Cell Analysis System for 96h with 2h imaging intervals (10x objective). Medium was changed every second day.

**Migration assay.** 50 kPa Softwell® Easy Coat (Matrigen) 24-well plates were coated with 10 µg/ml collagen I (C8919, Sigma) and 10 µg/ml fibronectin (341631, Sigma) diluted in PBS, at +37 °C for 1 h. Coated plates were washed three times with PBS prior to seeding 1000 cells in culture medium. Time-lapse live-imaging was performed using Nikon Eclipse Ti2-E (10x/ 0.3 objective) for 24h with 10 min imaging intervals. Single-cell tracking was performed using TrackMate plugin in FIJI (National Institutes of Health; NIH).

**Invasion assay.** 200 000 cells were seeded in serum free medium on Matrigel transwell inserts (354480, Corning) and placed in culture medium. After 45h of invasion, uninvaded cells in the inner well were wiped off with cotton buds and invaded cells were fixed with 4 % PFA diluted in PBS for 10 min at RT. Inserts were washed 3 times with PBS and stained overnight with Dapi. Invaded cells were assessed by confocal imaging (3i Marianas CSU-W1; 20×/0.8 objective) and quantifying the number of invaded cells per field of view (FIJI).

**Viability assay.** 5000 cells were per 96-plate well in culture medium. DMSO (D265, Sigma) or YAP-TAZ-TEAD inhibitors K-975 (HY-138565, MedChemExpress) or IK-930 (HY-153585, MedChemExpress) were added at 10 nM, 30 nM, 100 nM, 300 nM, 1µM, 3µM 10 µM, 30 µM and 100 µM concentrations the following day. Relative cell viability was measured as absorbance at 450 nm after a 2-hour incubation with a cell counting kit at +37°C as per the manufacturer's instructions (Cell Counting Kit 8, ab228554) 48 h after addition of inhibitor treatment.

**Western blotting.** Cells were kept on ice and washed with cold PBS and lysed with heated (+90 °C) TX- lysis buffer (50 mM Tris-HCl, pH 7.5, 150 mM NaCl, 0.5% Triton-X, 0.5% glycerol, 1% SDS, Complete protease inhibitor [SigmaAldrich], and phos-stop tablet [Sigma-Aldrich]). Lysed cells were scraped into an Eppendorf tube and boiled for 5 min at +90 °C followed by 10 min sonication and 10 min centrifugation at 13000 rpm at +4°C in a microcentrifuge. Protein concentrations were determined from the supernatant with DC Protein assay (Bio-Rad) as per the manufacturer's instructions. Samples were boiled at +90 °C for 5 min prior to protein separation using precast SDS-PAGE gradient gels (4–20% Mini-PROTEAN TGX, Bio-Rad) and transferred onto nitrocellulose membranes with the semi-dry Trans-Blot Turbo Transfer System (Bio-Rad). Membranes were blocked with AdvanceBlock-Fluor blocking solution (AH Diagnostics) diluted 1:1 in PBS for 1h at room temperature (RT) and incubated over night at +4°C with primary antibodies diluted in AdvanBlock-Fluor blocking solution. Membranes were washed for 5 min three times with TBST (Tris-buffered saline and 0.1% Tween 20) and incubated 1:2500 with fluorophore-conjugated Azure secondary antibodies (AH Diagnostics) in blocking solution for 1 h at RT. Membranes were washed three times with TBST for 5 min at RT. Membranes were scanned using an infrared imaging system (Azure Sapphire RGBNIR Biomolecular Imager) and band intensities were analyzed using Image Studio Lite (Licor) by normalizing the signal to GAPDH or HSP70, which were used as a loading controls.

**Particle-image velocity analysis (PIV).** A custom PIV algorithm was developed in Python to measure cell velocities within monolayers and derive different indicators of cellular motility. Velocity fields were first extracted by processing sequences of images. In short, each image is divided in square regions of interest (ROI), for each ROI located at position  $\vec{x}$  the local cell displacement  $\Delta\vec{r}$  is quantified by cross correlating the intensity of two ROI-images separated by  $\Delta t$ , which allows estimating the local velocity as  $\vec{v}_t(\vec{x}) = \frac{\Delta\vec{r}}{\Delta t}$ , where the index  $t$  corresponds to the time of the frame pair used to compute the velocity field. We used ROIs of size  $80 \times 80$  px<sup>2</sup>, which are slightly larger than the typically observed cell size of  $\sim 50$  px, with a spatial overlap factor between different ROIs of 50%. To improve statistics, we also performed a temporal average of the so-obtained velocity fields over chunks of length 20 frames (200 minutes), again with a temporal overlap of 50%. The previous parameters were carefully optimized to find the best tradeoff between increasing the spatiotemporal resolution and averaging a sufficient number of data samples to obtain smoother velocity maps, which will be indicated in the following with  $\vec{v}_t(\vec{x})$ . We then followed Garcia et al.<sup>55</sup> to compute the total root mean square (RMS) velocity  $v_{RMS}^{tot}(\mathbf{t}) = \sqrt{\langle |\vec{v}_t(\vec{x})|^2 \rangle_{\vec{x}}}$  and the drift corrected

RMS velocity  $v_{RMS}^{dc}(\mathbf{t}) = \sqrt{\langle |\vec{v}_t^{dc}(\vec{x})|^2 \rangle_{\vec{x}}}$  as spatial averages of the velocity fields, where we have introduced the drift collected velocity  $\vec{v}_t^{dc}(\vec{x}) = \vec{v}_t(\vec{x}) - \langle \vec{v}_t(\vec{x}) \rangle_{\vec{x}}$ . In cell lines with no strong collective motion,  $\vec{v}_t(\vec{x})$  and  $\vec{v}_t^{dc}(\vec{x})$  are similar, but in the presence of collective motion these two quantities can differ substantially. As suggested by Garcia et al.<sup>55</sup>, we used the drift-corrected velocity to calculate the radial velocity-velocity correlation function, obtained as

$$C_{vv}(\delta\mathbf{x}, \mathbf{t}) = \left\langle \frac{\langle \vec{v}_t^{dc}(\vec{x} + \delta\vec{x}) \cdot \vec{v}_t^{dc}(\vec{x}) \rangle_{\vec{x}}}{\langle |\vec{v}_t^{dc}(\vec{x})|^2 \rangle_{\vec{x}}} \right\rangle_{|\delta\vec{x}|=\delta x}$$

and we fitted this function to a model exponential  $e^{-\frac{\delta x}{\xi}}$  to extract the spatial correlation length  $\xi$  of the velocity field, quantifying the size of regions with similar velocities once the average monolayer velocity has been removed. Finally, to better visualize spatial correlations in the velocity field, we followed Malinverno et al.<sup>56</sup> and calculated the alignment index  $\mathbf{a}_t(\vec{x})$  as the cosine of the angle between the average velocity vector of a single velocity field with every other velocity vector.

**Cell stretching assay.** Stretch chambers (STB-CH-4W, STREX Cell Stretching Systems) were autoclaved and coated with 10µg/ml collagen I (C8919, Sigma) and 10µg/ml fibronectin (341631, Sigma) diluted in PBS at +37 °C for 2 h. Coated chambers were washed three times with PBS prior to seeding 200 000 cells per well in culture medium. Cells were stretched the following day with STREX cell stretching system (model # STB-140-10) with 20 % stretch (6.40mm), 1 Hz frequency for varying periods (5 min, 30 min 1 h).

**Cell vibration assay.** Flexible-bottomed silicone elastomer plates (BF-3001U, BioFlex®) were coated with 10µg/ml collagen I (C8919, Sigma) and 10µg/ml fibronectin (341631, Sigma) diluted in PBS for 2h at +37 °C. Coated chambers were washed three times with PBS prior to seeding 500 000-900 000 cells in culture medium. On the following day, stimulation sound files were played for varying periods (5 min, 30 min 1h, 6h) 1 min off /1 min on at a frequency range of 50-250 Hz with a phonomimetic bioreactor<sup>88</sup> connected to a Crown XLS 1502 amplifier.

**3D spheroid assay.** Spheroid formation in a 3D environment was assessed by embedding cells between two layers of Matrigel (Corning, 354230). Firstly, the bottom of an angiogenesis 96-well µ-plate (89646, Ibidi GmbH) was coated with 10 µl of 50% Matrigel diluted in culture medium and centrifuged at +4°C, 200 g for 20 min followed by 1-hour incubation at +37°C. Next, wells were filled with 20 µl of cell suspension in 25% Matrigel diluted in culture medium (500 cells/well), centrifuged for 10 min at 100 g and incubated at +37°C for 4h. Wells were filled with culture medium supplemented with 10 µg/ml function blocking antibodies or IgG control; mouse anti-IgG (31903, Invitrogen), mouse anti-human α3 integrin (P1B5, In-house hybridoma), mouse anti-human α6 integrin (P5G10, In-house hybridoma) and rat anti-human β1 integrin (mAb13, In-house hybridoma). Spheroid formation was imaged for 10 days with IncuCyte S3 Live-Cell Analysis system (10x objective). Culture medium was changed every 2-3 days. Analysis was performed using OrganoSeg software<sup>89</sup> and ImageJ.

**Wetting assay.** Cells were seeded in a low attachment round bottom 96-well plate to allow the formation of spheroids. The following day, spheroids were transferred to a multiwell plate previously coated with 10ug/ml Fibronectin (diluted in PBS, incubated overnight at +4°C, and washed twice with PBS). Spheroids were monitored as they wet the substrate by time lapse imaging for 48h using iXplore live Microscope (Olympus Evident) (4x Objective, 10 min timeframe). Analysis of spreading area over time was performed using ImageJ. The data were normalized to the area of the spheroid at time 0. To evaluate the impact of Integrin perturbations, spheroids were treated with the blocking antibodies described above before starting the wetting experiment.

**Immunostaining.** Coated (as previously mentioned) µ-slide 8-well chambered coverslips (Ibidi), standard culture plates (Corning) or Softwell® Easy Coat (Matrigen) were fixed at indicated endpoint with 4% PFA in culture medium for 10 min at RT. Cells were washed with PBS three times for 5 min. Permeabilization and blocking was performed using 0.3% Triton-X-100 in 10% normal horse serum diluted in PBS for 20 min at RT. Cells were stained with primary antibodies diluted in 10% normal horse serum overnight at 4°C. Cells were washed three times for 5 min with PBS and incubated with secondary antibodies diluted in PBS for 1h at RT, followed by three 5-min washes with PBS. Samples were either imaged right away or stored at 4°C covered from light until imaging.



**Imaging.** Confocal imaging was performed with a 3i spinning disk confocal (Marianas spinning disk imaging system with a Yokogawa CSU-W1 scanning unit on an inverted Carl Zeiss Axio Observer Z1 microscope, Intelligent Imaging Innovations, Inc., Denver, USA) with 10x Zeiss Plan-Apochromat objective (without immersion, 2mm working distance, 0.45 numerical aperture), 40x Zeiss LD C-Apochromat objective (water immersion, 0.62mm working distance, 1.1 numerical aperture) and 63x Zeiss Plan-Apochromat objective (oil immersion, 0.19 mm working distance, 1.4 numerical aperture). Widefield imaging was performed with Nikon Eclipse Ti2-E (Hamamatsu sCMOS Orca Flash4.0, Lumencor Spectra X LED excitation). Live imaging was performed with Incucyte S3 or ZOOM Live-Cell Analysis System.

**Mass Cytometry.** Cells were grown on a 10 cm plate to 90% confluence, washed once with PBS and detached with cell dissociation buffer (#13150-016, Gibco). Detached cells were dispensed into 15 ml falcon tubes, centrifuged at 300 x g for 5 min followed by removal of supernatant and mixing the pellet by pipetting. Cells were resuspended in 1 ml of serum free medium. 1 ml of 1 $\mu$ M cisplatin in serum free medium was added to cells for 5 min, mixed well by pipetting and incubated for 5 min at room temperature. The mixture was quenched with Cell Staining Buffer (Maxpar<sup>®</sup>), 5x vol of the stained cells. Cells were centrifuged at 300xg for 5 min, the supernatant aspirated and cells resuspended by pipetting. Cells were washed with 4 ml of Cell Staining Buffer (Maxpar<sup>®</sup>). Cells were counted and 3 million cells aliquoted into 5 ml polypropylene tube followed by centrifugation at 300xg for 5 min. The supernatant was aspirated and cells gently mixed by pipetting. Cells were resuspended in 50 ul of Cell Staining Buffer (Maxpar<sup>®</sup>). Cells were then stained with the antibody panel, starting with Fc-blocking. Fc Receptor Blocking Solution was added 1:100 to each tube and incubated 10 min at room temperature. 50 ul of the prepared antibody cocktail was added to each tube and gently mixed by pipetting and incubated at room temperature for 15 min. Samples were gently vortexed and incubated for an additional 15 min at room temperature. After a total of 30 min incubation, samples were washed by adding 2 ml Cell Staining Buffer (Maxpar<sup>®</sup>) to each tube, centrifuged at 300xg for 5 min and the supernatant was removed. Sample wash was repeated three times and cells were resuspended in residual volume by gently vortexing after final wash and aspiration. Cells were fixed with 1 ml of 1.6% FA diluted in PBS and gently vortexed before 10 min incubation at room temperature. Samples were centrifuged at 800x g for 5 min and the supernatant was removed. Samples were gently vortexed to resuspend in residual volume. After cell staining, 1 ml of cell intercalation solution was prepared for each sample by diluting Cell-ID Intercalator-103Rh 1:1000 into Fix and Perm Buffer (Maxpar<sup>®</sup>) and mixed by vortexing. 1 ml of intercalation solution was added to each tube and gently vortexed. Samples were incubated 1h at room temperature or left overnight at + 4°C (up to 48h). Before acquisition with Helios (WB Injector) cells were at 800 x g for 5 min and washed by adding 2 ml of Cell Staining Buffer (Maxpar<sup>®</sup>), followed by another round of centrifugation. The supernatant was removed and samples gently vortexed to resuspend cells in residual volume. Cells were washed by adding 2 ml of CAS to each tube and gently vortexed before counting and transferring 1 million cells into a new tube. Tubes were centrifuged at 800 x g for 5 min, followed by careful aspiration of supernatant. Cells were gently vortexed to resuspend in residual volume and finally 1 million cells were resuspended in 900 ul CAS. Cells were filtered into cell strainer cap tubes. Sufficient volume of 0.1X EQ beads to re-suspend all samples in the experiment were prepared by diluting 1-part beads to 9-parts CAS. Cells were left pelleted until ready to run on Helios. Immediately prior to data acquisition, cell concentration was adjusted to 1.0 x 10<sup>6</sup> cells/ml diluted EQ bead solution. Cells were filtered into cap tubes. Samples were run and data acquired with Helios CyTOF. Mass cytometry antibodies were either purchased from Fluidigm or self-conjugated.

Table1 list antibodies used for Mass Cytometry.

*Table 1.*

Metal tag	Target protein	Conjugation
106CD	a11 integrin	Self-conjugated
110CD	HER3	Self-conjugated
111CD	a3 integrin (CD49c)	Self-conjugated
112CD	EGFR	Self-conjugated
113CD	CD10	Self-conjugated
114CD	av integrin (CD51)	Self-conjugated
116CD	HER4	Self-conjugated
89Y	allb integrin (CD41)	3089004B
141PR	EpCAM (CD326)	3141006B
142ND	PETA-3 (CD151)	3142011B
143ND	N-Cadherin (CD325)	3143016B
144ND	Syndecan-4	Self-conjugated
145ND	Syndecan-1 (CD138)	3145003B
146ND	b3 integrin (CD61)	3146011B
147SM	ALCAM (CD166)	Self-conjugated
148ND	HER2 (ErbB2/EGFR2)	3148011A
149SM	CD34	3149013B
150ND	avb3 integrin (CD51/61)	3150026B
151EU	ICAM-2 (CD102)	3151015B
152SM	avb5 integrin	Self-conjugated
153EU	b6 integrin	Self-conjugated
154SM	Notch1	Self-conjugated
155GD	a8 integrin	Self-conjugated
156GD	b1 integrin (CD29)	3156007B
158GD	E-Cadherin (CD324)	3158018B
159TB	LAT1 (CD98)	3159022B
160GD	a5 integrin (CD49e)	3160015B
161DY	a2 integrin (CD49b)	3161012B
162DY	b7 integrin	3162026B
163DY	a1 integrin (CD49a)	3163015B
164DY	a6 integrin (CD49F)	3164006B
165HO	Notch2	3165026B
166ER	CD44	3166001B
167ER	Notch3	Self-conjugated
168ER	a9b1 integrin	3168013B
169TM	CD24	3169004B
170ER	ICAM-1 (CD54)	3170014B
171YB	CD9	3171009B
172YB	Neuropilin-1 (CD304)	Self-conjugated
173YB	b4 integrin (CD104)	3173008B

174YB	a4 integrin (CD49d)	3174018B
175LU	b8 integrin	Self-conjugated
176YB	NCAM (CD56)	3176001B
209BI	CD47	3209004B

**RNA-sequencing.** RNA was isolated from three biological replicates of cells seeded on coated BioFlex® plates. Cells were washed with cold PBS followed by RNA extraction using NucleoSpin RNA -kit (#740955.250, Macherey-Nagel) as per the manufacturer's instructions. Total RNA concentration was measured with Nanodrop and samples were normalized by diluting with RNase free water. Sample quality was verified using Agilent Bioanalyzer 2100, and final concentrations were measured using Qubit®/Quant-IT® Fluorometric Quantitation (Life Technologies). Illumina stranded total RNA prep library was prepared using 100 ng of RNA) as per the manufacturer's instructions (Illumina Stranded mRNA Preparation and Ligation kit, (Illumina) and sequenced with Novaseq 6000 (S4 instrument, v1.5 (Illumina), 2x50 bp, SP flow cell, 2 lanes (650-800 M reads). Library quality was verified using Advanced Analytical Fragment Analyzer. The sequencing data read quality was ensured using the FastQ (v.0.11.14) and MultiQC (v.1.5) tools<sup>90</sup>. Differentially expressed genes were assessed using Bioconductor R package ROTS (v.1.14.0) defining genes with FDR < 0.05 as differentially expressed.

**Tissue microarray (TMA).** TMA blocks with duplicate core biopsies were made from formalin-fixed, paraffin-embedded tissue samples using a TMA Grand Master (3DHISTECH, Budapest, Hungary) at Helsinki University hospital. A total of 218 patients with known TNM staging and survival endpoints were included in the study.

### Primary antibodies

Table 2: Details of primary antibodies used in the study. IF= immunofluorescence, MP= multiplex fluorescence immunohistochemistry, WB= western blot.

<b>Reagent</b>	<b>Dilution</b>	<b>Application</b>	<b>Supplier</b>	<b>Catalog number</b>
<i>4',6-Diamidino-2-Phenylindole, Dihydrochloride (DAPI)</i>	1:2000	IF	Life technologies	D1306
<i>Sir-Actin</i>	1: 1000	IF	Tebu-Bio	SC001
<i>Mouse anti-β1 integrin</i>	1:1000	WB	BD Biosciences	610468
<i>Mouse anti-α3 integrin (ASC-1)</i>	1:100	IF	Abcam	ab228425
<i>Rabbit anti-α3 integrin</i>	1:1000	MP	Abcam	ab131055
<i>Rabbit anti-α3 integrin</i>	1:1000	WB	Abcam	ab131055
<i>Mouse anti-β4 integrin</i>	1:100	IF, WB	Millipore	MAB1964
<i>Rat anti-β4 integrin</i>	1:100	MP	Abcam	ab95583
<i>Rat anti-α6 integrin (CD49f, cloneGoH3)</i>	1:100	IF	Serotec	MCA699
<i>Rat anti-α6 integrin</i>	1:500	MP	Novus	85747
<i>Rabbit anti-α6 integrin</i>	1:1000	WB	Abcam	ab97760
<i>Rabbit anti-β-catenin (E247)</i>	1:100	IF	Abcam	ab32572
<i>Mouse anti-β-catenin</i>	1:500	MP	Cell Marque	224M-14
<i>Mouse anti-CD151</i>	1:100	IF	Abcam	ab33315

<i>Rabbit anti-phospho-MLC 2 (Thr18/Ser19)</i>	1:100, 1:1000, 1:1000	IF, MP, WB	Cell Signaling Technology	3674
<i>Rabbit anti-COLXVII (EPR18614)</i>	1:100, 1:500, 1:1000	IF, MP, WB	Abcam	ab184996
<i>Mouse anti-vinculin</i>	1:100, 1:1000	IF, WB	Sigma	V9131
<i>Rat anti-Hsc70/Hsp73</i>	1:1000	WB	Enzo	ADI-SPA-815
<i>Guinea pig anti-keratin 14</i>	1: 100, 1:1000	IF, WB	Covance	PRB-155P
<i>Guinea pig anti-keratin 14</i>	1: 1000	MP	Progen	GP-CK14
<i>Mouse anti-pan cytokeratin</i>	1:150	MP	Abcam	ab7753
<i>Mouse anti-pan cytokeratin</i>	1: 100	MP	Invitrogen	MA5 13156
<i>Rabbit anti-Fibronectin</i>	1:1000, 1:1000	MP, WB	Sigma	F3648
<i>Rabbit anti-Collagen I</i>	1:1000	MP	Novus	NB600-408
<i>Rabbit anti-pan-laminin</i>	1:100	MP	Sigma	L9393
<i>Mouse anti-E-cadherin</i>	1:200	MP	BD Biosciences	610182
<i>Mouse anti-<math>\alpha</math>-SMA</i>	1:2000	MP	DAKO	M0851
<i>Rabbit anti-AMOTL2</i>	1:100, 1:1000	IF, WB	Proteintech	23351-1-AP
<i>Mouse anti-YAP</i>	1:100, 1:50	IF, MP	Santa Cruz	sc-101199

**Multiplexed fluorescent immunohistochemical staining and imaging.** Multiplexed fluorescent immunohistochemical staining and imaging was performed in three cycles as previously described<sup>91</sup> for two sets of seven to eight antibodies and the nuclear marker DAPI (Table 2), stained on two serial TMA sections. After the first-round staining and whole-slide imaging of the TMAs, the fluorescence signal was bleached, and the antibodies from the first-round staining were denatured, after which the second-round staining was performed. The process was repeated for the third round of staining. Imaging was performed using a Zeiss Axio Scan.Z1 slide scanner, with each round of staining recorded as an independent .CZI image file containing up to five fluorescent channels.

**Image analysis of multiplexed TMA datasets.** Images of individual TMA cores were extracted from the whole-slide images using the TMA dearrayer functionality in QuPath<sup>92</sup>. Images from the three staining rounds were registered using an affine image registration method operating through the pyStackReg Python dependency<sup>93</sup>, aligning the DAPI channels of the three staining rounds. Autofluorescent signal from red blood cells and other histology artefacts (e.g. wrinkled or folded tissue section areas) were removed using a pixel classifier in Ilastik<sup>94</sup>. Nuclei were segmented from the DAPI channel using a trained StarDist model<sup>95</sup>. The nuclear regions of interest (ROIs) were expanded by 6 pixels to generate extra-nuclear ROIs. Pan-epithelial staining was used to threshold cells into epithelial and stromal compartments. A custom python script was then used to calculate fluorescence intensity in all channels for the relevant nuclear or extra-nuclear ROI in the relevant tissue compartments. Finally, patient-level average expression values were calculated for all cells and all TMA cores originating from the same patient.

**Calculation of ECM and YAP scores.** For ECM scores, the median patient-level expression of stromal Fibronectin, Collagen-I, SMA, Laminin and Vinculin was determined across the full patient dataset. Next, each patient was assigned one point for each instance that the expression of each of the above markers was above the dataset median. The sum of all points was determined as that patient's ECM score. YAP scores were determined in the same way, with patients being assigned

into the “YAP-High” group if their mean nuclear YAP expression in the tumor epithelium fell above the dataset median. All other patients were assigned into the “YAP-Low” group.

**Survival analysis.** Kaplan-Meier analysis was used to compare survival outcomes between patient groups with different phenotypic signatures, with Log-rank test used to measure statistical significance.  $P \leq 0.05$  was used as a cut-off for statistical significance.

**Quantification and statistical analysis.** GraphPad Prism (version 9.3.1) was used for all statistical analyses. Outliers were identified with 0.1 % ROTS and distribution was determined with D'Agostino-Pearson normality test. Two-sample testing was performed using Student's t-test (unpaired, two-tailed) with Welch's correction (normally distributed data) or nonparametric Mann-Whitney U-test (non-normally distributed data). Multiple comparisons were performed using ANOVA with Holm-Sidak's post hoc test (normally distributed data) or Dunnett's post hoc test (non-normally distributed data). Data are presented as column graphs or dot plots (mean $\pm$ s.d.). P-values less than 0.05 were considered to be statistically significant.

**Data and material availability.** Data supporting the findings of this study are available within the paper and its supplementary information files.

### Acknowledgements

We thank J. Siivonen and P. Laasola for technical assistance and the Ivaska lab for scientific discussion. For services, instrumentation and expertise, we would like to thank the Cell Imaging and Cytometry Core (Turku Bioscience Centre, University of Turku) supported by Biocenter Finland, the Euro-BiImaging Finnish Node (Turku Finland), The Finnish Functional Genomics Centre supported by University of Turku, Åbo Akademi University and Biocenter Finland, The Medical Bioinformatics Centre of Turku Bioscience Centre supported by University of Turku, Åbo Akademi University, Biocenter Finland and Elixir-Finland, for the sequencing data analysis. FIMM Digital Microscopy and Molecular Pathology Unit supported by HiLIFE and Biocenter Finland for multiplex fluorescence immunohistochemistry and high-content imaging services. This study has been supported by Molecular Regulatory Networks of Life (R'Life) (330033 JI and SW), Finnish Cancer Institute (K. Albin Johansson Professorship, J.I.); a Research Council of Finland Centre of Excellence program (# 346131, J.I. and S.W.); the Cancer Foundation Finland (J.I.); the Sigrid Juselius Foundation (J.I.); the Research Council of Finland's Flagship InFLAMES (# 337530 & 357910) and the Jane and Aatos Erkko Foundation (J.I.). JK is supported by the University of Turku Doctoral Program for Molecular Medicine and the Finnish Cultural Foundation. MRC was supported by a Research Council of Finland postdoctoral research grant (# 343239). JRWC. was supported by the European Union's Horizon 2020 research and innovation programme under the Marie Skłodowska-Curie grant agreement [841973] and an Academy of Finland postdoctoral research grant (338585). HA is supported by a fellowship from Fondazione Umberto Veronesi. GF was supported by a Research Council of Finland postdoctoral research grant (332402) and a Turku Collegium for Science Medicine and Technologies postdoctoral fellowship. GS is supported by ERC-Synergy (Grant# 101071470), AIRC-IG (Grant#22821), AIRC 5x1000 (#22759), the Italian Ministry of University and Research (PRIN202223GSCIT\_01/G53D23002570006/20229RM8A\_001; COMBINE/G53D23007040001/P2022RH4HH002; PNRR\_CN3RNA\_SPOKE/G43C22001320007. YAM is supported by the Intramural Research Program of the NIH, National Institute of Diabetes and Digestive and Kidney Diseases (NIDDK).

## Author contributions

Conceptualization: JK, SW, JI. Methodology: JK, JI, RC, KP, SW. Formal Analysis: JK, KP, MRC, YAM, FB, HA, FK, JF, JRWC, GF. Investigation: JK, KP, YAM, HA, JH, KV, EP, MN. Visualization: JK, KP, HA, FK, HH. Resource: HI, SV, AM. Writing: JK, GC, RC, JI. Supervision: AM, HI, SV, GS, RC, SW, JI. Funding: JI.

## Competing interests

The authors declare no competing interests.

## References

1. Gray, S. D. CELLULAR PHYSIOLOGY OF THE VOCAL FOLDS. *Otolaryngol. Clin. North Am.* **33**, 679–697 (2000).
2. Sato, K., Umeno, H., Nakashima, T., Nonaka, S. & Harabuchi, Y. Histopathologic investigations of the unphonated human child vocal fold mucosa. *J. Voice* **26**, 37–43 (2012).
3. Hirschi, S. D., Gray, S. D. & Thibeault, S. L. Fibronectin: An interesting vocal fold protein. *J. Voice* **16**, 310–316 (2002).
4. Schultz, P. Vocal fold cancer. *Eur. Ann. Otorhinolaryngol. Head Neck Dis.* **128**, 301–308 (2011).
5. Levendoski, E. E., Leydon, C. & Thibeault, S. L. Vocal Fold Epithelial Barrier in Health and Injury: A Research Review. *J. Speech, Lang. Hear. Res.* **57**, 1679–1691 (2014).
6. Madruga de Melo, E. C. *et al.* Distribution of Collagen in the Lamina Propria of the Human Vocal Fold. *Laryngoscope* **113**, 2187–2191 (2003).
7. Hirano, M., Kurita, S., Matsuoka, H. & Tateishi, M. Vocal Fold Fixation in Laryngeal Carcinomas. *Acta Otolaryngol.* **111**, 449–454 (1991).
8. Winkler, J., Abisoye-Ogunniyan, A., Metcalf, K. J. & Werb, Z. Concepts of extracellular matrix remodelling in tumour progression and metastasis. *Nat. Commun.* **11**, 5120 (2020).
9. Mohan, V., Das, A. & Sagi, I. Emerging roles of ECM remodeling processes in cancer. *Semin. Cancer Biol.* **62**, 192–200 (2020).
10. Coban, B., Bergonzini, C., Zweemer, A. J. M. & Danen, E. H. J. Metastasis: crosstalk between tissue mechanics and tumour cell plasticity. *Br. J. Cancer* **124**, 49–57 (2021).
11. Hayward, M.-K., Muncie, J. M. & Weaver, V. M. Tissue mechanics in stem cell fate, development, and cancer. *Dev. Cell* **56**, 1833–1847 (2021).
12. Northey, J. J., Przybyla, L. & Weaver, V. M. Tissue Force Programs Cell Fate and Tumor Aggression. *Cancer Discov.* **7**, 1224–1237 (2017).
13. Paszek, M. J. *et al.* Tensional homeostasis and the malignant phenotype. *Cancer Cell* **8**, 241–54 (2005).
14. Chastney, M. R., Conway, J. R. W. & Ivaska, J. Integrin adhesion complexes. *Curr. Biol.* **31**, R536–R542 (2021).
15. Kanchanawong, P. & Calderwood, D. A. Organization, dynamics and mechanoregulation of integrin-mediated cell–ECM adhesions. *Nat. Rev. Mol. Cell Biol.* **24**, 142–161 (2023).
16. Kechagia, J. Z., Ivaska, J. & Roca-Cusachs, P. Integrins as biomechanical sensors of the microenvironment. *Nat. Rev. Mol. Cell Biol.* **20**, 457–473 (2019).

17. Sun, Z., Guo, S. S. & Fässler, R. Integrin-mediated mechanotransduction. *J. Cell Biol.* **215**, 445–456 (2016).
18. Dupont, S. *et al.* Role of YAP/TAZ in mechanotransduction. *Nature* **474**, 179–183 (2011).
19. Pocaterra, A., Romani, P. & Dupont, S. YAP/TAZ functions and their regulation at a glance. *J. Cell Sci.* **133**, (2020).
20. Low, B. C. *et al.* YAP/TAZ as mechanosensors and mechanotransducers in regulating organ size and tumor growth. *FEBS Lett.* **588**, 2663–70 (2014).
21. Piccolo, S., Panciera, T., Contessotto, P. & Cordenonsi, M. YAP/TAZ as master regulators in cancer: modulation, function and therapeutic approaches. *Nat. Cancer* **4**, 9–26 (2022).
22. Zanconato, F., Cordenonsi, M. & Piccolo, S. YAP/TAZ at the Roots of Cancer. *Cancer Cell* **29**, 783–803 (2016).
23. Nardone, G. *et al.* YAP regulates cell mechanics by controlling focal adhesion assembly. *Nat. Commun.* **8**, 15321 (2017).
24. Elbediwy, A. *et al.* Integrin signalling regulates YAP and TAZ to control skin homeostasis. *Dev.* **143**, 1674–1687 (2016).
25. Andreu, I. *et al.* The force loading rate drives cell mechanosensing through both reinforcement and cytoskeletal softening. *Nat. Commun.* **12**, 4229 (2021).
26. Nava, M. M. *et al.* Heterochromatin-Driven Nuclear Softening Protects the Genome against Mechanical Stress-Induced Damage. *Cell* **181**, 800-817.e22 (2020).
27. Hirano, S. *et al.* Histologic Characterization of Human Scarred Vocal Folds. *J. Voice* **23**, 399–407 (2009).
28. Weinstein, J. N. *et al.* The Cancer Genome Atlas Pan-Cancer analysis project. *Nat. Genet.* **45**, 1113–1120 (2013).
29. Ashburner, M. *et al.* Gene Ontology: tool for the unification of biology. *Nat. Genet.* **25**, 25–29 (2000).
30. Aleksander, S. A. *et al.* The Gene Ontology knowledgebase in 2023. *Genetics* **224**, (2023).
31. Petrov, P. B., Considine, J. M., Izzi, V. & Naba, A. Matrisome AnalyzeR – a suite of tools to annotate and quantify ECM molecules in big datasets across organisms. *J. Cell Sci.* **136**, jcs261255 (2023).
32. Shao, X., Taha, I. N., Clauser, K. R., Gao, Y. (Tom) & Naba, A. MatrisomeDB: the ECM-protein knowledge database. *Nucleic Acids Res.* **48**, D1136–D1144 (2020).
33. Tateya, T., Tateya, I. & Bless, D. M. Collagen Subtypes in Human Vocal Folds. *Ann. Otol. Rhinol. Laryngol.* **115**, 469–476 (2006).
34. Marinkovich, M. P. Laminin 332 in squamous-cell carcinoma. *Nat. Rev. Cancer* **7**, 370–380 (2007).
35. Krause, C. J. *et al.* Human Squamous Cell Carcinoma: Establishment and Characterization of New Permanent Cell Lines. *Arch. Otolaryngol. - Head Neck Surg.* **107**, 703–710 (1981).
36. Grenman, R. *et al.* Radiosensitivity of Head and Neck Cancer Cells In Vitro: A 96-Well Plate Clonogenic Cell Assay for Squamous Cell Carcinoma. *Arch. Otolaryngol. - Head Neck Surg.* **114**, 427–431 (1988).
37. Grénman, R. *et al.* In vitro radiation resistance among cell lines established from patients with squamous cell carcinoma of the head and neck. *Cancer* **67**, 2741–2747 (1991).

38. Winograd-Katz, S. E., Fässler, R., Geiger, B. & Legate, K. R. The integrin adhesome: from genes and proteins to human disease. *Nat. Rev. Mol. Cell Biol.* **15**, 273–288 (2014).
39. Horton, E. R. *et al.* Definition of a consensus integrin adhesome and its dynamics during adhesion complex assembly and disassembly. *Nat. Cell Biol.* **17**, 1577–1587 (2015).
40. Jones, J. C., Kurpakus, M. A., Cooper, H. M. & Quaranta, V. A function for the integrin alpha 6 beta 4 in the hemidesmosome. *Cell Regul.* **2**, 427–38 (1991).
41. Gehlsen, K. R., Dillner, L., Engvall, E. & Ruoslahti, E. The human laminin receptor is a member of the integrin family of cell adhesion receptors. *Science* **241**, 1228–9 (1988).
42. Sterk, L. M. T. *et al.* The Tetraspan Molecule Cd151, a Novel Constituent of Hemidesmosomes, Associates with the Integrin  $\alpha 6\beta 4$  and May Regulate the Spatial Organization of Hemidesmosomes. *J. Cell Biol.* **149**, 969–982 (2000).
43. Zevian, S. C. *et al.* CD151 promotes  $\alpha 3\beta 1$  integrin-dependent organization of carcinoma cell junctions and restrains collective cell invasion. *Cancer Biol. Ther.* **16**, 1626–40 (2015).
44. Ozawa, M. *et al.* Adherens junction regulates cryptic lamellipodia formation for epithelial cell migration. *J. Cell Biol.* **219**, (2020).
45. Larjava, H. *et al.* Novel function for  $\beta 1$  integrins in keratinocyte cell-cell interactions. *J. Cell Biol.* **110**, 803–815 (1990).
46. Marchisio, P. C., Bondanza, S., Cremona, O., Cancedda, R. & De Luca, M. Polarized expression of integrin receptors (alpha 6 beta 4, alpha 2 beta 1, alpha 3 beta 1, and alpha v beta 5) and their relationship with the cytoskeleton and basement membrane matrix in cultured human keratinocytes. *J. Cell Biol.* **112**, 761–73 (1991).
47. Tenchini, M. L. *et al.* Evidence against a major role for integrins in calcium-dependent intercellular adhesion of epidermal keratinocytes. *Cell Adhes. Commun.* **1**, 55–66 (1993).
48. Park, J. A., Atia, L., Mitchel, J. A., Fredberg, J. J. & Butler, J. P. Collective migration and cell jamming in asthma, cancer and development. *J. Cell Sci.* **129**, 3375–3383 (2016).
49. Oswald, L., Grosser, S., Smith, D. M. & Käs, J. A. Jamming transitions in cancer. *J. Phys. D. Appl. Phys.* **50**, (2017).
50. Iliina, O. *et al.* Cell-cell adhesion and 3D matrix confinement determine jamming transitions in breast cancer invasion. *Nat. Cell Biol.* **22**, 1103–1115 (2020).
51. Grosser, S. *et al.* Cell and Nucleus Shape as an Indicator of Tissue Fluidity in Carcinoma. *Phys. Rev. X* **11**, 011033 (2021).
52. Blauth, E., Kubitschke, H., Gottheil, P., Grosser, S. & Käs, J. A. Jamming in Embryogenesis and Cancer Progression. *Front. Phys.* **9**, (2021).
53. Palamidessi, A. *et al.* Unjamming overcomes kinetic and proliferation arrest in terminally differentiated cells and promotes collective motility of carcinoma. *Nat. Mater.* **18**, 1252–1263 (2019).
54. Angelini, T. E. *et al.* Glass-like dynamics of collective cell migration. *Proc. Natl. Acad. Sci. U. S. A.* **108**, 4714–4719 (2011).
55. Garcia, S. *et al.* Physics of active jamming during collective cellular motion in a monolayer. *Proc. Natl. Acad. Sci. U. S. A.* **112**, 15314–9 (2015).
56. Malinverno, C. *et al.* Endocytic reawakening of motility in jammed epithelia. *Nat. Mater.* **16**, 587–596 (2017).
57. Giavazzi, F. *et al.* Flocking transitions in confluent tissues. *Soft Matter* **14**, 3471–3477 (2018).



58. Nagai, T., Ishikawa, T., Minami, Y. & Nishita, M. Tactics of cancer invasion: solitary and collective invasion. *J. Biochem.* **167**, 347–355 (2020).
59. Gonzalez-Rodriguez, D. *et al.* Cellular Dewetting: Opening of Macroapertures in Endothelial Cells. *Phys. Rev. Lett.* **108**, 218105 (2012).
60. Pérez-González, C. *et al.* Active wetting of epithelial tissues. *Nat. Phys.* **15**, 79–88 (2019).
61. Beaune, G. *et al.* Spontaneous migration of cellular aggregates from giant keratocytes to running spheroids. *Proc. Natl. Acad. Sci. U. S. A.* **115**, 12926–12931 (2018).
62. Sackmann, E. & Bruinsma, R. F. Cell adhesion as wetting transition? *Chemphyschem* **3**, 262–9 (2002).
63. Douezana, S. & Brochard-Wyart, F. Dewetting of cellular monolayers. *Eur. Phys. J. E* **35**, (2012).
64. Cristina Oliveira, R., Gama, A. C. C. & Magalhães, M. D. C. Fundamental Voice Frequency: Acoustic, Electroglottographic, and Accelerometer Measurement in Individuals With and Without Vocal Alteration. *J. Voice* **35**, 174–180 (2021).
65. Eisenhoffer, G. T. *et al.* Crowding induces live cell extrusion to maintain homeostatic cell numbers in epithelia. *Nature* **484**, 546–549 (2012).
66. Xue, J. *et al.* Tumour suppressor TRIM33 targets nuclear  $\beta$ -catenin degradation. *Nat. Commun.* **6**, (2015).
67. Brabletz, T. *et al.* Nuclear overexpression of the oncoprotein  $\beta$ -Catenin in colorectal cancer is localized predominantly at the invasion front. *Pathol. Res. Pract.* **194**, 701–704 (1998).
68. Elosegui-Artola, A. *et al.* Force Triggers YAP Nuclear Entry by Regulating Transport across Nuclear Pores. *Cell* **171**, 1397-1410.e14 (2017).
69. Tsherniak, A. *et al.* Defining a Cancer Dependency Map. *Cell* **170**, 564-576.e16 (2017).
70. Zhao, B. *et al.* Angiomotin is a novel Hippo pathway component that inhibits YAP oncoprotein. *Genes Dev.* **25**, 51–63 (2011).
71. Wang, W., Huang, J. & Chen, J. Angiomotin-like proteins associate with and negatively regulate YAP1. *J. Biol. Chem.* **286**, 4364–4370 (2011).
72. Chan, S. W. *et al.* Hippo pathway-independent restriction of TAZ and YAP by angiomotin. *J. Biol. Chem.* **286**, 7018–7026 (2011).
73. Hildebrand, S. *et al.* The E-cadherin/AmotL2 complex organizes actin filaments required for epithelial hexagonal packing and blastocyst hatching. *Sci. Rep.* **7**, 9540 (2017).
74. Kaneda, A. *et al.* The novel potent TEAD inhibitor, K-975, inhibits YAP1/TAZ-TEAD protein-protein interactions and exerts an anti-tumor effect on malignant pleural mesothelioma. *Am. J. Cancer Res.* **10**, 4399–4415 (2020).
75. Tolcher, A. W. *et al.* A phase 1, first-in-human study of IK-930, an oral TEAD inhibitor targeting the Hippo pathway in subjects with advanced solid tumors. *J. Clin. Oncol.* **40**, TPS3168–TPS3168 (2022).
76. Hirata, E. *et al.* Intravital Imaging Reveals How BRAF Inhibition Generates Drug-Tolerant Microenvironments with High Integrin  $\beta$ 1/FAK Signaling. *Cancer Cell* **27**, 574–588 (2015).
77. Isomursu, A. *et al.* Directed cell migration towards softer environments. *Nat. Mater.* **21**, 1081–1090 (2022).
78. DuChez, B. J., Doyle, A. D., Dimitriadis, E. K. & Yamada, K. M. Durotaxis by Human Cancer Cells. *Biophys. J.* **116**, 670–683 (2019).

79. Benham-Pyle, B. W., Pruitt, B. L. & Nelson, W. J. Mechanical strain induces E-cadherin-dependent Yap1 and  $\beta$ -catenin activation to drive cell cycle entry. *Science* (80-. ). **348**, 1024–1027 (2015).
80. Omori, H. *et al.* YAP1 is a potent driver of the onset and progression of oral squamous cell carcinoma. *Sci. Adv.* **9**, 3324–3342 (2023).
81. Ge, L. *et al.* Yes-associated protein expression in head and neck squamous cell carcinoma nodal metastasis. *PLoS One* **6**, e27529 (2011).
82. Chen, N. *et al.* YAP1 maintains active chromatin state in head and neck squamous cell carcinomas that promotes tumorigenesis through cooperation with BRD4. *Cell Rep.* **39**, 110970 (2022).
83. Tsinias, G., Nikou, S., Mastronikolis, N., Bravou, V. & Papadaki, H. Expression and prognostic significance of YAP, TAZ, TEAD4 and p73 in human laryngeal cancer. *Histol. Histopathol.* **35**, 983–995 (2020).
84. Sorgini, A. *et al.* Analysis of the TCGA Dataset Reveals that Subsites of Laryngeal Squamous Cell Carcinoma Are Molecularly Distinct. *Cancers (Basel)*. **13**, 105 (2020).
85. Azzolin, L. *et al.* YAP/TAZ incorporation in the  $\beta$ -catenin destruction complex orchestrates the Wnt response. *Cell* **158**, 157–170 (2014).
86. Suomi, T., Seyednasrollah, F., Jaakkola, M. K., Faux, T. & Elo, L. L. ROTS: An R package for reproducibility-optimized statistical testing. *PLoS Comput. Biol.* **13**, e1005562 (2017).
87. Wu, T. *et al.* clusterProfiler 4.0: A universal enrichment tool for interpreting omics data. *Innov.* **2**, 100141 (2021).
88. Kirsch, A. *et al.* Development and validation of a novel phonomimetic bioreactor. *PLoS One* **14**, e0213788 (2019).
89. Borten, M. A., Bajikar, S. S., Sasaki, N., Clevers, H. & Janes, K. A. Automated brightfield morphometry of 3D organoid populations by OrganoSeg. *Sci. Rep.* **8**, 5319 (2018).
90. Ewels, P., Krueger, F., Käller, M. & Andrews, S. Cluster Flow: A user-friendly bioinformatics workflow tool. *F1000Research* **5**, 2824 (2016).
91. Blom, S. *et al.* Systems pathology by multiplexed immunohistochemistry and whole-slide digital image analysis. *Sci. Rep.* **7**, 15580 (2017).
92. Bankhead, P. *et al.* QuPath: Open source software for digital pathology image analysis. *Sci. Rep.* **7**, 16878 (2017).
93. Thevenaz, P., Ruttimann, U. E. & Unser, M. A pyramid approach to subpixel registration based on intensity. *IEEE Trans. Image Process.* **7**, 27–41 (1998).
94. Berg, S. *et al.* ilastik: interactive machine learning for (bio)image analysis. *Nat. Methods* **16**, 1226–1232 (2019).
95. Schmidt, U., Weigert, M., Broaddus, C. & Myers, G. Cell Detection with Star-Convex Polygons. in *Lecture Notes in Computer Science (including subseries Lecture Notes in Artificial Intelligence and Lecture Notes in Bioinformatics)* (eds. Frangi, A. F., Schnabel, J. A., Davatzikos, C., Alberola-López, C. & Fichtinger, G.) vol. 11071 LNCS 265–273 (Springer International Publishing, Cham, 2018).

# Extended Data information

## Restoring mechanophenotype reverts malignant properties of ECM-enriched vocal fold cancer

Jasmin Kaivola<sup>1</sup>, Karolina Punovuori<sup>2</sup>, Megan R. Chastney<sup>1</sup>, Yekaterina A. Miroshnikova<sup>2,3</sup>, Hind Abdo<sup>4</sup>, Fabien Bertillot<sup>2,5</sup>, Fabian Krautgasser<sup>6</sup>, Jasmin Di Franco<sup>6,7</sup>, James R.W. Conway<sup>1</sup>, Gautier Follain<sup>1</sup>, Jaana Hagström<sup>8,9,10</sup>, Antti Mäkitie<sup>12,13,14</sup>, Heikki Irjala<sup>15</sup>, Sami Ventelä<sup>1,15</sup>, Hellyeh Hamidi<sup>1</sup>, Giorgio Scita<sup>5,16</sup>, Roberto Cerbino<sup>6</sup>, Sara A. Wickström<sup>2,4,17,18</sup> and Johanna Ivaska<sup>1,19,20,21</sup> \*

Extended Data Figures and Figure Legends:

Extended Data Figure 1, Related to Figure 1.

Extended Data Figure 2, Related to Figure 2.

Extended Data Figure 3, Related to Figure 3.

Extended Data Figure 4, Related to Figure 4.

Extended Data Figure 5, Related to Figure 5.

Extended Data Figure 6, Related to Figure 6

Extended Data Figure 7, Related to Figure 7

### Extended data videos:

**Video 1:** T1 VFC cell proliferation (single cells) on 0.5 kPa Collagen-Fibronectin coated hydrogel. Imaged using Incucyte (ZOOM) every 2 hours for 116 hours, 10x magnification.

**Video 2:** T3 VFC cell proliferation (single cells) on 0.5 kPa Collagen-Fibronectin coated hydrogel. Imaged using Incucyte (ZOOM) every 2 hours for 116 hours, 10x magnification.

**Video 3:** T1 VFC cell proliferation (single cells) on 50 kPa Collagen-Fibronectin coated hydrogel. Imaged using Incucyte (ZOOM) every 2 hours for 116 hours, 10x magnification.

**Video 4:** T3 VFC cell proliferation (single cells) on 50 kPa Collagen-Fibronectin coated hydrogel. Imaged using Incucyte (ZOOM) every 2 hours for 116 hours, 10x magnification.

**Video 5:** T1 VFC cell proliferation (single cells) on Collagen-Fibronectin coated plastic. Imaged using Incucyte (ZOOM) every 2 hours for 116 hours, 10x magnification.

**Video 6:** T3 VFC cell proliferation (single cells) on Collagen-Fibronectin coated plastic. Imaged using Incucyte (ZOOM) every 2 hours for 116 hours, 10x magnification.

**Video 7:** T1 VFC cell proliferation (single cells) on 0.5 kPa Matrigel coated hydrogel. Imaged using Incucyte (ZOOM) every 2 hours for 116 hours, 10x magnification.

**Video 8:** T3 VFC cell proliferation (single cells) on 0.5 kPa Matrigel coated hydrogel. Imaged using Incucyte (ZOOM) every 2 hours for 116 hours, 10x magnification.

**Video 9:** T1 VFC cell proliferation (single cells) on 50 kPa Matrigel coated hydrogel. Imaged using Incucyte (ZOOM) every 2 hours for 116 hours, 10x magnification.

**Video 10:** T3 VFC cell proliferation (single cells) on 50 kPa Matrigel coated hydrogel. Imaged using Incucyte (ZOOM) every 2 hours for 116 hours, 10x magnification.

**Video 11:** T1 VFC cell proliferation (single cells) on Matrigel coated plastic. Imaged using Incucyte (ZOOM) every 2 hours 116 hours, 10x magnification.

**Video 12:** T3 VFC cell proliferation (single cells) on Matrigel coated plastic. Imaged using Incucyte (ZOOM) every 2 hours for 116 hours, 10x magnification.

**Video 13:** NC cell proliferation (colony) on Collagen-Fibronectin coated plastic. Growth medium supplemented with anti- $\alpha 3\alpha 6$  antibody (P1B5 and P5G10, 10  $\mu\text{g/ml}$ ) at 17h. Imaged using Incucyte (S3) every 60 minutes for 23 hours, 20x magnification.

**Video 14:** T1 VFC cell proliferation (colony) on Collagen-Fibronectin coated plastic. Growth medium supplemented with anti- $\alpha 3\alpha 6$  antibody ((P1B5 and P5G10, 10  $\mu\text{g/ml}$ ) at 17h. Imaged using Incucyte (S3) every 60 minutes for 23 hours, 20x magnification.

**Video 15:** T3 VFC cell proliferation (colony) on Collagen-Fibronectin coated plastic. Growth medium supplemented with anti- $\alpha 3\alpha 6$  antibody (P1B5 and P5G10, 10  $\mu\text{g/ml}$ ) at 17h. Imaged using Incucyte (S3) every 60 minutes for 23 hours, 20x magnification.

**Video 16:** NC cell proliferation (colony) on Collagen-Fibronectin coated plastic. Growth medium supplemented with anti-E-cadherin antibody (DECMA-1) at 17h. Imaged using Incucyte (S3) every 60 minutes for 23 hours, 20x magnification.

**Video 17:** T1 VFC cell proliferation (colony) on Collagen-Fibronectin coated plastic. Growth medium supplemented with anti-E-cadherin antibody (DECMA-1) at 17h. Imaged using Incucyte (S3) every 60 minutes for 23 hours, 20x magnification.

**Video 18:** T3 VFC cell proliferation (colony) on Collagen-Fibronectin coated plastic. Growth medium supplemented with anti-E-cadherin antibody (DECMA-1) at 17h. Imaged using Incucyte (S3) every 60 minutes for 23 hours, 20x magnification.

**Video 19:** NC cell proliferation (monolayer) on Collagen-Fibronectin coated plastic. Growth medium supplemented with anti-IgG antibody (10  $\mu\text{g/ml}$ ). Imaged using Incucyte (S3) every 10 minutes for 24 hours, 20x magnification.

**Video 20:** NC cell proliferation (monolayer) on Collagen-Fibronectin coated plastic. Growth medium supplemented with anti- $\alpha 3$  integrin antibody (P1B5, 10  $\mu\text{g/ml}$ ). Imaged using Incucyte (S3) every 10 minutes for 24 hours, 20x magnification.

**Video 21:** NC cell proliferation (monolayer) on Collagen-Fibronectin coated plastic. Growth medium supplemented with anti- $\alpha 6$  integrin antibody (P5G10, 10  $\mu\text{g/ml}$ ). Imaged using Incucyte (S3) every 10 minutes for 24 hours, 20x magnification.

**Video 22:** NC cell proliferation (monolayer) on Collagen-Fibronectin coated plastic. Growth medium supplemented with anti- $\alpha 3\alpha 6$  integrin antibody (P1B5 and P5G10, 10  $\mu\text{g/ml}$ ). Imaged using Incucyte (S3) every 10 minutes for 24 hours, 20x magnification.

**Video 23:** NC cell proliferation (monolayer) on Collagen-Fibronectin coated plastic. Growth medium supplemented with anti- $\beta 1$  integrin antibody (mAb13, 10  $\mu\text{g/ml}$ ). Imaged using Incucyte (S3) every 10 minutes for 24 hours, 20x magnification.

**Video 24:** T1 VFC cell proliferation (monolayer) on Collagen-Fibronectin coated plastic. Growth medium supplemented with anti-IgG antibody (10  $\mu\text{g/ml}$ ). Imaged using Incucyte (S3) every 10 minutes for 24 hours, 20x magnification.

**Video 25:** T1 VFC cell proliferation (monolayer) on Collagen-Fibronectin coated plastic. Growth medium supplemented with anti- $\alpha 3$  integrin antibody (P1B5, 10  $\mu\text{g/ml}$ ). Imaged using Incucyte (S3) every 10 minutes for 24 hours, 20x magnification.

**Video 26:** T1 VFC cell proliferation (monolayer) on Collagen-Fibronectin coated plastic. Growth medium supplemented with anti- $\alpha 6$  integrin antibody (P5G10, 10  $\mu\text{g/ml}$ ). Imaged using Incucyte (S3) every 10 minutes for 24 hours, 20x magnification.

**Video 27:** T1 VFC cell proliferation (monolayer) on Collagen-Fibronectin coated plastic. Growth medium supplemented with anti- $\alpha 3\alpha 6$  integrin antibody (P1B5 and P5G10, 10  $\mu\text{g/ml}$ ). Imaged using Incucyte (S3) every 10 minutes for 24 hours, 20x magnification.

**Video 28:** T1 VFC cell proliferation (monolayer) on Collagen-Fibronectin coated plastic. Growth medium supplemented with anti- $\beta 1$  integrin antibody (mAb13, 10  $\mu\text{g/ml}$ ). Imaged using Incucyte (S3) every 10 minutes for 24 hours, 20x magnification.

**Video 29:** T3 VFC cell proliferation (monolayer) on Collagen-Fibronectin coated plastic. Growth medium supplemented with anti-IgG antibody (10  $\mu\text{g/ml}$ ). Imaged using Incucyte (S3) every 10 minutes for 24 hours, 20x magnification.

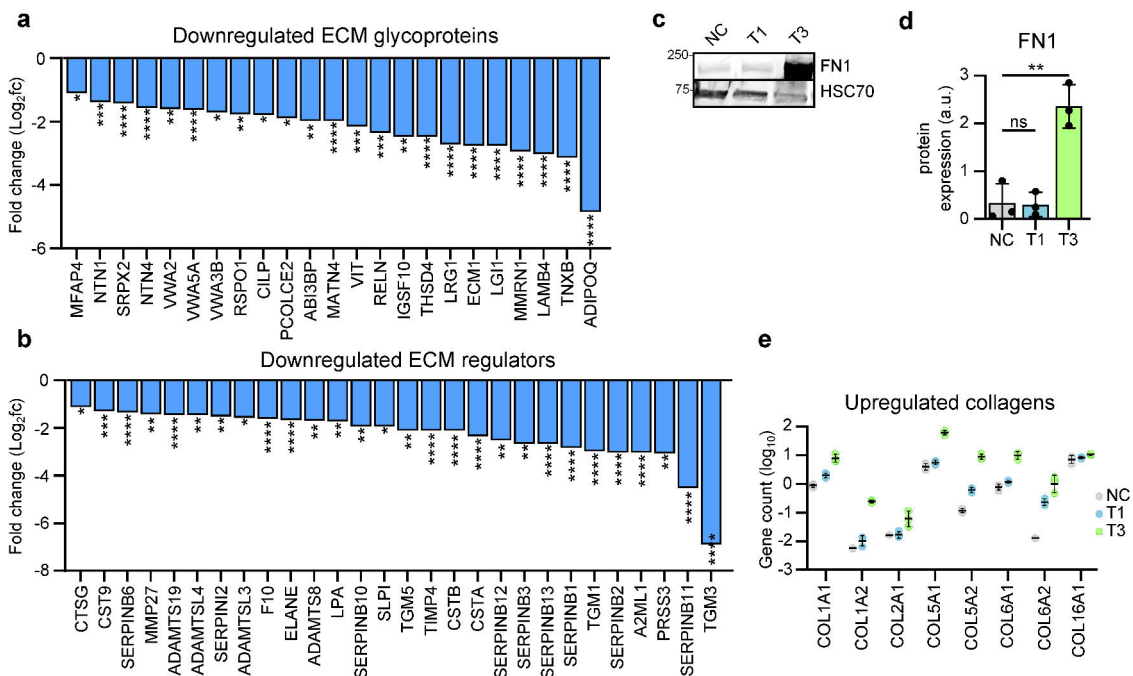
**Video 30:** T3 VFC cell proliferation (monolayer) on Collagen-Fibronectin coated plastic. Growth medium supplemented with anti- $\alpha 3$  integrin antibody (P1B5, 10  $\mu\text{g/ml}$ ). Imaged using Incucyte (S3) every 10 minutes for 24 hours, 20x magnification.

**Video 31:** T3 VFC cell proliferation (monolayer) on Collagen-Fibronectin coated plastic. Growth medium supplemented with anti- $\alpha 6$  integrin antibody (P5G10, 10  $\mu\text{g/ml}$ ). Imaged using Incucyte (S3) every 10 minutes for 24 hours, 20x magnification.

**Video 32:** T3 VFC cell proliferation (monolayer) on Collagen-Fibronectin coated plastic. Growth medium supplemented with anti- $\alpha 3\alpha 6$  integrin antibody (P1B5 and P5G10, 10  $\mu\text{g}/\text{ml}$ ). Imaged using Incucyte (S3) every 10 minutes for 24 hours, 20x magnification.

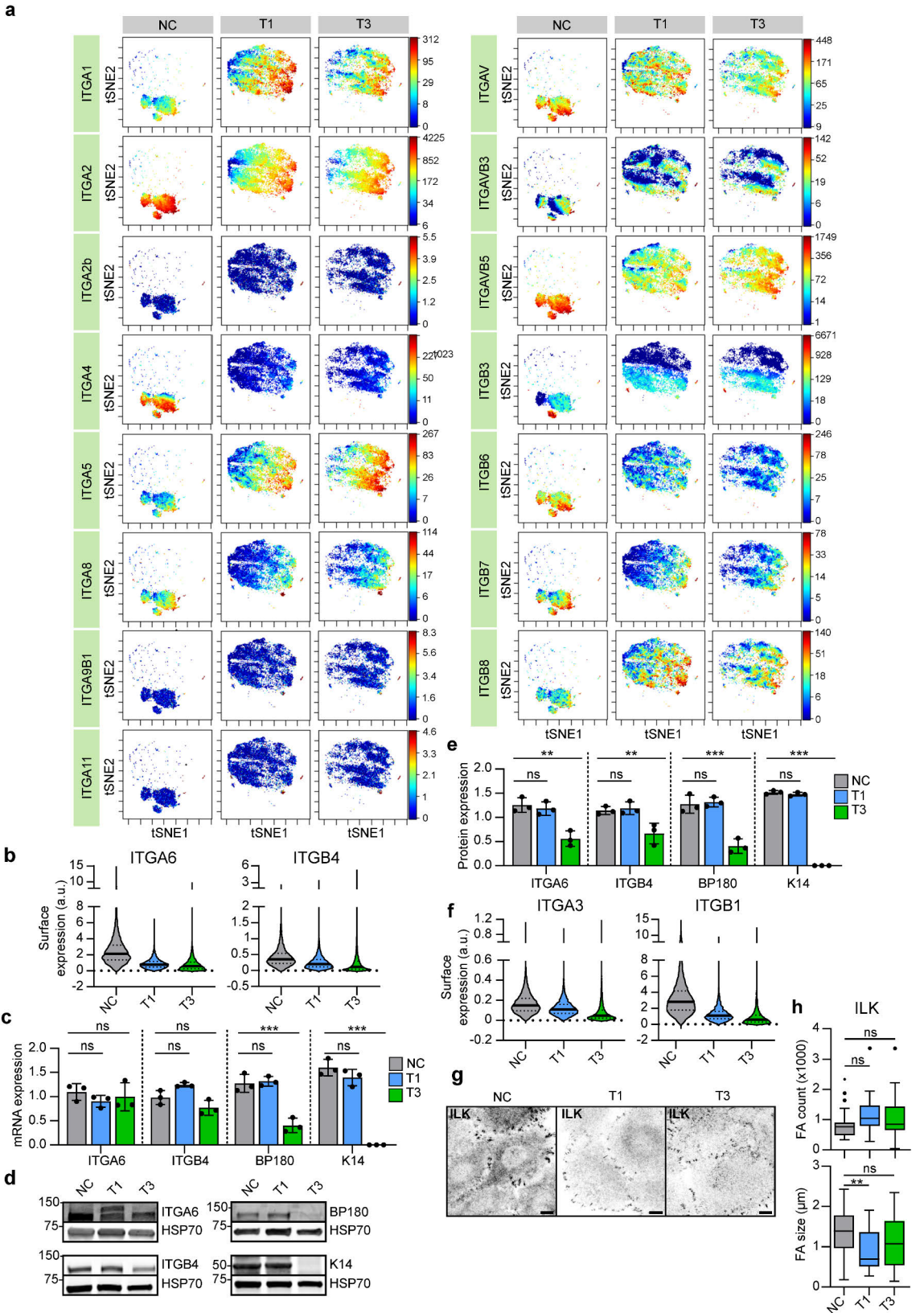
**Video 33:** T3 VFC cell proliferation (monolayer) on Collagen-Fibronectin coated plastic. Growth medium supplemented with anti- $\beta 1$  integrin antibody (mAb13, 10  $\mu\text{g}/\text{ml}$ ). Imaged using Incucyte (S3) every 10 minutes for 24 hours, 20x magnification.

## Extended data Figures



## Extended Data Figure 1 | Vocal fold cancer is associated with elevated gene expression of ECM components and stiffening of tissue

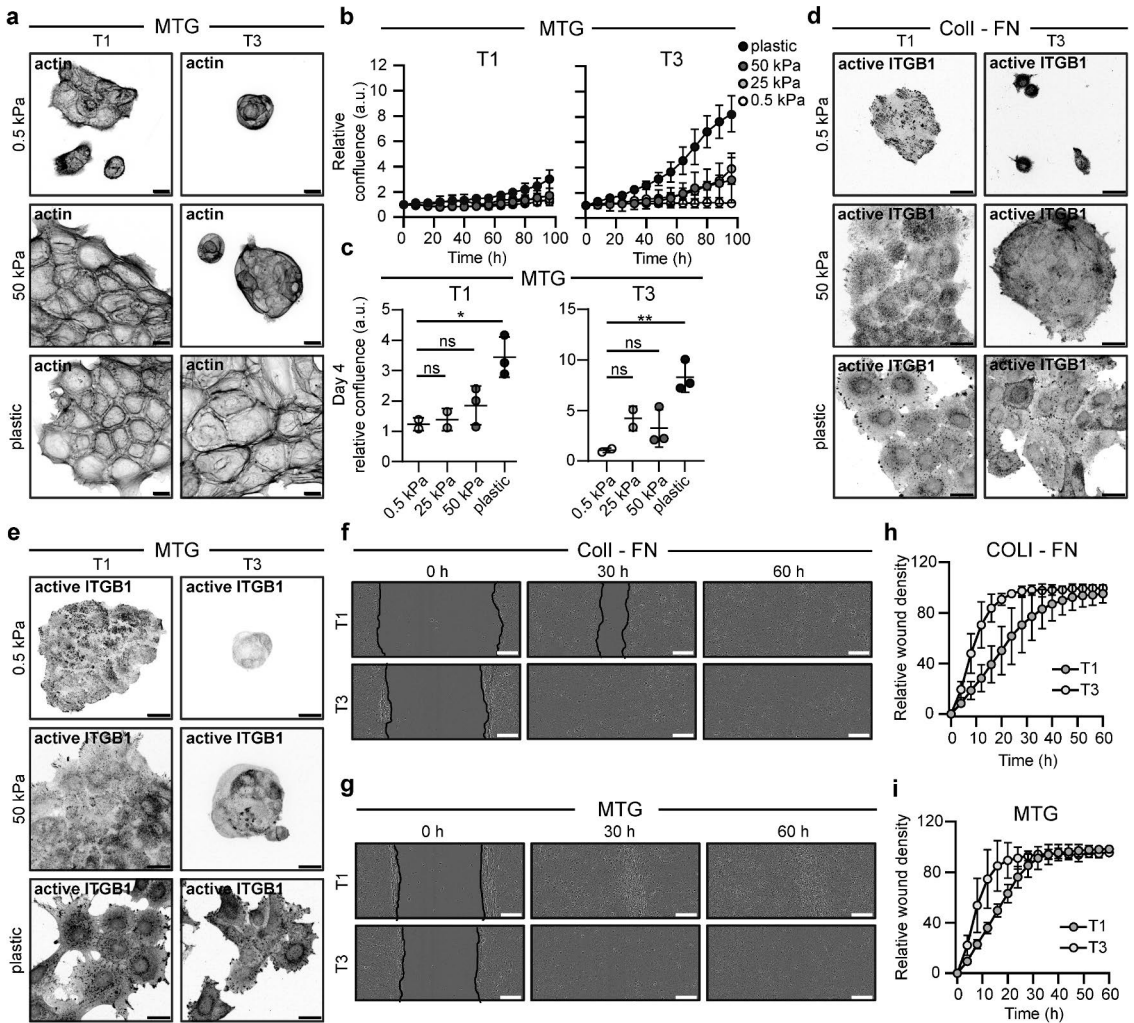
**a & b** Differentially downregulated (fold change,  $\text{log}_2$ ) ECM glycoproteins (**a**) and ECM regulators (**b**) in VFC tissue (T1-T4,  $n=54$ ) compared to normal tissue ( $n=12$ ) in patients (TCGA-data,  $\text{FDR} < 0.05$ ). **c & d**, Representative immunoblot (**c**) and quantification (**d**) of fibronectin protein expression (mean $\pm$ s.d.,  $n=3$ ) in NC cells and vocal fold T1 and T3 cancer cells. **e**, Upregulated gene count ( $\text{log}_{10}$ , RNA-seq) of collagens in NC cells and vocal fold T1 and T3 cancer cells ( $n=3$ ). Data are mean ( $\pm$ s.d.).  $\text{FDR}$  was used to assess statistical significance of differentially expressed genes and ordinary one-way Anova followed by post hoc Dunnett's multiple comparisons test was used to assess statistical significance of protein expression.



## **Extended Data Figure 2 | Expression and subcellular localization of laminin-binding integrins is altered in vocal fold cancer**

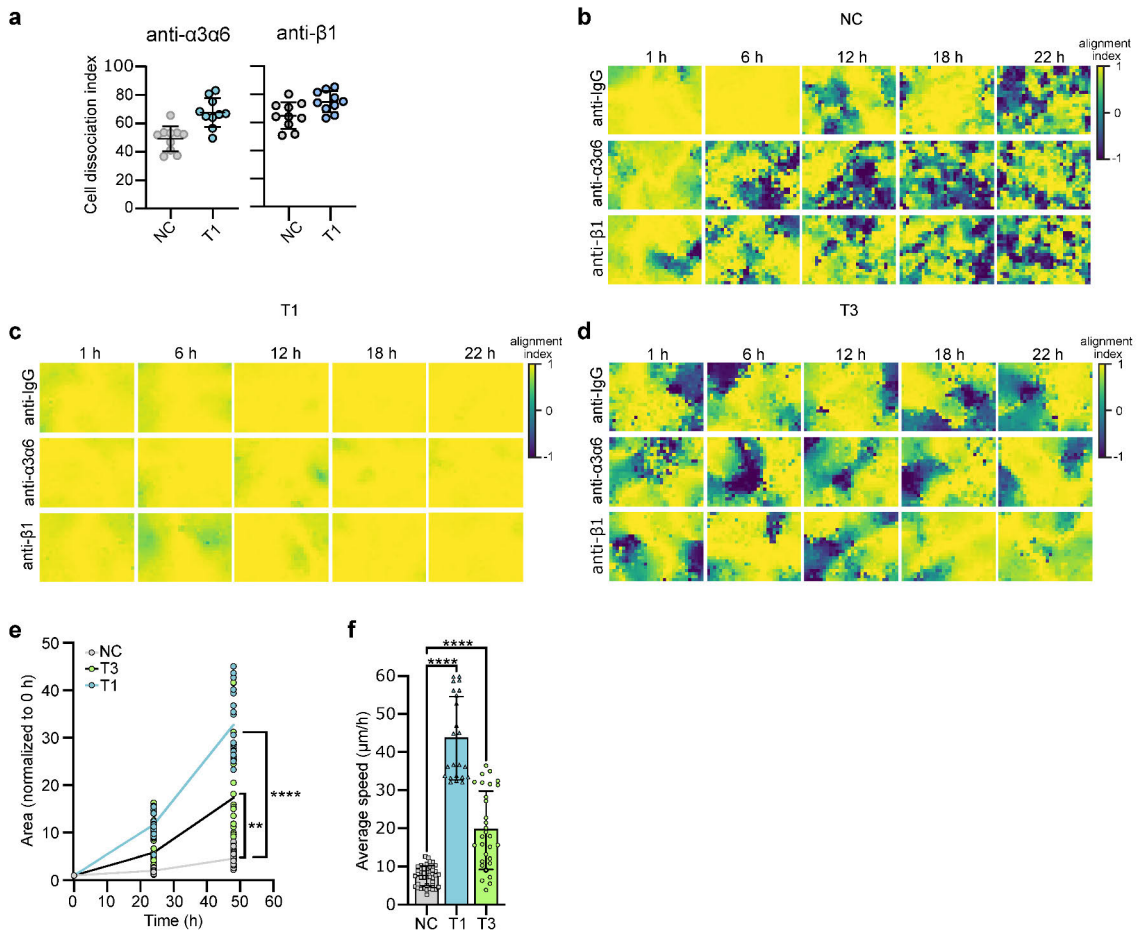
**a**, t-SNE visualization of ITGA1, ITGA2, ITGA2b, ITGA4, ITGA5, ITGA8, ITGA9B1, ITGA11, ITGAV, ITGAVB3, ITGAVB5, ITGB3, ITGB6, ITGB7 and ITGB8 single-cell surface expression (MassCytof) in NC cells and vocal fold T1 and T3 cancer cells. **b**, Violin plot representation of mean ITGA6 and ITGB4 single-cell surface expression (MassCytof) in NC cells and vocal fold T1 and T3 cancer cells. **c**, Relative ITGA6, ITGB4, BP180 and K14 mRNA expression levels (gene count) in NC cells and vocal fold T1 and T3 cancer cells (n=3). **d & e**, Representative immunoblots (**d**) and quantification (**e**) of relative ITGA6, ITGB4, BP180 and K14 protein expression levels in NC cells and vocal fold T1 and T3 cancer cells (n=3). **f**, Violin plot representation of mean ITGA3 and ITGB1 single-cell surface expression (MassCytof) in NC cells and vocal fold T1 and T3 cancer cells. **g**, Representative ILK confocal immunofluorescence images of NC cells and VFC T1 and T3 cells (n=3). Scale bar 10  $\mu\text{m}$ . **h**, Quantification of FA number (count) (left) and size (right) using ILK as a marker in NC cells (n=28), and VFC T1 (n=29-30) and T3 (n=28-30) cells. Data are mean box plots ( $\pm$  s.d.) or tukey box plots. n is the total number of average FA count/size per cell in FOV pooled from three independent experiments. Statistical significance was assessed using Kruskal-Wallis test followed by post hoc Dunn's multiple comparisons test.





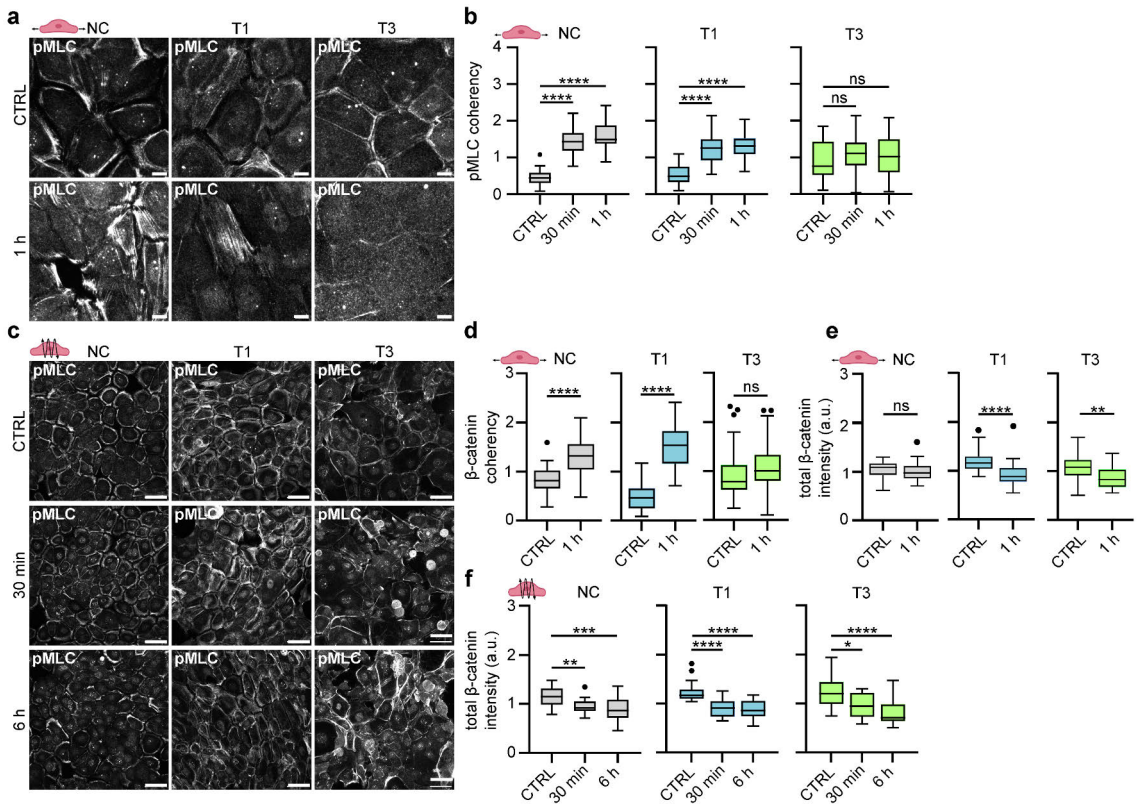
### Extended Data Figure 3 | Stiffening of vocal fold tissue supports increased cell proliferation, migration and invasion

**a**, Representative actin confocal immunofluorescence images of T1 and T3 VFC cells on 0.5 and 50 kPa hydrogels and plastic coated with Matrigel ( $n=3$ ). Scale bar 50  $\mu\text{m}$ . **b & c**, Proliferation (**b**) of T1 and T3 VFC cells on hydrogels of varying stiffnesses (0.5 kPa, 25 kPa, 50 kPa) and plastic and confluence at end-point (**c**). **d & e**, Representative active ITGB1 (12G10) confocal immunofluorescence images of T1 and T3 VFC cells on 50 kPa hydrogels coated with collagen and fibronectin (**d**) or Matrigel (**e**) ( $n=3$ ). Scale bar 50  $\mu\text{m}$ . **f & g**, Representative phase-contrast images of T1 and T3 VFC cells wound healing assay at different timepoints (0h, 30h and 60h) on collagen I and fibronectin (**f**) or Matrigel (**g**) coated plates. Scale bar 100  $\mu\text{m}$ . ( $n=3$ ). **h & i**, Relative wound density of T1 and T3 VFC cells on collagen I and fibronectin (**h**) or Matrigel (**i**) coated plates. ( $n=3$ ). Data are mean ( $\pm$  s.d.). Statistical significance was assessed using Kruskal-Wallis test followed by post hoc Dunn's multiple comparisons test.



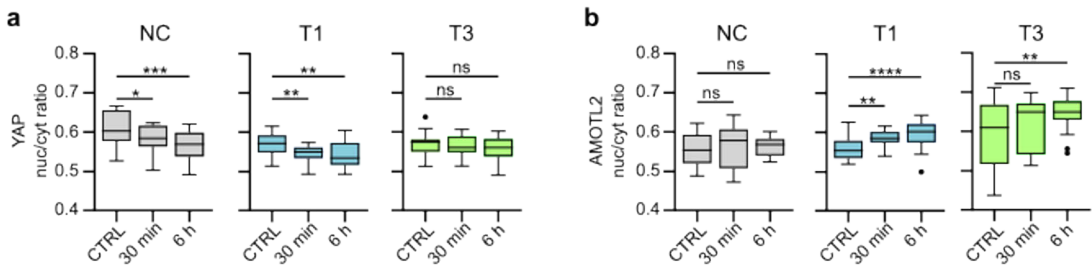
## Extended Data Figure 4 | Inhibition of laminin-binding integrins modulates monolayer dynamics and disrupts cell clustering in 3D-spheroids

**a** Quantification of cell dissociation index in NC and VFC T1 cells treated with anti- $\alpha3\alpha6$  or anti- $\beta1$  integrin blocking antibodies (n=3). **b-d**, Graphic visualization of cell velocity alignment index in NC (**b**), VFC T1 (**c**) and T3 (**d**) cells treated with anti- $\alpha3\alpha6$  or anti- $\beta1$  integrin blocking antibodies. **e & f**, Quantification of normalized wetting area (**e**) and average wetting speed ( $\mu\text{m/h}$ ) (**f**) of NC and VFC T1 and T3 cells (n=3). Data are mean  $\pm$  s.d. Statistical significance was assessed using Kruskal-Wallis test followed by post hoc Dunn's multiple comparisons test.



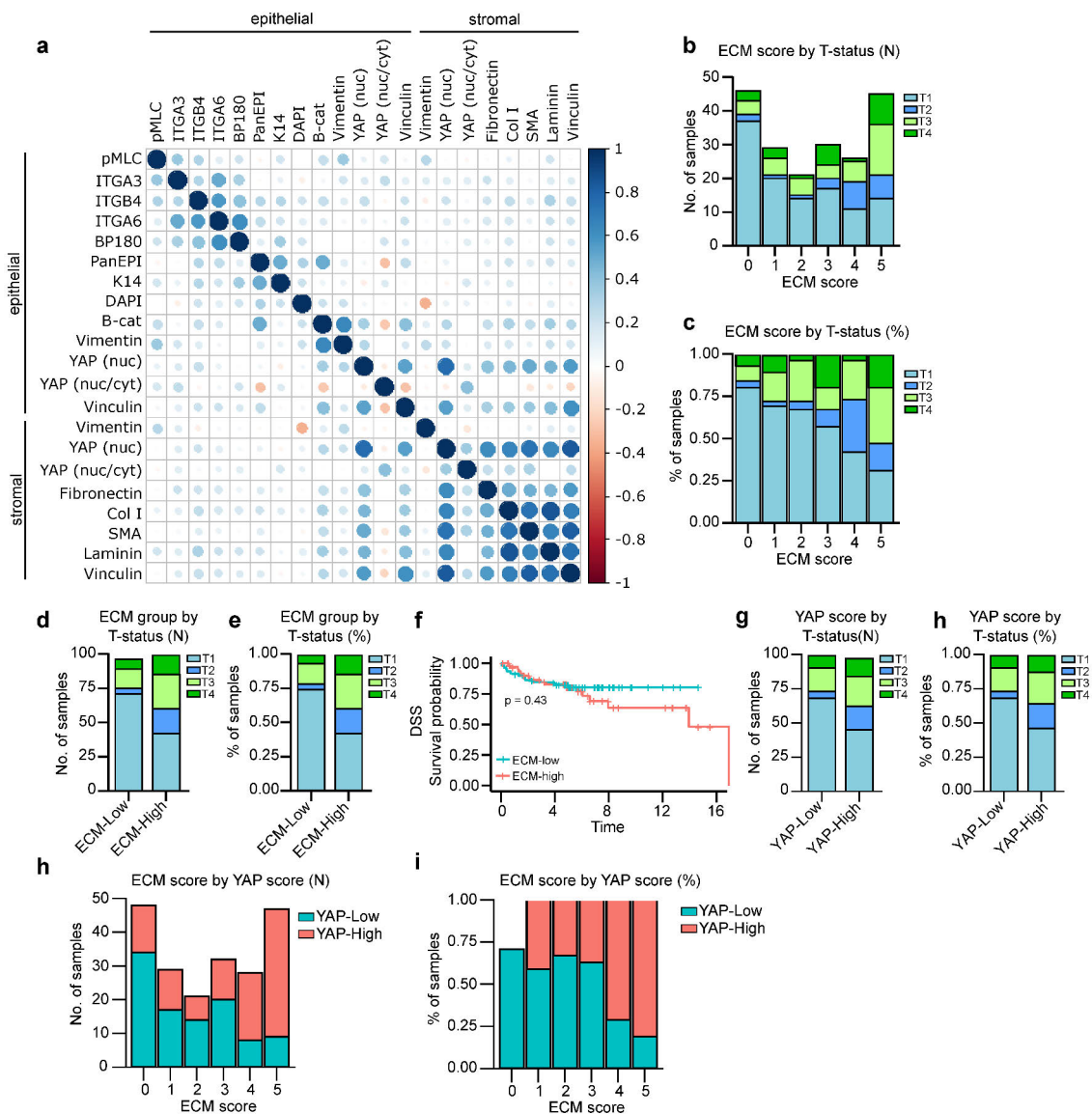
### Extended Data Figure 5 | Mechanical stimuli induce cytoskeletal and junctional alterations and cell extrusion in VFC

**a**, Representative pMLC confocal immunofluorescence images of NC cells and VFC T1 and T3 cells subjected to stretch ( $n=3$ ). **b**, Quantification of pMLC coherency of NC cells and vocal fold T1 and T3 cells subjected to stretching ( $n=3$ ). **c**, Representative pMLC confocal immunofluorescence images of NC cells and VFC T1 and T3 cells subjected to vibration ( $n=3$ ). Scale bar 20  $\mu\text{m}$ . **d**, Quantification of  $\beta$ -catenin coherency of NC cells and VFC T1 and T3 cells subjected to stretching ( $n=3$ ). **e & f**, Quantification of total  $\beta$ -catenin intensity of NC cells and VFC T1 and T3 cells subjected to stretching (**e**) or vibration (**f**) ( $n=3$ ). Data are illustrated as tukey box plots or violin blots (average of 8 FOV's pooled from three independent experiments). Kruskal-Wallis test followed by post hoc Dunn's multiple comparisons test was used to assess statistical significance.



**Extended Data Figure 6 | Phonomimetic mechanical stimuli decreases nuclear and total YAP levels**

**a**, Quantification of YAP nuclear to cytoplasmic ratio in NC cells and VFC T1 and T3 cells subjected to vibration (50-250 Hz, 1 min on/off) for 30 min or 6h compared to non-vibrated control. **b**, Quantification of AMOTL2 nuclear to cytoplasmic ratio in NC cells and VFC T1 and T3 cells subjected to vibration (50-250 Hz, 1 min on/off) for 30 min or 6h compared to non-vibrated control. Data are illustrated as tukey box plots (average of 8 FOV's pooled from three independent experiments). Ordinary one-way Anova followed by post hoc Dunnett's multiple comparisons test was used to asses statistical significance.



### Extended Data Figure 7 | High YAP levels correlate with high ECM expression and poor disease specific survival

**a**, Patient-level correlation of epithelial (pMLC, ITGA3, ITGB4, ITGA6, BP180, PanEpi, K14, dapi, vimentin, YAP and vinculin) and stromal (vimentin, YAP, fibronectin, COL I, SMA, laminin and vinculin) marker mean expression in TMA multiplex histology. **b**, ECM-score by T-status illustrated as number of samples (N). **c**, ECM score by T-status illustrated as percentage of samples (%). **d**, ECM group by T-status illustrated as number of samples (N). **e**, ECM group (ECM-low and ECM-high) by T-status illustrated as percentage of samples (%). **f**, Disease specific survival of ECM-high and ECM-low patients. **g** & **h**, YAP score by T-status illustrated as number of samples (N) (**g**) and percentage of samples (%) (**h**). **i** & **j**, ECM score by YAP score illustrated as number of samples (N) (**i**) and percentage of samples (%) (**j**). Data are mean expression and statistical significance of Kaplan-Meier analysis was assessed with Log-rank test.



**Lilja J\*, Kaivola J\*, Conway JRW, Vuorio J, Parkkola H, Roivas P,  
Dibus M, Chastney MR, Varila T, Jacquemet G, Peuhu E, Wang E,  
Pentikäinen U, Posada IMD, Hamidi H, Najumudeen AK, Sansom OJ,  
Barsukov IL, Abankwa D, Vattulainen I, Salmi M & Ivaska J (2024)**  
**SHANK3 depletion leads to ERK signalling overdose and cell death in  
KRAS-mutant cancers.**  
Nature Communications






# SHANK3 depletion leads to ERK signalling overdose and cell death in KRAS-mutant cancers

Received: 9 December 2022

Accepted: 3 September 2024

Published online: 12 September 2024

 Check for updates

Johanna Lilja<sup>1,18</sup>, Jasmin Kaivola<sup>1,18</sup>, James R. W. Conway<sup>1</sup>, Joni Vuorio<sup>2</sup>, Hanna Parkkola<sup>1</sup>, Pekka Roivas<sup>1,3</sup>, Michal Dibus<sup>1</sup>, Megan R. Chastney<sup>1</sup>, Taru Varila<sup>1</sup>, Guillaume Jacquemet<sup>1,4,5,6</sup>, Emilia Peuhu<sup>1,7</sup>, Emily Wang<sup>8</sup>, Ulla Pentikäinen<sup>1,3</sup>, Itziar Martinez D. Posada<sup>1</sup>, Hellyeh Hamidi<sup>1</sup>, Arafath K. Najumudeen<sup>9,10</sup>, Owen J. Sansom<sup>10,11</sup>, Igor L. Barsukov<sup>12</sup>, Daniel Abankwa<sup>1,12</sup>, Ilpo Vattulainen<sup>2</sup>, Marko Salmi<sup>3,13,14</sup> & Johanna Ivaska<sup>1,14,15,16,17</sup> ✉

The *KRAS* oncogene drives many common and highly fatal malignancies. These include pancreatic, lung, and colorectal cancer, where various activating *KRAS* mutations have made the development of *KRAS* inhibitors difficult. Here we identify the scaffold protein SH3 and multiple ankyrin repeat domain 3 (SHANK3) as a RAS interactor that binds active *KRAS*, including mutant forms, competes with RAF and limits oncogenic *KRAS* downstream signalling, maintaining mitogen-activated protein kinase/extracellular signal-regulated kinase (MAPK/ERK) activity at an optimal level. SHANK3 depletion breaches this threshold, triggering MAPK/ERK signalling hyperactivation and MAPK/ERK-dependent cell death in *KRAS*-mutant cancers. Targeting this vulnerability through RNA interference or nanobody-mediated disruption of the SHANK3–*KRAS* interaction constrains tumour growth in vivo in female mice. Thus, inhibition of SHANK3–*KRAS* interaction represents an alternative strategy for selective killing of *KRAS*-mutant cancer cells through excessive signalling.

Aberrant *KRAS* activity has been identified in >20% of *human* cancers<sup>1</sup> with a substantially higher incidence in some of the most inherently therapy-resistant cancer types, including non-small cell lung cancers (NSCLC; 30% incidence), colorectal cancer (CRC; 50% incidence), and pancreatic ductal adenocarcinoma (PDAC; 95% incidence)<sup>1,2</sup>. Oncogenic mutations in *KRAS* induce the constitutive activation of proliferative signalling cascades, promoting cancer progression and conferring resistance to standard-of-care

<sup>1</sup>Turku Bioscience Centre, University of Turku, FI-20520 Turku, Finland. <sup>2</sup>Department of Physics, University of Helsinki, Helsinki, Finland. <sup>3</sup>Institute of Biomedicine, University of Turku, FI-20520 Turku, Finland. <sup>4</sup>Faculty of Science and Engineering, Cell Biology, Åbo Akademi University, FI-20520 Turku, Finland. <sup>5</sup>Turku Bioimaging, University of Turku and Åbo Akademi University, FI-20520 Turku, Finland. <sup>6</sup>InFLAMES Research Flagship Center, Åbo Akademi University, FI-20520 Turku, Finland. <sup>7</sup>Institute of Biomedicine, Cancer Research Laboratory FICAN West, University of Turku, FI-20520 Turku, Finland. <sup>8</sup>Institute of Systems, Molecular and Integrative Biology, University of Liverpool, Liverpool, UK. <sup>9</sup>Institute of Biotechnology, HiLIFE, University of Helsinki, Helsinki, Finland. <sup>10</sup>CRUK Scotland Institute, Garscube Estate, Switchback Road, Glasgow G61 1BD, UK. <sup>11</sup>Institute of Cancer Sciences, University of Glasgow, Garscube Estate, Switchback Road, Glasgow G61 1QH, UK. <sup>12</sup>Department of Life Sciences and Medicine, University of Luxembourg, 4365 Esch-sur-Alzette, Luxembourg. <sup>13</sup>MediCity Research Laboratory, University of Turku, FI-20520 Turku, Finland. <sup>14</sup>InFLAMES Research Flagship Center, University of Turku, FI-20520 Turku, Finland. <sup>15</sup>Department of Life Technologies, University of Turku, Turku, Finland. <sup>16</sup>Foundation for the Finnish Cancer Institute, Tukholmankatu 8, FI-00014 Helsinki, Finland. <sup>17</sup>Western Finnish Cancer Center, University of Turku, Turku FI-20520, Finland. <sup>18</sup>These authors contributed equally: Johanna Lilja, Jasmin Kaivola. ✉e-mail: Johanna.ivaska@utu.fi

treatments<sup>3–5</sup>. Unfortunately, the survival of patients with *KRAS*-mutated NSCLC or PDAC has barely improved over the past few decades<sup>6</sup>, highlighting the urgent need to broaden our view on targeting oncogenic *KRAS*.

*KRAS* is a plasma membrane-associated small GTPase, active in its GTP-bound form and inactive in its GDP-bound state<sup>7</sup>. Active *KRAS* interaction with its effector RAF switches on downstream pathways such as the mitogen-activated protein kinase (MAPK)/extracellular signal-regulated kinase (ERK) signalling axis, triggering a pro-survival response in cancer cells through transcription factors that promote cell growth<sup>8,9</sup>. Given the central role of oncogenic *KRAS* as a driver mutation in many cancer types, pharmacological inhibition of *KRAS* has been a major research area for decades. Through the accrued knowledge of the structural and biochemical characteristics of different *KRAS* mutants, the field has seen a recent development of mutation-specific drugs with promising preclinical and clinical efficacy<sup>10–18</sup>. The only approved allele-specific inhibitors target KRASG12C, a mutation found in ~12% of all *KRAS*-driven tumours<sup>11–16,19,20</sup>, leaving ~88% of patients without a *KRAS*-targeted treatment option. In addition, various resistance mechanisms have already been reported, indicating significant limitations of mutation-specific inhibitors in heterogeneous tumours<sup>21–23</sup>. To address a broader patient population, vast efforts are being made in several new pan-*KRAS* approaches targeting all *KRAS* mutants<sup>10,24,25</sup>. These include pharmacological manipulation of *KRAS* upstream activators, such as SHP2 and SOS1<sup>26–28</sup>, and attempts to develop pan-*KRAS* protein degradation strategies, such as proteolysis-targeting chimeras (PROTACs)<sup>29</sup>. These Pan-*KRAS* inhibitors hold promise for patients for whom targeted therapy remains elusive.

A common precision medicine approach has been to treat cancer by inhibiting specific oncogenic mutations or pathways. Recently, however, deliberate MAPK/ERK pathway hyperactivation by ERK2 overexpression or inhibition of ERK phosphatases DUSP4 and 6 was shown to reduce NRAS and BRAF mutant cell viability<sup>30–32</sup> and a gain-of-function oncogene activation screen demonstrated that hyperactivation of oncogenic pathways can trigger context-specific lethality across cancer cell lines<sup>33</sup>.

We and others previously showed that the multidomain scaffold protein SH3 and multiple ankyrin repeat domain 3 (SHANK3) adopts a RAS-association (RA) domain-like fold, within its N-terminal Shank/ProSAP (SPN) domain, with high affinity for GTP-bound RAS and Rap small GTPases<sup>34,35</sup>. SHANK3 was initially identified in the excitatory synapses of the central nervous system<sup>36</sup>. We discovered that SHANK3 functions beyond the nervous system, regulating the cell cytoskeleton<sup>37</sup> and cell adhesion by binding to Rap1 and inhibiting the formation of an integrin-activating complex in non-neuronal cells and cancer cells<sup>34</sup>. However, whether SHANK3 plays a functional role in oncogenic RAS signalling remains unknown.

In this work, we identify SHANK3 as a RAS interactor that competes with RAF for binding to active *KRAS*. We show that this functionally limits oncogenic MAPK/ERK signalling to an optimal level for *KRAS*-mutant cancer cell growth. We further demonstrate that SHANK3 depletion results in hyperactivation of this pathway, leading to cancer cell death by signalling overdose in *KRAS*-mutant cancers with different *KRAS* mutations. Our data demonstrate that SHANK3 depletion impairs the growth of pre-existing *KRAS*-mutant tumours, highlighting the possibility of SHANK3 targeting as a potential actionable cancer dependency. We provide proof-of-concept evidence that SHANK3 can be targeted by developing nanobodies disrupting the SHANK3–*KRAS* protein-protein interaction. We demonstrate the efficacy of these nanobodies in inducing apoptosis in *KRAS*-mutant cancers. Collectively our data reveal that the SHANK3–*KRAS* interaction is an exploitable vulnerability of pan-*KRAS*-driven cancers.

## Results

### SHANK3 depletion impairs cell proliferation in a panel of *KRAS*-mutant cancer cell lines

To investigate the role of SHANK3 in cancer cell viability, we depleted endogenous SHANK3 using two unique RNA interference (RNAi) oligonucleotides (siSHANK3\_2 and siSHANK3\_7) in a large panel of *human* PDAC, NSCLC and CRC cell lines harbouring either distinct *KRAS* mutations or wild-type (WT) *KRAS* (Fig. 1a and silencing validated in Supplementary Fig. 1a). Cell proliferation was strongly impaired with both SHANK3 siRNAs in each of the 12 tested cancer cell lines with activating mutations in *KRAS* [mean inhibition of proliferation (%): 63.3 ± 4.4% (PANC-1), 66.1 ± 5.6% (Panc10.05), 38.9 ± 4.2% (AsPC-1), 63.0 ± 19.6% (Su86.86), 55.5 ± 4.7% (SW1990), 55.5 ± 8.8% (YAPC), 74.5 ± 4.6% (PaTu8902), 79.5 ± 19.1% (MIA PaCa-2), 50.8 ± 20.5% (A549), 72.1 ± 7.5% (H441), 38.0 ± 22.1% (HCT-15), 81.3 ± 8.6% (HCT-116)] (Fig. 1a). In contrast, the cancer cell lines harbouring WT *KRAS* did not show consistent and/or significant inhibition of proliferation following SHANK3 depletion with the two SHANK3 siRNA [mean inhibition of proliferation (%): -3.9 ± 33.2% (H292), 14.0 ± 20.9% (H226), 13.6 ± 8.0% (HT-29), 27.9 ± 21.6 (BxPC3) and 0.4 ± 2.5 (ARPE)] (Fig. 1a). Interestingly, the pan-cancer Broad and Sanger knock-out cancer cell line viability screens did not include guide RNAs or shRNA against SHANK3, suggesting that our current view of genes essential for cancer survival may be lacking some more important regulators<sup>38,39</sup>. Our data thus indicate that SHANK3 depletion, while dramatically affecting *KRAS*-mutant cell proliferation, has no or marginal effects on WT *KRAS* cells.

The growth of *KRAS*-mutant pancreatic (PANC-1) and lung cancer (A549) cell colonies was also reduced by ~90% after acute SHANK3 silencing with the two independent siRNAs (Supplementary Fig. 1b). Similarly, in a 3-dimensional (3D) setting, the growth of *KRAS*-mutant pancreatic (PANC-1 and AsPC-1) and lung (A549) cancer spheroids was also significantly inhibited (Fig. 1b and Supplementary Fig. 1c).

To examine if SHANK3 is also essential for tumorigenesis, we established pancreatic and lung cancer xenograft models on chick embryo chorioallantoic membranes (CAMs) in fertilised eggs (Supplementary Fig. 1d). In line with our *in vitro* results, we observed a significant decrease in both tumour weight and the number of proliferating cells, as indicated by Ki-67 staining, in SHANK3-silenced *KRAS*-driven PANC-1 and A549 xenografts (Fig. 1c–e), but not in WT *KRAS* BxPC3 tumours (Supplementary Fig. 1e–g).

These data collectively indicate that the depletion of endogenous SHANK3 effectively blocks cell proliferation and growth *in vitro* and *in vivo* in different cancer types driven by distinct *KRAS* mutations.

### SHANK3 interacts specifically with active *KRAS* to regulate *KRAS*-mutant cell survival

We had previously determined the crystal structure of the SHANK3 N-terminus, revealing an RA domain-like structure in the SPN domain (Fig. 2a)<sup>34</sup>. A subsequent study elucidated the structure of the SPN domain when bound to HRAS<sup>35</sup>. To understand the role of SHANK3 in regulating *KRAS*-driven tumour growth, we first explored the SHANK3–*KRAS* interaction. Microscale thermophoresis (MST) and isothermal titration calorimetry (ITC) measurements with purified recombinant proteins indicated that the N-terminal SHANK3 SPN domain alone and the SPN-ARR fragment (comprising the two adjacent N-terminal domains) (Fig. 2a) interact with active (GMPPCP-form) *KRAS* mutants with similar affinities (K<sub>d</sub> = 5.0 ± 0.6 μM for G12V with SPN; and K<sub>d</sub> = 5.4 ± 0.7 μM for Q61H with SPN-ARR; Fig. 2b, c and Supplementary Fig. 2a–d). Inactive (GDP-bound) *KRAS* showed no interaction with SHANK3 SPN-ARR in ITC measurements (Fig. 2d), indicating that the interactions were specific to GTP-bound *KRAS*. These data show direct SHANK3 SPN domain interaction with *KRAS* at low micromolar affinity that is dependent on *KRAS* activity, similar to established RA domain-containing proteins<sup>40</sup>.

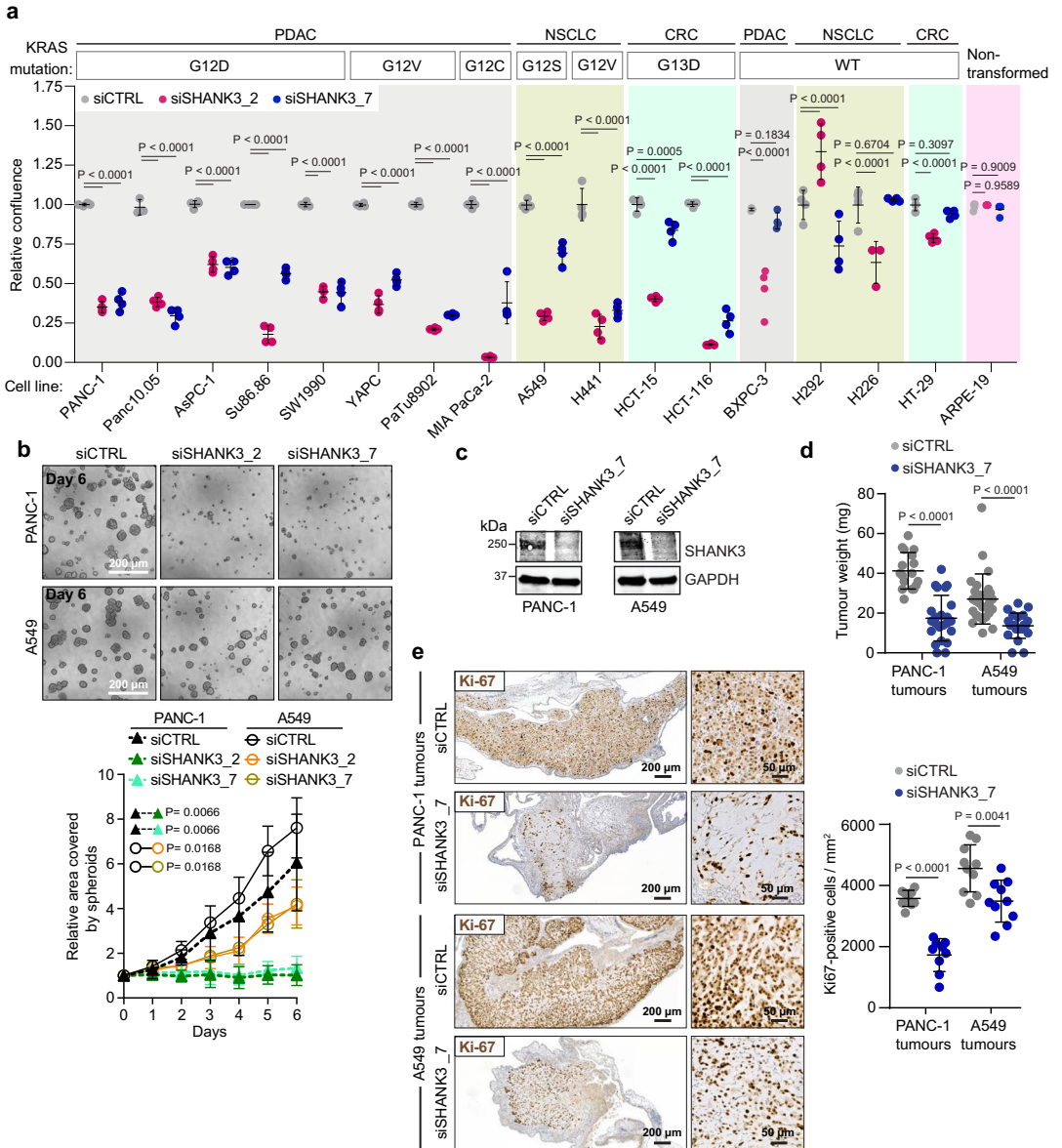
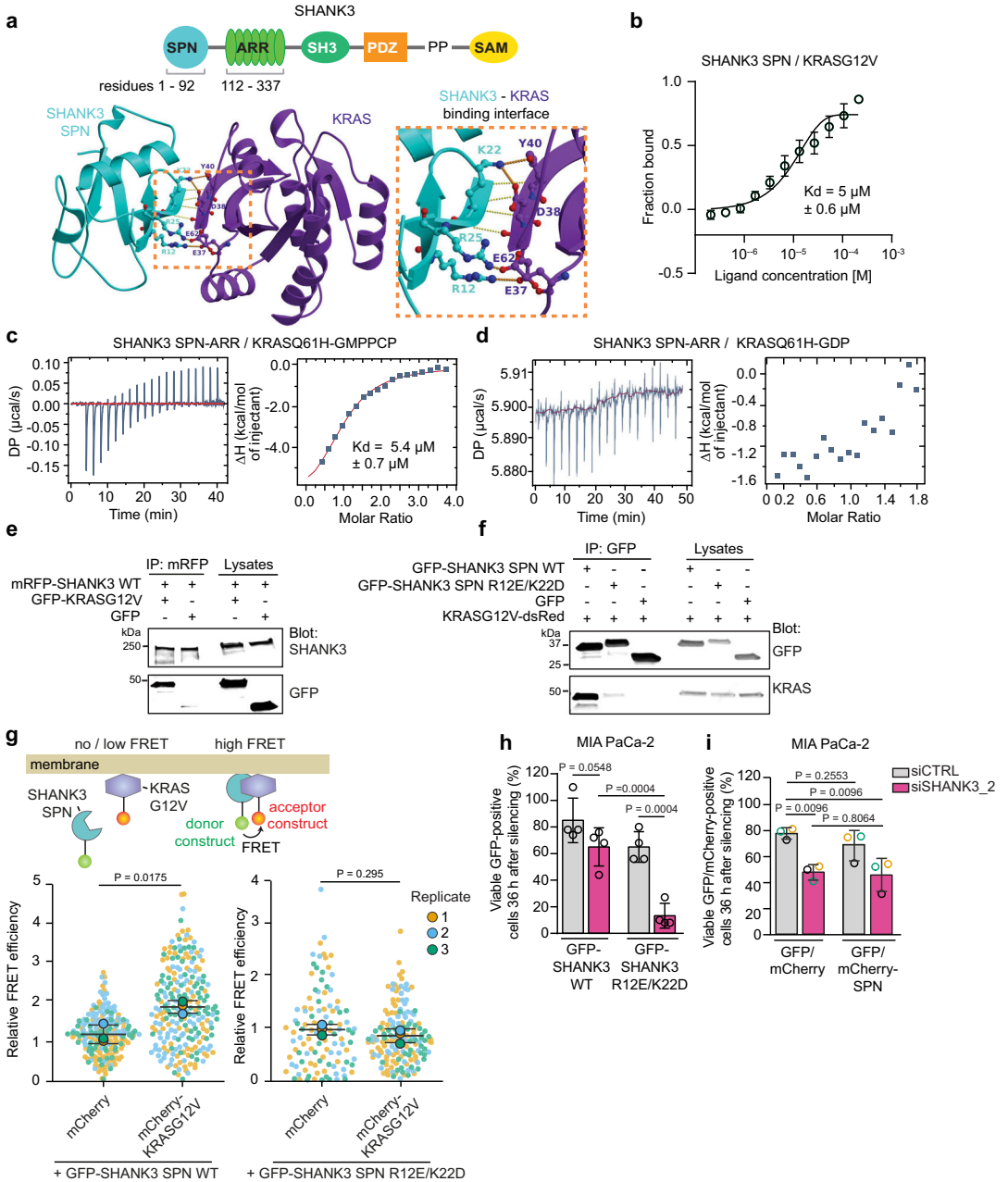


**Fig. 1 | SHANK3 depletion inhibits cell proliferation in vitro and in vivo in different cancer types driven by distinct *KRAS* mutations.** **a** Cell proliferation screen following control (siCTRL, grey) or *SHANK3* silencing (siSHANK3\_2 (red) or siSHANK3\_7 (blue)) in wild-type (WT) or *KRAS*-mutant pancreatic (PDAC), lung (NSCLC) and colorectal (CRC) cancer cell lines. ARPE-19, non-transformed retinal epithelial cells. Shown are the individual data points relative to control [the mean of the control is set to 1.0 by definition; data are mean ± s.d.;  $n = 3$  (Panc10.05 siCTRL and H226 siSHANK3\_2) or 4 (other samples) individually silenced wells; two-way ANOVA with Dunnett's multiple comparisons test]. **b** Spheroid growth of siCTRL or siSHANK3 PANC-1 or A549 cells. Shown are representative images and quantification of spheroid area (mean ± s.d.;  $n = 3$  independent experiments; statistical

analysis at end point, one-way ANOVA with Holm-Sidak's multiple comparison test). **c-e** Analysis of siCTRL or siSHANK3 PANC-1 and A549 tumour growth on chorioallantoic membranes (CAMs). **c** Immunoblots showing SHANK3 protein levels in cell suspensions inoculated onto the CAMs [ $n = 1$  (PANC1) and 2 (A549) independent experiments], **(d)** tumour weights, and **(e)** representative immunostainings and quantification of Ki-67-positive cells in tumours. Shown are individual data points [mean ± s.d.;  $n = 17$  (PANC-1 siCTRL), 23 (PANC-1 siSHANK3), 27 (A549 siCTRL) or 22 (A549 siSHANK3) (**d**) and 9 (PANC-1) or 10 (A549) (**e**) tumours per sample group from 1 (PANC-1) or 2 (A549) independent experiments; two-way ANOVA with Mann-Whitney test (**d**) and Unpaired two-tailed Student's *t*-test with Welch's correction (**e**)]. Source data are provided as a Source Data file.



To validate the SHANK3–KRAS protein-protein interaction in cells, we expressed fluorescently tagged KRASG12V and full-length SHANK3 and performed pull-down experiments. Immunoblotting analyses showed that KRASG12V co-immunoprecipitates with the full-length SHANK3 from cell lysates (Fig. 2e). Unfortunately, due to the lack of suitable reagents, we were unable to test endogenous SHANK3 and KRAS binding with co-immunoprecipitation. Based on its crystal structure<sup>34,35</sup>, the SHANK3 SPN domain contains the characteristic

positively charged RAS-recognizing residues, R12 and K22, which are optimally positioned to form salt-bridges with the E37 and D38/Y40 residues of the KRAS Switch I region (residues from D30 to Y40; Fig. 2a). To analyse the interaction specificity between SHANK3 and KRAS, we introduced charge-reversing mutations into the R12 and K22 residues of the SPN domain (R12E/K22D) and co-expressed the SHANK3 SPN domains (WT or SPN R12E/K22D mutant) with KRASG12V in cells. Pull-down analyses showed KRASG12V co-

**Fig. 2 | SHANK3 directly interacts with active KRAS, regardless of the activating mutation.** **a** Schematic of the SHANK3 protein domains and crystal structure model of the SHANK3 SPN domain in complex with active KRAS. The zoom-in shows the critical interacting amino acids. Modified from our previous publication<sup>34</sup>. SPN, Shank/ProSAP N-terminal domain; ARR, ankyrin repeat domain; SH3, Src homology 3 domain; PDZ, PSD-95/Disks large/ZO-1 domain; PP, proline-rich region; SAM, sterile alpha motif domain. **b** MST binding curve for the indicated proteins. The affinity curve and  $K_d$ -value are obtained from triplicate measurements (mean  $\pm$  s.e.m.; representative of two independent experiments). **c, d** ITC titration and isotherms for interaction between the indicated proteins. Solid line in **c** indicates fitting to the single-site-binding model at 25 °C with 350  $\mu$ M of KRASQ61H and 20  $\mu$ M of SPN-ARR (graphs are a representative of three technical replicates; one independent experiment). **e** Immunoprecipitation (IP) in HEK293 cells co-expressing mRFP-SHANK3 WT and GFP-KRASG12V using mRFP-trap beads. A representative western blot is shown (three independent experiments). **f** IP in HEK293 cells co-expressing the GFP-tagged SHANK3 SPN domain (WT or RAS-

binding-deficient mutant, R12E/K22D) and KRASG12V-dsRed using GFP-trap beads. A representative western blot is shown (three independent experiments). **g** FRET assay between GFP-tagged SHANK3 SPN domain (WT or R12E/K22D; FRET donor) and mCherry-KRASG12V (FRET acceptor) in HEK293 cells. Quantification of relative FRET efficiency, normalised to mCherry control vector (see methods). Individual data points and the population average of each biological replicate are shown [mean  $\pm$  s.d.; three independent experiments; unpaired two-tailed Student's *t*-test with Welch's correction; 190 (mCherry + WT SPN), 227 (mCherry-KRASG12V + WT SPN), 108 (mCherry + R12E/K22D SPN), 153 (mCherry-KRASG12V + R12E/K22D SPN) individual data points analysed]. **h, i** Rescue of cell viability after *SHANK3* silencing. Quantification of viable GFP- or mCherry-positive MIA PaCa-2 cells expressing either full-length GFP-SHANK3 WT or mutant R12E/K22D (**h**), or GFP/mCherry-tagged SHANK3 SPN domain (**i**) after endogenous *SHANK3* silencing (36 h). Shown are individual data points [mean  $\pm$  s.d.,  $n = 4$  (**h**) and 3 (**i**) independent experiments (**i**, each replicate is shown in a different colour); one-way ANOVA with Holm-Sidak's multiple comparison test]. Source data are provided as a Source Data file.

immunoprecipitation with SHANK3 SPN WT, an interaction that was abolished with the SPN R12E/K22D double mutant (Fig. 2f). Accordingly, FLIM-FRET (Förster Resonance Energy Transfer by Fluorescence Lifetime Imaging Microscopy) experiments demonstrated a significant increase in FRET efficiency between mCherry-tagged KRASG12V and GFP-tagged SHANK3 SPN WT, but not the SPN R12E/K22D mutant, in line with SHANK3 and KRASG12V protein-protein interaction (Fig. 2g). Taken together, these data demonstrate that SHANK3 directly interacts with active KRAS, independent of the specific KRAS mutation in question, through the conserved R12 and K22 residues, characteristic of a RAS-effector interface<sup>41</sup>.

To validate our hypothesis of SHANK3–KRAS interaction-dependent tumour growth, we tested whether re-expression of siRNA-resistant full-length SHANK3 WT or R12E/K22D mutant could rescue the growth inhibitory effect of *SHANK3* silencing. To test this, we chose the KRAS-mutant MIA PaCa-2 pancreatic cancer cell line, as these cells were particularly sensitive to *SHANK3* siRNA-induced growth inhibition (Fig. 1a). We found that the re-expression of SHANK3 WT in *SHANK3*-silenced MIA PaCa-2 cells restores cell viability (Fig. 2h). In contrast, the re-expression of the KRAS-interaction-deficient mutant, SHANK3 R12E/K22D (Fig. 2h), or the SHANK3 SPN domain alone (Fig. 2i) failed to rescue the cell death triggered by loss of SHANK3. Thus, an intact KRAS-binding SPN domain in full-length SHANK3 is critical for the ability of SHANK3 to regulate KRAS-mutant cell survival.

### SHANK3 competes with RAF for KRAS binding and modulates downstream MAPK/ERK signalling

KRAS association with the plasma membrane and the ability to recruit downstream effectors, such as RAF, are required for active KRAS signalling<sup>2,42</sup>. We observed that GFP-SHANK3 and endogenous SHANK3 localise to the plasma membrane (Supplementary Fig. 3a), and that GFP-SHANK3 localization overlapped with mutant mCherry-KRASG12V at the membrane (Fig. 3a), prompting us to investigate the possibility of SHANK3 interacting with KRAS on the cell membrane.

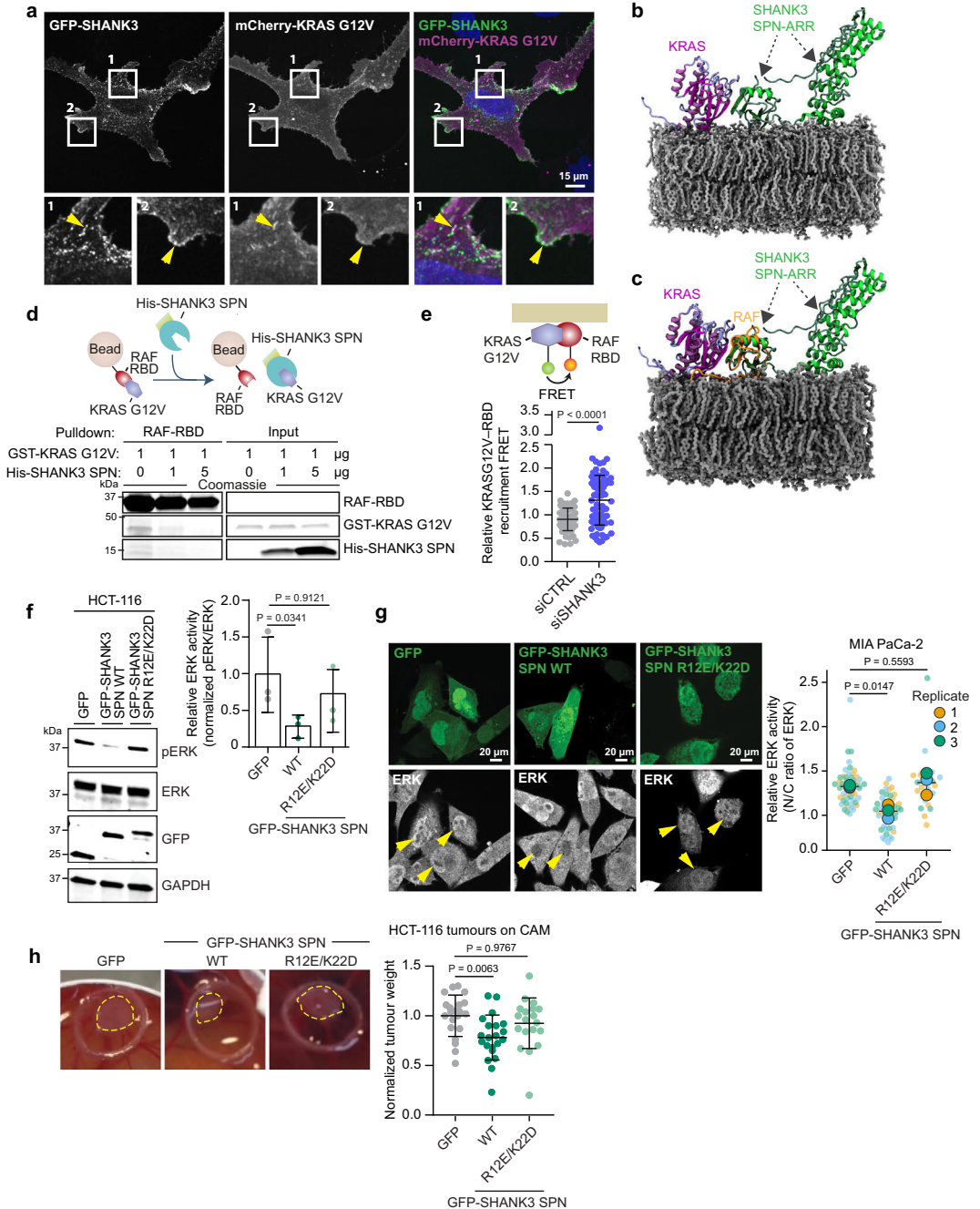
Based on the available SHANK3 structural data (SHANK3 SPN-ARR<sup>34,35</sup>) and our recent identification of the conformational opening of the SHANK3 SPN-ARR interface<sup>37</sup>, we generated atomistic in silico models of the SHANK3 SPN and SPN-ARR fragments and simulated their binding to the plasma membrane (Supplementary Fig. 3b–e). These simulations indicated that SHANK3 SPN and ARR domains contain positively charged regions that interact with the negatively charged plasma membrane. A recently published NMR structure defined a possible configuration of active KRAS binding to its downstream effector RAF on a lipid nanodisc membrane<sup>43</sup>. Intrigued by the striking structural homology of the RAF RBD (Ras-binding domain) and

SHANK3 SPN domains<sup>34,35,43</sup>, and our simulation data indicating a SHANK3 SPN-ARR membrane interaction, we generated a simulation model of the SHANK3 SPN-ARR–KRAS complex on the cell membrane (Fig. 3b). We observed that KRAS-bound SHANK3 (SPN-ARR domains) has evident interactions with the plasma membrane in its open configuration (Supplementary Fig. 3b–e<sup>37</sup>). An alignment between the SHANK3 SPN-ARR–KRAS model in an open conformation (Fig. 3b) and the nanodisc-bound KRAS-RAF<sup>43</sup> indicates a strong overlap of SPN with the space occupied by the KRAS-interacting RAF (Fig. 3c and Supplementary Fig. 3b–e). These structural data give mechanistic insight into, and support the notion that, SHANK3 (SPN-ARR) competes with RAF for KRAS binding on the plasma membrane, thus limiting KRAS downstream signalling.

To test this model, we first performed competition assays in vitro. Purified recombinant RAF-RBD and mutant KRASG12V proteins were incubated with increasing His-SHANK3 SPN protein concentrations followed by RAF-RBD pulldown (Fig. 3d). We observed a reduction in KRAS binding to the RAF-RBD beads with increasing concentrations of His-SPN (note that His-SPN and SPN-interacting KRAS are washed away in the pulldown; Fig. 3d). ITC measurements for the interaction between active KRASQ61H and RAF-RBD (Supplementary Fig. 3f;  $K_d = 1.1 \mu\text{M} \pm 0.7 \mu\text{M}$ ) and SHANK3 SPN-ARR (Fig. 2c;  $K_d = 5.4 \mu\text{M} \pm 0.7 \mu\text{M}$ ) under the same buffer conditions showed a relatively small difference in affinities, further strengthening our hypothesis that SHANK3 competes with RAF-RBD for KRAS binding.

We then examined whether KRAS effector recruitment was affected in the absence of SHANK3. Silencing of endogenous *SHANK3* enhanced RAF-RBD and KRASG12V interaction in cells, as determined using an established cell-based FRET assay for KRAS effector recruitment (Fig. 3e)<sup>44</sup>. Collectively, these data indicate that SHANK3 can effectively compete with RAF to interact with mutant KRAS and thus may be able to influence KRAS downstream signalling in cells.

The MAPK/ERK pathway is a critical signalling node in KRAS-mutant cancers. Active RAS mutants recruit RAF to signal through this pathway to induce ERK phosphorylation and nuclear translocation, and to promote ERK-dependent cell proliferation<sup>8,9</sup>. We thus sought to test whether the ability of SHANK3 to compete with RAF for active KRAS binding could subsequently modulate downstream MAPK/ERK signalling. Transient overexpression of SHANK3 SPN WT in KRAS-mutant HCT-116 cells significantly decreased ERK1/2 phosphorylation (Fig. 3f) and diminished ERK1/2 nuclear translocation in KRAS-mutant MIA PaCa-2 cells (Fig. 3g). The KRAS-binding-deficient SPN mutant (R12E/K22D), in contrast, did not suppress ERK1/2 phosphorylation (Fig. 3f) or affect ERK1/2 translocation to the nucleus (Fig. 3g). In line with SHANK3 SPN-mediated attenuation of ERK-activity, SHANK3 SPN



WT overexpression, but not SPN R12E/K22D, in HCT-116 cells restrained *KRAS*-driven tumour growth in the chick embryo CAM CRC xenografts (Fig. 3h).

Together, these data demonstrate that SHANK3 SPN competes with RAF for active *KRAS* binding and limits oncogenic signalling via the MAPK/ERK pathway.

**SHANK3 depletion triggers cell death through RAS-MAPK pathway hyperactivation**

Recent studies indicate that the level of MAPK/ERK activity in tumour cells needs to be carefully maintained within a precise range; the signalling has to be sufficiently high to support tumour growth and yet below the toxic level that triggers apoptosis or senescence<sup>31–33,45–47</sup>.

**Fig. 3 | SHANK3 competes with RAF for the binding of active KRAS and limits downstream MAPK/ERK signalling.** **a** Representative images of GFP-SHANK3 and mCherry-KRASG12V localisation in A549 cells (maximum projections shown; one experiment with this cell line). Insets and yellow arrows indicate colocalization of GFP-SHANK3 with mCherry-KRASG12V at membrane protrusions. **b** KRAS–SHANK3 SPN-ARR in an open conformation modelled by aligning the RBD and SPN domains of RAF and SHANK3, respectively, on a membrane composed of POPC (1-Palmitoyl-2-oleoyl-sn-glycero-3-phosphocholine)/ Phosphatidylinositol 4,5-bisphosphate/ Cholesterol. **c** Structural alignment between KRAS–SHANK3 SPN-ARR (model) and nanodisc-bound KRAS–RAF complex (PDB:6PTW). **d** Analysis of RAF-RBD–KRAS binding in the presence of the SHANK3 SPN domain using the depicted pull-down assay. Samples were resolved on SDS-PAGE gel and stained with Coomassie. A representative gel is shown (three independent experiments). **e** Quantification of relative FRET efficiency between GFP-KRASG12V (FRET donor) and mRFP-RAF-RBD (FRET acceptor) in siCTRL or siSHANK3 (smartpool SHANK3 siRNA) HEK293 cells. Shown are the individual data points [mean  $\pm$  s.d.,  $n = 79$  (siCTRL) or 87 (siSHANK3)] from three independent experiments. Unpaired two-tailed Student's *t*-test with

Welch's correction]. **f** A representative immunoblot and quantification of ERK activation levels (phospho-ERK1/2 (Thr202/Y204) / total ERK relative to loading) in HCT-116 cells expressing GFP-SHANK3 SPN WT or GFP-SHANK3 SPN R12E/K22D (data represent the individual values; mean  $\pm$  s.d.; mean of control is set to 1.0 by definition; three independent experiments; Kruskal-Wallis one-way ANOVA and Dunn's post hoc test). **g** Representative confocal images (middle plane) and quantification of nuclear ERK (indicating ERK activity) in MIA PaCa-2 cells. Yellow arrowheads point to representative nuclei. N/C, nuclear to cytoplasmic ratio. Shown are the individual data points and the population average of each biological replicate (mean  $\pm$  s.d.; three independent experiments; one-way ANOVA with Holm-Sidak's multiple comparison test). **h** Representative images and quantification of tumour growth of HCT-116 cells, transiently expressing GFP-SHANK3 SPN WT or GFP-SHANK3 SPN R12E/K22D, on CAMs. Tumours are delimited by the yellow circles [mean  $\pm$  s.d.;  $n = 21$  (GFP, SPN WT) or 19 (SPN R12E/K22D) tumours from two independent experiments; Kruskal-Wallis one-way ANOVA and Dunn's post hoc test]. Source data are provided as a Source Data file.

We observed a marked increase in ERK1/2 phosphorylation in *SHANK3*-silenced *KRAS*-mutant pancreatic (PANC-1) and lung (A549) cancer cells (Fig. 4a), while AKT activity was not significantly changed (Supplementary Fig. 4a). In some experiments ERK and AKT total protein levels were also decreased upon *SHANK3*-silencing. However, this varied greatly between experiments and was not significant. In contrast, ERK activity was not significantly affected in WT *KRAS* pancreatic (BxPC3) and colorectal (HT-29) cancer cells upon *SHANK3* loss (Supplementary Fig. 4b, c). To further validate these results in living *SHANK3*-silenced cells on the single cell level, we used an ERK kinase translocation reporter (ERK-KTR)<sup>48</sup> that shuttles between the cytoplasm and the nucleus in response to changes in ERK activation state (Fig. 4b). *SHANK3* silencing in PANC-1 cells significantly increased the cytoplasmic-to-nuclear (C/N) ratio of the KTR, indicative of increased ERK activity, compared to control cells. These data further demonstrate that the loss of *SHANK3* induces MAPK/ERK signalling hyperactivation in *KRAS*-mutant cells (Fig. 4b).

In addition to ERK hyperactivation, *SHANK3* silencing significantly increased the levels of cleaved-PARP1 in PANC-1 and A549 cells (Fig. 4a, c), and the number of Annexin V/PI-positive PANC-1 cells (Fig. 4d and Supplementary Fig. 5). In contrast, cleaved-PARP1 levels were not markedly increased in WT *KRAS* HT-29 cells in the same conditions (Supplementary Fig. 4c). Moving from 2D to 3D and in vivo, *SHANK3* silencing impaired PANC-1 spheroid formation and growth in Matrigel (Fig. 1b) and significantly increased the number of Annexin V-positive apoptotic cells over time (Fig. 4e). We also detected notably higher cleaved caspase-3 staining in *SHANK3*-silenced *KRAS*-mutant A549 CAM tumours, compared to control tumours (Fig. 4f). These data indicate that loss of *SHANK3* induces apoptosis in *KRAS*-mutant cells.

We then asked whether the cytotoxic effects of *SHANK3* silencing in *KRAS*-mutant cells depend on the increased activity of the MAPK/ERK pathway. First, we treated PANC-1 cells with low doses of the MEK inhibitor trametinib and analysed cell proliferation (measured as confluence %) (Fig. 4g–i). In control silenced cells, trametinib inhibited ERK activation (Fig. 4g), but had no effect on cell proliferation (Fig. 4h). In *SHANK3*-silenced cells, trametinib clearly dampened the elevation in ERK activity observed following *SHANK3* loss and counteracted the proliferation defect in a dose- and time-dependent manner (Fig. 4g–i, Supplementary Fig. 6a). Of note, we found that the highest trametinib concentration (1  $\mu$ M) increased *SHANK3* protein expression/stability in control cells (Fig. 4g), which is in line with a previous study reporting ERK-mediated downregulation of *SHANK3* protein stability in neurons<sup>49</sup>. Next, we measured the proliferation/viability of PANC-1 cells treated with the MEK inhibitor selumetinib or the ERK inhibitor SCH72984. MEK or ERK inhibition had no/modest effect on cell viability of control-silenced cells (Fig. 4j, k; as previously described<sup>50</sup>), whereas both selumetinib and SCH72984 partially rescued the

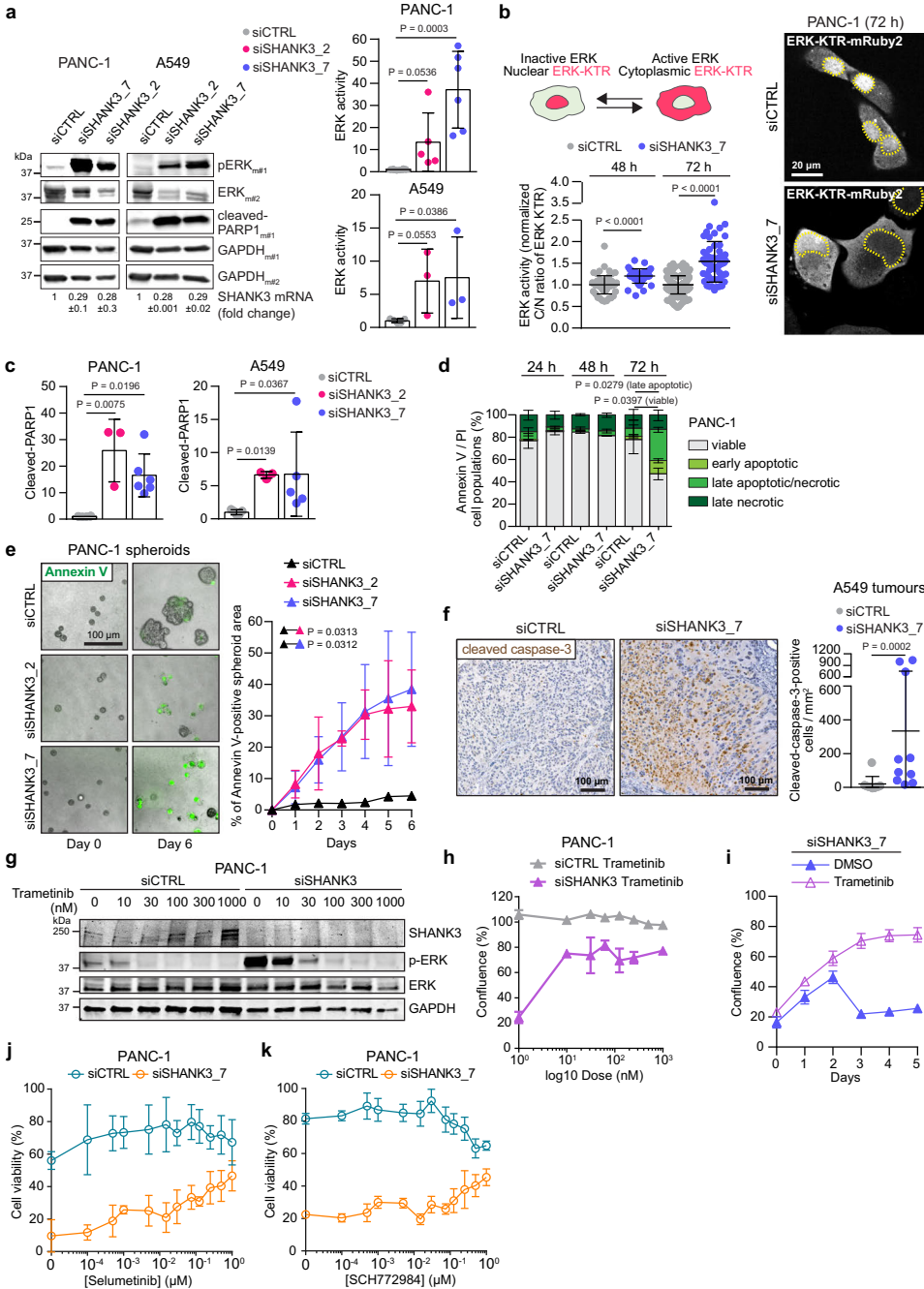
proliferation defect of *SHANK3*-silenced cells in a dose-dependent manner (Fig. 4j, k). Notably, inhibition of integrin signalling with Rap1 or focal adhesion kinase (FAK) inhibitors did not rescue the observed phenotype (Supplementary Fig. 6a–c); However, we cannot formally exclude that Rap1 or FAK functions not influenced by the inhibitors contribute to siSHANK3-induced apoptosis. On the other hand, *KRAS* silencing inhibited *SHANK3*-silencing-induced ERK activation and PARP1 cleavage and showed a modest trend towards increasing cell viability (Supplementary Fig. 6d–f). Finally, we tested whether overexpression of mutant active *KRAS* would override the inhibition of endogenous *SHANK3* and trigger hyperactivation of ERK and apoptosis in *KRAS*-mutant cells. Overexpression of GFP-KRASG12V failed to hyperactivate ERK or trigger substantial apoptosis in A549 cells (Supplementary Fig. 6g, h). This is most likely due to significant upregulation of endogenous *SHANK3* (Supplementary Fig. 6g, h), suggesting that *KRAS*-mutant cells are able to fine-tune *KRAS* signalling via altered *SHANK3* expression. The exact mechanism of this crosstalk will be interesting to explore in the future.

These results indicate that the anti-proliferative effects and reduced cell viability triggered by *SHANK3* depletion in *KRAS*-mutant cells are linked to dysregulated MAPK/ERK activity and not due to increased integrin signalling in these cells<sup>34</sup>.

### **SHANK3 depletion impairs the growth of established KRAS-mutant tumours**

To evaluate the requirement of *SHANK3* in maintaining the growth of established tumours, we generated PANC-1 cell clones with a doxycycline (dox)-inducible shRNA against *SHANK3* (Fig. 5a). Dox-induced *SHANK3* depletion suppressed cell proliferation in vitro similar to the siRNA approach (Fig. 5a–e and Supplementary Figs. 7 and 8). Consistent with the results obtained by siRNA-mediated silencing, inducible silencing of *SHANK3* (shRNA targeting sequence is distinct from the two siRNAs) strongly increased ERK phosphorylation and, consequently, PARP1 cleavage in a time-dependent fashion (Fig. 5b and Supplementary Fig. 7). The induction of *SHANK3* silencing also abolished the growth of established 3D spheroids and was accompanied by a significant increase in AnnexinV-positive regions within the spheroids over time (Fig. 5c–e and Supplementary Fig. 8). To further investigate the apoptotic pathways activated by *SHANK3* loss, we analysed the activity of caspases. *SHANK3*-silenced cells showed notably higher caspase-3 and caspase-8 activity in a time-dependent manner (Fig. 5f, g; activity peak at 5 days post dox induction), whereas caspase-9 showed no elevated activity (Supplementary Fig. 9). These data indicate that *SHANK3* depletion induces caspase-3/caspase-8-dependent apoptosis in *KRAS*-mutant cells.

To study the effect of dox-induced *SHANK3* depletion in established tumours in vivo, we implanted sh*SHANK3*-expressing



PANC-1 cells into the flanks of athymic Nude mice, allowed tumours to form (~100 mm<sup>3</sup>) and thereafter subjected the mice to a dox-supplemented or normal diet (Fig. 5h). shRNA induction was monitored by imaging red fluorescence (tRFP reporter) and tumour growth was followed bi-weekly. *SHANK3* depletion in the established tumours led to robust inhibition of tumour growth when

compared to control tumours (Fig. 5i, j and Supplementary Fig. 10). At the end of the experiment, *SHANK3* mRNA expression remained significantly suppressed in the dox-induced tumours (Fig. 5k). The reduced growth of established tumours upon *SHANK3*-depletion was also reflected in the tumour masses at the end of the experiment (Fig. 5l). These in vivo data highlight the potential of *SHANK3*



**Fig. 4 | SHANK3 depletion triggers RAS-MAPK pathway hyperactivation and apoptosis in KRAS-mutant cells.** **a** ERK activity in PANC-1 and A549 cells post SHANK3 silencing (3 days). Samples blotted on duplicate membranes, m#1 and m#2. SHANK3 mRNA levels (fold change) indicated below [mean  $\pm$  s.d.; PANC-1,  $n = 8$  (siCTRL), 5 (siSHANK3\_2) or 6 (siSHANK3\_7); A549,  $n = 5$  (siCTRL) or 3 (siSHANK3\_2 and siSHANK3\_7) independent experiments; Kruskal-Wallis one-way ANOVA and Dunn's post hoc tests]. **b** Confocal images of ERK-KTR-mRuby2-expressing siCTRL and siSHANK3 cells (nuclei outlined by yellow dashed lines). **c** N, ERK-KTR-mRuby2 cytoplasmic/nuclear ratio [mean  $\pm$  s.d.;  $n = 61$  (siCTRL, 48 h), 38 (siSHANK3\_7, 48 h), 185 (siCTRL, 72 h) or 59 (siSHANK3\_7, 72 h) cells from three independent experiments; unpaired two-tailed Student's *t*-test with Welch's correction]. **c** Immunoblotting analysis of cleaved-PARP1 from 4a [mean  $\pm$  s.d., normalized to siCTRL; PANC-1,  $n = 6$  (siCTRL, siSHANK3\_7) or 3 (siSHANK3\_2); A549,  $n = 5$  (siCTRL, siSHANK3\_7) or 3 (siSHANK3\_2) independent experiments; Kruskal-Wallis and Dunn's post hoc tests]. **d, e** siSHANK3 PANC-1 cell death in 2D (annexin

V-FITC flow cytometry analysis, **d**) and 3D (annexin-positive spheroid area, **e**) [mean  $\pm$  s.d.; five independent experiments; unpaired two-tailed Student's *t*-test with Welch's correction (**d**); one-way ANOVA with Holm-Sidak's multiple comparison test at endpoint (**e**)]. **f** Cleaved caspase-3-positive cells in siSHANK3 A549 tumours (CAM assay) (mean  $\pm$  s.d.;  $n = 10$  tumours from two independent experiments; two-tailed Mann-Whitney test; no/residual siSHANK3 PANC-1 tumours detected). **g** ERK activity in siSHANK3 PANC-1 cells  $\pm$  MEK inhibitor (trametinib) (two independent experiments). **h** siSHANK3 PANC-1 cell proliferation (confluence % at day 5)  $\pm$  trametinib (mean  $\pm$  s.d.;  $n = 4$  technical replicates; representative of three independent experiments). **i** siSHANK3 PANC-1 cell proliferation  $\pm$  300 nM trametinib over time (mean  $\pm$  s.e.m.;  $n = 4$  technical replicates; representative of three independent experiments). **j, k** siSHANK3 PANC-1 cell viability  $\pm$  selumetinib (MEK inhibitor) (**j**) or SCH772984 (ERK inhibitor) (**k**) [mean  $\pm$  s.d.;  $n = 4$  (**j, k** siSHANK3) or 3 (**k**, siCTRL) technical replicates; representative of three independent experiments]. Source data are provided as a Source Data file.

targeting as an anti-cancer therapy in pre-existing KRAS-mutant tumours.

### Nanobodies disrupting the SHANK3-KRAS interaction drive KRAS-mutant cells into apoptosis

To further explore the possibility of SHANK3 targeting as a therapeutic vulnerability, we generated nanobodies that interfere with the SHANK3-KRAS interaction and assessed their efficacy in KRAS-mutant cancer cells. A phage display library screen identified two distinct single-domain antibody fragments (VHH-binders; nanobodies A01 and E01) directed against the SHANK3 SPN domain. Using MST, the affinity of the E01 nanobody for SHANK3 was determined to be  $137 \pm 6$  nM (Supplementary Fig. 11). We detected clear binding of A01 to SHANK3; however, the relatively low affinity precluded precise affinity determination. Both nanobodies robustly inhibited SHANK3-KRAS-GTP interaction in an enzyme-linked immunosorbent assay (ELISA) as well as in *in vitro* pull-down assays (Fig. 6a, b). When expressed in cells, both anti-SHANK3 SPN nanobodies co-precipitated endogenous SHANK3 (Fig. 6c). In functional viability studies with KRAS-mutant pancreatic (PANC-1) and lung (A549 and H441) cancer cells, both nanobodies increased the number of Annexin V-positive apoptotic cells (Fig. 6d, e and Supplementary Fig. 12). Finally, while control cells rapidly formed tumours in the CAM xenograft model, overexpression of A01 and E01 anti-SHANK3 nanobodies significantly reduced the KRAS-driven tumour growth (Fig. 6f). These data indicate that disrupting SHANK3 interaction with KRAS results in a similar loss of cell viability and apoptosis induction in KRAS-mutant cells as with RNAi-mediated SHANK3 depletion (Fig. 6g).

Together, these findings support the concept that hyperactivating the RAS-MAPK pathway in KRAS-mutant cells by ablating SHANK3 could have a therapeutic impact on KRAS-mutant cancers.

### Discussion

Our work identified the SHANK3 scaffold protein as an essential regulator of active and mutant KRAS. SHANK3 directly interacts with KRAS, competes with RAF for KRAS binding on the plasma membrane, and sets downstream MAPK/ERK signalling to an optimal level to sustain proliferative capacity and prevent active ERK levels from reaching a lethal signalling threshold (Fig. 6g). We demonstrate that by disrupting the SHANK3-KRAS interaction, thus removing an endogenous KRAS signalling brake, we can trigger cytotoxic ERK activity that results in reduced cell proliferation, apoptosis induction and impaired tumour growth in KRAS-mutant xenograft models. This indicates that KRAS-driven cancer cells require intermediate levels of SHANK3-KRAS association to support tumour growth (Fig. 6g).

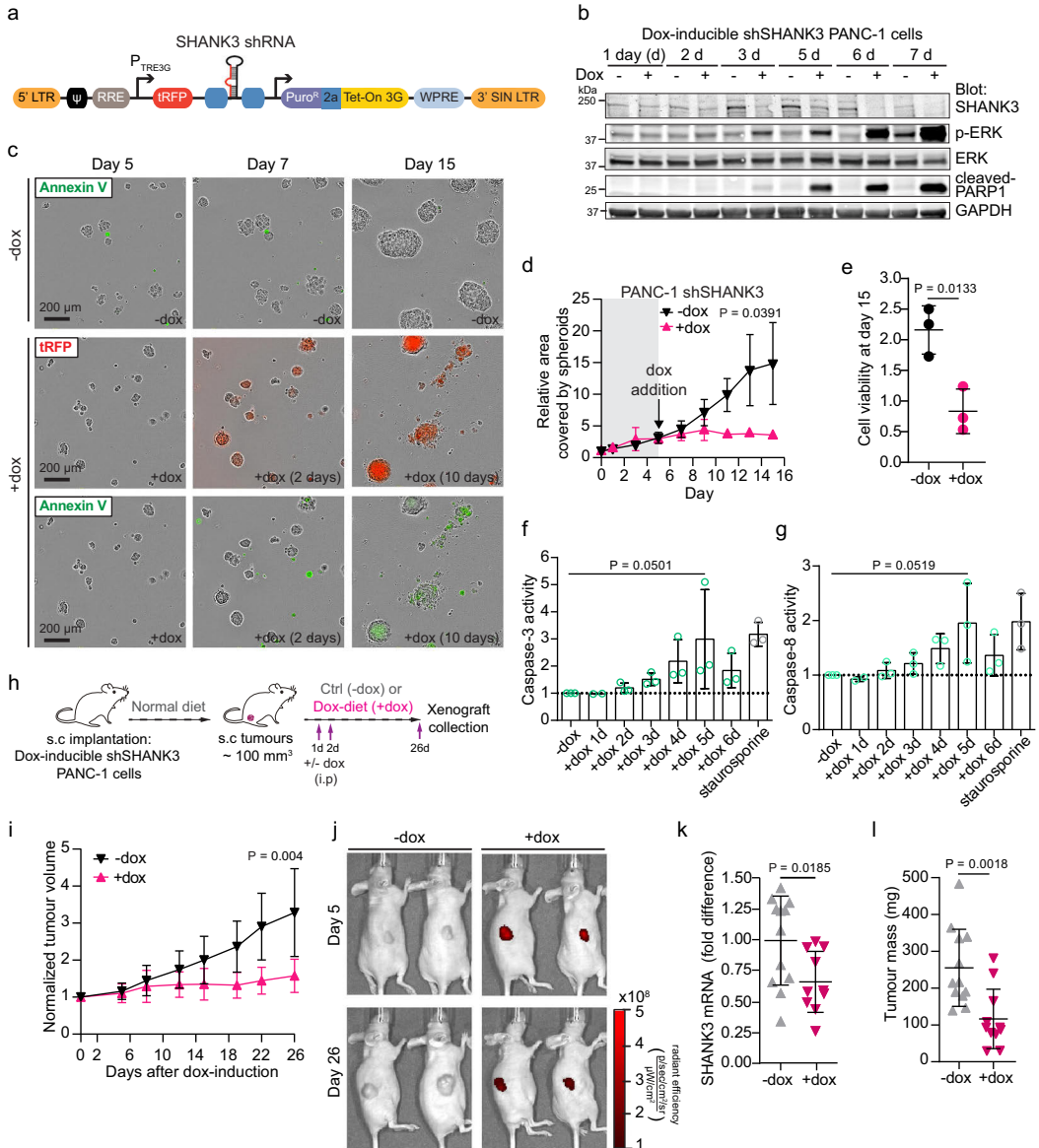
Targeting SHANK3 to induce RAS-MAPK hyperactivation-induced apoptosis represents an example of the emerging concept of context-specific lethality of oncogenic pathway activation<sup>51,52</sup>. Firstly, we show

that SHANK3 binding to oncogenic KRAS does not depend on specific KRAS-activating mutations. Therefore, targeting the SHANK3-KRAS interaction could represent a pan-KRAS-mutant compatible strategy for the selective killing of KRAS-mutant cancer cells. Secondly, while the current efforts strive to develop KRAS inhibitors<sup>12,15-17,53</sup>, we describe a mechanism to hyperactivate KRAS-MAPK signalling to cytotoxic levels by disrupting KRAS interaction with SHANK3. This is in line with the recently emerging concept of pathway overactivation as an exploitable vulnerability in cancer<sup>33,47,51,52</sup>.

We provide proof-of-concept evidence of the ability of inhibitors targeting the SHANK3-KRAS interaction to trigger apoptosis and limit the growth of KRAS-mutant cancers. Although targeting intracellular proteins by antibodies has been difficult, the use of nanobodies with nanoparticles and cell-penetrating peptides offers new opportunities<sup>54,55</sup>. Furthermore, pharmaceutical development of small molecule inhibitors of protein-protein interactions has recently become possible, as exemplified by the successful generation of BH3-mimetics<sup>56</sup>. Similarly, several siRNA therapeutics have already gained FDA approval<sup>57-59</sup>. Our findings that KRAS-mutant tumour growth can be inhibited in *in vivo* settings either by modulating SHANK3 expression or by blocking SHANK3-KRAS protein-protein interaction using nanobodies, demonstrate that SHANK3 might represent a therapeutic vulnerability in KRAS-mutant cancers.

Many important questions remain to be investigated regarding the emerging but currently incompletely understood concept of hyperactivation-induced cell death. Focusing here on the SHANK3-dependent pathway, the detailed mechanism of SHANK3 control of ERK signalling is not fully characterized. We show that SHANK3 depletion hyperactivates ERK and induces cell death, which can be rescued by three distinct MEK/ERK inhibitors. However, KRAS silencing does not fully restore cell viability and the KRAS-binding SPN-domain alone fails to rescue cell viability in siSHANK3 cells. These data imply that SHANK3 control of apoptosis extends beyond the KRAS-RAF interaction. SHANK3 is a large multi-domain scaffold protein binding to cell surface receptors and actin in the postsynaptic density of neurons<sup>36,60</sup>. At present, SHANK3 has not been widely investigated beyond the central nervous system and currently unknown protein interactions and biology may enable SHANK3 to control not only ERK activity but its spatial localisation in cells in a manner that contributes to limiting pathway activity. Furthermore, SHANK3 interacts with ERK and ERK regulates SHANK3 stability<sup>49</sup>, implying a possibly complex crosstalk between the two proteins.

Oncogene overactivation-induced loss of cell viability was recently reported for several distinct oncogenic pathways and seems in all cases to be dependent on further activation of an already highly active signalling axis<sup>33,51,52</sup>. How cancer cells recognise favourable versus unfavourable levels of oncogenic signalling is not clear. In terms of SHANK3, this recognition may translate into tight modulation of its



expression levels. We find that overexpression of mutant active KRAS in KRAS-mutant cells fails to over-activate KRAS-ERK signalling and trigger cell death, most likely owing to a concomitant upregulation of endogenous SHANK3. Thus, cancer cells seem to optimally regulate oncogenic signalling below a cytotoxic level and we propose SHANK3 inhibition of KRAS interaction as one mechanism employed by KRAS-mutant cancer cells to prevent signalling overdose. While the mechanisms regulating SHANK3 expression in cancer remain to be elucidated, investigating the impact of oncogene-induced stress on SHANK3 expression could shed light on its potential involvement in tumorigenesis. In addition, understanding how SHANK3 regulates physiological RAS signalling in response to growth factors or the interplay between SHANK3 and other RAS-binding partners might

offer insights into KRAS-driven cancer development. Our study has focused on the SHANK3 role in modulating KRAS signalling, however, the SHANK3 RA-like domain can interact with other RAS family members<sup>34,35</sup>. Therefore, it is possible that SHANK3 has a broader role in other RAS-isoform-driven cancers but this remains to be validated. Lastly, while the safety concerns regarding SHANK3 targeting are mitigated by the observation that individuals with genetic SHANK3 loss (Phelan-McDermid syndrome) do not exhibit increased tumour formation, this aspect requires thorough investigation.

In summary, our work provides an important example of conditional pathway activation limiting viability of KRAS-mutant cancers. We have discovered here that SHANK3 control of ERK activity is essential for cancer cell viability. Therefore, SHANK3 emerges as a

**Fig. 5 | *SHANK3* depletion impairs the growth of pre-existing *KRAS*-mutant PDAC tumours.** **a** A schematic representation of the lentiviral vector for tetracycline/doxycycline (dox)-inducible synthesis of *SHANK3* shRNA with a tRFP (TurboRFP) reporter for visual confirmation of shRNA expression following dox induction. 5'LTR, 5' long terminal repeat;  $\Psi$ , Psi packaging sequence; PuroR, puromycin resistance gene; 2a, self-cleaving peptide; WPRE, Woodchuck Hepatitis Post-transcriptional Regulatory Element; 3' SIN LTR, 3' Self-inactivating Long Terminal Repeat (see methods for more detail). **b** ERK activation kinetics in sh*SHANK3* *KRAS*-mutant cells. Representative immunoblots showing SHANK3, p-ERK and cleaved-PARP1 levels in control (-dox) and dox-induced (+dox) sh*SHANK3*-expressing PANC-1 cells (mix of two independent clones) collected at different time points. GAPDH, loading control ( $n = 3$  three independent experiments). **c–e** Analysis of the growth and viability of sh*SHANK3*-expressing PANC-1 spheroids  $\pm$  dox (dox added at day 5, when spheroids were established, and continued until day 15). Representative images show *SHANK3* depletion as observed by the tRFP reporter and apoptotic Annexin V-positive cells (**c**). Quantification of

spheroid growth over time (**d**), shaded region denotes sphere growth prior to treatment and cell viability at endpoint (**e**) (mean  $\pm$  s.d. from  $n = 3$  independent experiments; unpaired two-tailed Student's *t*-test with Welch's correction at endpoint). **f, g** Caspase-3 (**f**) and caspase-8 activity (**g**) in sh*SHANK3*-expressing PANC-1 cells  $\pm$  dox at the indicated time points (shown is normalized fluorescence intensity). Staurosporine used as a positive control (mean  $\pm$  s.d.;  $n = 3$  independent experiments; one-way ANOVA with Holm-Sidak's multiple comparison test). **h–l** Analysis of the growth of established tumours in mice following *SHANK3* depletion. **h** Outline of animal experiments. **i** Tumour volumes after starting the dox treatment (normalised to tumour volumes at the start of dox induction). **j** Representative IVIS images of the tRFP reporter expression in tumours 5 and 26 days after dox induction. **k** *SHANK3* gene expression (mRNA levels) in tumours at the end of the experiment. **l** Tumour weights at the end of the experiment (26 days after dox-induction) (data represent individual tumours and the mean  $\pm$  s.d.;  $n = 11$  (-dox) and 12 (+dox) tumours; unpaired Student's *t*-test with Welch's correction). Source data are provided as a Source Data file.

cancer vulnerability across different *KRAS*-mutant cells and cancer types.

## Methods

All animal experiments were ethically assessed and authorised by the National Animal Experiment Board and in accordance with The Finnish Act on Animal Experimentation (Animal license numbers ESAVI/9339/2016 and ESAVI/37571/2019). All experiments respected the maximum tumour diameter (15 mm) permitted by the authorisation bodies.

### Cell lines and culture

All cell lines were purchased from ATCC, unless otherwise indicated. PANC-1 (Cat. no. CRL-1469), AsPC-1 (Cat. no. CRL-1682) SW1990 (Cat. no. CRL-2172) PaTu8902 (Cat. no. ACC 179, DSMZ), MIA PaCa-2 (Cat. no. CRL-1420) (*human* pancreatic ductal adenocarcinoma cell lines), A549 (*human* lung adenocarcinoma) (Cat. no. CCL-185), HCT-116 (*human* colorectal carcinoma) (Cat. no. CCL-247), HT-29 (*human* colorectal adenocarcinoma) (Cat. no. HTB-38) and HEK293 (*human* embryonic kidney) (Cat. no. CRL-1573) cells were grown in DMEM (Dulbecco's modified Eagle's medium; Cat. no. D5796, Sigma-Aldrich) supplemented with 10% FBS and 2 mM L-glutamine (Cat. no. G7513-100ML, Sigma-Aldrich).

Su86.86 (*human* pancreatic adenocarcinoma) (Cat. no. CRL-1837), YAPC (*human* pancreatic carcinoma) (Cat. no. ACC 382, DSMZ), H441 (*human* lung adenocarcinoma) (Cat. no. HTB-174), HCT-15 (*human* colorectal adenocarcinoma) (Cat. no. CCL-225), H292 (*human* lung carcinoma) (Cat. no. CRL-1848) and H226 (*human* lung squamous cell carcinoma) (Cat. no. CRL-5826) cells were cultured in RPMI-1640 medium supplemented with 10% FBS and 2 mM L-glutamine.

BXP-3 (Cat. no. CRL-1687) and Panc10.05 (Cat. no. CRL-2547) (*human* pancreatic adenocarcinoma) cells were cultured in RPMI-1640 medium supplemented with 10% FBS and 2 mM L-glutamine plus 10 units/ml *human* recombinant insulin (Cat. no. I9278-5ML, Sigma-Aldrich) for the Panc10.05 cells only. ARPE-19 (*human* retinal pigmented epithelium) (Cat. no. CRL-2302) cells were grown in DMEM:F12 (Cat. no. I1320074, Gibco) supplemented with 10% FBS and 2 mM L-glutamine.

Cells were regularly tested by MycoAlert™ Mycoplasma Detection Kit (Cat. no. LT07-418, Lonza) with MycoAlert™ Assay Control Set (Cat. no. LT07-518, Lonza) and found to be free from mycoplasma contamination. All cell lines were authenticated by STR profiling using the services of the Leibniz Institute DSMZ.

### siRNAs and DNA constructs

The siRNAs used were SMARTpool ON-TARGETplus *Human SHANK3* siRNA (Cat. no. L-024645-00-0010, Dharmacon™, Horizon Discovery), individual *Human SHANK3* siRNA\_2 (Cat. no. S100717110

Hs\_SHANK3\_2 siRNA, Qiagen; target sequence: 5'-CAGGGATGTC GCAACTACAA -3'), individual ON-TARGETplus *Human SHANK3* siRNA\_7 (Cat. no. J-024645-07, Dharmacon™, Horizon Discovery; target sequence: 5'-GGGCTTCACCTGACTACAA -3') and ON-TARGETplus *Human KRAS* siRNA SMARTpool (Cat. no. L-005069-00-0010, Dharmacon™, Horizon Discovery). The control siRNA was Allstars negative control siRNA (Cat. no. I027281, Qiagen).

EGFP-tagged SPN domain and mRFP-tagged SHANK3 were generated previously<sup>34</sup>. pHAGE-EGFP-Shank3 (GFP-SHANK3 WT) was kindly supplied by Alex Shcheglovitov. The R12E/K22D mutation was introduced by site-directed mutagenesis (Gene Universal). pmGFP-KRASG12V and mRFP-RBD with the RAS binding domain (RBD) of CRAF have been described earlier<sup>61,62</sup>. The pmCherry-KRASG12V construct was generated by replacing pmGFP from pmGFP-KRASG12V with pmCherry from the pmCherry-C1 vector (Clontech Laboratories Inc.) using NheI and BsrGI restriction sites. DsRed-KRASG12V has been described before<sup>63</sup> and was a gift from James Lorens. His6-KRASQ61H (Plasmid #25153, Addgene) was a gift from Cheryl Arrowsmith. pLentiPGK-Blast-DEST-ERKTRmRuby2 (Plasmid #90231, Addgene) was a kind gift from Markus Cover<sup>48</sup>. mCherry-tagged anti-SHANK3-SPN nanobodies A01 and E01 were generated by Hybrigenics. In addition, pEGFP-C1 and pHAGE-CMV-eGFP-W (PlasmID, Harvard Medical School) and pmCherry-C1 were used as controls.

### Generation of ERK biosensor cells

HEK293T packaging cells were co-transfected with pMDLg/prRE (Plasmid #12251, Addgene), pRSV-Rev (Plasmid #12253, Addgene), pMD2.G (Plasmid #12259, Addgene) and pLentiPGK-Blast-DEST-ERKTRmRuby2, using Lipofectamine 3000 (Cat. no. L3000-015, Life Technologies) as per the manufacturer's instructions. Packaged lentiviruses were then applied to PANC-1 cells in the presence of polybrene (8  $\mu$ g/ml, Cat. no. TR-1003-G, Sigma-Aldrich) and incubated overnight. Successfully transduced cells were then selected using blasticidin (6  $\mu$ g/ml, Cat. no. I5205, Sigma-Aldrich).

### Generation of doxycycline-inducible sh*SHANK3* PANC-1 cell line

SMART lentiviral shRNA vectors for doxycycline-inducible suppression of *human SHANK3* gene expression were purchased from Dharmacon as viral particles (Dox-inducible SMARTvector sh*SHANK3*, Cat. no. V3SH7669-228381856, Dharmacon). The lentiviral vector contains a PTRE3G inducible promoter (Fig. 5a). The tetracycline response element is activated by the Tet-On® 3G transactivator protein in the presence of dox. The vector also contains a TurboRFP reporter (visual tracking of expression upon dox induction), a puromycin resistance gene, a self-cleaving peptide (enables the expression of both PuroR and Tet-On® 3G transactivator from a single RNA pol II promoter) and Tet-On® 3G (encodes the dox-regulated transactivator protein, which binds to PTRE3G promoter in the presence of dox).

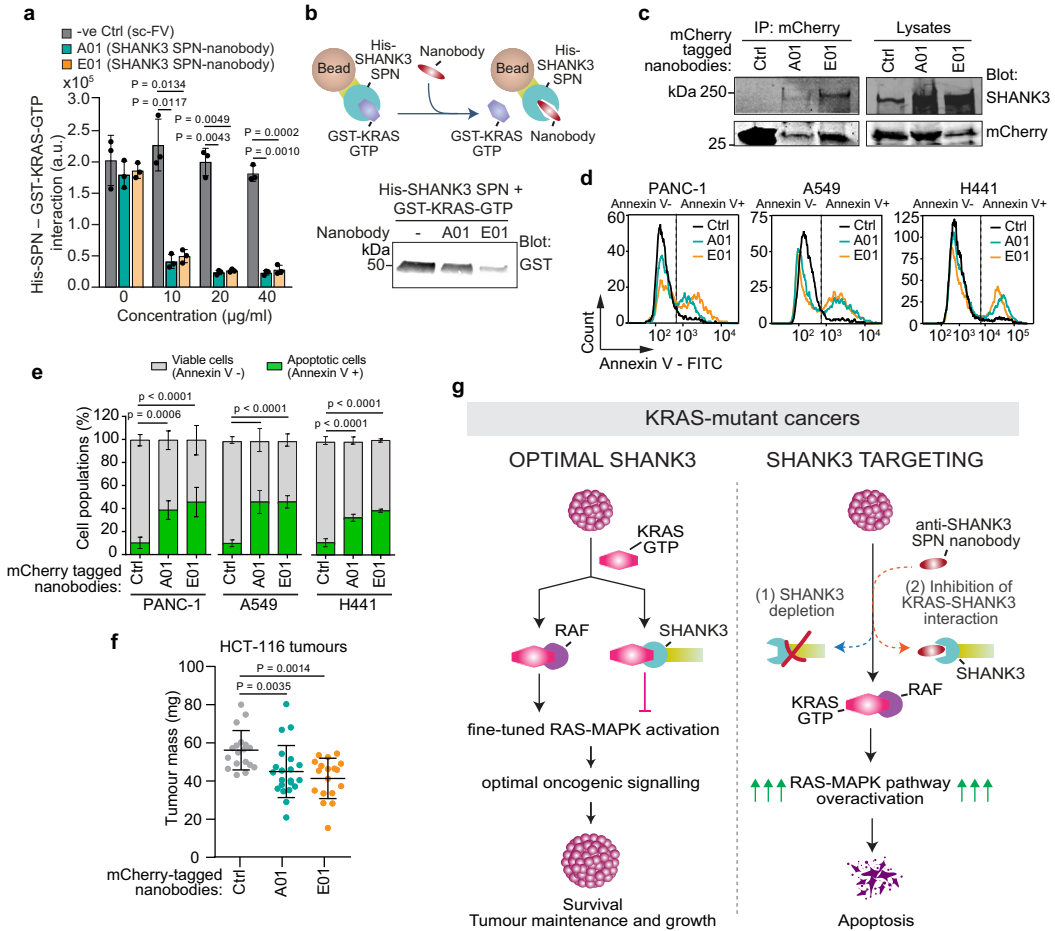


**Fig. 6 | Targeting of KRAS–SHANK3 interaction by anti-SHANK3 nanobodies induces apoptosis and inhibits KRAS-driven tumour growth.** **a–c** The inhibitory function of anti-SHANK3 SPN nanobodies on KRAS–SHANK3 interaction. **a** The effect of two independent SHANK3 SPN nanobodies (A01 and E01) at the indicated concentration on the binding of His-tagged SHANK3 SPN to GST-tagged KRAS-GTP as measured by ELISA (data are mean  $\pm$  s.d. of the Eu-signal; three independent experiments; Unpaired two-tailed Student’s *t*-test with Welch’s correction). **b** Top: The experimental outline showing His-SHANK3 SPN pull-down of GST-KRAS-GTP in the presence of anti-SHANK3 SPN nanobodies. Bottom: A representative blot showing loss of SHANK3–KRAS interaction in the presence of the nanobodies ( $n = 2$  independent experiments). **c** Specificity analysis of anti-SHANK3 SPN nanobodies. A549 cells expressing mCherry alone (control; Ctrl) or mCherry-tagged anti-SHANK3 SPN nanobodies (A01, E01) were subjected to IP. A representative western blot, probed with the indicated antibodies is shown ( $n = 2$  independent experiments). **d, e**, Analysis of cell viability in the presence of anti-SHANK3 nanobodies. Representative flow cytometry assay histograms (**d**) and quantification (**e**) of

apoptosis (Annexin V-FITC-positive (+) cells) in PANC-1, A549 and H441 cells, expressing mCherry (Ctrl) or mCherry-tagged anti-SHANK3 SPN-nanobodies, 4 days after transfections [mean  $\pm$  s.d.;  $n = 3$  (PANC-1) and 4 (A549) independent experiments; two-way ANOVA and Sidak’s post hoc test; example scatter plots and gating strategy are shown in Supplementary Fig. 12]. **f** Analysis of tumour growth with HCT-116 cells transiently expressing mCherry-tagged anti-SHANK3 SPN nanobodies (A01 and E01) or mCherry (Ctrl) and inoculated on CAM membranes (data represent individual tumours and the mean  $\pm$  s.d.;  $n = 18$  (Ctrl, E01) or 21 (A01) tumours/treatment group; Kruskal-Wallis one-way ANOVA and Dunn’s post hoc test). **g** Schematic model of SHANK3-controlled cell fate in KRAS-mutant cancers. SHANK3 directly interacts with active KRAS and competes with RAF for KRAS binding to sustain oncogenic RAS-MAPK/ERK signalling at an optimal level (i.e. below toxic oncogenic signalling) in KRAS-mutant cancers. SHANK3 loss (1) or inhibition of SHANK3–KRAS interaction (2) drive KRAS-mutant cells into cell death. Source data are provided as a Source Data file.

Packaged lentiviruses (40 MOI) were applied to PANC-1 cells in the presence of polybrene (8  $\mu$ g/ml) for 48 h; first, cells were incubated with the transduction mix in serum-free medium for 20 h, and then full medium was added to cells without removing the transduction mix. Two days after transduction, the medium was replaced with full medium and cells were cultured for an additional 48 h. Four days after transduction, cells were selected using puromycin

(4  $\mu$ g/ml, Cat. no. 15205, Sigma-Aldrich). Single-cell clones were created by screening for high induction efficacy (bright tRFp-positive clones after dox-induction, indicative of shRNA expression). All established PANC-1 shSHANK3 expressing cell lines (single and a mix of clones 1C and 4S) were cultured in DMEM supplemented with 10% FBS and 2 mM L-glutamine, 2  $\mu$ g/ml puromycin. For doxycycline inductions, treatment (+ dox; 1–2  $\mu$ g/ml) was

started 24 h post-plating. Culture medium (+/- dox) was changed every 2nd day.

### Transient transfections

Lipofectamine 3000 and P3000™ Enhancer Reagent (Cat. no. L3000001, Thermo Fisher Scientific) or jetPRIME (Cat. no. 101000046, Polyplus) were used to transiently transfect cells with plasmids according to the manufacturer's protocol. siRNA silencing was performed using 30–67 nM siRNA (siRNA targeting *SHANK3* or negative control siRNA) and Lipofectamine® RNAiMAX Reagent (Cat. no. 13778075, Thermo Fisher Scientific) according to the manufacturer's protocol. Cells were cultured for 24 h with transfection reagents and, one day post-transfection, medium was changed to full culture medium, and cells were used for the experiments at the indicated time points.

### Proliferation assays using IncuCyte

**2D assay:** Cells were seeded on a 96-well plate and transfected with siRNAs on the following day, as described above. To perform a proliferation screen in multiple cancer cell lines, 5000–10000 cells were seeded in the 96-wells depending on the growth rate of control cells.

Inhibitor treatments were started a day post-silencing and cells were treated with complete medium containing DMSO (control), Trametinib (Cat. no. GSK1120212, Selleckchem), Rap1 inhibitor (Cat. no. GGTI 298, Sigma) or FAK inhibitor (FAK-14, Sigma) at the indicated concentrations. For sh*SHANK3* PANC-1 cells, dox induction (+dox; 2 µg/ml) was started 24 h post-plating. Culture medium with or without dox was changed every other day. Proliferation was measured for 4 days.

**3D spheroid assay:** Spheroid formation was performed with cells embedded between two layers of Matrigel<sup>®</sup>. Briefly, the inner wells of an angiogenesis 96-well µ-plate (Cat. no. 89646, Ibbidi GmbH) were coated with 10 µl of 50% Matrigel (diluted in full cell culture medium; Matrigel stock 9 mg/ml, Cat. no. 354230, Corning), centrifuged for 20 min at 200 g (4 °C) and incubated for 1 h at 37 °C. Next, the upper wells were filled with 20 µl of cell suspension in 25% Matrigel (500 cells/well), centrifuged for 10 min at 100 × g and incubated at 37 °C for 4–16 h. Wells were then filled with complete culture medium and spheroid formation was measured for 6–15 days. *SHANK3* depletion was induced by doxycycline (+ dox; 2 µg/ml) in established sh*SHANK3* PANC-1 spheroids at day 5. Annexin V (1:200, Annexin V-FITC Apoptosis Detection Kit, Cat. no. BMS500FI-300, eBioscience™) was added at the same time as dox and spheroid growth and apoptosis were monitored for 10 days. Culture medium (+/- dox and Annexin V) was changed every other day.

For both 2D and 3D assays, proliferation was measured using the IncuCyte S3 Live-Cell Analysis system (10x objective). Wells were imaged every 2 h (brightfield). Culture medium was changed every 2–3 days. Analysis was performed using IncuCyte S3 software. The analysis definition was set using the following parameters: segmentation (background-cells), clean-up (hole fill), filters (area, eccentricity, mean intensity, integrated intensity). A mask was set to the best fit of cell confluence to quantify the area covered by cells. Normalised proliferation was calculated from time-lapse imaging by dividing the area covered by cells at every time point by the area of the first time point ( $t = 0$ ; averaged reading used from replicate wells).

### Colony formation

Cells previously silenced with the indicated siRNAs for 24 h were seeded on a 6-well plate (250 cells/well) in full medium. The culture medium was changed every 2–3 days, ending the assay on day 10–14. Colonies were fixed with 4% paraformaldehyde (PFA) in phosphate-buffered saline (PBS) for 15 min and washed with PBS. Then, colonies were stained with 0.2% crystal violet in 10% ethanol for 10 min at room temperature and washed with PBS. Plates were scanned and analysed using a Colony area ImageJ plugin<sup>65</sup>.

### Cell viability assays

Annexin V-FITC/PI flow cytometry was used to evaluate apoptotic and necrotic cell death in cells cultured in monolayers. One to three days after silencing or four days post transfection of mCherry-tagged anti-*SHANK3* nanobodies (A01 and E01) or control-mCherry, cells were stained by Annexin V-FITC Apoptosis Detection Kit (Cat. no. BMS500FI-100, eBioscience™) according to the manufacturer's instructions. Apoptotic cells were detected using BD LSR Fortessa™ analyser (BD Biosciences).

The viability of *SHANK3*-silenced PANC-1 cells treated with ERK and MEK inhibitors was measured using Cell Counting Kit-8 (WST-8/CCK-8; Cat. no. ab228554, Abcam). Cells were silenced for 24 h as described above and then seeded on a 96-well plate with full medium containing DMSO (control), Selumetinib (ADZ6244; Cat. no. S1008, Selleckchem) or a selective ERK1/2 inhibitor (SCH727984; Cat. no. S7101, Selleckchem) at different concentrations (concentrations used: 0, 0.1 nM, 0.5 nM, 1 nM, 5 nM, 10 nM, 31.3 nM, 62.5 nM, 124 nM, 250 nM, 500 nM and 1 µM). Cell viability was measured 96 h after silencing (drugs for 72 h). For some 3D spheroid assays, growth/viability was measured using Cell Counting Kit-8 (WST-8/CCK-8; Cat. no. ab228554, Abcam) instead of IncuCyte. At culture end point, the medium was replaced with fresh medium supplemented with WST-8 solution and, after a 2 h incubation in the dark at 37 °C, absorbance was measured at 460 nm.

### Caspase activity assay

PANC-1 cells expressing doxycycline-inducible *SHANK3* shRNA were seeded in a 96-well plate (4000 cells/well) and treated with doxycycline (2 µg/ml) for 1–6 days. Untreated cells and cells treated for 24 h with staurosporine (2 µM) were used as controls. The activity of caspase-3, caspase-8 and caspase-9 was measured using a commercial kit (Cat. no. ab219915, Abcam) according to the manufacturer's instructions. Briefly, each caspase substrate as a 1X solution was diluted in 100 µl assay buffer per well and added to cells. Cells were incubated at room temperature in the dark for 30–60 min and caspase activity was evaluated by measuring fluorescence intensity (Ex/Em = 535/620 nm [red] for caspase-3, Ex/Em = 490/525 [green] for caspase-8 and Ex/Em = 370/450 nm [blue] for caspase-9) with a Synergy H1 Hybrid Multi-Mode reader (BioTek, Winooski, VT).

### Quantitative real-time polymerase chain reaction (qRT-PCR)

Total cellular RNA was extracted using the NucleoSpin® RNA kit (Cat. no. 740955.50 Macherey-Nagel), and 1 µg of the extracted RNA was used as a template for cDNA synthesis by high-capacity cDNA reverse transcription kit (Cat. no. 4368814, Applied Biosystems) according to the manufacturer's protocol. Tumours were homogenised with T 25 ULTRA-TURRAX® (Ika), and total RNA was extracted using TRIreagent™ (Cat. no. BIO-38032, Bioline Ltd). Expression levels of *SHANK3* were determined by TaqMan® qRT-PCR reaction using QuantStudio™ 12 K Flex Real-Time PCR System (Thermo Fisher Scientific). The level of glyceraldehyde 3-phosphate dehydrogenase (*GAPDH*) expression was used as a reference (endogenous control). Taqman® Universal Master Mix II included the necessary components for qRT-PCR reactions (Cat. no. 4440040, Thermo Fisher Scientific). TaqMan® Gene Expression Assays (Thermo Fisher Scientific) were used to detect *SHANK3* (Assay ID: Hs00873185\_m1) and *GAPDH* (Assay ID: Hs02786624\_g1). Relative quantification (RQ) of *SHANK3* levels was derived from three technical replicates by a comparative CT ( $\Delta\Delta Ct$ ) method using *GAPDH* levels as a reference.  $RQ_{\{min\}} = 2^{-\{\Delta\Delta Ct + SE\}}$  and  $RQ_{\{max\}} = 2^{-\{\Delta\Delta Ct - SE\}}$ , where SE is the standard error of the  $\Delta\Delta Ct$  values.

### Immunoblotting

Inhibitor treatments [DMSO control, Trametinib (GSK1120212, Selleckchem), Rap1 inhibitor (GGTI 298, Sigma) or FAK inhibitor (FAK-14, Sigma)], in complete medium at the indicated

concentrations, were started 1 h before siRNA-mediated silencing and repeated 48 h later.

Cells were collected in lysis buffer [50 mM Tris-HCl (pH 7.5), 150 mM NaCl, 0.5% Triton-X, 0.5% glycerol, 1% SDS, complete protease inhibitor (Sigma-Aldrich) and PhosSTOP (Sigma-Aldrich)] and protein extracts were sonicated. Protein levels were measured using a Bio-Rad protein quantification kit. Sample buffer was added, and samples were boiled for 5 min at 95 °C. Proteins were then separated using SDS-PAGE under denaturing conditions (4–20% Mini-PROTEAN TGX Gels) and transferred onto nitrocellulose membranes by semi-dry turbo blot (BioRad Laboratories). Membranes were blocked with 5% bovine serum albumin (BSA) in TBST (Tris-buffered saline and 0.1% Tween 20) for 1 h at room temperature. Primary antibodies were diluted in 5% BSA in TBST and incubated with membranes overnight at 4 °C. After primary antibody incubation, membranes were washed thrice with TBST for 5 min at room temperature. Fluorophore-conjugated or ECL HRP-linked secondary antibodies (GE Healthcare) were diluted 1:5000 in 5% BSA in TBST or in blocking buffer (Cat. no. 37538, Thermo Fisher Scientific) in PBS (1:1) and were incubated with membranes for 1 h at room temperature. Membranes were scanned using an infrared imaging system (Odyssey; LI-COR Biosciences) or using ECL Plus Western blotting reagent (Cat. no. RPN2232, GE Healthcare) and film. Band intensity was determined using Fiji<sup>66</sup> (ImageJ; National Institutes of Health) or Image Studio Lite (LI-COR).

The following primary antibodies were used: SHANK3 (Cat. No. HPA003446, Atlas antibodies and Cat. no. sc-30193, Santa Cruz), GFP (Cat. no. ab1218, Abcam), KRAS (Cat. no. WH0003845MI, Sigma-Aldrich), GAPDH (Cat. no. 5G4-6C5, Hycest), HSP70 (Hsc70/Hsp73; Cat. no. ADI-SPA-815, Enzo), phospho-ERK1/2 (Thr202/Tyr204; Cat. no. 4370S, Cell Signalling), ERK1/2 (Cat. no. 91025, Cell Signalling), phospho-AKT (Ser473) (Cat. no. 9271, Cell Signalling), AKT (Cat. no. 9272, Cell Signalling) and cleaved-PARP1 (Cat. no. ab4830 and ab32064 [E51], both from Abcam; recognise a larger 89 kD and a smaller 28 kD band, respectively). All primary antibodies were used at 1:1000 dilution, except the SHANK3 antibody, which was used at a 1:100 (Cat. no. sc-30193, Santa Cruz) or 1:500 (Cat. No. HPA003446, Atlas antibodies) dilution.

### Co-immunoprecipitations and pulldown assays

HEK293 cells were transiently transfected with (1) mRFP-tagged SHANK3 WT together with GFP-tagged KRASG12V or control (GFP only); or (2) GFP-tagged SHANK3 SPN WT, SHANK3 SPN R12E/K22D or control (GFP only) together with dsRed-tagged KRASG12V. A549 cells were transiently transfected with the control plasmid (pmCherry) or the nanobodies (pmCherry-AO1 or pmCherry-E01). 24 h post-transfection the cells were lysed using IP-lysis buffer (40 mM Hepes-NaOH, 75 mM NaCl, 2 mM MgCl<sub>2</sub>, 1% NP40, protease and phosphatase inhibitors), cleared by centrifugation, and subjected to immunoprecipitation of RFP/mCherry/dsRed-tagged or GFP-tagged fusion proteins using RFP-trap or GFP-trap matrix (Cat. no. rtma-100 and gtma-100, Chromotek), respectively. Input and precipitate samples were analysed by immunoblotting. The KRAS pulldown assays were done by incubating the indicated recombinant proteins with RAF-RBD glutathione affinity beads from the Ras Pull-Down Activation Assay Biochem Kit (Cat. no. BK008, Cytoskeleton) according to the manufacturer's instructions.

### Production and purification of recombinant proteins

All proteins were produced in *E. coli* BL21 cultures using IPTG induction and verified with sodium dodecyl sulphate polyacrylamide gel electrophoresis (SDS-PAGE).

**KRASG12V.** The sequence of the synthetic gene of KRAS 4B was designed according to *E. coli* codon usage. KRAS was PCR amplified and cloned into a modified pGEX vector (GE Healthcare, Chicago, IL). The

G12V mutation to KRAS 4B was purchased from BioCat (<https://www1.biocat.com>).

Glutathione S-transferase (GST) fusion KRASG12V protein was expressed in Terrific Broth (TB) medium (2.4% w/v yeast extract, 1.2% w/v tryptone, 0.5% w/v glycerol, 0.017 M KH<sub>2</sub>PO<sub>4</sub>, 0.072 M K<sub>2</sub>HPO<sub>4</sub>, 100 µg/ml Ampicillin) by the addition of 0.4 mM isopropyl-β-D-1-thiogalactopyranoside (IPTG) at 20 °C for 20 h using *E. coli* BL21 Gold cells. The cells were lysed by sonication on ice (Sonopulus 4000) at 40% amplitude (4x, 1 s pulse on and 1 s pulse off) for 1 min and subsequently centrifuged at 35000 g for 30 min at 4 °C to clear the lysate. The GST KRASG12V fusion protein was purified with Protino Glutathione Agarose 4B (Macherey-Nagel, Düren, Germany) and GST was cleaved by Tobacco Etch Virus (TEV) protease (Invitrogen, Life Technologies, Carlsbad, CA) at 4 °C for 16 h. The TEV protease cleavage extended KRASG12V construct in the N-terminal by four amino acid residues, G, A, M and G. The proteins were further purified by size exclusion chromatography (SEC) with a HiLoad 26/60 Superdex 200 pg column (GE Healthcare, Chicago, IL) in SEC buffer (50 mM Tris, pH 7.3, 300 mM NaCl, 1 mM DTT, 0.1% CHAPS) using an ÄKTA pure chromatography system (GE Healthcare). The protein was concentrated with Amicon ultracentrifugal 10 K filter device (Millipore, Sigma, Burlington, MA). The homodispersity of the proteins was verified with SDS-PAGE.

**KRASQ61H.** The plasmid containing *human* His6-KRASQ61H activating oncogenic mutant (residues 1-169) was a gift from Cheryl Arrow-smith (Plasmid #25153, Addgene). The protein was expressed using *E. coli* BL21(DE3) competent cells (Invitrogen) cultured in Luria Broth (LB) medium. Cells were grown at 37 °C in LB medium supplemented with antibiotics to an OD<sub>600</sub> of 0.6, cooled to 18 °C and induced using 300 µM IPTG for 16 h. Cells were pelleted by centrifugation and resuspended in 20 mM Na<sub>2</sub>HPO<sub>4</sub> pH 7.4, 500 mM NaCl, 5 mM MgCl<sub>2</sub>, 2 mM DTT and 25 mM imidazole, treated with protease cocktail inhibitor VII (Cat. no. 539138, Calbiochem) and sonicated on ice. The protein was purified using nickel-affinity chromatography with a linear gradient of lysis buffer containing 500 mM imidazole, but without DTT. Immediately after purification, 2 mM DTT was added to the protein fractions. Protein purity was checked by SDS-PAGE. Bound nucleotide was exchanged for GDP or non-hydrolysable GTP analogue GMPPCP using alkaline phosphatase beads (Sigma-Aldrich) and following the protocol of John et al.<sup>67</sup>.

**RBD domain of B-Raf.** The RBD domain of *human* BRAF (Uniprot P15056) corresponding to residues Ser151-Leu232 was cloned into pOPNB vector (OPPF-UK) from codon-optimised synthetic DNA at GeneMill facility, University of Liverpool. The protein was expressed using BL21 competent cells (Invitrogen) cultured in LB and purified using Ni-NTA column with standard protocol. His-tag was cleaved with recombinant His-tagged 3 C protease and removed by a reverse pass on the Ni-NTA column.

**SPN domain of SHANK3.** His-tagged SPN protein was expressed in TB medium with 100 µg/ml ampicillin by the addition of 0.4 mM IPTG at 18 °C for 20 h in *E. coli* BL21 Gold cells. Prior to cell lysis, small amounts of both lysozyme and DNase were added and then the cells were lysed by sonication on ice (Sonopulus 4000) at 40% amplitude (4x, 1 s pulse on and 1 s pulse off) for 1 min and subsequently centrifuged at 15000 g for 60 min at 4 °C to clear the lysate. The His-SPN fusion protein was purified with Protino Ni-Ted resin (Macherey-Nagel, Düren, Germany) using the elution buffer: 50 mM Tris, pH 7.2, 300 mM NaCl, 250 mM imidazole, 1 mM DTT, 0.1% CHAPS and protease inhibitor cocktail (#11873580001, Sigma). The protein was further purified by size exclusion chromatography (SEC) with a HiLoad 26/60 Superdex 200 pg column (GE Healthcare, Chicago, IL) in SEC buffer (50 mM Tris, pH 7.2, 300 mM NaCl, 1 mM DTT, 0.1% CHAPS) using an ÄKTA pure chromatography system (GE Healthcare). The protein was

concentrated with Amicon ultracentrifugal 3 K filter device (Millipore, Sigma, Burlington, MA). The homodispersity of the proteins was verified with SDS-PAGE.

**SPN-ARR domains of SHANK3.** The SPN-ARR fragment of rat SHANK3 (residues 1-348) was cloned into the pET-SUMO vector (Champion™ pET SUMO Protein Expression System, Invitrogen) to contain an N-terminal His6-SUMO tag. The protein was purified using nickel-affinity chromatography with a linear gradient containing 500 mM imidazole. The SUMO tag was cleaved with recombinant His-tagged SUMO protease and removed by a reverse pass on the Ni-NTA column. SHANK3 was shown to have >95% purity by SDS-PAGE gel.

### Microscale thermophoresis (MST)

The interaction between recombinant SHANK3 SPN and KRASG12V and SHANK3 SPN and E01 nanobody were measured using MST. His-SPN was labelled using the Monolith His-Tag Labelling Kit Red-tris-NTA fluorescent dye (Cat no. L008, NanoTemper Technologies) and applied at the final concentration of 50 nM in His-SPN SEC buffer having 0.05% Tween-20. A 12-point two-fold dilution series of unlabelled KRASG12V or E01 nanobody was mixed with labelled His-SPN protein and the indicated concentration ranges. MST experiments were conducted in triplicate using Monolith automated capillaries (Cat no. MO-AK002, NanoTemper Technologies) with a Monolith NT Automated system (NanoTemper Technologies) to determine the binding affinity between His-SPN and KRASG12V. The dissociation constant was then calculated using a single-site binding model to fit the curve using GraphPad Prism version 8.4.2 for Windows (GraphPad Software Inc.).

### Isothermal titration calorimetry (ITC)

For ITC measurements, the buffer of purified recombinant proteins (SPN-ARR fragment of SHANK3, GMPPCP-or GDP-loaded His6-KRASQ61H and RBD domain of *human* BRAF) was exchanged for ITC buffer (20 mM Tris pH 7.5, 500 mM NaCl, 0.5 mM TCEP (tris-carboxyethyl-phosphine) and 5 mM MgCl<sub>2</sub>) and ITC experiments were performed using an ITC-200 (Microcal). Protein concentrations were estimated from UV absorbance at 280 nm. ITC titrations were performed at 25 °C using 20 μM of SHANK3 with 350 μM of KRASQ61H and 20 μM of KRASQ61H with 200 μM of RAF-RBD. Data were integrated and fitted to a single-site binding equation using Origin 7 software with an ITC module (Microcal).

### Atomistic simulation models and methods

To probe the spontaneous membrane-binding capabilities of SHANK3, simulations were performed within three different lipid bilayer systems. Spontaneously formed KRAS-membrane complexes were also analysed. Finally, the KRAS-SHANK3 complex was obtained by aligning the structures of SHANK3 SPN<sup>35</sup> to the RAF RBD<sup>43</sup> coordinates. To run the simulations, we used the GROMACS simulation package version 2020<sup>68</sup> and the CHARMM36m force field<sup>69</sup>. Every simulation system was inspected with four independent replicas. Total simulation sampling time was about 24 μs. The model systems and simulation parameters are described in detail below.

**SHANK3 with a lipid bilayer (Systems 1-3).** System S1 was comprised of SHANK3 SPN-ARR with a pure 1-palmitoyl-2-oleoyl-sn-glycero-3-phosphocholine (POPC) lipid bilayer. System S2 with SHANK3 SPN-ARR entails a symmetric three-component bilayer, containing 65 mol% POPC, 30 mol% cholesterol, and 5 mol% phosphatidylinositol 4,5-bisphosphate (PIP2). The SPN-ARR domain was initially placed about 2 nm away from the bilayer surface, with the SPN-ARR linker and the residues 105-115 of the ARR domain facing the bilayer. System S3 includes an isolated SPN domain (residues 2-93) together with the above-described three-component (POPC/cholesterol/PIP2) bilayer.

The SPN domain was placed initially about 2 nm from the membrane surface. These constructs were based on the 5G4X structure<sup>34</sup>. Together these systems were used to probe spontaneous membrane binding capabilities of SHANK3. That is, the protein complex was initially placed in a random orientation such that the protein was allowed to bind the membrane without any bias, and these processes were simulated through four independent repeats (Supplementary Table 1). Hence, we refer to these systems as Spontaneous (see Supplementary Fig. 3).

**KRAS with a lipid bilayer (System S4).** System S4 entailed KRAS in an initially soluble state and a POPC/cholesterol/PIP2 lipid bilayer. The protein coordinates were extracted from the PDB id 6PTW structure<sup>43</sup>. The resulting spontaneously formed KRAS-membrane complexes were analysed and compared to the known orientations in System S5 (see below). As in the previous case, System 4 was also studied through spontaneous binding.

**SHANK3 and KRAS with a lipid bilayer (System S5).** System S5 included a KRAS-SHANK3 SPN-ARR complex and a POPC/cholesterol/PIP2 lipid bilayer. The KRAS-SHANK3 complex was obtained by aligning the structures of SHANK3 SPN<sup>34,35</sup> to the RAF RBD coordinates extracted from the PDB id 6PTW<sup>43</sup>. The resulting KRAS-SHANK3 model was then equilibrated for 100 ns with 5 kJ/mol restraints on the backbone atoms. In this model, the (initial) protein-lipid configuration was extracted from the RAF RBD structure. Hence, we refer to these systems as Model (see Supplementary Fig. 3).

Simulations were initiated using the CHARMM-GUI portal<sup>70,71</sup>. Interactions between the atoms were described using the all-atom CHARMM36m force field<sup>72</sup>. Water molecules were described using the TIP3P water model<sup>73</sup>. Potassium and chloride ions were added to neutralise the charge of the systems and to reach the physiological saline concentration (150 mM).

**Simulation parameters.** To run the simulations, we used the GROMACS simulation package version 2020<sup>68</sup>. Initiation of the systems followed the general CHARMM-GUI protocol: the simulation systems were first energy-minimised and then equilibrated with position restraints acting on the solute atoms<sup>72</sup>. We used the leap-frog integrator with a timestep of 2 fs to propagate the simulations<sup>74</sup>. Periodic boundary conditions were applied in all three dimensions, atomic neighbours were tracked with the Verlet lists, and bonds were constrained with the LINCS algorithm<sup>75</sup>. Lennard-Jones interactions were cut off at 1.2 nm, while electrostatic interactions were calculated using the smooth particle mesh Ewald (PME) algorithm<sup>76</sup>. The pressure of the system was coupled semi-isotropically using the Parrinello-Rahman barostat with a time constant of 5 ps<sup>76</sup>. Protein, membrane, and solvent atoms were coupled separately with a time constraint of 1 ps. Simulation trajectories were saved every 100 ps. Random initial velocities were assigned for the atoms from the Boltzmann distribution at the beginning of each simulation. For the remaining parameters, we refer to the GROMACS 2020.2 defaults<sup>68</sup>. Production simulations are listed in Supplementary Table 1. The total simulation time of the atomistic simulations was >24 microseconds. In every system simulated, the first 100 ns were used for equilibration and were discarded from analysis. The analysis was performed for the remaining part of trajectories and over all four independent repeats/replicas (Supplementary Table 1). The error analysis, resulting in standard errors, was based on these data.

### Immunofluorescence

Cells were transfected as indicated and then fixed with 4% PFA in PBS for 10 min at room temperature and washed with PBS. For antibody staining, fixed cells were permeabilized with 0.5% Triton-X-100 in PBS for 10 min at room temperature and PFA was quenched with 1M

glycine for 30 min at room temperature. For imaging ERK1/2, cells were stained with the primary antibody diluted in PBS (ERK1/2, 1:100, Cat. no. 91025, Cell Signalling) for 30 min at room temperature. Cells were washed 3 times with PBS and incubated with Alexa Fluor-conjugated secondary antibody (L300, Life Technologies) and 4',6'-diamidino-2-phenylindole (DAPI, nuclei staining, 1:10000; Cat. no. D1306, Life Technologies) diluted in PBS for 30 min at room temperature and then washed thrice with PBS. For imaging SHANK3, fixed and permeabilized cells were stained with anti-SHANK3 antibody (1:200 in PBS with 10% horse serum; SHANK3, Cat. no. HPA003446, Sigma-Aldrich) overnight at 4 °C before being washed 3 times with PBS and incubated with Alexa Fluor-conjugated secondary antibody (1:500, Life Technologies) and Phalloidin-Atto 647N (1:500, Sigma-Aldrich) for 1 h at room temperature. Cells were then washed 3 times with PBS and incubated with DAPI (1:10000) for 5 min at room temperature, and washed thrice with PBS.

For the ERK biosensor, PANC-1 ERK-KTR-mRuby2 cells were plated on glass-bottom dishes (Cat. no. P35G-1.5-20-C, MatTek Corporation) and silenced by siRNAs for two or three days, as described above. Then, cells were fixed with 4% PFA in PBS for 10 min at room temperature and washed with PBS.

Imaging was performed with a 3i spinning disk confocal (Marianas spinning disk imaging system with a Yokogawa CSU-W1 scanning unit on an inverted Carl Zeiss Axio Observer Z1 microscope, Intelligent Imaging Innovations, Inc.). To obtain a quantitative estimate for the extent of ERK nuclear translocation (indicative of ERK activity), captured images of cells were then analysed by calculating the ratio of staining intensity measured in the nucleus to that of a cytoplasmic region of the cell. This procedure accounts for potential variability in staining efficiency between different cell cultures.

### FRET imaging using fluorescence lifetime imaging microscopy (FLIM)

To visualise SHANK3–KRAS interaction in cells, we used FRET-FLIM. HEK293 cells were grown on coverslips overnight and transfected with an eGFP-tagged donor construct (GFP-SHANK3 SPN WT or GFP-SHANK3 SPN R12E/K22D) and mCherry-tagged acceptor construct (mCherry-KRASG12V). For the donor fluorophore-only samples, 0.8 µg GFP SHANK3 SPN WT or R12E/K22D mutant was used. For the donor-acceptor FRET pairs, cells were transfected with one of the donor plasmids and mCherry-KRASG12V as the acceptor (mCherry-C1 for control) at a construct ratio of 1: 3 (donor: acceptor). Media was changed 5 h after transfection. 48 h post-transfection, cells were fixed with 4% PFA/PBS and mounted in Mowiol 4-88 on microscope slides. Fluorescence lifetimes of the GFP-tagged donor constructs were measured using a fluorescence lifetime imaging attachment (Lambert Instruments, Leutingwolde, The Netherlands) on an inverted microscope (Zeiss Axio Observer.D1). Fluorescein (0.01 mM, pH 9) was used as a lifetime reference standard. The apparent FRET efficiency (Eapp) was calculated as the percentage of each donor-acceptor pair (τDA) and the average lifetime of the donor only (τD) samples (Eapp = (1 – τDA/τD) × 100%)<sup>44</sup>. Apparent FRET efficiency values were normalized to the average of the replicate 1 mCherry control. To analyse SHANK3 regulation of effector recruitment, HEK293 cells were first silenced with control or SHANK3-targeting siRNA for 48 h, and then, seeded on a 6-well plate with glass coverslips, and transfected with the donor alone plasmid (mGFP-tagged KRASG12V construct) in control samples, or with the donor plasmid and the acceptor plasmid mRFP-RBD in CRAF-RBD-recruitment FRET experiments. After 48 h of plasmid transfection, coverslips were fixed with 4% PFA/PBS for 15 min and then washed with PBS, and coverslips were mounted with Mowiol 4-88 (Sigma-Aldrich) on microscope slides.

### In vivo chick embryo chorioallantoic membrane (CAM) assay

The shells of fertilised chicken eggs were cleaned with 70% ethanol prior to starting development, before placing the eggs in a humidified incubator (50% moisture, 37 °C). On day 3 of development, a small hole was made with a needle and tweezers in the eggshell to drop the CAM away from the shell. On developmental day 7, the hole was widened with tweezers in order to place a plastic ring on the CAM. One million cells (transiently transfected with plasmids or siRNAs) were implanted inside the ring in 20 µl of 50% Matrigel (Cat. no. 354230, Corning) diluted in PBS, after which the hole was covered with parafilm to avoid drying of the CAM. The tumours were harvested 4–5 days post-implantation by placing the eggs on ice for 30 min before dissecting, weighing and fixing the tumours in 10% PBS (pH 7; Cat. no. FCHFF1195000, VWR).

### Subcutaneous tumour xenografts in Nude mice

To evaluate the requirement for SHANK3 in established tumours, six- to eight-week-old female athymic Nude mice (Hsd:ATHymic Nude-foxn1nu, Envigo, France) were injected in the flank with 5 million PANC-1 cells, expressing dox-inducible SHANK3 shRNA (pool of clones 4S and 1C), resuspended in 100 µl PBS with 50% Matrigel (Cat. no. 354230, Corning). When tumours reached an average mean volume of 100 mm<sup>3</sup>, the mice with similarly sized tumours were blindly randomised into two cohorts. Then, mice were fed either a normal chow (control group; Teklad 2914 diet, Envigo) or dox-containing chow (SHANK3-depleted group; Teklad doxycycline-diet, 625 mg/kg, in 2014 diet base, irradiated (2914), colour red, Envigo) daily. In addition, mice received two intraperitoneal (i.p) injections of PBS or doxycycline (80 mg/kg of body weight) according to their treatment group on day 1 and 2 of dox induction. Successful induction of SHANK3 shRNA expression (tRFP expression after dox-induction) was confirmed by imaging on an IVIS spectrum (PerkinElmer) and the radiant efficiency calculated by the IVIS software. Tumours were measured with a digital calibre twice a week and tumour volumes were calculated according to the formula  $V = (\pi/6)(d1 \times d2)^2 \times 3/2$ , where d1 and d2 are perpendicular tumour diameters. Mice were sacrificed at 26 days post-induction (74 post-engraftment), and tumours were dissected, weighed and snap-frozen in liquid nitrogen for mRNA isolation.

All animal experiments were ethically assessed and authorised by the National Animal Experiment Board and in accordance with The Finnish Act on Animal Experimentation (Animal license numbers ESAVI/9339/2016 and ESAVI/37571/2019). Mice were housed in standard conditions (12 h light/dark cycle) with food (as indicated above) and water available ad libitum, and randomly assigned to experimental groups. All experiments respected the maximum tumour diameter (15 mm) permitted by the authorisation bodies.

### Immunohistochemistry analysis of tumours

Formalin-fixed, paraffin-embedded tissue samples were cut to 4 µm sections, deparaffinised and rehydrated with standard procedures. For immunohistochemistry (IHC) of CAM tumours, heat-mediated antigen retrieval was done in citrate buffer (pH 6 for cleaved caspase-3, pH 9 for Ki-67). Sections were washed with washing buffer (0.05 M Tris-HCl pH 7.6, 0.05% Tween20), blocked for endogenous hydrogen peroxide activity, and incubated with Normal Antibody Diluent (NABD; Cat. no. BD09-125, Immunologic). Sections were then incubated with a Ki-67 antibody (Cat. no. AB9260, Millipore, diluted 1:1000) or a Cleaved Caspase-3 (Asp175) antibody (Cat. no. 9664, clone 5A1E, Cell Signalling Technology, diluted 1:500) for 1 h. The samples were washed thrice with TBS, incubated for 30 min with a BrightVision Goat anti-Rabbit HRP (Cat. no. DPVR110HRP, Immunologic) secondary antibody and washed again with TBS. DAB solution (Cat. no. K3468, DAKO) was added for 10 s followed by washing thrice with TBS. After counter-staining with Mayer's HTX, slides were dehydrated, and cleared in xylene, and mounted in Pertex. Stained samples were imaged with



Pannoramic P1000 Slide Scanner (3DHISTECH Ltd) and analysed with QuantCenter software using the NuclearQuant quantification module (3DHISTECH Ltd).

### Production of recombinant anti-SHANK3 SPN nanobodies

**Nanobody generation.** Nanobodies (single domain antibodies) against SHANK3 SPN were produced by Hybrigenics Services SAS (Evry, France; [www.hybricbody.com](http://www.hybricbody.com)) by three rounds of Phage Display selection of their naive VHH-library against recombinant biotinylated GST-SHANK3 SPN protein as briefly described below.

Prior to the Phage Display selection, SPN-Biotin and a non-related protein, GST-HIS-MBP-FLAG-Biotin, were bound to Streptavidin Magnetic Beads (Dynabeads® M-280 Streptavidin, Life Technologies) at a final concentration of 50 nM (1st round) and 10 nM (2nd and 3rd rounds).

For phage display selection, unspecific binders were first removed from the hs2dAb Phage Display library by incubation with the GST-HIS-MBP-FLAG-Biotin beads. Then, the unbound VHHs expressed as an *E. coli* supernatant were incubated with the SPN-Biotin beads and a total of three rounds of Phage Display were performed. The depletion step was repeated before each round of Phage Display to remove non-specific VHHs. At the end of the third round of Phage Display, *E. coli* clones were analysed by Hybrigenics' non-adsorbed phage ELISA, which allows for the proper folding of the native SPN protein, in 384-well plates with HRP-conjugated anti-M13 antibody (GE Healthcare) and a colorimetric substrate (TMB, TetraMethylBenzidine, Thermo Fischer). VHH clones with a significant ELISA signal in the presence of SPN-Biotin and a very low signal in the presence of GST-HIS-MBP-FLAG-Biotin were considered as specific SPN binders and selected for sequence analysis. Sequencing revealed that all binders represented one of two VHH variants (hereafter called nanobodies A01 and E01). These were provided by Hybrigenics in the bacterial expression vector pHEN2 (C-terminal 6xHis and 3 Myc tags) for use in ELISA assays and in *in vitro* pull-downs, and in an mCherry mammalian expression vector (tag on C terminus) for use in cell-based assays. A single-chain variable fragment (scFv) against an unrelated protein (SorLA) was used as a negative control in ELISA assays.

**Recombinant nanobody production.** Nanobodies in the pHEN2 vector were produced as recombinant proteins in BL21 bacteria using IPTG induction and purified according to Hybrigenics' protocol. Briefly, transformed bacteria were cultured overnight in TB medium (2.4% w/v yeast extract, 1.2% w/v tryptone, 0.4% w/v glycerol, 0.017 M KH<sub>2</sub>PO<sub>4</sub>, 0.072 M K<sub>2</sub>HPO<sub>4</sub>, 1% glucose, 100 µg/ml ampicillin) at 37 °C. 2 ml of this starter culture were then reincubated at 37 °C until optical density at 600 nm was between 0.6 and 0.8, induced with IPTG (0.5 mM) overnight at 28 °C, pelleted and freeze-thawed in liquid nitrogen. The pellet was resuspended in sonication buffer (50 mM NaPO<sub>4</sub>, pH 8, 300 mM NaCl, bacterial protease inhibitors, 1 mM PMSF, 1 mg/ml lysozyme), sonicated on ice (3 times for 1 s) and centrifuged to remove debris. Lysates were then incubated with prewashed Talon metal affinity resin (BD) at 4 °C for 30 min with shaking. Resin was then spun, flow-through removed, and washed with sonication buffer. Nanobodies were then eluted in sonication buffer plus 250 mM imidazole.

### Functional ELISA assay for nanobody testing

Nunc maxisorp 96-well plates were coated with 5 µg/ml purified recombinant His-SHANK3 SPN protein in TBS, 100 µl/well, overnight at 4 °C. Wells coated with BSA alone were included as a background binding control. The coating solution was removed, the wells were blocked with 100 µl/well 5% BSA in TBS-0.1% Tween20 (TBST) for 1 h at room temperature. The His-SPN coated wells were preincubated with the nanobodies for 15 min at room temperature prior to addition of GST-tagged purified recombinant KRAS protein loaded with non-

hydrolysable GTP analogue. An irrelevant anti-SorLA single-chain antibody (sc-Fv) was added as a negative control. These were incubated for 1 h at room temperature in TBST + 1 mM DTT + 2 mM MgCl<sub>2</sub>. Wells were washed 3 times with TBST + 2 mM MgCl<sub>2</sub>. To detect GST, DELFIA® Eu-Ni Anti-GST antibody (Perkin Elmer catalogue number AD0250) diluted at 1:000 in TBST + 1 mM DTT + 2 mM MgCl<sub>2</sub> was added and incubated 1 h at room temperature. The wells were washed thrice with Tecan plate washer with PBS, 100 µl of DELFIA® Enhancement Solution (Perkin Elmer catalogue number 124-105) was added to the wells and europium signal was measured with a time resolved fluorescence plate reader (PerkinElmer's VICTOR X5 multilabel plate reader).

### Pull-down interaction assay

The ability of anti-SHANK3 SPN nanobodies (A01 and E01) to disrupt the interaction between SHANK3 SPN and KRASG12V was tested with a pull-down. 5 µg of His-SHANK3 SPN protein was bound to 20 µl of Macherey Nagel Protino Ni-Ted resin beads in TBS + 1 mM DTT + 2 mM MgCl<sub>2</sub> for 1 h under rotation at 4 °C. 20 µg of nanobodies A01 or E01 or BSA as control were incubated with this for 30 min under rotation at 4 °C. 5 µg/ml GST-KRAS-GTP or GST alone was added and incubated under rotation at 4 °C for 1 h. Beads were washed thrice with 500 µl TBS + 1 mM DTT + 2 mM MgCl<sub>2</sub>, eluted into 20 µl 4x SDS sample buffer (200 mM Tris-HCl pH 6.8, 8% SDS, 40% glycerol, 4% β-mercaptoethanol, 50 mM EDTA, 0.08% bromophenol blue) with heating at 90 °C for 5 min and separated on an SDS-PAGE gel. The proteins were transferred to a filter and western blotted with anti-GST antibody.

### Statistics and Reproducibility

The sample size for studies was chosen according to previous studies in the same area of research. The GraphPad program was used for all statistical analyses. Normal distribution of the data was tested with the D'Agostino & Pearson omnibus normality test. Student's *t*-test (unpaired, two-tailed) with Welch's correction was used for two groups when normality could be confirmed. Nonparametric Mann-Whitney U-test was used when two non-normally distributed groups were compared or when normality could not be tested [due to a too small data set ( $n < 8$ )]. ANOVA with Holm-Sidak's or Dunnett's multiple comparison test was used when comparing more than two normally distributed groups. The Kruskal-Wallis non-parametric test with Dunn's multiple comparison test was used when comparing more than two non-normally distributed groups. Data are presented in column graphs or scatter dot plots with mean ± standard error of the mean (s.e.m) or mean ± standard deviation (s.d) and *P*-values. Individual data points per condition are shown, and *n*-numbers are indicated in the figure legends. The graphs in Figs. 2g and 3g were generated using SuperPlotsofData<sup>77</sup> and all data points and the average of each biological replicate are shown. *P*-values less than 0.05 were considered to be statistically significant. Unless otherwise indicated, all micrographs (western blots and microscopy images) are representative of three or more independent experiments (*n* numbers are shown in the accompanying analyses for each micrograph). The original, uncropped western blots can be found in the Source Data file.

### Reporting summary

Further information on research design is available in the Nature Portfolio Reporting Summary linked to this article.

### Data availability

The authors declare that the data supporting the findings of this study are available within the paper and its supplementary information files. Source data are provided with this paper.

### Code availability

The molecular dynamics simulation files generated and analyzed during the current study are available in the Zenodo repository,

accessible at <https://doi.org/10.5281/zenodo.5541745>. These files include the initial structures, input files, and trajectory files.

## References

- Prior, I. A., Hood, F. E. & Hartley, J. L. The frequency of ras mutations in cancer. *Cancer Res.* **80**, 2969–2974 (2020).
- Simanshu, D. K., Nissley, D. V. & McCormick, F. RAS proteins and their regulators in human disease. *Cell* **170**, 17–33 (2017).
- DeStefanis, R. A., Kratz, J. D., Emmerich, P. B. & Deming, D. A. Targeted therapy in metastatic colorectal cancer: current standards and novel agents in review. *Curr. Colorectal Cancer Rep.* **15**, 61–69 (2019).
- Waters, A. M. & Der, C. J. KRAS: The critical driver and therapeutic target for pancreatic cancer. *Cold Spring Harb. Perspect. Med.* **8**, a031435 (2018).
- Salgia, R., Pharaon, R., Mambetsariev, I., Nam, A. & Sattler, M. The improbable targeted therapy: KRAS as an emerging target in non-small cell lung cancer (NSCLC). *Cell Rep. Med.* **2**, 100186 (2021).
- Siegel, R. L., Miller, K. D., Fuchs, H. E. & Jemal, A. Cancer Statistics, 2021. *CA Cancer J. Clin.* **71**, 7–33 (2021).
- Vetter, I. R. & Wittinghofer, A. The guanine nucleotide-binding switch in three dimensions. *Science* **294**, 1299–1304 (2001).
- Cox, A. D. & Der, C. J. Ras history: the saga continues. *Small GTPases* **1**, 2–27 (2010).
- Drosten, M. & Barbacid, M. Targeting the MAPK pathway in KRAS-driven tumors. *Cancer Cell* **37**, 543–550 (2020).
- Stalneck, C. A. & Der, C. J. RAS, wanted dead or alive: advances in targeting RAS mutant cancers. *Sci. Signal* **13**, eaay6013 (2020).
- Ostrem, J. M., Peters, U., Sos, M. L., Wells, J. A. & Shokat, K. M. K-Ras(G12C) inhibitors allosterically control GTP affinity and effector interactions. *Nature* **503**, 548–551 (2013).
- Fell, J. B. et al. Identification of the clinical development candidate MRTX849, a covalent KRASG12C inhibitor for the treatment of cancer. *J. Med. Chem.* **63**, 6679–6693 (2020).
- Hong, D. S. et al. KRASG12C inhibition with sotorasib in advanced solid tumors. *N. Engl. J. Med.* **383**, 1207–1217 (2020).
- Canon, J. et al. The clinical KRAS(G12C) inhibitor AMG 510 drives anti-tumour immunity. *Nature* **575**, 217–223 (2019).
- Lanman, B. A. et al. Discovery of a covalent Inhibitor of KRASG12C (AMG 510) for the treatment of solid tumors. *J. Med. Chem.* **63**, 52–65 (2020).
- Janes, M. R. et al. Targeting KRAS mutant cancers with a covalent G12C-specific inhibitor. *Cell* **172**, 578–589.e17 (2018).
- Mao, Z. et al. KRAS(G12D) can be targeted by potent inhibitors via formation of salt bridge. *Cell Discov.* **8**, 5 (2022).
- Zhang, Z. et al. GTP-state-selective cyclic peptide ligands of K-ras(G12D) block its interaction with Raf. *ACS Cent. Sci.* **6**, 1753–1761 (2020).
- Molina-Arcas, M., Samani, A. & Downward, J. Drugging the undruggable: advances on RAS targeting in cancer. *Genes (Basel)* **12**, 899 (2021).
- Di Nicolantonio, F. et al. Precision oncology in metastatic colorectal cancer - from biology to medicine. *Nat. Rev. Clin. Oncol.* **18**, 506–525 (2021).
- Awad, M. M. et al. Acquired resistance to KRASG12C inhibition in cancer. *N. Engl. J. Med.* **384**, 2382–2393 (2021).
- Tanaka, N. et al. Clinical acquired resistance to KRASG12C inhibition through a novel KRAS switch-II pocket mutation and polyclonal alterations converging on RAS-MAPK reactivation. *Cancer Discov.* **11**, 1913–1922 (2021).
- Zhao, Y. et al. Diverse alterations associated with resistance to KRAS(G12C) inhibition. *Nature* **599**, 679–683 (2021).
- Hofmann, M. H., Gerlach, D., Misale, S., Petronczki, M. & Kraut, N. Expanding the reach of precision oncology by drugging All KRAS mutants. *Cancer Discov.* **12**, 924–937 (2022).
- Kim, D. et al. Pan-KRAS inhibitor disables oncogenic signalling and tumour growth. *Nature* **619**, 160–166 (2023).
- Hofmann, M. H. et al. BI-3406, a potent and selective SOS1-KRAS interaction inhibitor, is effective in KRAS-driven cancers through combined MEK inhibition. *Cancer Discov.* **11**, 142–157 (2021).
- Kerr, D. L., Haderk, F. & Bivona, T. G. Allosteric SHP2 inhibitors in cancer: targeting the intersection of RAS, resistance, and the immune microenvironment. *Curr. Opin. Chem. Biol.* **62**, 1–12 (2021).
- Nichols, R. J. et al. RAS nucleotide cycling underlies the SHP2 phosphatase dependence of mutant BRAF-, NF1- and RAS-driven cancers. *Nat. Cell Biol.* **20**, 1064–1073 (2018).
- Bery, N., Miller, A. & Rabbitts, T. A potent KRAS macromolecule degrader specifically targeting tumours with mutant KRAS. *Nat. Commun.* **11**, 3233 (2020).
- Gutierrez-Prat, N. et al. DUSP4 protects BRAF- and NRAS-mutant melanoma from oncogene overdose through modulation of MITF. *Life Sci. Alliance* **5**, e202101235 (2022).
- Ito, T. et al. Paralog knockout profiling identifies DUSP4 and DUSP6 as a digenic dependence in MAPK pathway-driven cancers. *Nat. Genet.* **53**, 1664–1672 (2021).
- Leung, G. P. et al. Hyperactivation of MAPK Signaling Is Deleterious to RAS/RAF-mutant Melanoma. *Mol. Cancer Res.* **17**, 199–211 (2019).
- Chang, L. et al. Systematic profiling of conditional pathway activation identifies context-dependent synthetic lethals. *Nat. Genet.* **55**, 1709–1720 (2023).
- Lilja, J. et al. SHANK proteins limit integrin activation by directly interacting with Rap1 and R-Ras. *Nat. Cell Biol.* **19**, 292–305 (2017).
- Cai, Q., Hosokawa, T., Zeng, M., Hayashi, Y. & Zhang, M. Shank3 binds to and stabilizes the active form of Rap1 and HRas GTPases via its NTD-ANK tandem with distinct mechanisms. *Structure* **28**, 290–300.e4 (2020).
- Sheng, M. & Kim, E. The Shank family of scaffold proteins. *J. Cell Sci.* **113**, 1851–1856 (2000).
- Salomaa, S. I. et al. SHANK3 conformation regulates direct actin binding and crosstalk with Rap1 signaling. *Curr. Biol.* **31**, 4956–4970.e9 (2021).
- Dempster, J. M. et al. Agreement between two large pan-cancer CRISPR-Cas9 gene dependency data sets. *Nat. Commun.* **10**, 5817 (2019).
- Cowley, G. S. et al. Parallel genome-scale loss of function screens in 216 cancer cell lines for the identification of context-specific genetic dependencies. *Sci. Data* **1**, 140035 (2014).
- Rezaei Adariani, S. et al. A comprehensive analysis of RAS-effector interactions reveals interaction hotspots and new binding partners. *J. Biol. Chem.* **296**, 100626 (2021).
- Nassar, N. et al. Ras/Rap effector specificity determined by charge reversal. *Nat. Struct. Biol.* **3**, 723–729 (1996).
- Hancock, J. F., Paterson, H. & Marshall, C. J. A polybasic domain or palmitoylation is required in addition to the CAAX motif to localize p21ras to the plasma membrane. *Cell* **63**, 133–139 (1990).
- Fang, Z. et al. Multivalent assembly of KRAS with the RAS-binding and cysteine-rich domains of CRAF on the membrane. *Proc. Natl Acad. Sci. USA* **117**, 12101–12108 (2020).
- Guzmán, C. et al. The efficacy of raf kinase recruitment to the GTPase H-ras depends on H-ras membrane conformer-specific nanoclustering. *J. Biol. Chem.* **289**, 9519–9533 (2014).
- Unni, A. M. et al. Hyperactivation of ERK by multiple mechanisms is toxic to RTK-RAS mutation-driven lung adenocarcinoma cells. *Elife* **7**, e33718 (2018).
- Cho, E., Lou, H. J., Kuruvilla, L., Calderwood, D. A. & Turk, B. E. PPP6C negatively regulates oncogenic ERK signaling through dephosphorylation of MEK. *Cell Rep.* **34**, 108928 (2021).
- Timofeev, O., Giron, P., Lawo, S., Pichler, M. & Noeparast, M. ERK pathway agonism for cancer therapy: evidence, insights, and a target discovery framework. *npj Precis. Onc.* **8**, 1–16 (2024).

48. Kudo, T. et al. Live-cell measurements of kinase activity in single cells using translocation reporters. *Nat. Protoc.* **13**, 155–169 (2018).
49. Wang, L. et al. A kinome-wide RNAi screen identifies ERK2 as a druggable regulator of Shank3 stability. *Mol. Psychiatry* **25**, 2504–2516 (2020).
50. Hayes, T. K. et al. Long-term ERK inhibition in KRAS-mutant pancreatic cancer is associated with MYC degradation and senescence-like growth suppression. *Cancer Cell* **29**, 75–89 (2016).
51. Dias, M. H. & Bernards, R. Playing cancer at its own game: activating mitogenic signaling as a paradoxical intervention. *Mol. Oncol.* **15**, 1975–1985 (2021).
52. Wood, K. C. Hyperactivation of oncogenic driver pathways as a precision therapeutic strategy. *Nat. Genet.* **55**, 1613–1614 (2023).
53. Nakajima, E. C. et al. FDA approval summary: sotorasib for KRAS G12C-mutated metastatic NSCLC. *Clin. Cancer Res.* **28**, 1482–1486 (2022).
54. Jovčevska, I. & Muyldermans, S. The therapeutic potential of nanobodies. *BioDrugs* **34**, 11–26 (2020).
55. Jameson, K. L. et al. IQGAP1 scaffold-kinase interaction blockade selectively targets RAS-MAP kinase-driven tumors. *Nat. Med.* **19**, 626–630 (2013).
56. Diepstraten, S. T. et al. The manipulation of apoptosis for cancer therapy using BH3-mimetic drugs. *Nat. Rev. Cancer* **22**, 45–64 (2022).
57. Ledford, H. Gene-silencing technology gets first drug approval after 20 year wait. *Nature* **560**, 291–292 (2018).
58. Honor, A., Rudnick, S. R. & Bonkovsky, H. L. Givosiran to treat acute porphyria. *Drugs Today (Barc.)* **57**, 47–59 (2021).
59. Shah, V. N. & Pyle, L. Lumasiran, an RNAi therapeutic for primary hyperoxaluria type 1. *N. Engl. J. Med.* **385**, e69 (2021).
60. Kreienkamp, H.-J. Scaffolding proteins at the postsynaptic density: shank as the architectural framework. *Handb. Exp. Pharmacol.* **186**, 365–380 (2008).
61. Abankwa, D. et al. A novel switch region regulates H-ras membrane orientation and signal output. *EMBO J.* **27**, 727–735 (2008).
62. Najumudeen, A. K. et al. Cancer stem cell drugs target K-ras signaling in a stemness context. *Oncogene* **35**, 5248–5262 (2016).
63. Vuoriluoto, K. et al. Vimentin regulates EMT induction by slug and oncogenic H-Ras and migration by governing Axl expression in breast cancer. *Oncogene* **30**, 1436–1448 (2011).
64. Härmä, V. et al. A comprehensive panel of three-dimensional models for studies of prostate cancer growth, invasion and drug responses. *PLoS ONE* **5**, e10431 (2010).
65. Guzmán, C., Bagga, M., Kaur, A., Westermarck, J. & Abankwa, D. ColonyArea: an ImageJ plugin to automatically quantify colony formation in clonogenic assays. *PLoS ONE* **9**, e92444 (2014).
66. Schindelin, J. et al. Fiji: an open-source platform for biological-image analysis. *Nat. Methods* **9**, 676–682 (2012).
67. John, J. et al. Kinetics of interaction of nucleotides with nucleotide-free H-ras p21. *Biochemistry* **29**, 6058–6065 (1990).
68. Abraham, M. J. et al. GROMACS: High performance molecular simulations through multi-level parallelism from laptops to supercomputers. *SoftwareX* **1–2**, 19–25 (2015).
69. Huang, J. et al. CHARMM36m: an improved force field for folded and intrinsically disordered proteins. *Nat. Methods* **14**, 71–73 (2017).
70. Jo, S., Kim, T., Iyer, V. G. & Im, W. CHARMM-GUI: a web-based graphical user interface for CHARMM. *J. Comput. Chem.* **29**, 1859–1865 (2008).
71. Wu, E. L. et al. CHARMM-GUI membrane builder toward realistic biological membrane simulations. *J. Comput. Chem.* **35**, 1997–2004 (2014).
72. Lee, J. et al. CHARMM-GUI input generator for NAMD, GROMACS, AMBER, OpenMM, and CHARMM/OpenMM simulations using the CHARMM36 additive force field. *J. Chem. Theory Comput.* **12**, 405–413 (2016).
73. Mark, P. & Nilsson, L. Structure and dynamics of the TIP3P, SPC, and SPC/E water models at 298 K. *J. Phys. Chem. A* **105**, 9954–9960 (2001).
74. Van Gunsteren, W. F. & Berendsen, H. J. C. A leap-frog algorithm for stochastic dynamics. *Mol. Simul.* **1**, 173–185 (1988).
75. Hess, B., Bekker, H., Berendsen, H. J. C. & Fraaije, J. G. E. M. LINC: A linear constraint solver for molecular simulations. *J. Comput. Chem.* **18**, 1463–1472 (1997).
76. Parrinello, M. & Rahman, A. Polymorphic transitions in single crystals: a new molecular dynamics method. *J. Appl. Phys.* **52**, 7182–7190 (1981).
77. Goedhart, J. SuperPlotsOfData—a web app for the transparent display and quantitative comparison of continuous data from different conditions. *Mol. Biol. Cell* **32**, 470–474 (2021).

## Acknowledgements

We thank P. Laasola, J. Siivonen, E.-M. Vesilahti, M. Miihkinen, S. Salomaa and A. Isomursu for technical assistance and scientific discussion, the Ivaska lab for critical reading and feedback on the manuscript and O. Pentikäinen for protein complex modelling. The Cell Imaging and Cytometry Core (Turku Bioscience Centre, University of Turku) and Turku Centre for Disease Modelling (TCDM), both supported by Biocenter Finland, the Euro-BiImaging Finnish Node (Turku Finland), the University of Turku Histocore and Genome Editing core are acknowledged for services, instrumentation, and expertise. We also gratefully acknowledge CSC – IT Center for Science (Espoo, Finland) for providing ample computing resources. This work was supported by the Research Council of Finland through the following programs: an InFLAMES Flagship Programme (337530, UTU and 337531, Åbo Akademi), Research project grants (325464, J.L. and 331349, I.V.), Research Fellowships (338537 G.J. and 323096 E.P.), the CoE for Biological Barrier Mechanics and Disease (346131 & 364182, J.L. and 346135 & 364185, I.V.). Additional funding was provided by an ERC consolidator (615258, J.L.) and a proof of concept grant (899155, J.L.), the Sigrid Juselius Foundation (J.L., G.J., E.P., and I.V.), the Finnish Cultural Foundation (J.L. and E.P.), the Cancer Foundation Finland (J.L., M.S., G.J., and I.V.), the Frontier Science Program (RGPO059/2019, I.V.), the Helsinki Institute of Life Science (HiLIFE) Fellow program (I.V.), the Lundbeck Foundation (I.V.) and a Novo Nordisk pre-seed grant (J.L.). J.L. and J.K. were supported by the Turku Doctoral Programme of Molecular Medicine (TuDMM), J.L. by the Instrumentarium Foundation, the Orion Research Foundation Sr and the K. Albin Johansson Foundation, and P.R. by the Drug Research Doctoral Programme at the University of Turku. J.R.W.C. was supported by the European Union’s Horizon 2020 research and innovation programme under the Marie Skłodowska-Curie grant agreement [841973] and a Research Council of Finland postdoctoral research grant (338585), M.D. by the European Union’s Horizon Europe research and innovation programme under Marie Skłodowska-Curie grant [101108089], M.C. by a Research Council of Finland postdoctoral research grant (343239) and AKN by CRUK Scotland Institute core funding (A17196, and A31287 - awarded to O.J.S.). O.J.S. was supported by CRUK grants (A21139, A12481, A17196 and A31287) and an ERC Starting grant (311301).

## Author contributions

Conceptualization: J.L., J.I. Methodology: J.L., J.K., J.R.W.C., U.P., I.B., J.V., M.R.C., M.D., D.A., I.V., E.P., J.I. Formal Analysis: J.L., J.K., U.P., I.B., J.V., E.P., H.P. Investigation: J.L., J.K., H.P., T.V., G.J., E.P., M.R.C., M.D., J.V., P.R., I.M.D.P., E.W., A.K.N. Visualization: J.L., J.V., H.H. Writing – Original Draft: J.L., M.S., J.I. Writing – review & editing: J.L., J.K., H.H., J.R.W.C., G.J., E.P., A.K.N., O.J.S., D.A., J.V., I.V., M.S., J.I. Supervision: O.J.S., I.B., I.V., D.A., U.P., J.I. Funding Acquisition: I.V., J.I.

## Competing interests

The authors J.L. and J.I. declare that they have filed patent applications related to these findings (Therapy of Ras-Dependent Cancers, WO/2021/

160937; Nanobodies specifically binding to SH3 and multiple ankyrin repeat domains 3 (SHANK3), WO/2023/021181). All other authors declare no competing interests.

### Additional information

**Supplementary information** The online version contains supplementary material available at <https://doi.org/10.1038/s41467-024-52326-1>.

**Correspondence** and requests for materials should be addressed to Johanna Ivaska.

**Peer review information** *Nature Communications* thanks Mark Philips and the other, anonymous, reviewer(s) for their contribution to the peer review of this work. A peer review file is available.

**Reprints and permissions information** is available at <http://www.nature.com/reprints>

**Publisher's note** Springer Nature remains neutral with regard to jurisdictional claims in published maps and institutional affiliations.

**Open Access** This article is licensed under a Creative Commons Attribution-NonCommercial-NoDerivatives 4.0 International License, which permits any non-commercial use, sharing, distribution and reproduction in any medium or format, as long as you give appropriate credit to the original author(s) and the source, provide a link to the Creative Commons licence, and indicate if you modified the licensed material. You do not have permission under this licence to share adapted material derived from this article or parts of it. The images or other third party material in this article are included in the article's Creative Commons licence, unless indicated otherwise in a credit line to the material. If material is not included in the article's Creative Commons licence and your intended use is not permitted by statutory regulation or exceeds the permitted use, you will need to obtain permission directly from the copyright holder. To view a copy of this licence, visit <http://creativecommons.org/licenses/by-nc-nd/4.0/>.

© The Author(s) 2024

## Supplementary information

### SHANK3 depletion leads to ERK signalling overdose and cell death in KRAS-mutant cancers

Johanna Lilja<sup>1#</sup>, Jasmin Kaivola<sup>1#</sup>, James R.W. Conway<sup>1</sup>, Joni Vuorio<sup>2</sup>, Hanna Parkkola<sup>1</sup>, Pekka Roivas<sup>1,3</sup>, Michal Dibus<sup>1</sup>, Megan Chastney<sup>1</sup>, Taru Varila<sup>1</sup>, Guillaume Jacquemet<sup>1,4,5,6</sup>, Emilia Peuhu<sup>1,7</sup>, Emily Wang<sup>8</sup>, Ulla Pentikäinen<sup>1,3</sup>, Itziar Martinez D. Posada<sup>1</sup>, Hellyeh Hamidi<sup>1</sup>, Arafath K. Najumudeen<sup>9,10</sup>, Owen J. Sansom<sup>10,11</sup>, Igor L. Barsukov<sup>8</sup>, Daniel Abankwa<sup>1,12</sup>, Ilpo Vattulainen<sup>2</sup>, Marko Salmi<sup>3,13,14</sup> and Johanna Ivaska<sup>1,14,15,16,17\*</sup>

The supplementary information file contains the following:

#### Supplementary Figures:

Supplementary Figure 1, Related to Figure 1.

Supplementary Figure 2, Related to Figure 2.

Supplementary Figure 3, Related to Figure 3.

Supplementary Figures 4-6, Related to Figure 4.

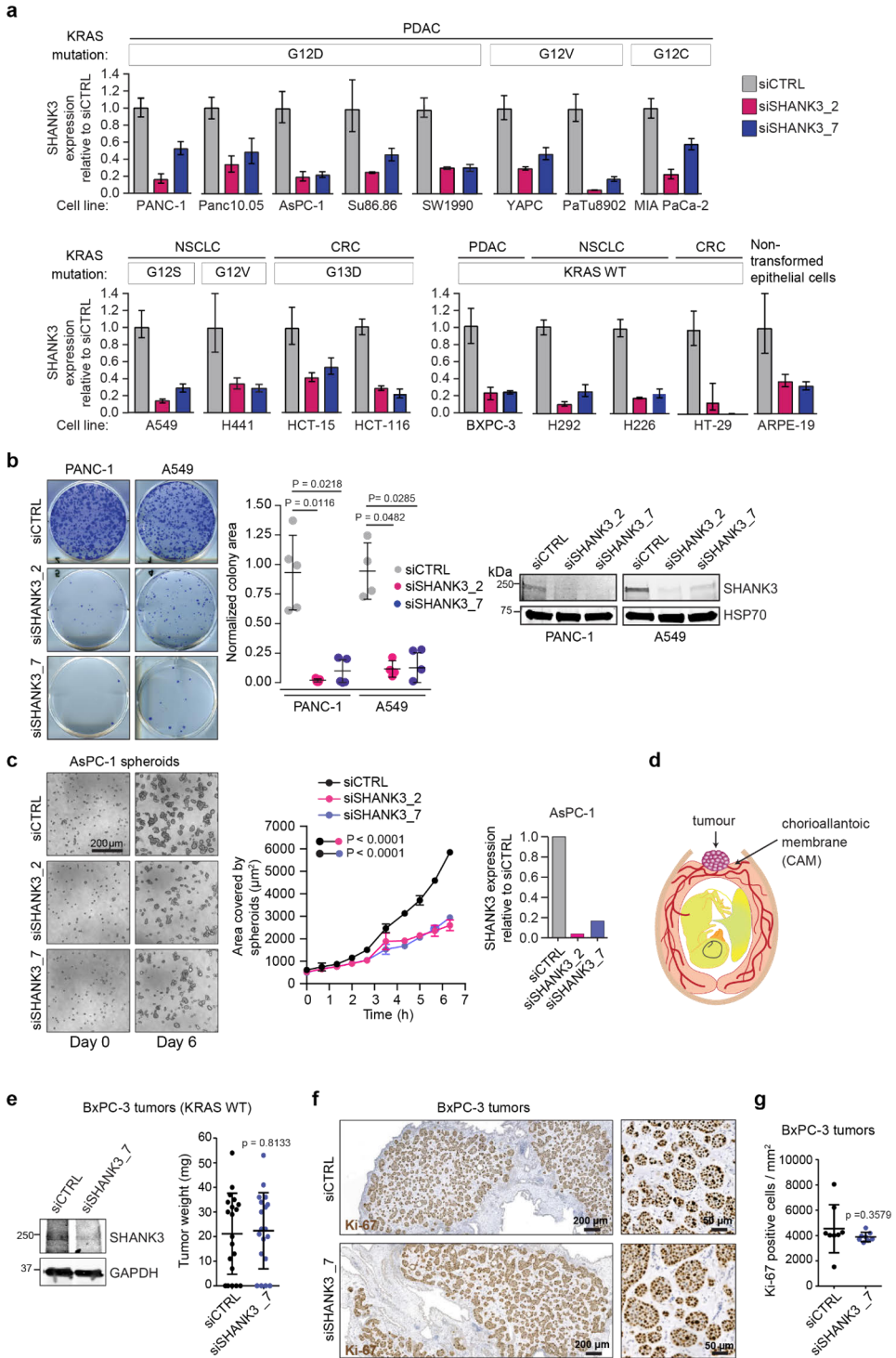
Supplementary Figures 7-10, Related to Figure 5.

Supplementary Figure 11, Related to Figure 6.

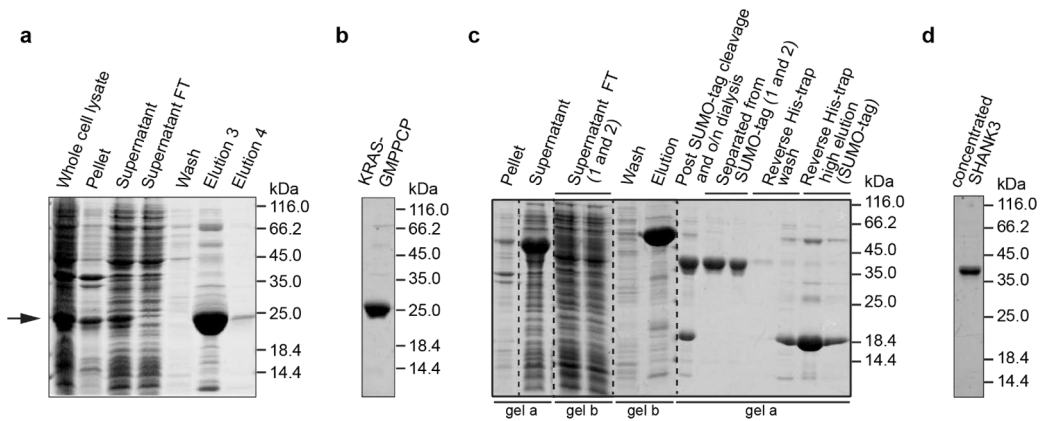
Supplementary Figure 12, Related to Figure 6.

Supplementary Table 1, Related to Figure 3.

Supplementary References

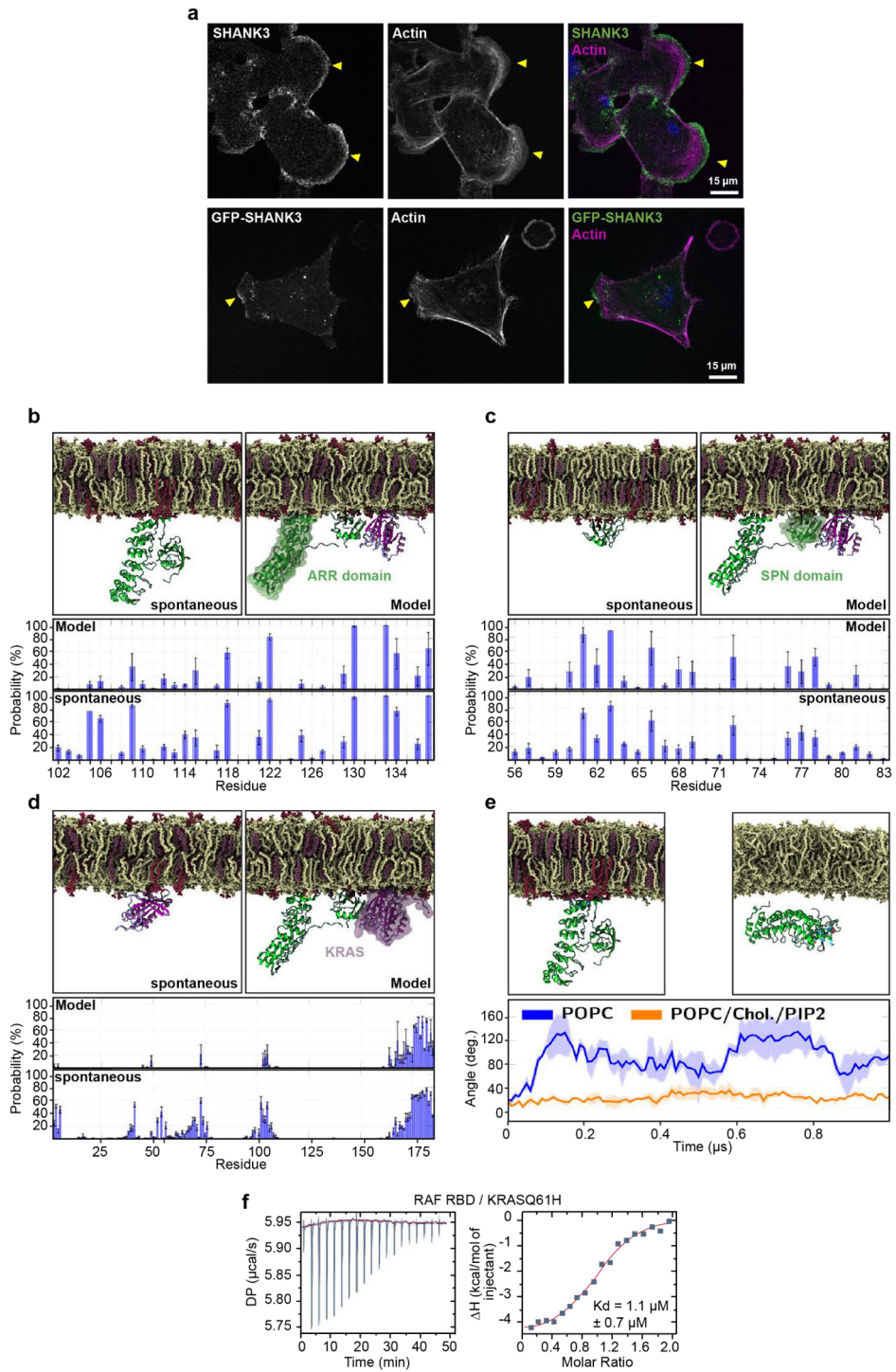


**Supplementary Figure 1. *SHANK3* depletion impairs *KRAS*-driven cancer cell proliferation and tumour growth.** Related to Figure 1. **a**, *SHANK3* mRNA expression in cancer cell lines with distinct *KRAS* mutations (PDAC: PANC-1, Panc10.05, AsPC-1, Su86.86, SW1990, YAPC, PaTu8602 and MIA PaCa-2; NSCLC: A549 and H441; CRC: HCT-15 and HCT-116) or with wild-type *KRAS* (PDAC: BxPC3; NSCLC: H292 and H226; CRC: HT-29) following control (siCTRL) or *SHANK3* silencing (siSHANK3\_2 and siSHANK3\_7 are two different *SHANK3*-targeting siRNAs) (data are mean relative quantification (RQ) and min and max RQ; RQ was derived from three technical replicates, one experiment). **b**, Colony growth of control or *SHANK3*-silenced PANC-1 (KRASG12D) and A549 (KRASG12S) cells. Shown are representative images, quantification of the colony areas and western blots confirming SHANK3 knockdown (shown are individual data points, mean  $\pm$  s.d.; n = 5 (PANC-1) or 4 (A549) independent experiments; Kruskal-Wallis one-way ANOVA and Dunn's post hoc test). **c**, Spheroid growth of control or SHANK3-silenced KRAS-mutant AsPC-1 cells. Representative images, quantification of spheroid growth and SHANK3 mRNA levels are shown (data are mean  $\pm$  s.d. of spheroid area; three independent experiments; one-way ANOVA with Holm-Sidak's multiple comparison test at the endpoint). **d**, A schematic illustration of the chick embryo chorioallantoic membrane (CAM) xenograft assay. **e-g**, Tumour growth of control or *SHANK3*-silenced BxPC-3 cells on CAM membranes. Shown are immunoblots of SHANK3 and GAPDH (loading control) and tumour weight (e), representative IHC images (f) and quantification of Ki-67 staining (g) in tumour tissues at the end of the experiments (data are mean  $\pm$  s.d.; n = 19 (siSHANK3) and 20 (siCTRL) (e) and 8 (g) tumours per sample group from two independent experiments; unpaired two-tailed Student's t-test with Welch's correction). Source data are provided as a Source Data file.

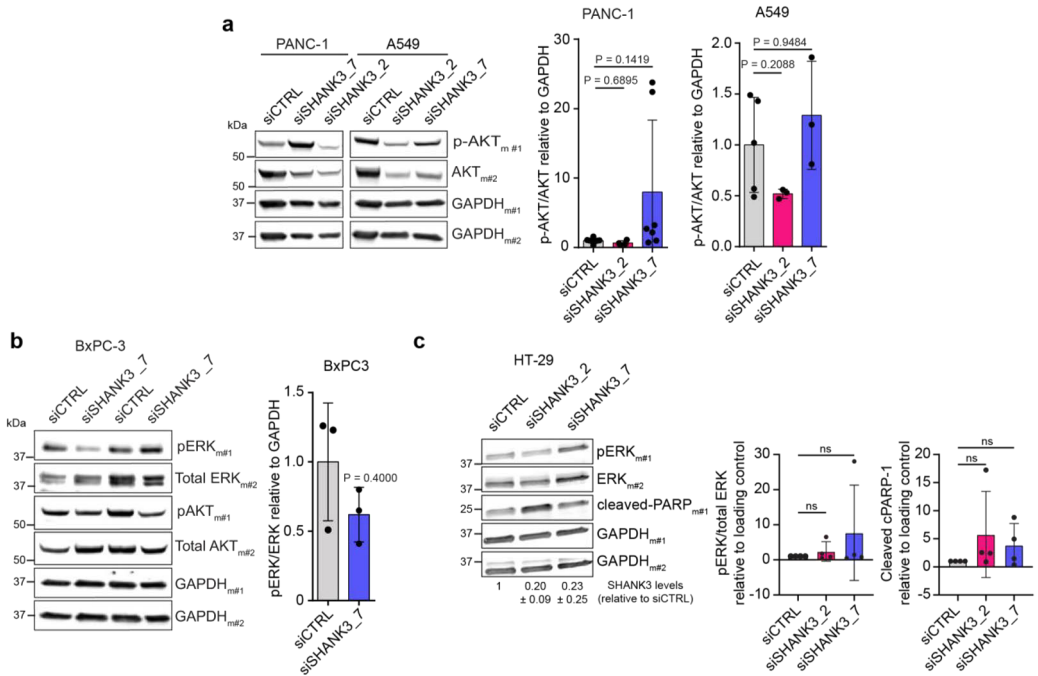


**Supplementary Figure 2. SHANK3 interacts directly with active/mutant KRAS. Related to Figure 2. a-c,** Coomassie-stained gels showing the purification of proteins used in ITC experiments (one experiment). **a,** KRASQ61H purification by  $\text{Ni}^{2+}$ -NTA affinity chromatography. Supernatant FT = supernatant flow-through from His-trap column. Arrow points to the expected mw of KRASQ61H. **b,** Pure KRASQ61H after overnight exchange with GMPPCP used for ITC. **c,** Purification of SHANK3 WT amino acid residues 1-348 (SPN-ARR domain). The 6xHis-SUMO-tag was removed via overnight dialysis and cleavage with SUMO protease, followed by a second  $\text{Ni}^{2+}$ -NTA affinity chromatography to separate the tag from the protein. Samples were run on different gels as indicated. **d,** Concentrated sample of SHANK3 WT amino acid residues 1-348 (SPN-ARR domain) used for ITC.

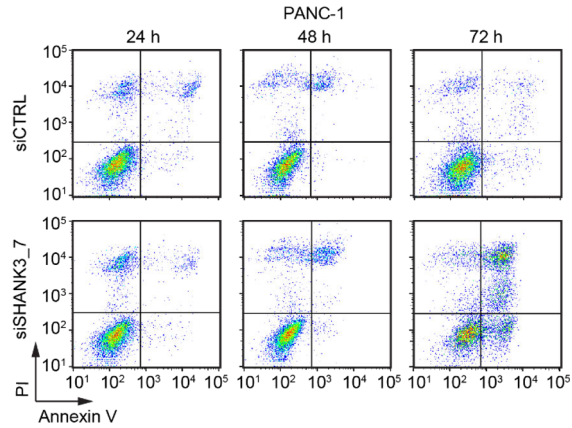




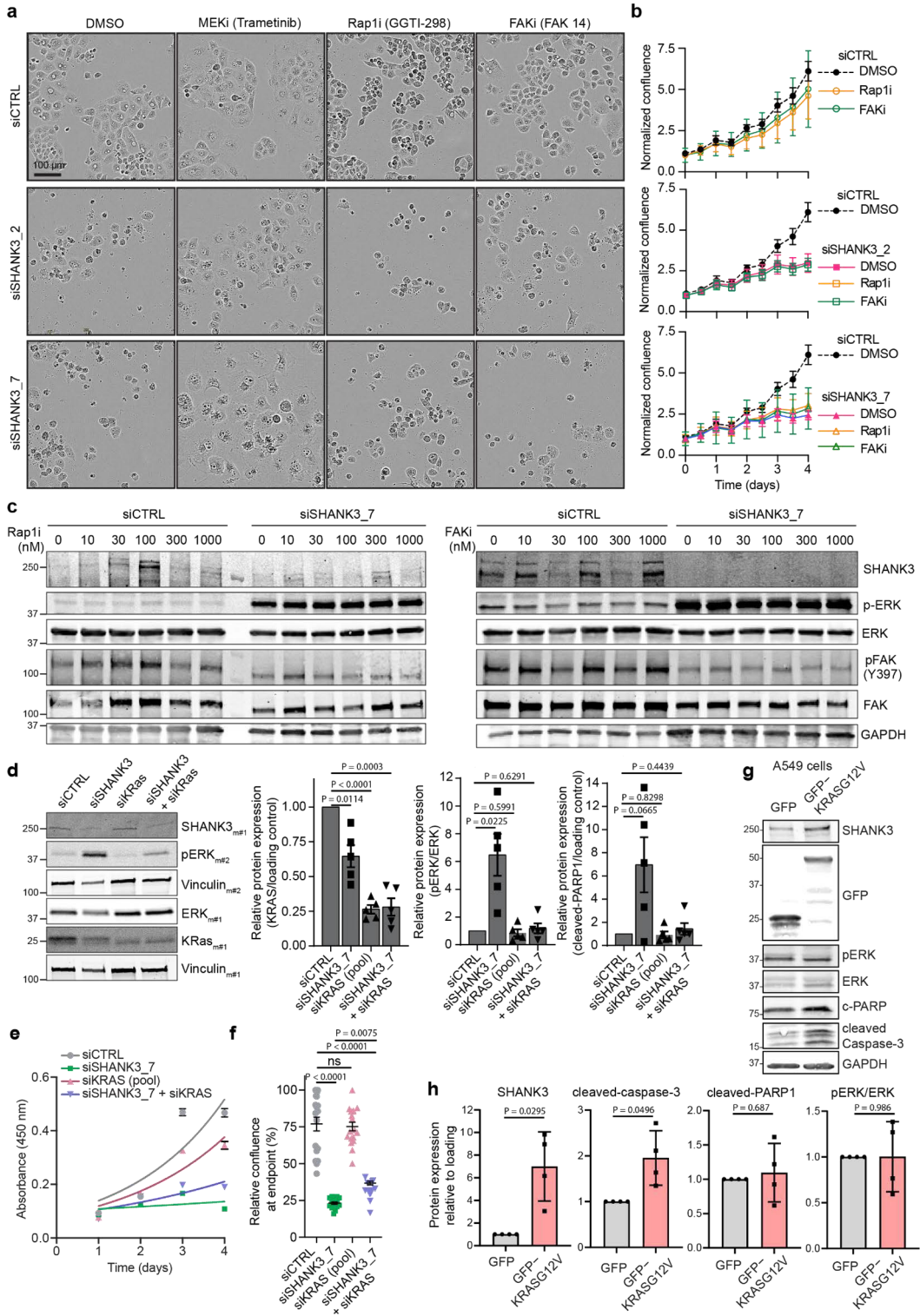
**Supplementary Figure 3. SHANK3 competes with RAF for active KRAS binding. Related to Figure 3.** **a**, Endogenous SHANK3 (top, representative of three independent experiments) and GFP-SHANK3 (bottom, one experiment) localisation in A549 cells. Yellow arrows indicate localisation at the cell leading edge. **b-d**, Final simulation frames (1000 ns; top panels) of the interaction between the indicated proteins and lipids and the probability of contacts, and the residues involved, in this interaction (minimum distance < 0.6 nm; bottom panels; errors are s.e.m). **b**, Spontaneous membrane binding of isolated SHANK3 SPN-ARR (left, System S2) and modelled membrane binding of SHANK3 SPN-ARR with KRAS (right, System S5). **c**, Spontaneous membrane binding of isolated SHANK3 SPN (left, System S3) and modelled membrane binding of SHANK3 SPN-ARR with KRAS (right, System S5). The SPN-domain residues that contact the PIP2 lipids in both cases are indicated. Only residues at the membrane-binding region are listed (b, c). **d**, Simulation of KRAS with a PIP2-containing bilayer (left, System S4), indicating spontaneous binding, and modelled membrane binding of SHANK3 SPN-ARR with KRAS (right, System S5). **e**, Final simulation frames (1000 ns) of SPN-ARR with a PIP2-containing bilayer (left, System S2) and SPN-ARR with a POPC (1-Palmitoyl-2-oleoyl-sn-glycero-3-phosphocholine)/Phosphatidylinositol 4,5-bisphosphate/Cholesterol bilayer (right, System S1). Bottom image shows the tilt angle of the vector between the C $\alpha$  atoms of the SHANK3 residues 114 and 286 (residues chosen to span the long axis of the ARR domain (long axis of the protein). Zero degrees corresponds to the alignment of the vector with the bilayer normal. The data were calculated with the *gmx bundle* tool within the GROMACS package. **f**, ITC titration and isotherms for the interaction between the active GMPPCP-form of KRASQ61H and RAF-RBD. Solid lines indicate fitting to the single-site-binding model at 25°C with 20  $\mu$ M of KRASQ61H and 200  $\mu$ M of RAF-RBD in the same buffer conditions as in Fig. 2c. The calculated K<sub>d</sub> value is higher than earlier reports<sup>1,2</sup>, likely due to the higher salt concentration in the buffer reducing the electrostatic contribution into the binding energy, with a potentially smaller effect from the mutation (graph is a representative of three technical replicates, one independent experiment). Source data are provided as a Source Data file.



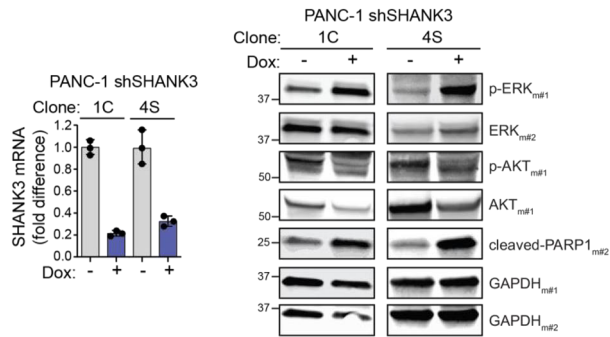
**Supplementary Figure 4. Loss of SHANK3 has no significant effect on ERK in WT *KRAS* cells or on AKT signalling in *KRAS*-mutant cells. Related to Figure 4. a**, Representative immunoblots of the indicated proteins from PANC-1 and A549 cells analysed three days after silencing. Loading controls are from 4a and the efficiency of *SHANK3* silencing is shown in Fig. 4a. Quantifications show AKT phosphorylation levels (relative to total AKT) [mean  $\pm$  s.d.; PANC-1, n = 8 (siCTRL), 4 (siSHANK3\_2) or 6 (siSHANK3\_7); A549, n = 5 (siCTRL) or 3 (siSHANK3\_2 and siSHANK3\_7) independent experiments; Kruskal-Wallis test and Dunn's post hoc test]. **b,c**, Representative immunoblots of the indicated proteins in control or *SHANK3*-silenced BxPC-3 cells (b) and HT29 cells (c) analysed three days post silencing; loading control is either GAPDH or HSC70 [mean  $\pm$  s.d.; n = 3 (b) and 4 (c) independent experiments; two-tailed Mann Whitney test (b) and Dunn's post hoc test (c)]. Samples were resolved and blotted on duplicate membranes (m#1, membrane 1 and m#2, membrane 2). GAPDH was used as a loading control on each membrane. Source data are provided as a Source Data file.



**Supplementary Figure 5. SHANK3 depletion triggers apoptosis in *KRAS*-mutant cells, Related to Figure 4d.** Representative scatter plots of Annexin V-FITC / PI flow cytometry data from 2D-cultured control and *SHANK3*-silenced cells at the indicated timepoints post silencing. Quadrant analysis: viable cells (Annexin V-negative / PI-negative), early apoptotic cells (Annexin V-positive / PI-negative), late apoptotic/necrotic cells (Annexin V-positive / PI-positive), late necrotic cells (Annexin V-negative / PI-positive).

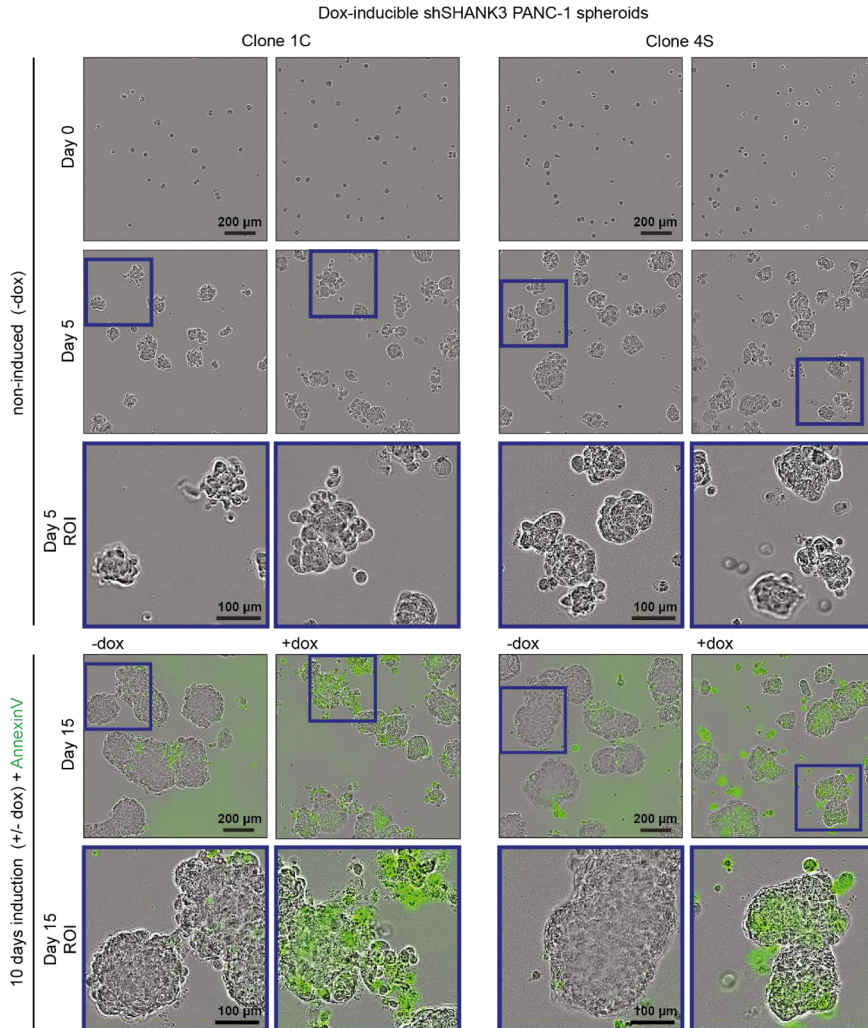
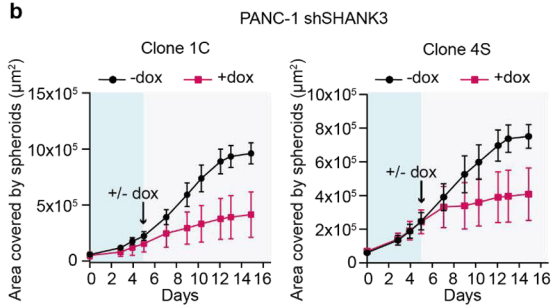
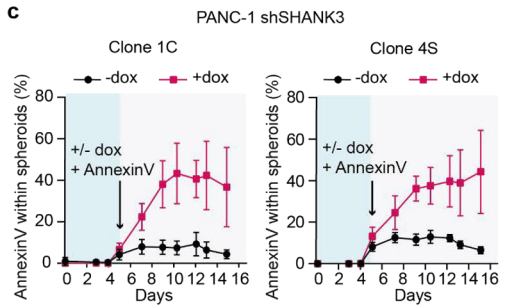


**Supplementary Figure 6. Inhibition of integrin signalling does not rescue the proliferation defect of *SHANK3*-silenced cells, Related to Figure 4.** **a**, Representative images of cell confluence for control (siCTRL) or *SHANK3*-silenced (siSHANK3\_2 and siSHANK3\_7) PANC-1 cells treated vehicle (DMSO), MEK inhibitor (trametinib), Rap1 inhibitor (GGTI-298) or FAK inhibitor (FAK-14) (300 nM concentration) at day 3. **b**, Growth curves (proliferation; % confluence) for control or *SHANK3*-silenced PANC-1 cells treated with the aforementioned inhibitors over several days (mean  $\pm$  s.e.m.; 3 (siCTRL) and 4 (siSHANK3) wells/condition/replicate; a representative graph from three independent experiments is shown for each condition). **c**, Representative immunoblots of control or *SHANK3*-silenced PANC-1 cells treated with the indicated concentration of the Rap1 inhibitor (GGTI-298) or FAK inhibitor (FAK-14). Shown is the efficiency of *SHANK3* silencing and the levels ERK activation (phospho-ERK1/2 (Thr202/Y204) / total ERK relative to GAPDH) and FAK activation (phospho-FAK (Tyr397) / total FAK relative to GAPDH) (two independent experiments). **d**, Representative western blot analysis of the indicated proteins from PANC-1 cells after transfection with siRNAs against *SHANK3* (siSHANK3\_7), *KRAS* (siKRAS (smart pool)) or both targets, compared to AllStars control (siCTRL). Samples were resolved and blotted on duplicate membranes (five independent experiments). Quantification of protein levels is shown on the right (mean  $\pm$  s.e.m.; one sample t test). **e**, Representative growth curves from a non-linear fit of PANC-1 cells transfected as in (d) over a 4-day time course (mean  $\pm$  s.e.m.; 6 wells/condition/replicate; representative of three independent experiments is shown). **f**, Endpoint analysis from absorbance measurements (arbitrary units) in (e), normalising to the maximum of each replicate (mean  $\pm$  s.e.m.; three independent experiments; 6 wells/replicate/condition; one-way ANOVA with a Tukey correction for multiple comparisons (ns, not significant). **g, h** Representative western blots and quantification of apoptosis markers, ERK activity and endogenous *SHANK3* expression in GFP and GFP-KRASG12V-expressing A549 cells 2 days after transfections. GFP was blotted to validate transfection efficiency (data points are the individual experiments; mean  $\pm$  s.e.m.; n = 4 independent experiments; two-tailed one-sample t test). Source data are provided as a Source Data file.



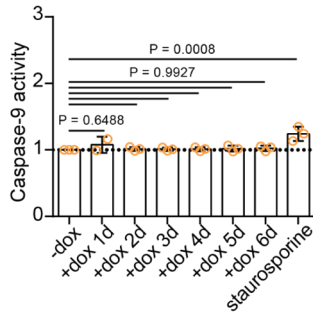
**Supplementary Figure 7. Inducible silencing of *SHANK3* activates ERK and induces apoptosis, Related to Figure 5.**

Left: *SHANK3* gene expression (mRNA levels) showing the efficiency of *SHANK3* silencing in control or doxycycline-induced (Dox: +; 72 h) shSHANK3 expressing PANC-1 clones (clones 1C and 4S). Right: Representative immunoblots of the indicated proteins collected three days after induction. Samples were resolved and blotted on duplicate membranes (m#1 and m#2). p-ERK, phospho-ERK1/2 (Thr202/Y204); ERK, total ERK; AKT, total AKT; p-AKT, phospho-AKT S473; cleaved-PARP1, indicative of apoptosis; GAPDH, a loading control (mean  $\pm$  s.d.; three independent experiments). Source data are provided as a Source Data file.

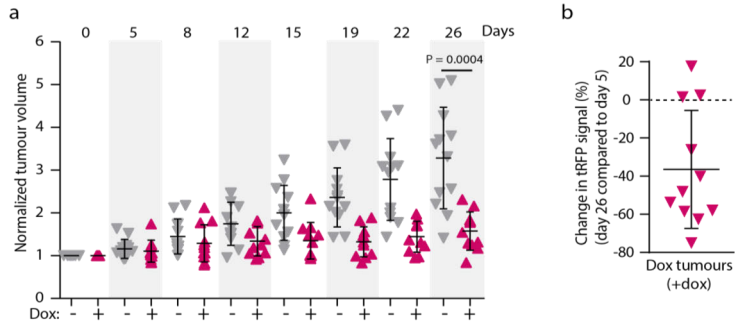
**a****b****c**



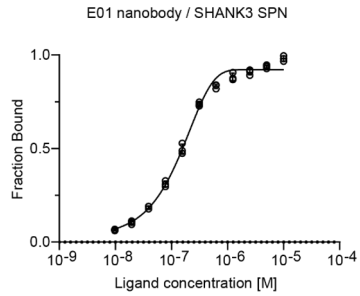
**Supplementary Figure 8. SHANK3 depletion in established KRAS-mutant spheroids induces apoptosis, Related to Figure 5.** **a**, Representative images of spheroids and apoptosis (green Annexin V-positive cells) levels for control or doxycycline-induced (+dox) shSHANK3-expressing PANC-1 clones (clones 1C and 4S); doxycycline-induction was started after 5 days of spheroid growth and continued until day 15. ROI, region of interest (within blue squares). **b**, Quantification of spheroid growth (data represent mean  $\pm$  s.d.; n = 6 technical replicates from two independent experiments). **c**, Analysis of apoptosis (Annexin V-positive area) in established spheroids. Both doxycycline and Annexin V were added to spheroids at day 5 (arrow) [data represent mean  $\pm$  s.d.; n = 4 (clone 1C +dox), 5 (clone 4S) or 6 (clone 1c, -dox) technical replicates from two independent experiments]. Source data are provided as a Source Data file.



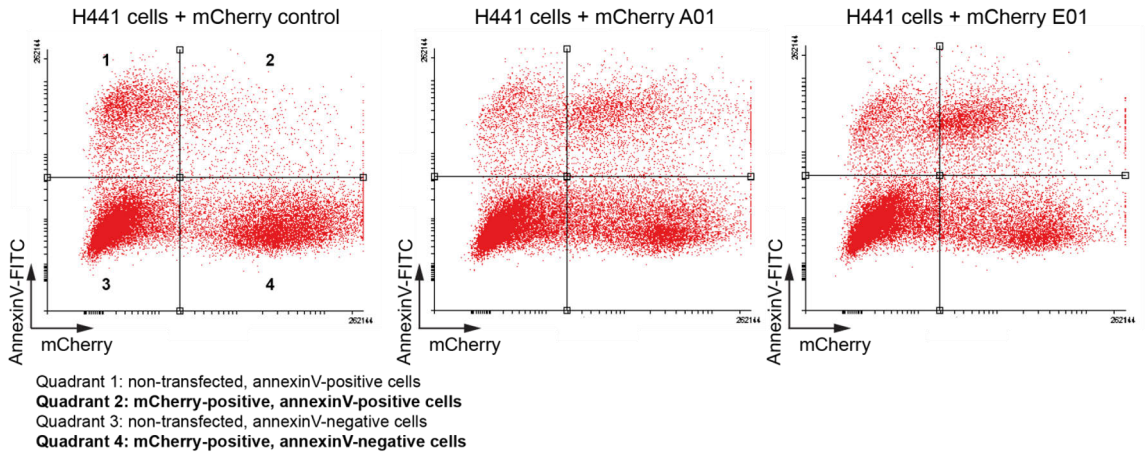
**Supplementary Figure 9. SHANK3 depletion has no significant effect on caspase-9 activity in *KRAS*-mutant PANC-1 cells, Related to Figure 5.** Caspase-9 activity in control (-dox) and doxycycline-induced (+dox) sh*SHANK3*-expressing PANC-1 cells. Caspase activity was measured using a fluorometric assay at the indicated time points (shown is normalized fluorescence intensity). Staurosporine was included as a positive control (mean  $\pm$  s.d. from three independent experiments; one-way ANOVA with Holm-Sidak's multiple comparison test). Source data are provided as a Source Data file.



**Supplementary Figure 10. SHANK3 depletion in established PDAC tumours impairs tumorigenic growth *in vivo*, Related to Figure 5. a**, Growth rate of subcutaneously injected PANC-1 xenografts with doxycycline-inducible *SHANK3* knockdown (+dox) over the indicated time. Tumour growth was monitored with bi-weekly palpations (mean  $\pm$  s.d. of  $n = 11$  (+dox) and 12 (-dox) tumours; two-tailed unpaired Student's t-test with Welch's correction). **b**, *SHANK3* depletion was observed by tRFP reporter (visual tracking of transduction and expression of shRNA). Shown is a change in tRFP signal (%) in tumours with doxycycline-inducible *SHANK3* knockdown at the end of the experiment (mean  $\pm$  s.d.;  $n = 11$  (+dox)). Each data point represents an individual mouse (**a,b**). Source data are provided as a Source Data file.



**Supplementary Figure 11. The binding affinity of the anti-SHANK3 nanobody E01 for SHANK3 SPN.** Microscale thermophoresis (MST) binding curve for the interaction between the His-tagged SHANK3 SPN and E01 nanobody recombinant proteins. MST measurements were performed using His-tag labelled SPN protein as a target and unlabelled E01 nanobody as a ligand. The affinity curve and  $K_d$ -value ( $137 \pm 6$  nM) are obtained from triplicate measurements (mean  $\pm$  s.e.m; one independent experiment). Source data are provided as a Source Data file.



**Supplementary Figure 12. Targeting KRAS–SHANK3 interaction by anti-SHANK3 nanobodies induces apoptosis.** Related to Figures 6d,e. Representative scatter plots of Annexin V-FITC / mCherry signal in H441 cells expressing either mCherry alone or mCherry-tagged anti-SHANK3 SPN nanobodies A01 or E01. Quadrant 2 represents apoptotic cells expressing the indicated control or nanobody. Gating strategy and data analysis was similarly performed for all cell lines in Figures 6d,e.

**Supplementary Table 1. Key details of the simulated systems, Related to Figure 3.**

System	Protein components (mutation, residue range, other information)	Number of lipids (POPC/ cholesterol/ PIP2)	Number of water molecules, and number of ions (K <sup>+</sup> ,Cl <sup>-</sup> )	Number of replicas x duration (ns)	PDB Ref.
S1	SHANK3 SPN-ARR (wt, 2–347)	500/0/0	63047 (173, 171)	4 x 1000	5G4X
S2	SHANK3 SPN-ARR (wt, 2–347)	364/168/28	61451 (282, 168)	4 x 1000	5G4X
S3	SHANK3 SPN (wt, 2–93)	182/84/14	24276 (121, 66)	4 x 1000	5G4X
S4	KRAS (wt, 1–185)	166/76/14	29032 (132, 78)	4 x 2000	6PTW
S5	SHANK3 SPN-ARR (wt, 5–363) KRAS (wt, 1–185) GNP	414/190/26	74534 (303,204)	4 x 1000	6PTW / 6KYK

## Supplementary References

1. Johnson, C. W. *et al.* Isoform-Specific Destabilization of the Active Site Reveals a Molecular Mechanism of Intrinsic Activation of KRas G13D. *Cell Rep* **28**, 1538-1550.e7 (2019).
2. Johnson, C. W. *et al.* The small GTPases K-Ras, N-Ras, and H-Ras have distinct biochemical properties determined by allosteric effects. *J Biol Chem* **292**, 12981–12993 (2017).

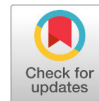




**Conway JRW, Dinç DD, Follain G, Paavolainen O, Kaivola J, Boström  
P, Hartiala P, Peuhu E & Ivaska J. (2023)  
IGFBP2 secretion by mammary adipocytes limits breast cancer  
invasion.  
Science Advances**







## CELL BIOLOGY

# IGFBP2 secretion by mammary adipocytes limits breast cancer invasion

James R. W. Conway<sup>1\*</sup>, Defne D. Dinç<sup>1,2,3</sup>, Gautier Follain<sup>1</sup>, Oona Paavolainen<sup>1,2,3</sup>, Jasmin Kaivola<sup>1</sup>, Pia Boström<sup>4</sup>, Pauliina Hartiala<sup>5,6</sup>, Emilia Peuhu<sup>1,2,3</sup>, Johanna Ivaska<sup>1,3,7,8,9\*</sup>

The progression of noninvasive ductal carcinoma in situ to invasive ductal carcinoma for patients with breast cancer results in a significantly poorer prognosis and is the precursor to metastatic disease. In this work, we have identified insulin-like growth factor-binding protein 2 (IGFBP2) as a potent adipocrine factor secreted by healthy breast adipocytes that acts as a barrier against invasive progression. In line with this role, adipocytes differentiated from patient-derived stromal cells were found to secrete IGFBP2, which significantly inhibited breast cancer invasion. This occurred through binding and sequestration of cancer-derived IGF-II. Moreover, depletion of IGF-II in invading cancer cells using small interfering RNAs or an IGF-II-neutralizing antibody ablated breast cancer invasion, highlighting the importance of IGF-II autocrine signaling for breast cancer invasive progression. Given the abundance of adipocytes in the healthy breast, this work exposes the important role they play in suppressing cancer progression and may help expound upon the link between increased mammary density and poorer prognosis.

## INTRODUCTION

As breast cancer incidence continues to increase globally, the progression to metastatic disease remains the leading cause of death (1). Metastasis is a multistep process, beginning with a switch from a noninvasive ductal carcinoma to an invasive phenotype at the primary site. Extensive research into the trigger for this switch has revealed both cancer cell-intrinsic and -extrinsic drivers, where reciprocal signaling between the extracellular environment and the tumor leads to a concomitant progression of both stromal and cancer cells toward an aggressive disease state (2). Healthy mammary gland stroma has a sparse extracellular matrix (ECM) and is dominated by an abundance of adipocytes (3). Conversely, the breast cancer microenvironment is characterized by a high degree of desmoplasia and a reduced number and size of adipocytes adjacent to the tumor (4, 5). It has been shown that changes in the composition and architecture of the mammary ECM during breast cancer development support invasive progression, and loss of this ECM can result in reversion to a less-aggressive disease state (6, 7). While the importance of the ECM is clear, the established link between increased mammary density and a higher risk of breast cancer development has, so far, failed to address the role of adipocytes in containing the disease (3). Adipose tissue is a significant endocrine organ, and secretion of adipocrine factors plays a key role in tissue homeostasis (4). Notably, the processes through which tumors are able to overwhelm the homeostatic mechanisms

aimed at their containment remains poorly explored. In this work, we uncover a mechanism by which mammary adipocytes provide a barrier to cancer invasive progression and, through antibody-based therapeutic intervention, suggest possible routes for reintroduction of this mechanism into a clinical setting.

## RESULTS

### HUVEC-derived angiocrine factor(s) reduce breast cancer invasion

Cancer cell invasion away from the primary tumor commonly leads to intravasation into the adjacent blood and lymphatic vessels (8). To model this process in vitro, we assessed the invasion of cancer cells into fibroblast-contracted collagen I matrices toward human umbilical vein endothelial cells (HUVECs; Fig. 1A) (9). The presence of proximal endothelial cells did not promote the invasion of the MDA-MB-231 (MM231) triple-negative breast cancer cells (TNBCs), but instead markedly inhibited this process (Fig. 1B; quantified in Fig. 1C), while having no effect on proliferation (fig. S1, A and B). This indicated the presence of an anti-invasive angiocrine factor(s) secreted by the HUVECs. To confirm this hypothesis, we applied HUVEC- or MM231-conditioned medium to an inverted invasion assay platform (Fig. 1D) and found again that the presence of the HUVEC-derived angiocrine factor(s) markedly reduced the invasion of MM231 cancer cells (Fig. 1, E and F).

Endothelial cells from other tissues [conditioned medium from immortalized dermal microvascular endothelial, HMEC-1, cell line or primary human pulmonary microvascular endothelial cells (HPMECs)] did not secrete the same anti-invasive factor(s) as the HUVECs (fig. S1, C to F), suggesting that this could be a HUVEC-specific secreted factor(s), rather than a general feature of endothelia. In contrast to our work, others have shown that HUVECs cultured in three-dimensional (3D) microfluidic channels under flow induce the invasion of adjacent pancreatic cancer cells (10, 11). However, the HUVECs cultured in our study are not exposed to flow-induced shear stress, which is known to change gene

<sup>1</sup>Turku Bioscience Centre, University of Turku and Åbo Akademi University, FI-20520 Turku, Finland. <sup>2</sup>Institute of Biomedicine, and Cancer Research Laboratory FICAN West, University of Turku, FI-20520 Turku, Finland. <sup>3</sup>Western Finnish Cancer Center (FICAN West), University of Turku and Turku University Hospital, FI-20520 Turku, Finland. <sup>4</sup>Department of Pathology, Turku University Hospital, 20520 Turku, Finland; University of Turku, 20520 Turku, Finland. <sup>5</sup>Department of Plastic and General Surgery, Turku University Hospital, 20520 Turku, Finland. <sup>6</sup>Medicity Research Laboratory, InFLAMES Research Flagship, University of Turku, Turku, Finland. <sup>7</sup>Department of Life Technologies, University of Turku, FI-20520 Turku, Finland. <sup>8</sup>InFLAMES Research Flagship Center, University of Turku, Turku, Finland. <sup>9</sup>Foundation for the Finnish Cancer Institute, Tukholmantkatu 8, FI-00014 Helsinki, Finland.

\*Corresponding author. Email: jdconw@utu.fi (J.R.W.C.); joivaska@utu.fi (J.I.)

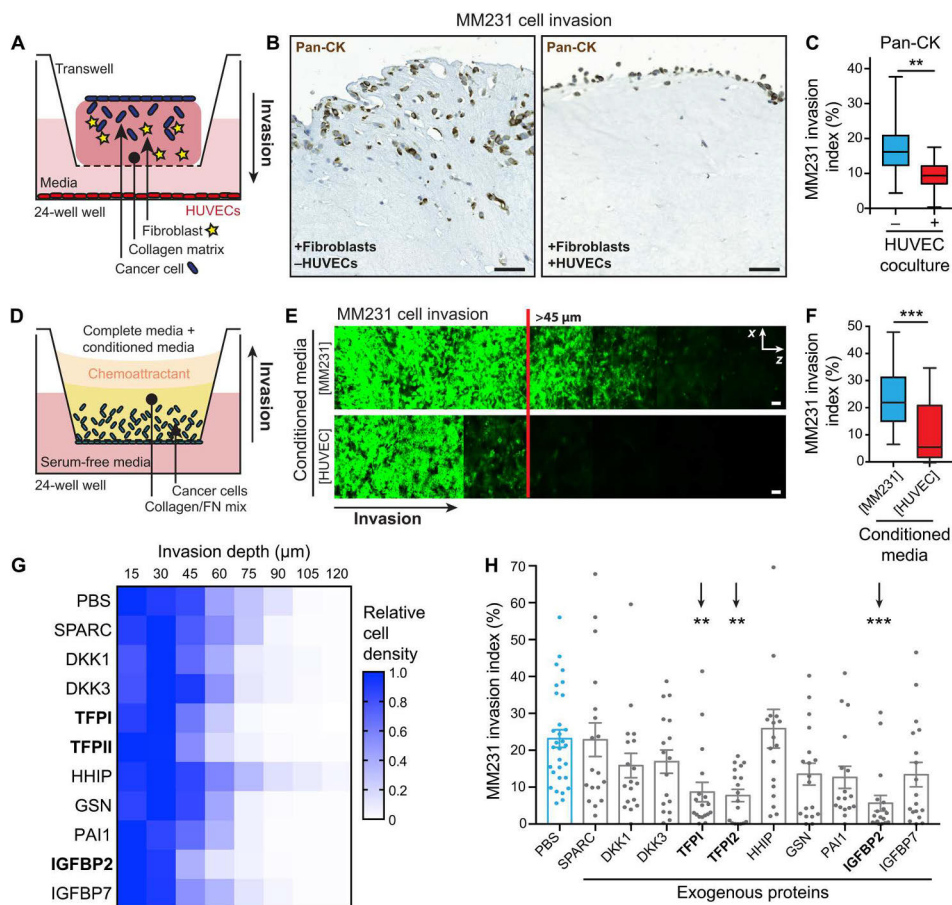


**Fig. 1. HUVECs secrete an anti-invasive factor effective against MM231 breast cancer cells.** (A) Schematic of the fibblast-contracted three-dimensional (3D) collagen matrix cancer cell invasion assay with HUVEC coculture. (B and C) Representative images (B) and quantification (C) of MM231 cell [stained with pan-cytokeratin (Pan-CK); epithelial cell marker] invasion into fibblast-contracted 3D collagen matrices ± HUVEC coculture, performed in the presence of endothelial growth factor-reduced medium. Scale bars, 50 μm. [n = 3 biological replicates, triplicate matrices, eight regions per condition per replicate; one-way analysis of variance (ANOVA) with Tukey correction; \*\*P < 0.01 and \*\*\*P < 0.001.] (D) Schematic of the inverted invasion assay platform. (E and F) Representative images (E) and quantification (F) of MM231 breast cancer cell (in green) invasion into inverted collagen/fibronectin matrices in the presence of concentrated conditioned media added to the normal culture medium (origin specified in square brackets). Scale bars, 50 μm. n = 3 biological replicates performed in triplicate, with three stacks per transwell; two-tailed Student's t test with Welch's correction; \*\*\*P < 0.001. (G and H) Inverted invasion screen heatmap (G) and quantification (H) of MM231 cell invasion in the presence of the indicated exogenously administered recombinant proteins (5 μM; n = 3 biological replicates performed with duplicate transwells per condition, with three stacks per transwell; one-way ANOVA with Tukey correction; \*\*P < 0.01 and \*\*\*P < 0.001).

expression profiles and cell alignment (12), and are not in direct contact with breast cancer cells. These factors, along with the cancer type, are most likely the key differentiating features between our study and prior work.

To determine the secreted angiocrine factor(s) responsible for the observed HUVEC-mediated anti-invasive effect, we selected four published HUVEC secretomes and found >296 common factors between two or more secretomes (data S1) (13–16). These were then filtered through the tumor suppressor gene database (TSGene 2.0) (17) to identify candidates with putative antitumor

activity. This analysis yielded a list of 10 candidate anti-invasive angiocrine factors with previous links to hedgehog [hedgehog-interacting protein (HHIP)], Wnt [Dickkopf-related protein 1 (DKK1) and DKK2], insulin-like growth factor (IGF) regulation [IGF-binding protein 2 (IGFBP2) and IGFBP7], or calcium [secreted protein acidic and cysteine rich (SPARC)] signaling, as well as protease inhibition [plasminogen activator inhibitor 1 (PAI1)], actin polymerization [gelsolin (GSN)], and blood coagulation [tissue factor pathway inhibitor (TFPI and TFPI2)]. We then screened for potential effects on proliferation and invasion. While none of

these factors significantly affected MM231 cell proliferation (fig. S1, G and H), the exogenous addition of TFPI, TFPI2, and IGFBP2 did significantly reduce MM231 cell invasion (Fig. 1, G and H).

### IGFBP2 secretion by HUVECs and fibroblasts exhibits a potent anti-invasive effect

The tissue factor pathway has a well-established link with cancer progression, and particularly with metastatic dissemination (18), while the IGFBPs are reported to have conflicting roles in breast cancer progression (19–22). Linked to the observed HUVEC-specific anti-invasive effect, we next assessed the levels of IGFBP2 secreted by different endothelial cell lines. We found that it was significantly expressed in the HUVECs alone (fig. S2A), suggesting that the presence of IGFBP2 in the HUVEC-conditioned medium may be essential for the observed anti-invasive effect (fig. S1, C to F). To confirm this hypothesis, we assessed the anti-invasive effect of conditioned medium collected from *IGFBP2*-silenced HUVECs. After silencing, the secreted IGFBP2 was significantly reduced, compared to the nontarget small interfering RNA (siRNA) control (siNTC; fig. S2, B and C), and where IGFBP2 was no longer secreted, the anti-invasive effect was also lost (Fig. 2A; quantified in Fig. 2B).

In the 3D coculture assay, cancer cells invade into collagen that has been remodeled by fibroblasts. To further validate the anti-invasive effect of IGFBP2 and to model the putative outcome of secreted IGFBP2, we generated telomerase immortalized fibroblasts (TIFs) with stable overexpression and secretion of IGFBP2 or a control fluorescent protein construct [mTurquoise2 (mT2); Fig. 2, C to E]. Consistent with earlier findings, the MM231 cells were significantly less efficient at invading into 3D collagen I matrices contracted by IGFBP2-secreting TIFs, compared to control mT2 TIFs (Fig. 2F), demonstrating that secreted IGFBP2 is anti-invasive. Concordant with the earlier results, TIF-secreted IGFBP2 had no detectable effect on the proliferation of MM231 cells (fig. S2D).

To assess the effect of IGFBP2 reintroduction on the breast tumor microenvironment, we co-xenografted MM231s with the IGFBP2- or mT2-overexpressing TIFs (Fig. 2G). In this mouse model, we observed no effect on the proliferation of cancer cells (fig. S2E). However, there was a clear reduction in cancer cell invasion into the surrounding stroma in the IGFBP2 TIF co-xenografts (Fig. 2H), supporting the idea that IGFBP2 plays a protective role in the stroma and, when present, is able to contain the tumor.

### Mammary stromal adipocytes secrete IGFBP2 and reduce breast cancer invasion

Changes in the breast stroma are an essential factor in breast cancer progression. This prompted us to stain patient samples for IGFBP2 in adjacent healthy breast tissue sections to judge the physiological relevance of our findings to invasive progression (Fig. 3A; patient details in data S2). Unexpectedly, this staining revealed a strong positive IGFBP2 signal in the adipocyte cells, whereas the signal exhibited by the vessels was lower or negative (Fig. 3A, i and ii). Similarly, when comparing the epithelial cells in the mammary ducts, it was again clear that the adipocytes were the main cells in the breast microenvironment that expressed IGFBP2 (Fig. 3A, iii). Together, these data suggest that adipocytes in the mammary stroma are the most prominent expressors of IGFBP2 in situ.

Having identified adipocytes as the cells in the mammary stroma with the highest expression of IGFBP2, we next investigated whether IGFBP2 was an adipocrine factor secreted into the breast

microenvironment. Several groups have isolated primary adipocytes from patients (23, 24). However, because of the scarcity of samples and the challenges associated with applying these protocols, we instead sought to differentiate isolated breast preadipocytes into mature adipocytes from human stromal samples collected from healthy reduction mammoplasty patients (see Materials and Methods for details). These differentiated primary patient cells were positive for the adipocyte marker peroxisome proliferator-activated receptor gamma (PPAR $\gamma$ ) and the presence of lipid droplets, which marked the mature and not the preadipocyte cells (Fig. 3B). Similarly, the mature adipocytes showed an increased mRNA level of established adipocyte markers, when compared to preadipocytes (Fig. 3C). The mature adipocytes had a higher level of IGFBP2, which was visible in the immunofluorescence staining and at the mRNA level. This was consistent with an increase in secretion of IGFBP2 in conditioned medium from mature adipocytes (Fig. 3D). The secreted IGFBP2 had no effect on the proliferation of MM231 cells (fig. S2, F and G), but resulted in a significant reduction in cancer invasion, when compared to the plain medium [adipocyte growth medium (AM-1) or complete medium] controls (Fig. 3, E and F).

Lastly, coculture of cancer cells with the IGFBP2-secreting adipocytes significantly reduced cancer cell invasion into fibroblast-contracted 3D collagen I matrices (Fig. 3G; quantified in Fig. 3H). The addition of adipocytes into the coculture system also significantly reduced cancer cell proliferation (Fig. 3, G and H), suggesting that adipocrine factors other than IGFBP2 may be able to exert additional anticancer effects. Cumulatively, these findings uncover a role for healthy mammary stromal adipocytes in the containment of cancer invasion.

### IGFBP2 did not detectably bind to the cancer cell surface or ECM

We hypothesized that IGFBP2 could exert its anti-invasive function by binding to and inhibiting cell surface receptors. To test this, we tagged IGFBP2 with the clover fluorescent protein to enable visualization in the extracellular space. TIFs were then engineered to overexpress clover-tagged IGFBP2, which resulted in efficient IGFBP2 secretion and, when applied to invading MM231s (fig. S3, A and B), recapitulated the anti-invasive effects observed with the addition of untagged IGFBP2 (fig. S3, C and D). Having established the biological activity of the clover-tagged IGFBP2, we next applied the concentrated IGFBP2 medium (from the TIFs) to MM231 cells and assessed IGFBP2 binding to cancer cells using flow cytometry. With this approach, we observed no increase in the fluorescence signal in MM231 cells treated with clover-tagged or untagged (negative control) IGFBP2, compared to MM231s stably expressing IGFBP2-Clover (positive control; fig. S3, E and F). These experiments demonstrate that exogenous IGFBP2 does not bind to the surface of cancer cells, suggesting that the anti-invasive effects are occurring through binding of IGFBP2 to something in the cancer microenvironment.

Next, we explored the possibility of IGFBP2 binding to the ECM and interfering with cell-ECM interactions. It has previously been shown that IGFBP2 binds to the ECM through two domains, one in the linker domain and one in the C domain, which mediate binding to fibronectin, vitronectin, collagen IV, laminin, and heparin (25, 26). To assess IGFBP2 binding to the ECM, we generated cell-derived matrices (CDMs) using TIFs stably expressing IGFBP2-

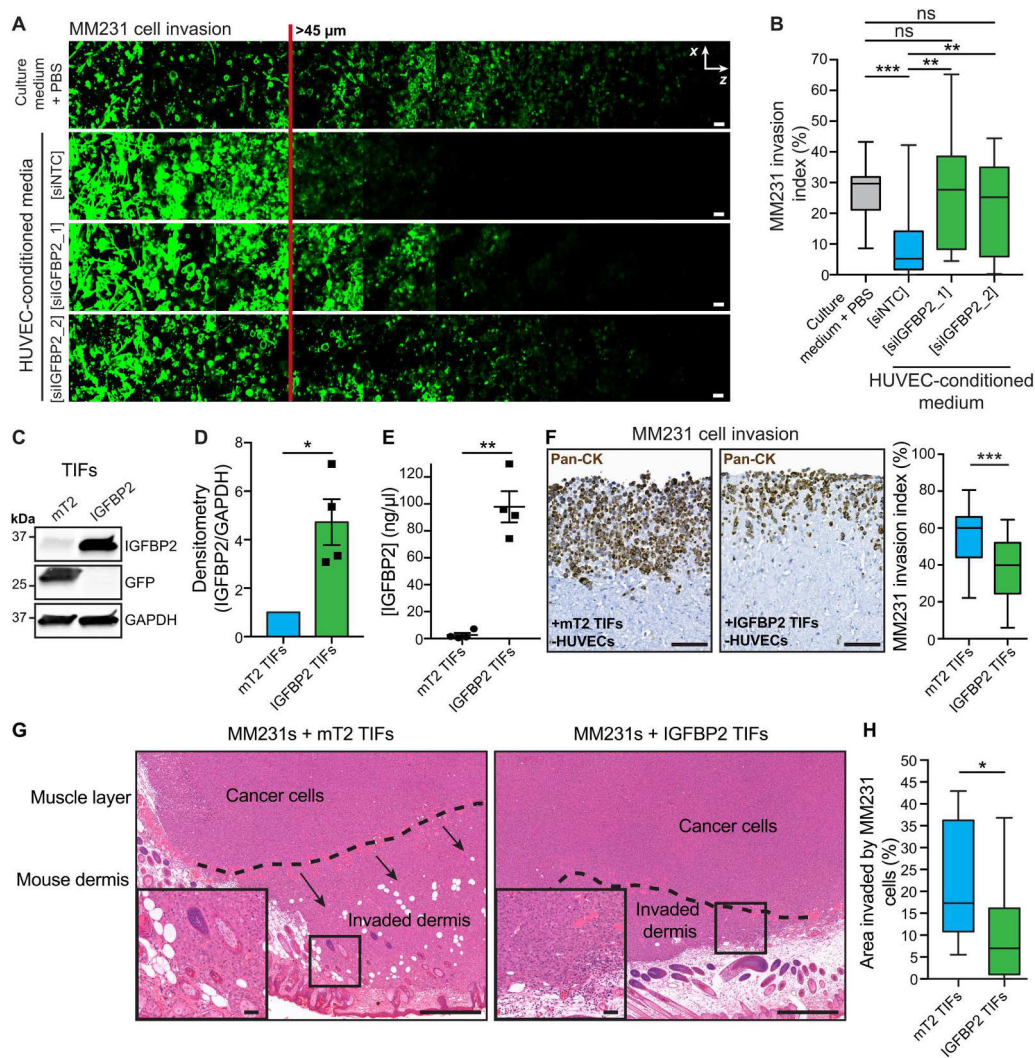
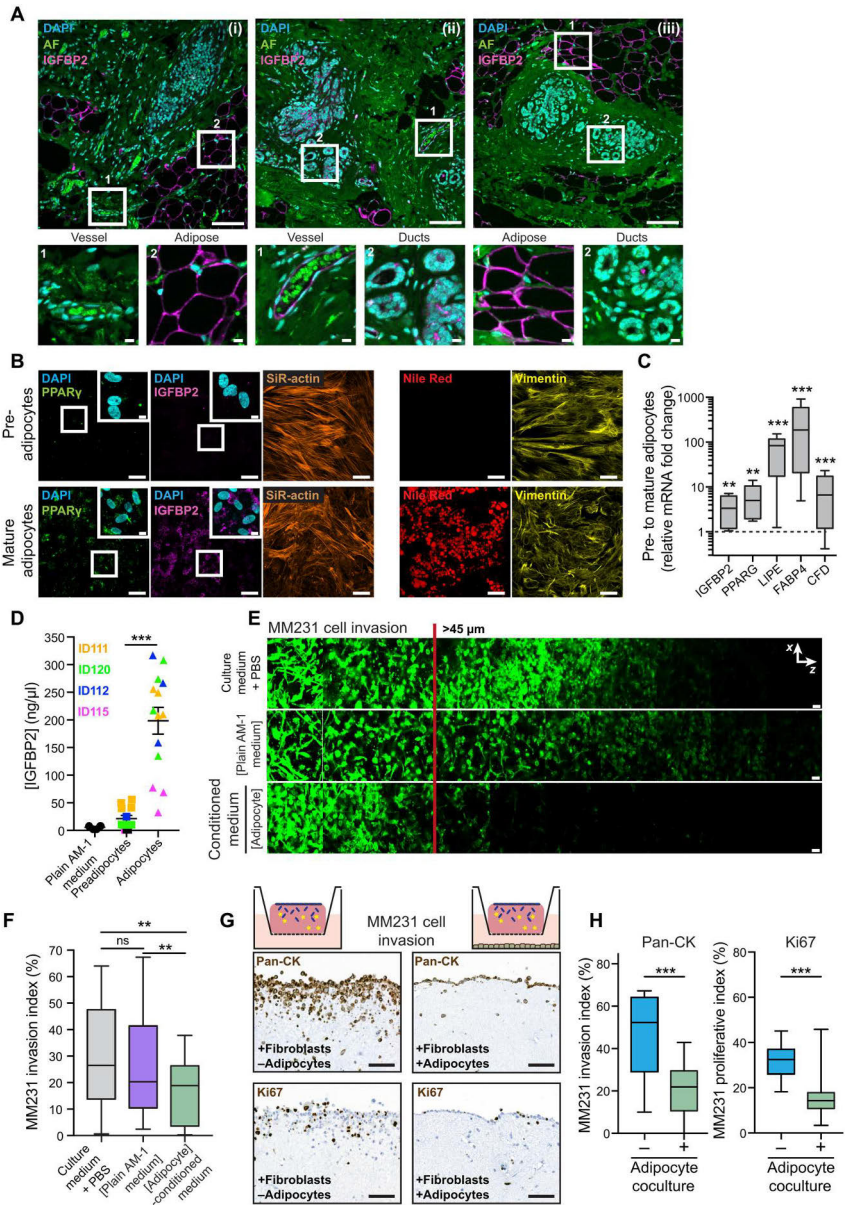


**Fig. 2. Stromal-derived IGFBP2 is sufficient to inhibit MM231 breast cancer cell invasion.** (A and B) Representative images (A) and quantification (B) of MM231 breast cancer cell invasion in inverted collagen/fibronectin matrices in the presence of conditioned medium from HUVECs transfected with siRNAs against IGFBP2 (siIGFBP2\_1 and siIGFBP2\_2) or siNTC. Scale bars, 50  $\mu$ m.  $n = 3$  biological replicates performed in triplicate, with three stacks per transwell; one-way ANOVA with Tukey correction;  $**P < 0.01$  and  $***P < 0.001$ ; ns, not significant. (C and D) Representative Western blot (C) and densitometry analysis (D) of TIFs stably overexpressing mTurquoise2 (mT2) or IGFBP2, measured in duplicate ( $n = 3$  biological replicates; two-tailed Student's  $t$  test;  $**P < 0.01$ ). (E) Enzyme-linked immunosorbent assay (ELISA) for human IGFBP2 in concentrated conditioned media from TIFs overexpressing mT2 or IGFBP2, measured in duplicate ( $n = 3$  biological replicates; two-tailed Student's  $t$  test;  $**P < 0.01$ ). (F) Representative images and quantification of fibroblast-contracted 3D collagen invasion assays of MM231 cancer cell invasion in mT2 or IGFBP2 TIF-contracted matrices after 14 days and stained for Pan-CK (brown). Scale bars, 100  $\mu$ m.  $n = 3$  biological replicates, triplicate matrices, eight regions per condition per replicate; one-way ANOVA with Tukey correction;  $***P < 0.001$ . (G and H) Representative hematoxylin and eosin (H&E) images (G) and quantification (H) of MM231 cell invasion into the mouse dermis from subcutaneous xenografts of MM231 co-injected with TIFs overexpressing either mT2 (control) or IGFBP2. Scale bars, 500  $\mu$ m; insets, 50  $\mu$ m.  $n = 10$  mice (mT2) or 12 mice (IGFBP2).

**Fig. 3. Breast adipocytes secrete the anti-invasive factor IGFBP2.**

**(A)** Three representative images ((i) to (iii)) of human breast tissue stained for IGFBP2 (magenta) and counterstained with 4',6-diamidino-2-phenylindole (DAPI) (cyan). Autofluorescence (AF) signal is green. Scale bars, 100  $\mu$ m; insets, 10  $\mu$ m.  $n = 2$  adjacent healthy breast tissue sections from ductal carcinoma in situ (DCIS) patient samples. **(B)** Representative images of primary human breast pre- and mature adipocytes with immunofluorescence staining for IGFBP2/PPAR $\gamma$ /actin or Nile Red/vimentin. Scale bars, 50  $\mu$ m; insets, 10  $\mu$ m.  $n = 4$  normal reduction mammoplasty patient samples from which preadipocytes were isolated, cultured, and differentiated into mature adipocytes. **(C)** Fold change in gene expression between pre- and mature adipocytes, normalized to glyceraldehyde-3-phosphate dehydrogenase (*GAPDH*), and detected by quantitative reverse transcription polymerase chain reaction [adipocytes from  $n = 4$  patient samples, differentiated as in (B), in triplicate; one-sample  $t$  test;  $^{**}P < 0.01$  and  $^{***}P < 0.001$ ]. *PPARG*, peroxisome proliferator activated receptor gamma; *LIPE*, lipase E; *FABP4*, fatty acid binding protein 4; *CFD*, complement factor D. **(D)** ELISA for human IGFBP2 from pre- and mature adipocyte conditioned media, compared to the adipocyte culture media [AM-1; adipocytes from  $n = 4$  patient samples processed as in (B) and media collected; two-tailed Student's  $t$  test with Welch's correction;  $^{***}P < 0.001$ ]. **(E and F)** Representative images (E) and quantification (F) of MM231 cell invasion in inverted collagen/fibronectin matrices in the presence of concentrated conditioned media from adipocytes or adipocyte growth medium, AM-1, or full culture medium with an equivalent volume of PBS added. Scale bars, 50  $\mu$ m. adipocytes from  $n = 4$  patient samples, processed as in (B) and media collected, performed in triplicate with three stacks per transwell; one-way ANOVA with Tukey correction;  $^{**}P < 0.01$ . **(G and H)** Representative images (G) and quantification (H) of a fibroblast-contracted 3D collagen matrix cancer cell invasion assay monitoring MM231 cancer cell invasion  $\pm$  mature adipocyte coculture and stained for either Pan-CK or the proliferation marker Ki67. Scale bars, 100  $\mu$ m.  $n = 3$  biological replicates, triplicate matrices, eight regions per condition per replicate; one-way ANOVA with Tukey correction;  $^{***}P < 0.001$ ).



Clover or mT2 (27, 28). However, IGFBP2-Clover did not appear to decorate the collagen or laminin fibers, instead giving a weak non-specific signal lower than the background signal observed with the mT2 control (fig. S3G). With this system, we also assessed the effect of IGFBP2 expression on ECM organization and fibronectin deposition within the collagen network and found no significant differences between the ECM generated by either mT2 or IGFBP2-Clover expressing fibroblasts (fig. S3, H to J). As CDMs involve a decellularization step that may have displaced the IGFBP2 from the CDM matrices, we also assessed the adhesion and spreading of MM231s on collagen/fibronectin in the presence of IGFBP2 and again found no significant effect (fig. S3, K and L). This led us to the conclusion that soluble rather than ECM-incorporated IGFBP2 is responsible for blocking invasion.

### IGFBP2 disrupts proinvasive IGF-II autocrine signaling

Given the above results, we hypothesized that soluble IGFBP2 was binding to and sequestering a proinvasive molecule secreted by cancer cells. To explore this possibility, we performed unbiased mass spectrometry, incubating MM231 cells with conditioned medium from TIFs overexpressing IGFBP2-Clover or TIF-conditioned medium containing recombinant green fluorescent protein (rGFP; negative control). We then performed GFP-trap-immunoprecipitation and proteomics analysis of the medium to identify IGFBP2-binding partners (Fig. 4A and data S3). Only IGF-II was notably enriched in the IGFBP2 condition, and this corresponds to one of the two canonical binding partners of IGFBP2 (25, 26).

To assess the role of IGF-II in MM231 invasion, we applied siRNAs to silence *IGF2* (Fig. 4B; quantified in Fig. 4C), and observed a clear reduction in invasion (Fig. 4D; quantified in Fig. 4E). Congruent with these data, sequestration of secreted IGF-II by exogenous administration of an anti-IGF-II antibody recapitulated the anti-invasive effect of IGFBP2 treatment (Fig. 4F; quantified in Fig. 4G). Treatment with recombinant IGF-II had no effect on invasion, suggesting that MM231s have already reached a proinvasive autocrine threshold (Fig. 4, F and G).

The anti-IGF-II antibody applied here has already shown promising efficacy as an anticancer agent in breast cancer xenografts (29). Given that TNBC remains the most aggressive breast cancer subtype with the poorest prognosis (30), we chose two additional TNBC cell lines, MDA-MB-468 (MM468) and HCC1937, to confirm the broader significance of IGF-II-driven invasion. We compared IGF-II levels across cell lines and found higher expression in MM468 and MM231 cells, compared to TIF and HCC1937 cells (Fig. 4H; quantified in Fig. 4I), which was paralleled by increased secretion (Fig. 4J). Notably, the pre- and mature adipocytes applied here also secrete IGF-II (fig. S4A), but at levels ~200-fold less than IGFBP2 (Fig. 3D), suggesting that IGFBPs are secreted in excess and likely completely sequester adipocyte-derived IGF-II in the extracellular space.

Breaching of the basement membrane is one of the first steps in breast cancer invasive progression, and when modeling this process using Matrigel invasion chambers, we again found a clear reduction in MM231 cell invasion in the presence of the anti-IGF-II function-blocking antibody and IGFBP2 (Fig. 4K). These results were recapitulated in the MM468s (Fig. 4L), which also showed high IGF-II expression (Fig. 4, H and I). In line with the IGFBP2 perturbations above, there was again no effect on proliferation when IGF-II was depleted from the extracellular space or when added exogenously

(fig. S4, B to E). Similarly, when we applied MCF10DCIS.com (DCIS.com; fig. S4, F and G) breast cancer cells, which also express IGF-II, to the Matrigel invasion chambers (31), we again saw a significant reduction in invasion after IGFBP2 or anti-IGF-II treatments (fig. S4, H and I). Notably, DCIS.com cells undergo a ductal carcinoma in situ (DCIS) to invasive ductal carcinoma (IDC) transition when xenografted (32), suggesting that targeting IGF-II autocrine signaling may act to contain a wide range of breast cancers in situ. Cumulatively, we see that IGF-II depletion phenocopies IGFBP2 anti-invasive action in the TNBC and DCIS.com cell lines, supporting a model of stromal IGFBP2 disrupting proinvasive IGF-II autocrine signaling in cancer cells (Fig. 4M).

### IGFBP2-positive adipocytes are reduced in patient samples from DCIS and IDC

To further explore the clinical significance of these findings, we stained a cohort of healthy mammary gland, DCIS and IDC patient samples. High mammographic density is the strongest risk factor for breast cancer (33–35), where an increase in fibroglandular tissue occurs in concert with increased tissue stiffness, immune infiltration, and fibrosis (36, 37). Increased density is paralleled by a reduction in adipose tissue, which also occurs during breast cancer progression (Fig. 5A; quantified in Fig. 5B). When we stained these patient samples, the number of IGFBP2-positive cells was severely reduced from healthy to disease states (Fig. 5, C to E). As the risk of breast cancer increases with age, we also investigated IGFBP2 expression in adipocytes in healthy breast tissue of younger (ages 18 to 26) and older (ages 40 to 45) patient cohorts (fig. S5). IGFBP2 expression, but not overall adiposity, was significantly lower in the older healthy patient cohort (fig. S5). Moreover, adipocytes in the IDC samples had significantly reduced IGFBP2 expression, compared to the DCIS and healthy samples (Fig. 5F), and this was further reduced in adipocytes contained within the tumor borders, compared to those at the invasive front (Fig. 5F). Together, these data are supportive of lower stromal IGFBP2 expression correlating with age-related cancer risk and disease progression. This IGFBP2 loss in the breast tissue microenvironment upon disease progression highlights that investigation of healthy stromal cells may provide key insights into the mechanisms of tissue homeostasis that is disrupted in cancer.

## DISCUSSION

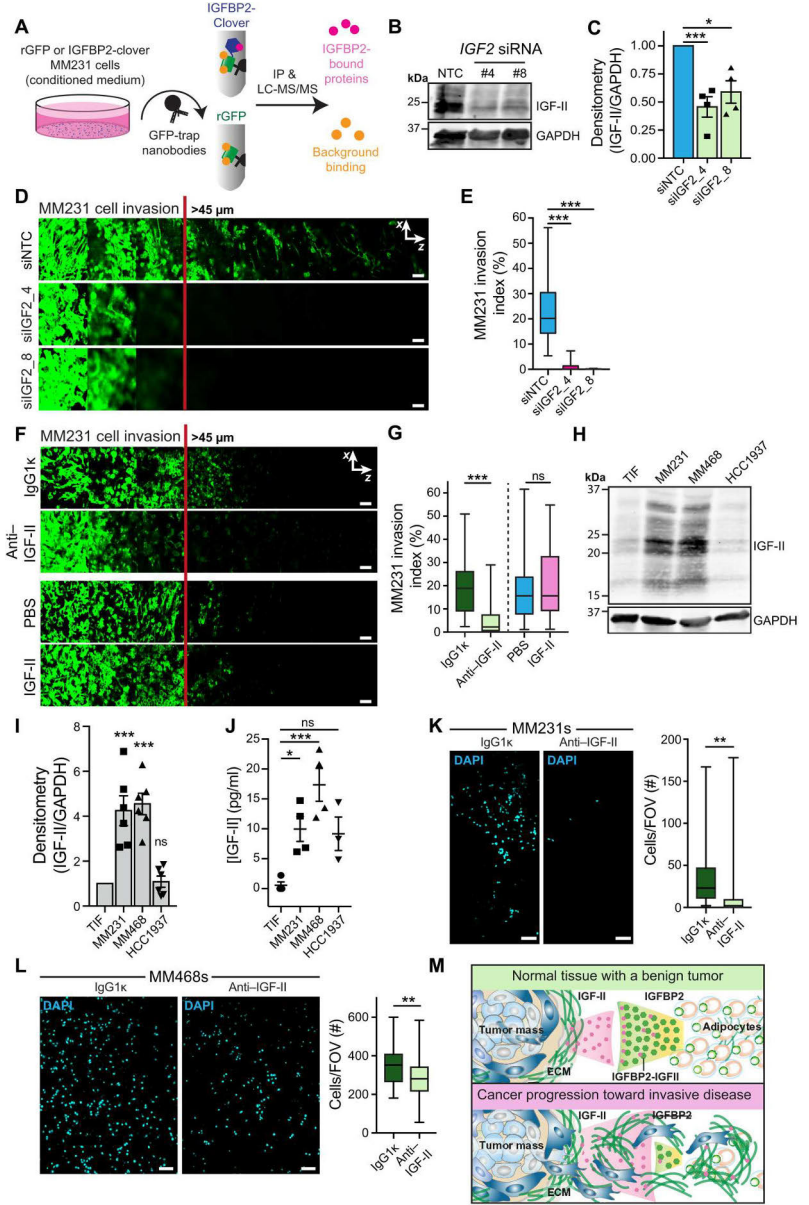
Here we show that healthy mammary adipocytes are able to restrain breast cancer invasion through secretion of IGFBP2, a novel anti-invasive adipocrine factor. Our experiments demonstrate that a healthy human mammary gland is rich in IGFBP2-expressing adipocytes and that IGFBP2 secreted by normal tissue-derived adipocytes efficiently blocks breast cancer invasion. Our study describes an anti-invasive mechanism in which autocrine proinvasive IGF-II signaling by cancer cells is disrupted by IGFBP2 acting as a stromal sequester of IGF-II. IGFBP2 action could be efficiently mimicked with an IGF-II-neutralizing antibody, implying direct clinical and therapeutic implications of our discovery.

The tissue composition of human breast is unique, with glandular structures surrounded by abundant adipocytes and low tissue rigidity. In contrast, desmoplasia (increased deposition of ECM) and subsequent stiffening of the tumor microenvironment plays a key role in breast cancer aggression (38). Our discovery of the cancer-



**Fig. 4. IGFBP2 acts through depletion of IGF-II from the cancer microenvironment.**

**(A)** Schematic of the proteomics experimental setup. LC-MS/MS, liquid chromatography–tandem mass spectrometry. IP, immunoprecipitation. **(B and C)** Representative Western blot (B) and densitometry analysis (C) after silencing of *IGF2* (IGF-II gene) using siRNAs in MM231 cells ( $n = 4$  biological replicates; one-sample  $t$  test;  $*P < 0.05$  and  $***P < 0.001$ ). **(D and E)** Representative images (D) and quantification (E) of MM231 cell invasion in inverted collagen/fibronectin matrices after *IGF2* silencing. Scale bars, 50  $\mu\text{m}$ .  $n = 3$  biological replicates, performed in duplicate with three stacks per transwell; one-way ANOVA with Tukey correction;  $***P < 0.001$ . **(F and G)** Representative images (F) and quantification (G) of MM231 cell invasion in inverted collagen/fibronectin matrices treated with PBS, IGF-II (10 ng/ml), IgG1k (10  $\mu\text{g/ml}$ ), or anti-IGF-II (10  $\mu\text{g/ml}$ ). Scale bars, 50  $\mu\text{m}$ .  $n = 3$  biological replicates, performed in duplicate with three stacks per transwell; one-way ANOVA with Tukey correction;  $***P < 0.001$ . **(H and I)** Representative IGF-II Western blot (H) and quantification (I) of TIF, MM231, MM468, and HCC1937 cells ( $n = 6$  biological replicates; one-sample  $t$  test;  $***P < 0.001$ ). **(J)** ELISA for human IGF-II in conditioned media from TIF, MM231, MM468, and HCC1937 cells ( $n = 4$  biological replicates; one-way ANOVA with Dunnett's correction;  $*P < 0.05$  and  $***P < 0.001$ ). **(K and L)** Matrigel invasion assays for MM231 (K) and MM468 (L) cells treated with IgG1k or anti-IGF-II ( $n = 3$ , eight fields of view (FOVs) per chamber, two to three invasion chambers per condition per replicate; two-tailed Student's  $t$  test with Welch's correction;  $**P < 0.01$ ). Scale bars, 100  $\mu\text{m}$ . **(M)** Schematic of the proposed mechanism for IGFBP2 inhibition of invasion through disruption of breast cancer IGF-II autocrine signaling.



limiting activity of mammary gland adipocytes is original and focuses on an understudied aspect of breast cancer stroma. Previous studies into the role of adipocytes in breast cancer progression have primarily focused on their loss during the process (3) and the concept of increased tissue rigidity contributing to breast cancer invasion through mechanochemical signaling in cancer cells (36). In addition, recent work has explored the changes in mammary

adipose tissue during tumor progression, finding that cancer-associated adipocytes express reduced adipogenesis-related genes, show increased browning, and secrete more inflammatory cytokines and matrix metalloproteinases, while furthering the desmoplastic reaction associated with breast cancer progression (4, 5, 39–42). In line with this work, we saw a loss of IGFBP2-positive adipocytes in DCIS and IDC patient samples, when compared to healthy breast tissue.

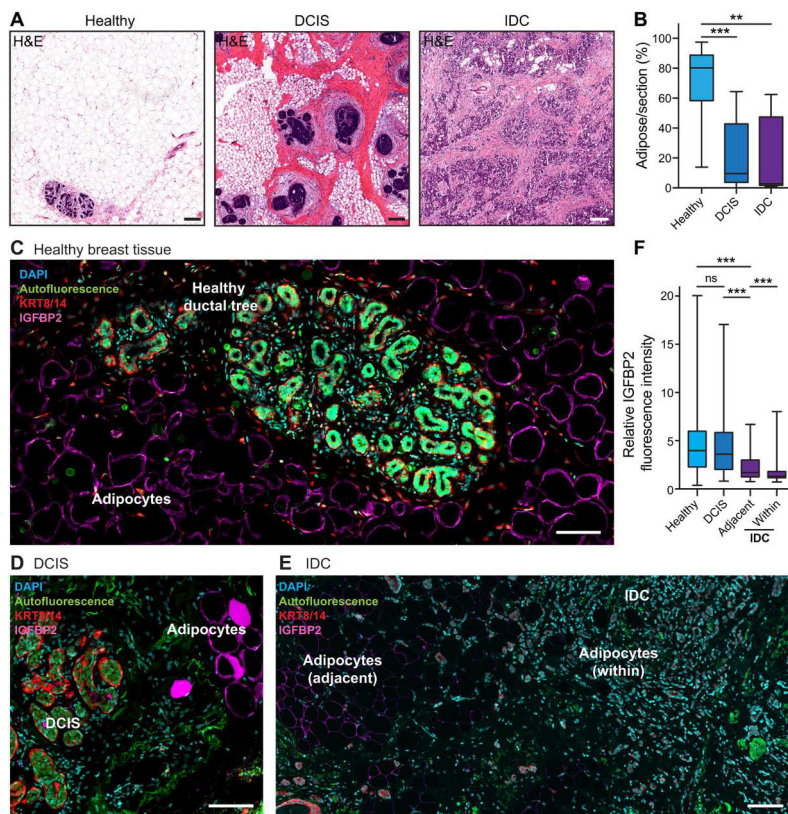


**Fig. 5. IGFBP2 expression during breast cancer progression.** (A) Representative H&E-stained breast tissue samples from healthy patients, patients with DCIS, or patients with IDC. Scale bars, 200  $\mu$ m. (B) Quantification of adipocytes per section from healthy ( $n = 8$  patients, three to eight sections per patient), DCIS ( $n = 6$  patients, one to four sections per patient), and IDC ( $n = 3$  patients, one to two sections per patient). Kruskal-Wallis test using Dunn's test to correct for multiple comparisons (\*\* $P < 0.01$  and \*\*\* $P < 0.001$ ). (C) Representative image from a patient sample stained for IGFBP2 (magenta) and counterstained with DAPI (cyan) and keratin-8/keratin-14 (KRT8/14; red). Scale bar, 100  $\mu$ m.  $n = 8$  normal reduction mammoplasty patient samples. Autofluorescence is given in green. (D) Representative image of human DCIS breast cancer tissue stained for IGFBP2 (magenta) and counterstained with DAPI (cyan) and KRT8/14 (red). Scale bar, 100  $\mu$ m ( $n = 4$  DCIS patient samples). Autofluorescence is given in green. (E) Representative image of human IDC breast cancer tissue stained for IGFBP2 (magenta) and counterstained with DAPI (cyan) and KRT8/14 (red;  $n = 3$  IDC patient samples). Scale bar, 100  $\mu$ m. Autofluorescence is given in green. The brightness of IGFBP2 staining was increased for display purposes only. (F) Quantification of IGFBP2 per adipocyte from healthy ( $n = 8$  patients, 143 to 280 adipocytes per patient), DCIS ( $n = 6$  patients, 39 to 410 adipocytes per patient), and IDC ( $n = 3$  patients, 75 to 283 adipocytes per patient). Kruskal-Wallis test using Dunn's test to correct for multiple comparisons (\*\*\*\* $P < 0.001$ ).

Previous studies using cocultured adipocytes differentiated from 3T3 cells or adipose-derived stem cells have demonstrated growth-promoting and promigratory effects on MM231 and MCF7 cells in vitro (43–45). In contrast, we find that coculture of breast cancer cells with adipocytes differentiated from patient-derived stromal cells significantly inhibits invasion. These somewhat opposing results could be owing to the different source/state of the cells. Notably, recent work by Silva and colleagues (46) has demonstrated that lipofilling with healthy human adipose into mouse MCF7 xenografts reduces tumor growth and proliferation. Moreover, recent studies exploring the heterogeneity of stromal cells have motivated assessment of adipose tissue in a similar fashion (47) and have revealed far greater diversity than the general classifications of brown, white, and brite/beige (48–50).

These findings highlight the significant impact that could be attained through restoration of IGFBP2 into the breast cancer micro-environment, along with an alternative perspective on the role of adipocytes in breast cancer progression.

IGFBP2 was identified as part of a screen for anti-invasive factors, where exogenous recombinant proteins were applied to invading MM231 breast cancer cells. IGFBP2 is involved in metabolic diseases (19, 51). High-serum IGFBP2 is associated with a decreased risk of diabetes, playing a protective role against insulin resistance and obesity (52, 53). Diabetes and obesity are associated with increased risk of breast cancer progression, as well as dysfunctional adipose tissue (54, 55). Here, we found that IGFBP2 was able to bind and sequester IGF-II, which prevents the autocrine signaling of breast cancer cells and limits their progression toward invasive

disease. However, the role of IGFBP2 in dysfunctional mammary adipocytes and the link to cancer is unclear, as it has been associated with both tumor progression and suppression (19, 56). However, many studies consider only the intracellular IGFBP2 pool in cancer cells, where it appears to play a protumorigenic role (19–21). In contrast, exogenously applied IGFBP2 has been reported to inhibit *in vitro* and *in vivo* tumor growth (57), which is in line with IGF-II inhibition suppressing the growth of breast cancer xenografts (29). We failed to observe any IGFBP2- or anti-IGF-II-mediated effects on cell proliferation and detected only robust anti-invasive properties in our experimental models. Nevertheless, these studies and our work indicate an anticancer role for secreted extracellular IGFBP2 and underline the importance of differentiating between intracellular and extracellular pools when investigating IGFBPs.

While disruption of healthy adipose function supports breast cancer progression and local invasion into the co-opted tissue (39, 58), approaches to recuperate or restore this adipose tissue could help restrain breast cancer progression before invasive disease. It has already been shown that the increased plasticity of breast cancer cells undergoing an epithelial-to-mesenchymal transition can be exploited to transdifferentiate them into adipocytes (59). This presents an exciting opportunity for the restoration of IGFBP2 into the cancer microenvironment to further contain the primary tumor. Furthermore, as high levels of *IGF2* have been linked to a poorer prognosis in breast cancer (29) and we find that IGF-II drives proinvasive autocrine signaling in breast cancer cells, this opens up a new avenue for therapeutic intervention through IGF-II depletion. In this way, this work places a spotlight on healthy stromal tissue in tumor containment and supports further investigation into IGFBPs in this process in other cancer subtypes.

## MATERIALS AND METHODS

### Animal experiments

Subcutaneous xenografts were performed with athymic nude mice (Foxn1<sup>nu</sup>; Envigo, UK) by co-injecting  $6 \times 10^6$  TIFs mT2/IGFBP2 and  $2 \times 10^6$  MM231 in phosphate-buffered saline (PBS). Tumors were then tracked by palpation with calipers until the tumor volume ( $\frac{\text{Length} \times \text{Width}^2}{2}$ ) was  $>300 \text{ mm}^3$ , at which point the mice were euthanized and tumors were collected. Mice were housed in standard conditions (12-hour light/12-hour dark cycle) with food and water available *ad libitum*. All animal experiments were performed in accordance with the Finnish Act on Animal Experimentation (animal license number ESAVI/12558/2021). Quantification of adipose tissue in sections was performed in QuPath (60). Quantification of local invasion and Ki67-positive nuclei were also performed in QuPath on tumors that showed local invasion, as described previously (61), building upon the approach by quantifying the percentage of local invasion in the xenograft by selecting areas of invaded cells and dividing those by the total tumor area.

### CDM generation

CDMs were generated as described previously for TIFs (28), with only the modification of the TIFs themselves to stably express mT2 or IGFBP2. To assess changes in the fibronectin or collagen I fiber orientation in the presence of IGFBP2, CDMs were treated with recombinant CNA35-mCherry before fixation with 4%

paraformaldehyde (PFA). These were then blocked overnight with 2.5% bovine serum albumin (BSA) (Sigma-Aldrich, A8022)/1 M glycine (ITW Reagents, A1067)/PBS before overnight staining with anti-fibronectin primary antibody (HFN7.1, mouse; Abcam, ab80923). Stained CDMs were then imaged on a spinning disk confocal microscope (3i Marianas CSU-W1; 40 $\times$ /1.1 objective) and analyzed for staining density in FIJI [National Institutes of Health (NIH)] and fiber coherency using the OrientationJ package (FIJI).

### Cell line models

TIFs [a gift from J. C. Norman (Beatson Institute, Glasgow, Scotland, UK)], MM231 [American Type Culture Collection (ATCC), HTB-26], and MM468 (ATCC, HTB-132) cells were all cultured in Dulbecco's modified Eagle's medium (DMEM; Sigma-Aldrich, D2429) supplemented with 10% fetal bovine serum (FBS) and L-glutamine (100 mM). DCIS.com cells [a gift from J. F. Marshall (Barts Cancer Institute, Queen Mary University of London, London, England, UK)] were cultured in DMEM/F12 (Invitrogen, 11330-032) supplemented with 5% horse serum, epidermal growth factor (EGF; 20 ng/ml; PeproTech, AF-100-15), hydrocortisone (0.5 mg/ml; Sigma-Aldrich, H0888), cholera toxin (100 ng/ml; Sigma-Aldrich, C8052), and insulin (10  $\mu\text{g}/\text{ml}$ ; Sigma-Aldrich, I9278). HUVECs (Lonza, C2519A) were cultured on plasticware precoated with gelatin (0.1%; Sigma-Aldrich, G2500) for 10 min at 37°C. Subconfluent cells that were actively dividing were grown in endothelial cell growth basal medium 2 (Lonza, CC-3156) with SingleQuots (Lonza, CC-4176). HPMECs (PromoCell, C-12281) were cultured in endothelial cell growth medium MV (PromoCell, C-22020). Experiments with HUVECs and HPMECs were conducted with monolayers where the medium was replaced with a reduced factor growth medium at least 24 hours before the experiment began or conditioned medium was collected: m199 medium (Sigma-Aldrich, M4530) supplemented with 20% FBS, L-glutamine (2 mM), endothelial cell growth factor supplements (30 mg/liter; Sigma-Aldrich, E2759), and heparin (10 U/ml; stock is 25 KU/ml in PBS; Sigma-Aldrich, H3393). HMEC-1 cells (ATCC, CRL-3243) were cultured in MCDDB131 medium (Life Technologies, 10372019) with 100 mM L-glutamine, EGF (10 ng/ml; PeproTech, AF-100-15), and 10% FBS.

### Conditioned medium isolation and concentration

For conditioned medium experiments, medium was collected from cells after at least 24 hours and then concentrated using 3-kDa cut-off filters (Millipore, Amicon Ultra-15, UFC900324), centrifuging three times to first concentrate the medium and then washed twice with PBS. Protein concentration was measured with a Pierce detergent compatible Bradford assay kit (Thermo Fisher Scientific, 23246).

### Enzyme-linked immunosorbent assay for IGFBP2 or IGF-II in cell media

Enzyme-linked immunosorbent assays (ELISAs) were performed in a 96-well plate format using the human IGFBP2 SimpleStep ELISA kit (Abcam, ab215082) or human IGF-II/IGF2 Quantikine ELISA kit (DG200, R&D Systems), as per the manufacturer's instructions.

### Flow cytometric analysis of IGFBP2 cell surface binding

MM231 cells were trypsinized, run through a single-cell filter, and then incubated with concentrated TIF medium (10 mg/ml) from

either IGFBP2 or IGFBP2-Clover overexpressing TIFs for 30 min at 37°C. Next, cells were fixed with 2% PFA for 10 min at 37°C and washed two times with PBS. Between 50,000 and 100,000 cells were resuspended in 200  $\mu$ l of PBS and loaded into a 96-well plate. Cytometry was then performed on an LSRFortessa cell analyzer using the High Throughput Sampler (BD Biosciences). The 488-nm laser power was adjusted using a positive control population of MM231 stably expressing IGFBP2-Clover before running the other conditions. Up to 10,000 single cells were collected per condition. Gating and statistical analysis of the cell population geometric means and robust SD were performed in FlowJo (BD Biosciences).

### Gene silencing

Gene silencing was performed by transfection of 10 nM siRNA using RNAiMAX, as per the manufacturer's instructions. The non-target control (NTC; AllStars negative control), *IGFBP2* siRNAs (Hs\_IGFBP2\_1, SI00012495, CACACGTATTATATTTGGAA and Hs\_IGFBP2\_1, SI00012502, ACAGTGCAAGATGTCTCTGA A), and *IGF2* siRNAs (Hs\_IGF2\_8, SI04949441, CAGGGTAAAC TGGCCATCCGA and Hs\_INS\_IGF2\_4, SI03495485, CC GGTCTCTTTATCCACTGT) were all purchased from QIAGEN.

### Generation of stable cell lines

Lentiviral particles were produced in human embryonic kidney 293FT packaging cells (Thermo Fisher Scientific, R70007) by co-transfecting with the third-generation lentiviral packaging system, pMDLg/pRRE (Addgene, plasmid #12251), pRSV-Rev (Addgene, plasmid #12253), and pMD2.G (Addgene, plasmid #12259), along with the pLenti6.3/TO/V5-DEST-mTurquoise2, pLenti6.3/TO/V5-DEST-IGFBP2, and pLenti6.3/TO/V5-DEST-IGFBP2-Clover transfer plasmids using Lipofectamine 3000 (Thermo Fisher Scientific) in OptiMEM (Gibco, 31985070), as per the manufacturer's protocol. Twenty-four hours after transfection, the medium was replaced with TIF growth medium and incubated for a further 24 hours, at which point the medium was collected and filtered through a 0.45- $\mu$ m syringe filter. MM231s or TIFs were then transduced with the lentiviral particles for 48 hours, in the presence of polybrene (8  $\mu$ g/ml; Sigma-Aldrich, TR-1003-G), before washing and selecting stable positive cells using puromycin (1  $\mu$ g/ml).

### Immunofluorescence

Staining of cultured cells was performed after fixation with 4% PFA (Thermo Fisher Scientific, 28908)/0.3% Triton X-100 for 10 min at 37°C. Samples were then washed with PBS before blocking overnight with 2.5% BSA (Sigma-Aldrich, A8022)/1 M glycine (ITW Reagents, A1067)/PBS. Blocked samples were then incubated overnight at 4°C with primary antibodies against human IGFBP2 (Santa Cruz Biotechnology, sc-25285), PPAR $\gamma$  (1:100; PA3-821A, Thermo Fisher Scientific, rabbit), paxillin (Y113; 1:100; ab32084, Abcam), or vimentin (D21H3; 1:100; rabbit, 5741, Cell Signaling Technology). Primary antibodies were then removed and the samples were washed with PBS before staining with secondary antibodies and/or Nile Red (10  $\mu$ M, 19123-10MG, Sigma-Aldrich; stock: 1 mM in methanol), SiR-actin (Tebu-Bio, SC001), and/or 4',6-diamidino-2-phenylindole (DAPI; D1306, Life Technologies).

For adhesion experiments in the presence of recombinant IGFBP2, 35-mm glass-bottom dishes were coated with 10  $\mu$ g/ml of both fibronectin (Millipore, 341631; stock: 1 mg/ml) and collagen

I (Millipore, 08-115; stock: 4 mg/ml) overnight at 4°C. MM231 cells were then seeded for 1.5 hours before fixation and staining, as above. Stained samples were then imaged on a spinning disk confocal microscope (3i Marianas CSU-W1; 20 $\times$ /0.8 objective) and analyzed for staining intensity, focal adhesion, or cell area in FIJI (NIH).

### Immunohistochemistry

Organotypic matrices and xenografts were fixed in 10% neutral buffered formalin and then paraffin embedded, before cutting 4- $\mu$ m sections for staining with either hematoxylin and eosin (H&E) or primary antibodies against Ki67 (1:500; Dako, M7240) or pan-cytokeratin (1:25; Invitrogen, MA5-13203). Slides were then scanned on a Panoramic P1000 (3DHISTECH, 20 $\times$ /0.8 objective).

Immunofluorescence of formalin-fixed paraffin-embedded (FFPE) sections was performed with standard protocols on deparaffinized sections after heat-mediated antigen retrieval in universal buffer (Retriever 2100, Aptum Bio) with the indicated antibodies against vimentin (1:500; D21H3; Cell Signaling Technology, 5741) or IGFBP2 (1:100; Santa Cruz Biotechnology, sc-25285). All samples were stained with DAPI (Life Technologies), mounted in Mowiol containing 1,4-diazabicyclo[2.2.2]octane (DABCO; Merck) antifade reagent.

For immunofluorescence of frozen tissue sections, samples were fixed overnight at +4°C in periodate-lysine-PFA buffer [1% PFA, 0.01 M sodium periodate, 0.075 M L-lysine, and 0.0375 M P-buffer (0.081 M Na<sub>2</sub>HPO<sub>4</sub> and 0.019 M NaH<sub>2</sub>PO<sub>4</sub>) (pH 7.4)]. After washing twice with P-buffer, samples were incubated in 30% sucrose (Merck, 107687) in P-buffer for a minimum of 2 days. Samples were mounted in Tissue-Tek O.C.T. Compound (Sakura, 4583) on dry ice and cut into 8- $\mu$ m sections. The frozen sections were thawed for 1 hour at room temperature (RT) before immunolabeling. The sections were blocked and permeabilized in 2% BSA and 0.1% Triton X-100 in PBS for 30 min at RT. Primary antibodies—vimentin (1:500; D21H3; Cell Signaling Technology, 5741), IGFBP2 (1:100; Santa Cruz Biotechnology, sc-25285), keratin-8 (1:1000; Hybridoma Bank, clone Troma-1), or keratin-14 (1:1000; Covance, PRB-1558)—were incubated in 2% BSA in PBS overnight at +4°C. The sections were washed 3  $\times$  10 min with PBS. The fluorescently conjugated secondary antibodies were incubated in 2% BSA in PBS for 1 hour at RT, after which the sections were washed 3  $\times$  10 min with PBS (1:1000; DAPI in the second wash) and then 5 min with milli-Q water. The sections were mounted under a glass coverslip with Mowiol (Calbiochem) supplemented with 2.5% DABCO (Sigma-Aldrich). Labeled sections were imaged on a spinning disk confocal microscope (3i Marianas CSU-W1; 20 $\times$ /0.8 objective). Autofluorescence was from 488-nm excitation and detecting 525-/50-nm emission. For the quantification of IGFBP2 intensity in FIJI (NIH), adipocytes were identified on the basis of morphological characteristics using the autofluorescence channel.

### Invasion into fibroblast-contracted 3D collagen I matrices

Fibroblast-contracted "organotypic" 3D collagen I matrices for invasion assays were generated as described previously (9), modifying the protocol only to place MM231-seeded matrices in Transwell inserts (8- $\mu$ m pore size; Greiner, ThinCert, 662638), after being cut to fit with a scalpel. These inserts were placed in 24-well wells

containing preformed HUVEC or adipocyte monolayers (adipocytes were differentiated in these wells before Transwell addition) on the bottom of the well. An air-liquid interface was then formed by adding media up to the bottom of the Transwell insert. In experiments without HUVEC/adipocyte monolayers, only the culture medium was added up to the bottom of the Transwell insert. After 14 days of invasion, matrices were carefully removed from the Transwells and fixed in 10% neutral buffered formalin overnight at 4°C, then paraffin embedded, sectioned, and stained as described above. Quantification of the proliferation or invasion indices was performed in QuPath using the positive cell detection algorithm over eight regions of interest. For invasion assessment, the fraction of cells in a region of interest that had invaded beyond 100  $\mu\text{m}$  was compared to the total number of cells in that region.

### Inverted invasion assay

Inverted invasion assays were performed as described previously (62). After 5 days, MM231 cells were fixed in 4% PFA/0.2% Triton X-100 (T8787, Sigma-Aldrich) in PBS for 1 hour at RT, washed three times in PBS, before incubation with phalloidin-488 (Invitrogen, A12379) overnight at 4°C, and then imaged on a Zeiss LSM880 inverted confocal microscope using a 40 $\times$ /1.2 objective and taking z-stacks with 15- $\mu\text{m}$  increments. Invasion indices were calculated in FIJI (NIH) by measuring the area of signal in increments beyond 45  $\mu\text{m}$  and then dividing this by the total area of the signal in all of the 15- $\mu\text{m}$  increments to get a percentage of invading cells beyond 45  $\mu\text{m}$ . For the exogenous protein inverse invasion screen, cells were treated with either PBS or one of the following recombinant proteins (5  $\mu\text{M}$ ): SPARC (R&D Systems, 941-SP), DKK1 (R&D Systems, 5439-DK), DKK3 (R&D Systems, 1118-DK), TFPI (R&D Systems, 2974-PI), TFPI2 (R&D Systems, 2545-PI), HHIP (R&D Systems, 9280-HP), PAI1 (R&D Systems, 1786-PI), IGFBP2 (R&D Systems, 674-B2), IGFBP7 (R&D Systems, 1334-B7), and GSN (Novus, H00002934-Q01). For assessment of the IGF-II pathway perturbation, the following were used: recombinant IGF-II (10 ng/ml; R&D Systems, 292-G2), anti-IGF-II (10  $\mu\text{g}/\text{ml}$ ; Sigma-Aldrich, 05-166), or immunoglobulin G1k (IgG1k; 10  $\mu\text{g}/\text{ml}$ ; Sigma-Aldrich, M7894).

### Mass spectrometry

MM231 cells were treated with concentrated conditioned media from TIFs overexpressing mT2 or IGFBP2-Clover (~30  $\mu\text{g}$ ). For the mT2 control medium, ~30- $\mu\text{g}$  recombinant GFP (Abcam, ab84191) was added. After 1 hour, medium was collected and fixed with Dimethyl dithiobispropionimidate (DTBP) (5 mM; Thermo Fisher Scientific, 20665). Fixation occurred at 37°C for 30 min with gentle mixing. This was then quenched by the addition of quenching buffer [500 mM tris-HCl (pH 8.0) and 750 mM NaCl] for a further 10 min at 4°C while gently mixing. Once quenched, GFP-trap beads (30  $\mu\text{l}$ , Chromotek, gfa) were added to the medium and incubated overnight at 4°C while gently mixing. Immunoprecipitations were then spun down at 300g for 5 min before washing beads thrice with PBS and then once with 50 mM tris-HCl (pH 8.0) and 150 mM NaCl. For the on-bead digestion, samples were reduced with 10 mM dithiothreitol (DTT)/50 mM tris-HCl (pH 8.0) in the presence of 8 M urea for 1 hour at 37°C and then alkylated in 40 mM iodoacetamide/50 mM tris-HCl (pH 8.0) for 1 hour in the dark. DTT was then added in excess to consume the

remaining alkylating agent and dilute the urea before overnight digestion with trypsin (Promega, V5111) at 37°C. Samples were then acidified with trifluoroacetic acid (pH ~2) before desalting using Sep-Pak C18 96-well plates (Waters, 186002321). Liquid chromatography–tandem mass spectrometry was then performed as described previously (63), modified only in the use of 300 ng of sample for the analysis and in the application of a 50-min two-step gradient from 5 to 21% of eluent B for 28 min to 36% of eluent B for 22 min, followed by a wash stage with 100% of eluent B to eluate peptides. Assignment of peptides and quantification of abundance ratios (normalized to total peptide amount) by label-free quantification was performed in Proteome Discoverer 2.5 (Thermo Fisher Scientific) using intensity values from the precursor ions.

### Matrigel invasion assay

Matrigel invasion chambers (354480, Corning) or Matrigel-coated Transwells (60  $\mu\text{l}$  per Transwell; allowed to set for 1 hour at 37°C; Greiner, ThinCert; 8- $\mu\text{m}$  pore size, 662638) were seeded with  $2 \times 10^5$  MM231, DCIS.com, or MM468 cells per chamber in 500- $\mu\text{l}$  serum-free medium. The bottom chamber was then filled with 1-ml complete medium and either PBS, recombinant IGFBP2 (5  $\mu\text{M}$ ; R&D Systems, 674-B2), anti-IGF-II (10  $\mu\text{g}/\text{ml}$ ; Sigma-Aldrich, 05-166), or IgG1k (10  $\mu\text{g}/\text{ml}$ ; Sigma-Aldrich, M7894). After allowing invasion to occur for 16 hours, the invasions were then fixed with 4% PFA in PBS. The cells in the top chamber were removed with a cotton tip and then the cells were stained with DAPI before imaging on a spinning disk confocal microscope (3i Marianas CSU-W1; 10 $\times$ /0.45 objective).

### Molecular cloning

To generate the lentiviral constructs pLenti6.3/TO/V5-DEST-IGFBP2 (Addgene, #191006), pLenti6.3/TO/V5-DEST-IGFBP2-Clover (Addgene, #191008), and pLenti6.3/TO/V5-DEST-mTurquoise2 (Addgene, #191010), entry clones were LR subcloned with the Gateway destination vector pLenti6.3/TO/V5-DEST (Invitrogen) using LR Clonase II (Invitrogen, 11791), as per the manufacturers' protocol. pENTR221-IGFBP2-Clover (Addgene, #191007) was synthesized by BioCat (Heidelberg, Germany), while pENTR2b-mTurquoise2 (Addgene, #191014) was generated by first polymerase chain reaction (PCR)–amplifying mT2 from pmTurquoise2-N1 [Addgene, #54843 (64)] using primers 5'-GGC TGGCCCGGTACCGCCACCATGGT GAGCAAGGGCG-3' and 5'-GGGTCTAGATATCTCGAGTCATTACTTGACAGCTCGTC CATGCCGAGAG-3'. This PCR fragment was then digested with Xho I/Kpn I (New England Biolabs), in parallel with digestion of the pENTR2b (Invitrogen, A10463) backbone with the same restriction enzymes. These fragments were then ligated using T4 DNA ligase (Thermo Fisher Scientific, EL0011). All plasmids were validated by analytical digests and sequencing.

### Proliferation assays

To assess the proliferation in cancer cells after siRNA gene knock-down or through treatment with recombinant proteins or conditioned media, parallel 96-well plates were seeded, and a single plate was assessed on each day of the assay using cell counting kit-8 (Sigma-Aldrich, 96992), as per the manufacturer's instructions. Relative cell density was measured as absorbance at 450 nm after a 4-hour incubation with the cell counting kit-8 reagent at 37°C. Day 0 was measured immediately after the cells had seeded

down in the wells, before any treatment. Doubling times were obtained through fitting an exponential growth equation to the data using Prism 7 (GraphPad Software).

### Patient samples

Human breast tissue samples were obtained at the Department of Plastic and General Surgery at Turku University Hospital (Turku, Finland) with approval from the Ethics Committee of the Hospital District of Southwestern Finland (permit number 23/1801/2018) and with a written consent from the patients (§279, 9/2001). Healthy breast samples were obtained from eight female patients undergoing reduction mammoplasty surgery (ages 18 to 45; data S2). Breast tumors of nine female patients with breast cancer (ages of 41 to 85) were excised and examined by a clinical pathologist (data S2). Tissue samples were processed to frozen tissue sections or FFPE tissue sections and H&E labeled with standard procedures.

### Primary human cell isolation and adipocyte culture

Adipocytes were differentiated from the stromal cells of healthy breast tissue obtained from reduction mammoplasty operations. The tissue was transferred in transport medium [DMEM/F12 GlutaMAX (Gibco, 10565018) supplemented with 5% FBS (Sigma-Aldrich, F7524) and 10 mM Hepes (Sigma-Aldrich)]. Extra fat was removed, and the tissue was dissected into pieces of ~1 mm<sup>3</sup> for enzymatic digestion in dissociation medium [penicillin/streptomycin (1:100), 5% FBS, filter-sterilized collagenase (300 U/ml; type XI, Sigma-Aldrich, C7657), and hyaluronidase (100 U/ml; type I-S, Sigma-Aldrich, H3506) in mammary epithelial cell growth medium (PromoCell, C-21010)] at 37°C with rotation overnight. The dissociated glandular tissue was centrifuged for 5 min at 600g. The cell pellet was then resuspended in 10 ml of transport medium with deoxyribonuclease I (DNase I; 10 µg/ml), shaken occasionally for 1 min to digest DNA, pelleted, and resuspended again in 10 ml of transport medium. The tissue was then pulse centrifuged two times for 1 min and two times for 30 s at 80g. After each pulse centrifugation, the supernatant containing the mammary stromal cell fraction was collected, pooled, and preserved at -150°C. For experiments, mammary stromal cells were thawed and plated on 6-well plates (Thermo Fisher Scientific), 24-well plates (Cellstar), or µ-Slide 8 well (Ibidi, 80826) in subcutaneous preadipocyte medium (PM-1; ZenBio) for 2 to 3 days to obtain preadipocytes. For differentiation initiation, PM-1 was carefully changed to subcutaneous preadipocyte differentiation medium (DM-2; ZenBio), and cells were kept in DM-2 for 1 week without medium change. Last, DM-2 was changed to subcutaneous adipocyte maintenance medium (AM-1; ZenBio). After a week of culture in AM-1, preadipocytes were fully differentiated to mature adipocytes with visible lipid droplets. For maintenance of preadipocyte control cells, cells were kept in PM-1 that was changed every other day.

### Recombinant protein purification

BL21 competent *Escherichia coli* (New England Biolabs, C2530H) were transformed with pET28a-CNA35-mCherry [Addgene, plasmid #61607 (65)] plasmid DNA and grown overnight on a shaker at 37°C to yield a 250-ml culture with an OD<sub>600</sub> (optical density at 600 nm) = 0.6. This was then incubated overnight again on a shaker at 30°C in the presence of isopropyl-β-D-thiogalactopyranoside (500 µM; Thermo Fisher Scientific, R0392). The bacteria

were then pelleted by centrifugation at 6000g for 15 min at 4°C before discarding the supernatant and resuspending in 9-ml tris-buffered saline (TBS) with protease inhibitors (cComplete™ Mini, EDTA-free, Roche). To this solution, 1 ml of BugBuster (Millipore, 10× protein extraction reagent, #70921-50ML), 1 µl of benzonase nuclease (Sigma-Aldrich, E1014-5KU), 4.5 µl of DNase I (Sigma-Aldrich, 11284932001), and lysozyme from chicken egg white (Sigma-Aldrich, 62970) were added. This mixture was then rotated for 30 min at 4°C before centrifugation at 6000g for 1 hour. The supernatant was then purified using a kit for His-tagged proteins (Macherey-Nagel, Protino Ni-TED2000 packed columns, #745120.25). The elution buffer was then exchanged against 4× changes of PBS using centrifugal filters (Millipore, Amicon Ultra-4, 10K UFC801024).

### RNA isolation, cDNA generation, and quantitative reverse transcription PCR

RNA from cultured cells was collected and isolated using the NucleoSpin RNA kit (Macherey-Nagel). For cDNA synthesis, 1 µg of the extracted RNA was then used as a template for the high-capacity cDNA reverse transcription kit (Applied Biosystems). Each PCR reaction was performed using 100 ng of cDNA and the appropriate TaqMan gene expression assays (with 6-carboxyfluorescein (FAM) dye label; Thermo Fisher Scientific) for each gene, according to the manufacturer's instructions (Thermo Fisher Scientific, TaqMan Fast Advanced Master Mix, 4444557). The following TaqMan gene expression assays were used: IGFBP2 (Hs01040719\_m1), complement factor D (Hs00157263\_m1), adiponectin receptor 1 (Hs00360422\_m1), PPARγ (Hs01115513\_m1), lipase E (Hs00943405\_g1), fatty acid binding protein 4 (Hs01086177\_m1), and glyceraldehyde-3-phosphate dehydrogenase (GAPDH; Hs02786624\_g1). Relative mRNA expression levels were normalized to GAPDH, and quantification was performed using the ΔΔCt method (66).

### Statistical analysis

Bar and line graphs are presented as means ± SEM of at least three independent experiments, where statistical significance is given by \**P* < 0.05, \*\**P* < 0.01, \*\*\**P* < 0.001, or ns (not significant). All box-plots include min/max whiskers. The specific statistical tests applied are given in the respective figure legends. All statistical tests were performed in Prism 7 (GraphPad Software Inc.).

### Western blotting

Cell lysates were prepared in TXLB lysis buffer [50 mM Hepes, 1% Triton X-100, 0.5% sodium deoxycholate, 0.1% SDS, 0.5 mM EDTA, 50 mM NaF, 10 mM Na<sub>2</sub>VO<sub>4</sub>, and protease inhibitor cocktail (cComplete Mini, EDTA-free, Roche)], and volumes were adjusted according to protein concentration measurements (DC protein assay kit, Bio-Rad, 5000111). Separation was performed by gel electrophoresis (Mini-PROTEAN TGX Precast Gels 4-20%, Bio-Rad, 4561096), before transferring onto a nitrocellulose membrane (Trans-Blot Turbo Transfer System, Bio-Rad) and blocking with AdvanBlock-Fluor (Advansta, R-03729-E10). Primary antibodies in AdvanBlock-Fluor were incubated overnight at 4°C; IGFBP2 (R&D Systems, AF674), IGF-II (Millipore, 05-166-MI), GAPDH (Hytest, 5G4MAB6C5), and GFP (Thermo Fisher Scientific, A11122). Membranes were washed between primary and secondary antibody treatments with Tris-buffered saline with 0.1% Tween 20

(TBST). IRDye secondary antibodies (1:5000 diluted in TBST; LI-COR) were incubated for at least 1 hour at RT, before detection on an Odyssey fluorescence imager CLx (LI-COR). Densitometry analysis was performed in FIJI (NIH) by normalizing the signal to GAPDH, which was used as a loading control.

## Supplementary Materials

This PDF file includes:

Figs. S1 to S5

Legends for data S1 to S3

Other Supplementary Material for this manuscript includes the following:

Data S1 to S3

[View/request a protocol for this paper from Bio-protocol.](#)

## REFERENCES AND NOTES

- Heer, A. Harper, N. Escandor, H. Sung, V. McCormack, M. M. Fidler-Benaoudia, Global burden and trends in premenopausal and postmenopausal breast cancer: A population-based study. *Lancet Glob. Health* **8**, e1027–e1037 (2020).
- K. C. Valkenburg, A. E. de Groot, K. J. Pienta, Targeting the tumour stroma to improve cancer therapy. *Nat. Rev. Clin. Oncol.* **15**, 366–381 (2018).
- V. Assi, J. Warwick, J. Cuzick, S. W. Duffy, Clinical and epidemiological issues in mammographic density. *Nat. Rev. Clin. Oncol.* **9**, 33–40 (2011).
- M. N. Duong, A. Geneste, F. Fallone, X. Li, C. Dumontet, C. Muller, The fat and the bad: Mature adipocytes, key actors in tumor progression and resistance. *Oncotarget* **8**, 57622–57641 (2017).
- L. Bochet, C. Lehuédé, S. Dauvillier, Y. Y. Wang, B. Dirat, V. Laurent, C. Dray, R. Guiet, I. Maridonneau-Parini, S. Le Gonidec, B. Couderc, G. Escourrou, P. Valet, C. Muller, Adipocyte-derived fibroblasts promote tumor progression and contribute to the desmoplastic reaction in breast cancer. *Cancer Res.* **73**, 5657–5668 (2013).
- R. Kaukonen, A. Mai, M. Georgiadou, M. Saari, N. De Franceschi, T. Betz, H. Sihto, S. Ventela, L. Elo, E. Jokitalo, J. Westermarck, P. L. Kellokumpu-Lehtinen, H. Joensuu, R. Grenman, J. Ivaska, Normal stroma suppresses cancer cell proliferation via mechanosensitive regulation of JMJD1a-mediated transcription. *Nat. Commun.* **7**, 12237 (2016).
- M. Papanicolaou, A. L. Parker, M. Yam, E. C. Filipe, S. Z. Wu, J. L. Chitty, K. Wyllie, E. Tran, E. Mok, A. Nadalini, J. N. Skhinas, M. C. Lucas, D. Herrmann, M. Nobis, B. A. Pereira, A. M. K. Law, L. Castillo, K. J. Murphy, A. Zaratzian, J. F. Hastings, D. R. Croucher, E. Lim, B. G. Oliver, F. V. Mora, B. L. Parker, D. Gallego-Ortega, A. Swarbrick, S. O'Toole, P. Timpson, T. R. Cox, Temporal profiling of the breast tumour microenvironment reveals collagen XII as a driver of metastasis. *Nat. Commun.* **13**, 4587 (2022).
- G. Follain, D. Herrmann, S. Harlepp, V. Hyenne, N. Osmani, S. C. Warren, P. Timpson, J. G. Goetz, Fluids and their mechanics in tumour transit: Shaping metastasis. *Nat. Rev. Cancer* **20**, 107–124 (2020).
- J. R. W. Conway, C. Vennin, A. S. Cazet, D. Herrmann, K. J. Murphy, S. C. Warren, L. Wullkopf, A. Boulghourjian, A. Zaratzian, A. M. Da Silva, M. Pajic, J. P. Morton, T. R. Cox, P. Timpson, Three-dimensional organotypic matrices from alternative collagen sources as pre-clinical models for cell biology. *Sci. Rep.* **7**, 16887 (2017).
- I. K. Zervantonakis, S. K. Hughes-Alford, J. L. Charest, J. S. Condeelis, F. B. Gertler, R. D. Kamm, Three-dimensional microfluidic model for tumor cell intravasation and endothelial barrier function. *Proc. Natl. Acad. Sci. U.S.A.* **109**, 13515–13520 (2012).
- D.-H. T. Nguyen, E. Lee, S. Alimperti, R. J. Norgard, A. Wong, J. J.-K. Lee, J. Eyckmans, B. Z. Stanger, C. S. Chen, A biomimetic pancreatic cancer on-chip reveals endothelial ablation via ALK7 signaling. *Sci. Adv.* **5**, eaav6789 (2019).
- G. Follain, N. Osmani, V. Gensbittel, N. Asokan, A. Larnicol, L. Mercier, M. J. Garcia-Leon, I. Busnelli, A. Pichot, N. Paul, R. Carapito, S. Bahram, O. Lefebvre, J. G. Goetz, Impairing flow-mediated endothelial remodeling reduces extravasation of tumor cells. *Sci. Rep.* **11**, 13144 (2021).
- D. G. Tunica, X. Yin, A. Sidibe, C. Stegemann, M. Nissum, L. Zeng, M. Brunet, M. Mayr, Proteomic analysis of the secretome of human umbilical vein endothelial cells using a combination of free-flow electrophoresis and nanoflow LC-MS/MS. *Proteomics* **9**, 4991–4996 (2009).
- X. Yin, M. Bern, Q. Xing, J. Ho, R. Viner, M. Mayr, Glycoproteomic analysis of the secretome of human endothelial cells. *Mol. Cell. Proteomics* **12**, 956–978 (2013).
- S. Burghoff, J. Schrader, Secretome of human endothelial cells under shear stress. *J. Proteome Res.* **10**, 1160–1169 (2011).
- S. E. Reid, E. J. Kay, L. J. Neilson, A. T. Henze, J. Serneels, E. J. McGhee, S. Dhayade, C. Nixon, J. B. Mackey, A. Santi, K. Swaminathan, D. Athineos, V. Papanalazarou, F. Patella, A. Roman-Fernandez, Y. ElMaghloob, J. R. Hernandez-Fernaud, R. H. Adams, S. Ismail, D. M. Bryant, M. Salmeron-Sanchez, L. M. Machesky, L. M. Carlin, K. Blyth, M. Mazzone, S. Zanivan, Tumor matrix stiffness promotes metastatic cancer cell interaction with the endothelium. *EMBO J.* **36**, 2373–2389 (2017).
- M. Zhao, P. Kim, R. Mitra, J. Zhao, Z. Zhao, TSGene 2.0: An updated literature-based knowledgebase for tumor suppressor genes. *Nucleic Acids Res.* **44**, D1023–D1031 (2016).
- Y. W. van den Berg, S. Osanto, P. H. Reitsma, H. H. Versteeg, The relationship between tissue factor and cancer progression: Insights from bench and bedside. *Blood* **119**, 924–932 (2012).
- A. Pickard, D. J. McCance, IGF-binding protein 2—Oncogene or tumor suppressor? *Front. Endocrinol. (Lausanne)* **6**, 25 (2015).
- A. I. So, R. J. Levitt, B. Eigl, L. Fazli, M. Muramaki, S. Leung, M. C. U. Cheang, T. O. Nielsen, M. Gleave, M. Pollak, Insulin-like growth factor binding protein-2 is a novel therapeutic target associated with breast cancer. *Clin. Cancer Res.* **14**, 6944–6954 (2008).
- H. Wang, B. K. Arun, H. Wang, G. N. Fuller, W. Zhang, L. P. Middleton, A. A. Sahin, IGFBP2 and IGFBP5 overexpression correlates with the lymph node metastasis in T1 breast carcinomas. *Breast J.* **14**, 261–267 (2008).
- N. M. Probst-Hensch, J. H. Steiner, P. Schraml, Z. Varga, U. Zurrer-Hardi, M. Storz, D. Korol, M. K. Fehr, D. Fink, B. C. Pestalozzi, U. M. Lutolf, J.-P. Theurillat, H. Moch, IGFBP2 and IGFBP3 protein expressions in human breast cancer: Association with hormonal factors and obesity. *Clin. Cancer Res.* **16**, 1025–1032 (2010).
- C. E. Harms, Q. Li, S. Lee, C. Zhang, B. Kull, S. Hallen, A. Thorell, I. Alexandersson, C. M. Hagberg, X. R. Peng, A. Mardinoglu, K. L. Spalding, J. Boucher, Mature human white adipocytes cultured under membranes maintain identity, function, and can transdifferentiate into brown-like adipocytes. *Cell Rep.* **27**, 213–225.e5 (2019).
- M. Picon-Ruiz, J. A. Marchal, J. M. Slingerland, Obtaining human breast adipose cells for breast cancer cell co-culture studies. *STAR Protoc.* **1**, 100197 (2020).
- V. C. Russo, B. S. Schutt, E. Andaloro, S. I. Ymer, A. Hoefflich, M. B. Ranke, L. A. Bach, G. A. Werther, Insulin-like growth factor binding protein-2 binding to extracellular matrix plays a critical role in neuroblastoma cell proliferation, migration, and invasion. *Endocrinology* **146**, 4445–4455 (2005).
- T. Arai, W. Busby Jr., D. R. Clemmons, Binding of insulin-like growth factor (IGF) I or II to IGF-binding protein-2 enables it to bind to heparin and extracellular matrix. *Endocrinology* **137**, 4571–4575 (1996).
- E. Cukierman, R. Pankov, D. R. Stevens, K. M. Yamada, Taking cell-matrix adhesions to the third dimension. *Science* **294**, 1708–1712 (2001).
- R. Kaukonen, G. Jacquemet, H. Hamidi, J. Ivaska, Cell-derived matrices for studying cell proliferation and directional migration in a complex 3D microenvironment. *Nat. Protoc.* **12**, 2376–2390 (2017).
- K. Tominaga, T. Shimamura, N. Kimura, T. Murayama, D. Matsubara, H. Kanauchi, A. Niida, S. Shimizu, K. Nishioka, E. I. Tsuji, M. Yano, S. Sugano, Y. Shimono, H. Ishii, H. Saha, M. Mori, K. Akashi, K. I. Tada, T. Ogawa, A. Tojo, S. Miyano, N. Gotoh, Addition to the IGF2-ID1-IGF2 circuit for maintenance of the breast cancer stem-like cells. *Oncogene* **36**, 1276–1286 (2017).
- K. J. Chavez, S. V. Garimella, S. Lipkowitz, Triple negative breast cancer cell lines: One tool in the search for better treatment of triple negative breast cancer. *Breast Dis.* **32**, 35–48 (2010).
- F. R. Miller, S. J. Santner, L. Tait, P. J. Dawson, MCF10DCIS.com xenograft model of human comedo ductal carcinoma in situ. *J. Natl. Cancer Inst.* **92**, 1185–1186 (2000).
- E. Peuhu, G. Jacquemet, C. Scheele, A. Isomursu, M.-C. Laisne, L. M. Koskinen, I. Paatero, K. Thol, M. Georgiadou, C. Guzman, S. Koskinen, A. Laiho, L. L. Elo, P. Bostrom, P. Hartiala, J. van Rheenen, J. Ivaska, MYO10-filopodia support basement membranes at pre-invasive tumor boundaries. *Dev. Cell* **57**, 2350–2364.e7 (2022).
- N. F. Boyd, H. Guo, L. J. Martin, L. Sun, J. Stone, E. Fishell, R. A. Jong, G. Hislop, A. Chiarelli, S. Minkin, M. J. Yaffe, Mammographic density and the risk and detection of breast cancer. *N. Engl. J. Med.* **356**, 227–236 (2007).
- V. A. McCormack, I. dos Santos Silva, Breast density and parenchymal patterns as markers of breast cancer risk: A meta-analysis. *Cancer Epidemiol. Biomarkers Prev.* **15**, 1159–1169 (2006).
- L. Yaghjian, G. A. Colditz, L. C. Collins, S. J. Schnitt, B. Rosner, C. Vachon, R. M. Tamimi, Mammographic breast density and subsequent risk of breast cancer in postmenopausal women according to tumor characteristics. *J. Natl. Cancer Inst.* **103**, 1179–1189 (2011).
- M. J. Paszek, N. Zahir, K. R. Johnson, J. N. Lakin, G. I. Rozenberg, A. Gefen, C. A. Reinhart-King, S. S. Margulies, M. Dembo, D. Boettiger, D. A. Hammer, V. M. Weaver, Tensional homeostasis and the malignant phenotype. *Cancer Cell* **8**, 241–254 (2005).

37. C. W. Huo, G. Chew, P. Hill, D. Huang, W. Ingman, L. Hodson, K. A. Brown, A. Magenau, A. H. Allam, E. McGhee, P. Timpson, M. A. Henderson, E. W. Thompson, K. Britt, High mammographic density is associated with an increase in stromal collagen and immune cells within the mammary epithelium. *Breast Cancer Res.* **17**, 79 (2015).
38. I. Acerbi, L. Cassereau, I. Dean, Q. Shi, A. Au, C. Park, Y. Y. Chen, J. Liphart, E. S. Hwang, V. M. Weaver, Human breast cancer invasion and aggression correlates with ECM stiffening and immune cell infiltration. *Integr. Biol. (Camb)* **7**, 1120–1134 (2015).
39. K. L. Andarawewa, E. R. Motrescu, M. P. Chenard, A. Gansmuller, I. Stoll, C. Tomasetto, M. C. Rio, Stromelysin-3 is a potent negative regulator of adipogenesis participating to cancer cell-adipocyte interaction/crosstalk at the tumor invasive front. *Cancer Res.* **65**, 10862–10871 (2005).
40. Q. Wu, J. Li, Z. Li, S. Sun, S. Zhu, L. Wang, J. Wu, J. Yuan, Y. Zhang, S. Sun, C. Wang, Exosomes from the tumour-adipocyte interplay stimulate beige/brown differentiation and reprogram metabolism in stromal adipocytes to promote tumour progression. *J. Exp. Clin. Cancer Res.* **38**, 223 (2019).
41. F. Wang, S. Gao, F. Chen, Z. Fu, H. Yin, X. Lu, J. Yu, C. Lu, Mammary fat of breast cancer: Gene expression profiling and functional characterization. *PLoS ONE* **9**, e109742 (2014).
42. L. Meng, J. Zhou, H. Sasano, T. Suzuki, K. M. Zeitoun, S. E. Bulun, Tumor necrosis factor alpha and interleukin 11 secreted by malignant breast epithelial cells inhibit adipocyte differentiation by selectively down-regulating CCAAT/enhancer binding protein alpha and peroxisome proliferator-activated receptor gamma: Mechanism of desmoplastic reaction. *Cancer Res.* **61**, 2250–2255 (2001).
43. H. Goto, Y. Shimono, Y. Funakoshi, Y. Imamura, M. Toyoda, N. Kiyota, S. Kono, S. Takao, T. Mukohara, H. Minami, Adipose-derived stem cells enhance human breast cancer growth and cancer stem cell-like properties through adipisin. *Oncogene* **38**, 767–779 (2019).
44. M. Coutinho de Miranda, A. da Fonseca Ferreira, M. I. Abreu de Melo, M. K. Lima, A. de Miranda Goes, M. A. Rodrigues, D. A. Gomes, J. A. Q. A. Faria, Adipose-derived stem/stromal cell secretome modulates breast cancer cell proliferation and differentiation state towards aggressiveness. *Biochimie* **191**, 69–77 (2021).
45. B. Dirat, L. Bochet, M. Dabek, D. Daviaud, S. Dauvillier, B. Majed, Y. Y. Wang, A. Meulle, B. Salles, S. Le Gondec, I. Garrido, G. Escourrou, P. Valet, C. Muller, Cancer-associated adipocytes exhibit an activated phenotype and contribute to breast cancer invasion. *Cancer Res.* **71**, 2455–2465 (2011).
46. M. M. A. Silva, L. E. Kokai, V. S. Donnenberg, J. L. Fine, K. G. Marra, A. D. Donnenberg, M. S. Neto, J. P. Rubin, Oncologic safety of fat grafting for autologous breast reconstruction in an animal model of residual breast cancer. *Plast. Reconstr. Surg.* **143**, 103–112 (2019).
47. I. Vitale, E. Shema, S. Loi, L. Galluzzi, Intratumoral heterogeneity in cancer progression and response to immunotherapy. *Nat. Med.* **27**, 212–224 (2021).
48. J. Backdahl, L. Franzen, L. Massier, Q. Li, J. Jalkanen, H. Gao, A. Andersson, N. Bhalla, A. Thorell, M. Ryden, P. L. Stahl, N. Mejhert, Spatial mapping reveals human adipocyte subpopulations with distinct sensitivities to insulin. *Cell Metab.* **33**, 1869–1882.e6 (2021).
49. M. Norreen-Thorsen, E. C. Struck, S. Oling, M. Zwahlen, K. Von Feilitzen, J. Odeberg, C. Lindskog, F. Ponten, M. Uhlen, P. J. Dusart, L. M. Butler, A human adipose tissue cell-type transcriptome atlas. *Cell Rep.* **40**, 111046 (2022).
50. M. P. Emont, C. Jacobs, A. L. Essene, D. Pant, D. Tenen, G. Colleluori, A. Di Vincenzo, A. M. Jorgensen, H. Dashti, A. Stefek, E. McGonagle, S. Strobel, S. Laber, S. Agrawal, G. P. Westcott, A. Kar, M. L. Veregge, A. Gulko, H. Srinivasan, Z. Kramer, E. De Filippis, E. Merkel, J. Ducie, C. G. Boyd, W. Gourash, A. Courcoulas, S. J. Lin, B. T. Lee, D. Morris, A. Tobias, A. V. Khera, M. Claussnitzer, T. H. Pers, A. Giordano, O. Ashenberg, A. Regev, L. T. Tsai, E. D. Rosen, A single-cell atlas of the human and mouse white adipose tissue. *Nature* **603**, 926–933 (2022).
51. J. B. Allard, C. Duan, IGF-binding proteins: Why do they exist and why are there so many? *Front. Endocrinol. (Lausanne)* **9**, 117 (2018).
52. S. B. Wheatcroft, M. T. Kearney, A. M. Shah, V. A. Ezzat, J. R. Miell, M. Modo, S. C. Williams, W. P. Cawthorn, G. Medina-Gomez, A. Vidal-Puig, J. K. Sethi, P. A. Crossey, IGF-binding protein-2 protects against the development of obesity and insulin resistance. *Diabetes* **56**, 285–294 (2007).
53. C. Wittenbecher, M. Ouni, O. Kuxhaus, M. Jahnert, P. Gottmann, A. Teichmann, K. Meidtnier, J. Kriebel, H. Gallert, T. Pischon, H. Boeing, M. B. Schulze, A. Schurmann, Insulin-like growth factor binding protein 2 (IGFBP-2) and the risk of developing type 2 diabetes. *Diabetes* **68**, 188–197 (2019).
54. V. D'Esposito, F. Passaretti, A. Hammarstedt, D. Liguoro, D. Terracciano, G. Molea, L. Canta, C. Miele, U. Smith, F. Beguinot, P. Formisano, Adipocyte-released insulin-like growth factor-1 is regulated by glucose and fatty acids and controls breast cancer cell growth in vitro. *Diabetologia* **55**, 2811–2822 (2012).
55. M. M. M. Almekinders, M. Schaapveld, B. Thijssen, L. L. Visser, T. Bismeyer, J. Sanders, E. Isnaldi, I. Hofland, M. Mertz, L. F. A. Wessels, A. Broeks, E. Hooijberg, W. Zwart, E. H. Lips, P. C. Grand Challenge, C. Desmedt, J. Wesseling, Breast adipocyte size associates with ipsilateral invasive breast cancer risk after ductal carcinoma in situ. *NPJ Breast Cancer* **7**, 31 (2021).
56. M. Pollak, The insulin and insulin-like growth factor receptor family in neoplasia: An update. *Nat. Rev. Cancer* **12**, 159–169 (2012).
57. C. L. Soh, K. McNeil, C. M. Owczarek, M. P. Hardy, L. J. Fabri, M. Pearce, C. A. Delaine, B. E. Forbes, Exogenous administration of protease-resistant, non-matrix-binding IGFBP-2 inhibits tumour growth in a murine model of breast cancer. *Br. J. Cancer* **110**, 2855–2864 (2014).
58. J. Yamaguchi, H. Ohtani, K. Nakamura, I. Shimokawa, T. Kanematsu, Prognostic impact of marginal adipose tissue invasion in ductal carcinoma of the breast. *Am. J. Clin. Pathol.* **130**, 382–388 (2008).
59. D. Ishay-Ronen, M. Diepenbruck, R. K. R. Kalathur, N. Sugiyama, S. Tiede, R. Ivanek, G. Bantug, M. F. Morini, J. Wang, C. Hess, G. Christofori, Gain fat - lose metastasis: Converting invasive breast cancer cells into adipocytes inhibits cancer metastasis. *Cancer Cell* **35**, 17–32.e6 (2019).
60. P. Bankhead, M. B. Loughrey, J. A. Fernandez, Y. Dombrowski, D. G. McArt, P. D. Dunne, S. McQuaid, R. T. Gray, L. J. Murray, H. G. Coleman, J. A. James, M. Salto-Tellez, P. W. Hamilton, QuPath: Open source software for digital pathology image analysis. *Sci. Rep.* **7**, 16878 (2017).
61. N. L. E. Harris, C. Vennin, J. R. W. Conway, K. L. Vine, M. Pinese, M. J. Cowley, R. F. Shearer, M. C. Lucas, D. Herrmann, A. H. Allam, M. Pajic, J. P. Morton; Australian Pancreatic Cancer Genome Initiative, A. V. Biankin, M. Ranson, P. Timpson, D. N. Saunders, SerpinB2 regulates stromal remodelling and local invasion in pancreatic cancer. *Oncogene* **36**, 4288–4298 (2017).
62. G. Jacquemet, H. Baghirov, M. Georgiadou, H. Sihto, E. Pehu, P. Cettour-Janet, T. He, M. Perala, P. Kronqvist, H. Joensuu, J. Ivaska, L-type calcium channels regulate filopodia stability and cancer cell invasion downstream of integrin signalling. *Nat. Commun.* **7**, 13297 (2016).
63. L. Oksa, A. Makinen, A. Nikkila, N. Hyvarinen, S. Laukkanen, A. Rokka, P. Haapaniemi, M. Seki, J. Takita, O. Kauko, M. Heinaniemi, O. Lohi, Arginine methyltransferase PRMT7 deregulates expression of RUNX1 target genes in T-cell acute lymphoblastic leukemia. *Cancers (Basel)* **14**, 2169 (2022).
64. J. Goedhart, D. von Stetten, M. Noircerc-Savoye, M. Lelimosin, L. Joosen, M. A. Hink, L. van Weeren, T. W. Gadella Jr., A. Royant, Structure-guided evolution of cyan fluorescent proteins towards a quantum yield of 93%. *Nat. Commun.* **3**, 751 (2012).
65. S. J. Aper, A. C. van Spreuwel, M. C. van Turnhout, A. J. van der Linden, P. A. Pieters, N. L. van der Zon, S. L. de la Rangelbe, C. V. Bouten, M. Merck, Colorful protein-based fluorescent probes for collagen imaging. *PLoS ONE* **9**, e114983 (2014).
66. T. D. Schmittgen, K. J. Livak, Analyzing real-time PCR data by the comparative CT method. *Nat. Protoc.* **3**, 1101–1108 (2008).
67. Y. Perez-Riverol, J. Bai, C. Bandla, D. Garcia-Seisdedos, S. Hewapathirana, S. Kamatchinathan, D. J. Kundu, A. Prakash, A. Frericks-Zipper, M. Eisenacher, M. Walzer, S. Wang, A. Brazma, J. A. Vizcaino, The PRIDE database resources in 2022: A hub for mass spectrometry-based proteomics evidences. *Nucleic Acids Res.* **50**, D543–D552 (2022).

**Acknowledgments:** We thank P. Laasola and J. Siivonen for technical assistance and the Ivaska lab for scientific discussion and feedback on the manuscript. We thank H. Hamidi for the illustrations and for editing the manuscript. For services, instrumentation, and expertise at Turku Bioscience (University of Turku, Turku, Finland), we would like to thank the Cell Imaging and Cytometry Core, Genome Editing Core, Turku Proteomics Facility, and Turku Centre for Disease Modelling, which are all supported by BioCenter Finland. Similarly, the Euro-Biologging Finnish Node (Turku, Finland) and University of Turku HistoCore are also acknowledged for services, instrumentation, and expertise. The clone pENTR221-IGFBP2 was from the ORFeome library at the Genome Biology Unit core facility, supported by HiLIFE and the Faculty of Medicine, University of Helsinki, as well as BioCenter Finland. We also thank L. Polari and D. Toivola (Åbo Akademi, Turku, Finland) for FPPE healthy mouse tissue sections. **Funding:** This work was supported by the Finnish Cancer Institute, K. Albin Johansson Professorship (to J.I.); Academy of Finland Research project 325464 (to J.I.); Academy of Finland Centre of Excellence program 346131 (to J.I.); Cancer Foundation Finland (to J.I.); Sigrid Juselius Foundation (to J.I.); Worldwide Cancer Research 23-0123 (to J.I.); Jane and Aatos Erkkö Foundation (to J.I.); Academy of Finland InFLAMES Flagship Programme 337530 (to J.I.); the European Union's Horizon 2020 research and innovation program under Marie Skłodowska-Curie grant agreement 841973 (to J.R.W.C.); Academy of Finland postdoctoral research grant 338585 (to J.R.W.C.); Academy of Finland postdoctoral research grant 332402 (to G.F.); Sigrid Juselius Foundation (to E.P.); Academy of Finland research fellowship 323096 (to E.P.); Hospital District of Southwest Finland 11083 (to E.P.); UTUGS graduate school (to D.D.D.); and UTUGS graduate school (to O.P.). **Author contributions:** J.R.W.C., D.D.D., G.F., and J.K. performed the experiments. J.R.W.C. and G.F. undertook the data analysis. D.D.D., O.P., P.B., and P.H. provided resources. D.D.D., G.F., and O.P. provided methodology. J.R.W.C., E.P., and J.I. reviewed and edited the manuscript. J.R.W.C. and J.I. wrote the original draft of the manuscript. E.P. and J.I. supervised the project. J.I. obtained research funding. **Competing interests:** The authors declare that they have no competing interests. **Data and materials availability:** All data needed to evaluate the conclusions in the



paper are present in the paper and/or the Supplementary Materials. The mass spectrometry proteomics data have been deposited to the ProteomeXchange Consortium via the PRIDE (67) partner repository with dataset identifier PXD036479. Plasmids are available through the Addgene plasmid repository using the given identifiers—pENTR221-IGFBP2-Clover (Addgene, #191007), pENTR2b-mTurquoise2 (Addgene, #191014), pLenti6.3/TO/V5-DEST-IGFBP2 (Addgene, #191006), pLenti6.3/TO/V5-DEST-IGFBP2-Clover (Addgene, #191008), or pLenti6.3/

TO/V5-DEST-mTurquoise2 (Addgene, #191010)—or through contacting one of the corresponding authors, J.R.W.C. (jdconw@utu.fi) or J.I. (joivaska@utu.fi).

Submitted 7 December 2022

Accepted 8 June 2023

Published 12 July 2023

10.1126/sciadv.adg1840

Supplementary Materials for  
**IGFBP2 secretion by mammary adipocytes limits breast cancer invasion**

James R. W. Conway *et al.*

Corresponding author: James R. W. Conway, [jdconw@utu.fi](mailto:jdconw@utu.fi); Johanna Ivaska, [joivaska@utu.fi](mailto:joivaska@utu.fi)

*Sci. Adv.* **9**, eadg1840 (2023)  
DOI: 10.1126/sciadv.adg1840

**The PDF file includes:**

Figs. S1 to S5  
Legends for data S1 to S3

**Other Supplementary Material for this manuscript includes the following:**

Data S1 to S3

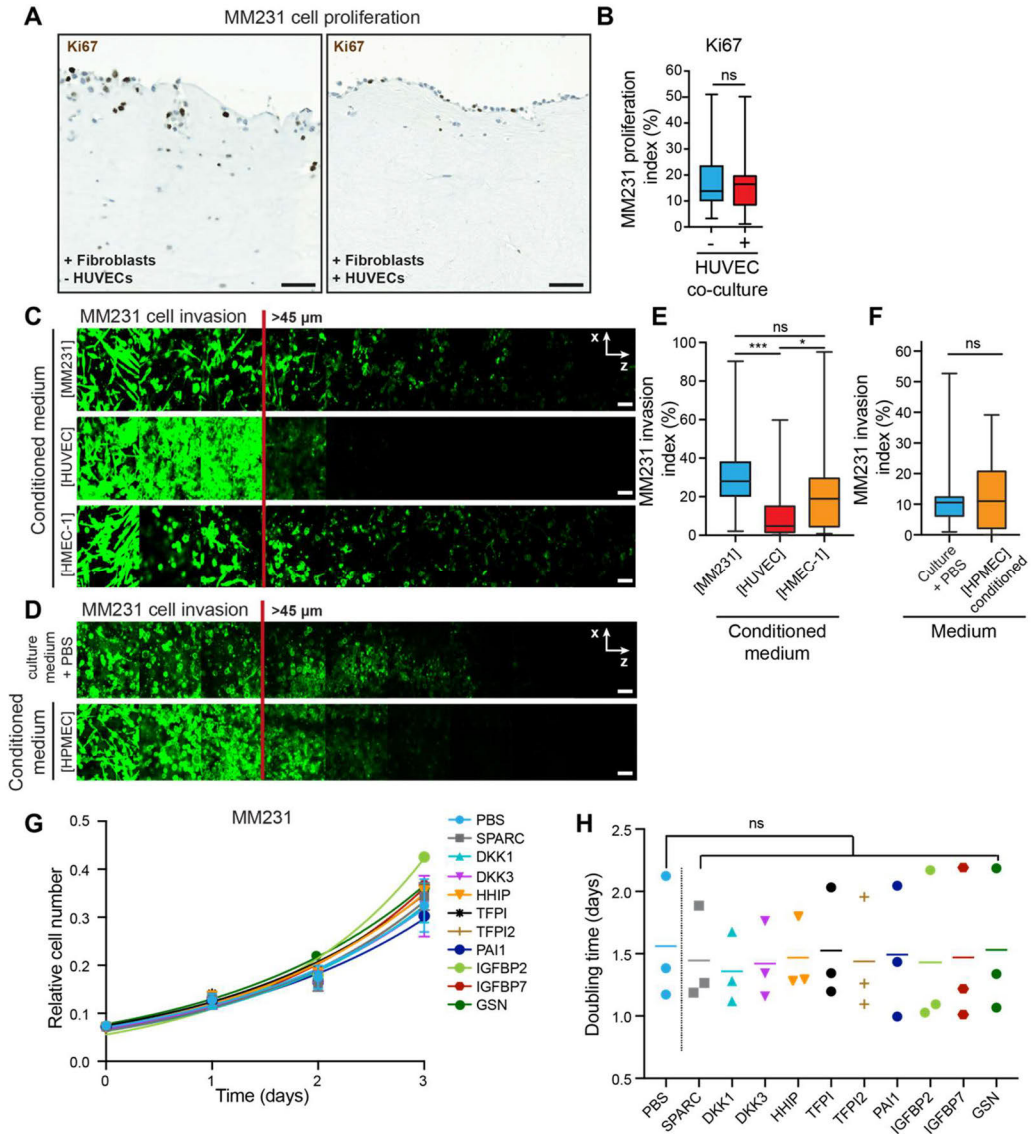


**Fig. S1. HUVEC co-culture and secreted factors had no significant effect on MM231 proliferation.**

(A and B) Representative images (A) and quantification (B) of MM231 cell proliferation (stained with Ki67) during invasion into fibroblast-contracted 3D collagen matrices  $\pm$  HUVEC co-culture, performed in the presence of endothelial growth factor-reduced medium. Scale bars, 50  $\mu$ m. (n = 3 biological replicates, triplicate matrices, 8 regions/condition/replicate; one-way ANOVA with a Tukey correction; \* $p < 0.05$ , \*\* $p < 0.01$ , \*\*\* $p < 0.001$ , ns – not significant). (C to F) Representative images (C and D) and quantification (E and F) of MM231 breast cancer cell invasion in inverted collagen/fibronectin matrices in the presence of concentrated conditioned media (given in square brackets) from either MM231, HMEC-1 or HUVEC cells (C) or from HPMEC cells, compared to medium with the same volume of PBS as a control (D). Scale bars, 50  $\mu$ m. (n=3 biological replicates performed in triplicate; one-way ANOVA

with a Tukey correction (E); two-tailed Student's t-test with a Welch's correction (F); \* $p < 0.05$ , \*\*\* $p < 0.001$ , ns – not significant). (G and H) Representative curves (G) and doubling times (H) from the relative cell density of MM231 cells treated with the given recombinant secreted factors (5  $\mu\text{M}$ ) on day 0, 1, 2, 3, against PBS as a control (Performed with 5 wells/treatment condition;  $n=3$  biological replicates; one-way ANOVA with a Dunnett correction; ns – not significant).

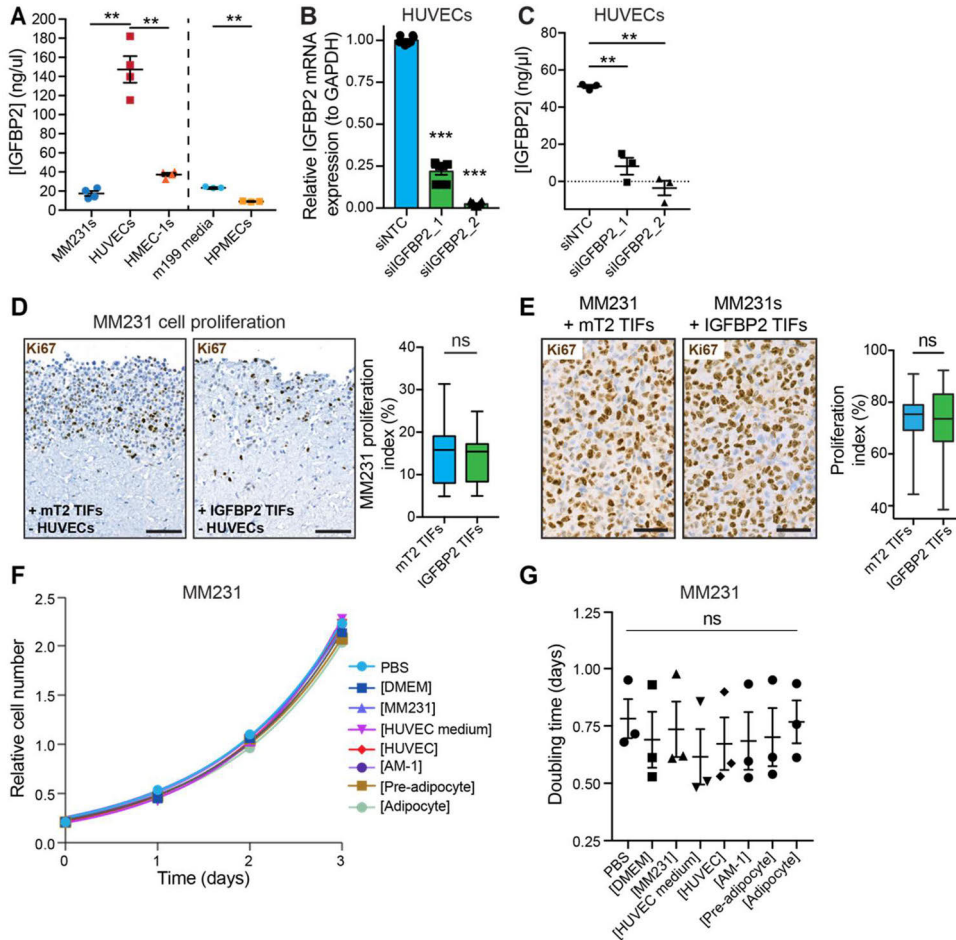


**Fig. S2. Neither conditioned media, nor TIF-derived IGFBP2, had any significant effect on MM231 proliferation.**

(A) ELISA assays for human IGFBP2 from conditioned media from MM231s, HUVECs, HMEC-1s, and from m199 media and HPMECs (n = 3-4; one-way ANOVA with a Tukey correction; \*\*p<0.01). (B) Assessment of relative mRNA levels by qRT-PCR of RNA isolated from HUVECs after transfection with siRNAs against *IGFBP2* (siIGFBP2\_1 and siIGFBP2\_2) and siNTC (n=3; one-sample t-test; \*\*\*p<0.001). (C) ELISA assays for human IGFBP2 from conditioned media measured in duplicate (n=3; one-way ANOVA with a Dunnett correction; \*\*\*p<0.001). (D) Representative images and quantification of Ki67 stained organotypic invasions from mT2 or IGFBP2 TIF-contracted matrices, where MM231 cancer cells invaded for 14 days and are positive for Ki67 (brown nuclei if actively proliferating; n=3 biological replicates, triplicate matrices, 8 regions/condition/replicate; one-way ANOVA with a Tukey correction; ns – not significant). Scale bars, 100  $\mu$ m. (E) Representative images of Ki67 stained MM231 xenografts, co-injected with TIFs overexpressing either mT2 (control) or IGFBP2. Quantification of positive (brown) to negative (blue) staining of Ki67 in 400  $\mu$ m<sup>2</sup> regions of interest from subcutaneous xenografts (n=10 (mT2) and 12 (IGFBP2); two-tailed Student's t test with a Welch's correction; ns – not significant). Scale bars, 50  $\mu$ m. (F and G) Representative curves (F) and doubling times (G) from the relative cell density of MM231 cells treated with conditioned media (given in square brackets) from MM231, HUVEC, pre- and mature adipocytes, against their respective concentrated growth medias as controls (Performed

with 3 wells/treatment condition; n = 3 biological replicates; one-way ANOVA with a Dunnett correction; ns – not significant).

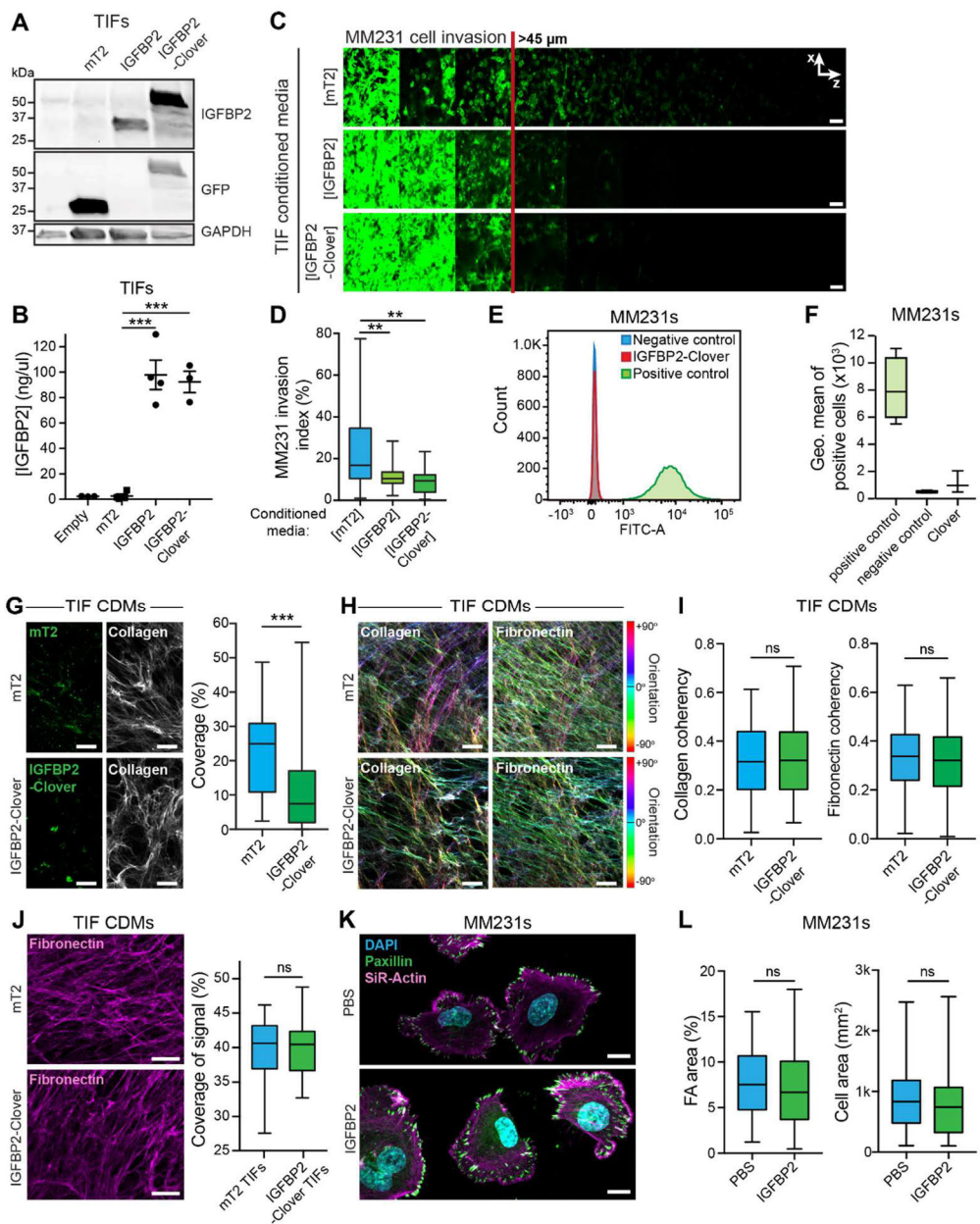


**Fig. S3. IGFBP2 does not bind to the cancer cell surface or ECM.**

(A) Representative western blot of TIFs stably overexpressing mT2, IGFBP2 or IGFBP2-Clover. (B) ELISA assays for human IGFBP2 from conditioned media (n=3; one-way ANOVA with a Tukey correction; \*\*\*p<0.01). (C and D) Representative images (C) and quantification (D) of MM231 breast cancer cells invading into inverted collagen/fibronectin matrices in the presence of concentrated conditioned media (given in square brackets) from mT2, IGFBP2 or IGFBP2-Clover overexpressing TIF cells (n=3 biological replicates performed in triplicate with 3 stacks/transwell; one-way ANOVA with a Tukey correction; \*\*p<0.01). Scale bars, 50 μm. (E and F) Representative flow cytometry plot (E) and geometric means (F) from MM231 cancer cells expressing either IGFBP2-Clover (positive control) or treated with IGFBP2-

Clover exogenously (IGFBP2-Clover treatment), compared to treatment with exogenous untagged IGFBP2 (negative control; n = 3). **(G)** Representative images and quantification of signal coverage beyond an equal intensity threshold of CDMs derived from TIFs overexpressing either IGFBP2-Clover or mT2. The brightness of the mT2 and IGFBP2-Clover fluorescence channels was increased for visualization purposes to show the weak non-specific background signal in both (n=4, 8 ROI/condition/replicate; two-tailed Student's t-test with a Welch's correction; \*\*\*p<0.001). Scale bars, 50  $\mu$ m. Images adjusted for display. **(H and I)** Representative images (H) and quantification of the coherency (I) from the fiber orientation analysis of the collagen I (CNA35-mCherry) or fibronectin labelling of CDMs from TIFs overexpressing either mT2 or IGFBP2. Scale bars, 50  $\mu$ m. (n=4, 8 ROI/condition/replicate; two-tailed Student's t-test with a Welch's correction; \*p<0.05, ns – not significant). **(J)** Representative images of fibronectin-stained CDMs derived from TIFs overexpressing either IGFBP2 or mT2, as well as quantification of the coverage of the fibronectin signal (n=4, 8 ROI/condition/replicate; two-tailed Student's t-test with a Welch's correction; \*p<0.05, ns – not significant). Scale bars, 50  $\mu$ m. **(K and L)** Representative immunofluorescence images (K) and quantification (L) of MM231 cell and focal adhesion (FA) area after seeding on a mixture of collagen/fibronectin in the presence or absence of IGFBP2 (5  $\mu$ M); stained with DAPI, paxillin and SiR-Actin. Scale bars, 10  $\mu$ m. (n = 3 biological replicates with >20 cells/replicate; two-tailed Student's t-test with a Welch's correction; ns – not significant).



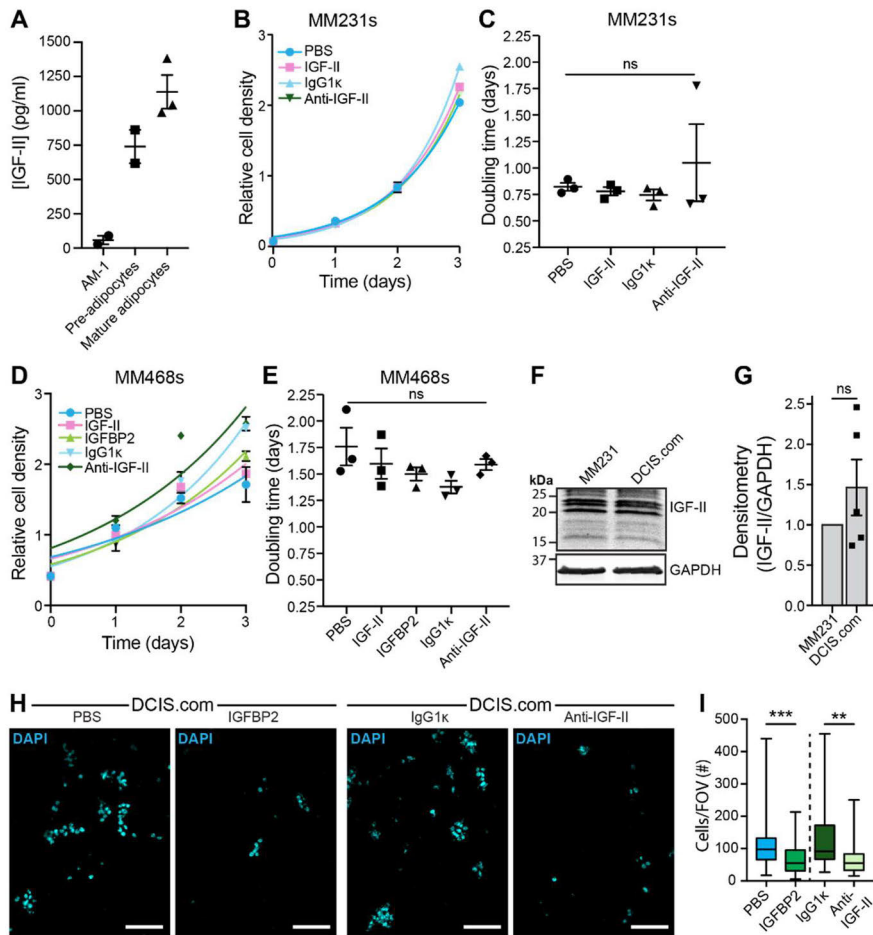


**Fig. S4. IGF-II is important for DCIS.com invasion, while having no effect on MM231 and MM468 cell proliferation.**

(A) ELISA assays for human IGF-II in conditioned media from pre- (n = 2 biological replicates) and mature adipocytes (n = 3 biological replicates), compared to the adipocyte culture media (AM-1). (B and C) Representative curves (B) and doubling times (C) from the relative cell density of MM231 cells treated with PBS, IGF-II (10 ng/ml), IgG (10 μg/ml) or anti-IGF-II (10 μg/ml; n = 3 biological replicates; one-way ANOVA with a Tukey correction; ns – not significant). (D and E) Representative curves (D) and doubling times (E) from the relative cell density of MM468 cells treated with PBS, IGF-II (10 ng/ml), IGFBP2 (5 μM), IgG (10 μg/ml) or anti-IGF-II (10 μg/ml; n = 3 biological replicates; one-way ANOVA with a Tukey correction; ns – not significant). (F and G) Representative IGF-II western blot (F) and quantification (G) from MM231 and DCIS.com cells (n = 5 biological replicates; one-sample t-test; ns – not significant). (H and I) Matrigel invasion assays for DCIS.com cells treated with PBS or IGFBP2, or IgG1κ or anti-IGF-II (n = 3, 8 fields of view (FOVs)/chamber, 2 invasion chambers/condition/replicate; two-tailed Student's t-test with a Welch's correction; \*\*\*p<0.001). Scale bars, 100 μm.

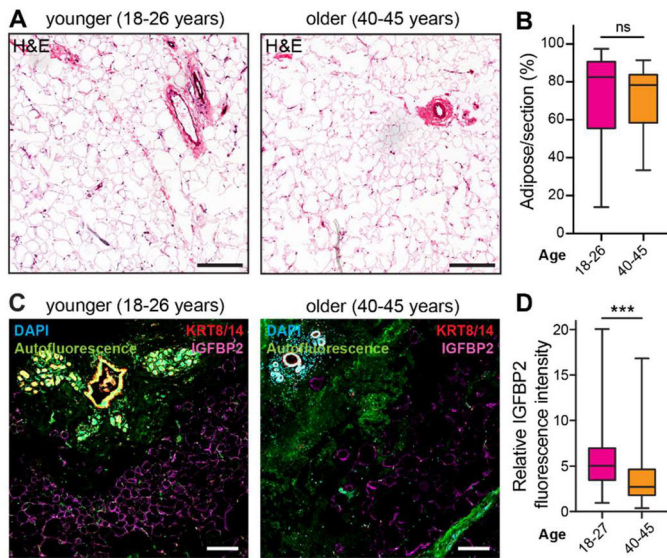


**Fig. S5. IGFBP2 levels in mammary adipocytes are reduced in older patients.**

(A) Representative H&E stained samples from younger (18-26 years; n = 4 patients) and older (40-45 years; n = 4 patients) healthy patient samples. Scale bars, 250  $\mu$ m. (B) Quantification of adipocytes/section from older and younger patients (3-8 sections/patient; two-tailed Student's t-test with a Welch's correction; ns, not significant). (C) Representative images from patients stained for IGFBP2 (magenta) and counterstained with DAPI (cyan) and keratin-8/-14 (KRT8/14; red). Autofluorescence signal is given in green. Scale bars, 200  $\mu$ m. (D) Quantification of IGFBP2 in adipocytes relative to unstained background (n = 4 normal reduction mammoplasty patient samples in each age group; 143-280 adipocytes/patient/group; two-tailed Mann-Whitney U test; \*\*\*p<0.001).

**Data S1. (separate file “Data S1 - Secretomes.xlsx”)**

Comparison of four published HUVEC secretomes for common angiocrine factors.

**Data S2. (separate file “Data S2 - Patient details.xlsx”)**

Patient details for those included in the study.

**Data S3. (separate file “Data S3 - Mass spectrometry analysis.xlsx”)**

Analysis of GFP-trap mass spectrometry data for IGFBP2- or GFP-bound protein.



**TURUN  
YLIOPISTO**  
UNIVERSITY  
OF TURKU

ISBN 978-951-29-9937-8 (PRINT)  
ISBN 978-951-29-9938-5 (PDF)  
ISSN 0355-9483 (Print)  
ISSN 2343-3213 (Online)